

## ABSTRACT

Title of Dissertation: MEASUREMENT OF ULTRAFAST DYNAMICS IN  
THE INTERACTION OF INTENSE LASER PULSES  
WITH GASES, ATOMIC CLUSTERS, AND PLASMAS

Ki-Yong Kim, Doctor of Philosophy, 2003

Dissertation directed by: Professor Howard M. Milchberg  
Institute for Physical Science and Technology

We have investigated the time resolved dynamics of intense, ultrashort pulse laser interactions with gases, nanometer-size clusters, and plasma waveguides. To probe the ultrafast dynamics in these interactions, we developed a new femtosecond optical diagnostic, *single-shot supercontinuum spectral interferometry* (SSSI), which measures ultra-rapid transients induced by an intense laser pulse in the complex index of refraction. The measurement of the transient refractive index in intense laser-heated materials provides a direct view of how the laser-produced perturbation evolves in time and space. Our SSSI diagnostic is capable of  $\sim 10$  fs temporal resolution on a temporal window  $\sim 1.5$  ps long, along with  $\sim 7$   $\mu\text{m}$  one-dimensional (1D) spatial resolution.

SSSI was first applied to probe the ionization dynamics of helium gas under the irradiation of high intensity ( $\sim 10^{17}$  W/cm<sup>2</sup>) laser pulses. It revealed a characteristic

stepwise transition process  $\text{He} \rightarrow \text{He}^+ \rightarrow \text{He}^{2+}$ , in agreement with the optical field ionization model. This measurement was used as a test case to demonstrate that finite laser-target interaction lengths can strongly affect the interpretation of all measurements involving extraction of transient phases.

The time-resolved explosion dynamics of intense ( $\sim 10^{15}$  W/cm<sup>2</sup>) laser-heated clusters was also studied with SSSI and additional ultrafast optical diagnostics. Here, the ultrafast processes are ionization and rapid cluster plasma explosion. The measurement strongly supports our laser-cluster interaction scenario in which laser-heated clusters explode layer-by-layer, and the laser is strongly coupled at critical density. For the cluster sizes and laser intensities of this experiment, the measured several hundred-femtosecond evolution timescale of laser-heated clusters can be understood in terms of plasma hydrodynamics. A major implication of our understanding of microscopic cluster dynamics was the prediction and observation of self-focusing in clustered gases.

Finally, using SSSI, we have explored the interaction of intense laser pulses with preformed plasma waveguides. This measurement revealed the presence of guided laser-induced distortions such as ionization, which can lead to degraded waveguide performance. To overcome this problem, a funnel-mouthed plasma waveguide was developed and diagnosed. In addition, a new plasma waveguide generation method has been demonstrated, which uses the unique features associated with the laser-cluster interaction – self-focusing and strong absorption.

MEASUREMENT OF ULTRAFAST DYNAMICS IN THE INTERACTION OF  
INTENSE LASER PULSES WITH GASES, ATOMIC CLUSTERS, AND PLASMAS

by

Ki-Yong Kim

Dissertation submitted to the Faculty of the Graduate School of the  
University of Maryland, College Park in partial fulfillment  
of the requirements for the degree of  
Doctor of Philosophy  
2003

Advisory Committee:

Professor Howard M. Milchberg, Chair  
Professor Thomas M. Antonsen, Jr.  
Professor Thomas E. Murphy  
Professor Steven Rolston  
Professor Rajarshi Roy

© Copyright by

Ki-Yong Kim

2003

## ACKNOWLEDGEMENTS

This dissertation, truly, would not have appeared without help from many individuals.

First, I would like to give my special thanks to my advisor, Prof. Howard Milchberg for making this research work achievable by inspiring and training me with his careful and enduring mentorship, as well as providing a well-equipped research environment through my doctoral training period. He also deserves special thanks for careful reading and editing of this dissertation. It is my joy to work with him.

I would also like to thank our young scientists – Dr. Ilya Alexeev, Dr. Jay Fan, Dr. Vinod Kumarappan, Dr. Stuart McNaught, Dr. Sergei Nikitin, Dr. Enrique Parra, Mr. Jianwei Liu, and Mr. Hua Sheng – for their vital help in many experiments and their friendships for many years. I also express my gratitude to our theorist colleagues – Prof. Thomas Antonsen, Dr. Zhigang Bian, Mr. James Cooley, Mr. Ayush Gupta, and Mr. Jianzhou Wu – for fruitful discussions on many scientific topics. I also express my gratitude to Dr. Anatoly Faenov and Dr. Tania Pikuz (VNIIFTRI Inst. of Moscow) for their devoted efforts in our recent collaborative experiment.

I am also indebted to our machinist, Edd Cole, for his teaching me the basics of machining. I also thank our undergraduate students, Mr. Brian Epstein and Mr. Brian Layer for their constant help in many mechanical machining.

Finally, I am grateful to my friends and family – parents, my wife (Yeonjung) and my son (Alex Joonwoo) – for their endless love and care so that I could complete this dissertation successfully.

## TABLE OF CONTENTS

Acknowledgments.....	ii
Table of Contents.....	iii
List of Table.....	viii
List of Figures .....	ix
Chapter 1: Introduction and overview.....	1
1.1 Overview of intense laser–matter interactions.....	1
1.2 Laser-driven ionization of gases.....	3
1.2.1 Ionization mechanisms.....	3
1.2.2 Optical field ionization and collisional ionization.....	5
1.3 Ultrafast optical diagnostics for high intensity laser–matter interaction.....	6
1.4 Interaction of intense femtosecond laser pulses with gases.....	9
1.5 Interaction of intense laser pulses with clusters.....	11
1.6 Interaction of intense laser pulses with plasma waveguides.....	14
1.7 Synopsis.....	15
Chapter 2: Single-shot supercontinuum spectral interferometry.....	21
2.1 Introduction.....	21
2.2 Spectral interferometry.....	21
2.3 Single-shot supercontinuum spectral interferometry (SSSI).....	23
2.3.1 Introduction.....	23
2.3.2 Principle of SSSI.....	24
2.4 Experimental demonstration of SSSI – cross phase modulation in glass.....	25

2.4.1 Experimental setup.....	26
2.4.2 Spectral phase extraction and chirp characterization.....	27
2.4.3 Experimental results.....	29
2.5 Limitations of SSSI.....	31
2.6 Conclusions.....	33
Chapter 3: Femtosecond multi-terawatt Ti:sapphire laser system.....	41
3.1 CPA technique and Ti:sapphire laser.....	41
3.2 Femtosecond pulse train generation (oscillator).....	42
3.3 Pulse stretcher.....	45
3.4 Laser pulse energy amplification.....	46
3.4.1 Regenerative pulse energy amplification.....	46
3.4.2 Multi-pass power amplification.....	49
3.5 Pulse compressor.....	51
3.6 Femtosecond laser pulse characterization.....	54
3.7 Conclusions and future upgrade.....	55
Chapter 4: Femtosecond laser-induced ionization of helium.....	63
4.1 Introduction.....	63
4.2 ADK tunneling ionization model of helium.....	64
4.3 Experimental results.....	66
4.4 Simulation of probe propagation in helium plasma: beam propagation method.....	68
4.5 Conclusions.....	72
Chapter 5: Characterization of cluster sources.....	82

5.1 Atomic and molecular cluster source.....	82
5.2 Rayleigh scattering by neutral clusters.....	85
5.3 Measurement of the average cluster size and density.....	87
5.3.1 Theory of Rayleigh scattering and neutral cluster gas interferometry.....	87
5.3.2 Experimental measurement of cluster size and density.....	89
5.3.3 Consideration of cluster size distribution and cluster-monomer ratio.....	92
5.4 Elongated cluster gas jet and its characterization.....	93
5.4.1 Elongated cluster source.....	93
5.4.2 Rayleigh scattering experiment.....	95
5.4.3 Interferometry and shadowgraphy of elongated cluster jet.....	97
5.4.4 Measurement of the average cluster size and density.....	98
5.5 Conclusions.....	99
Chapter 6: The interaction of intense laser pulses with atomic clusters.....	113
6.1 Introduction.....	113
6.2 1D plasma hydrodynamic laser-cluster interaction model.....	114
6.3 Scattering by laser-heated clusters.....	119
6.3.1 Rayleigh scattering by laser-heated clusters .....	120
6.3.2 The effect of laser prepulse.....	121
6.4 Time-resolved two-color scattering and absorption experiment.....	123
6.5 Measurement of transient complex polarizability of laser-heated clusters.....	124
6.5.1 Experimental setup and results.....	125

6.5.2 Interpretation of results.....	127
6.6 Conclusions.....	129
Chapter 7: Ultrafast measurements of guiding of intense femtosecond laser pulses in a plasma channel.....	138
7.1 Introduction.....	138
7.2 Pre-formed plasma waveguide and taper issue.....	140
7.3 Funnel-mouthed plasma waveguide generation and characterization.....	142
7.3.1 Experimental setup.....	142
7.3.2 Funnel generation and intense laser pulse injection.....	144
7.4 Generation of plasma waveguides in a cluster gas jet.....	147
7.4.1 Self-focusing of intense laser pulses in a clustered gas.....	147
7.4.2 Generation of plasma waveguides in cluster jets.....	150
7.5 Conclusions.....	152
Appendix A: Historical evolution of high peak power lasers.....	163
Appendix B: Brief overview of high intensity laser physics.....	168
Appendix C: Spectral interferometry (SI).....	173
C.1 Theoretical background.....	173
C.2 Principle of spectral interferometry (SI).....	174
C.3 Demonstration of multi-shot spectral interferometry.....	177
Appendix D: Generation of a supercontinuum light pulse.....	182
Appendix E: Transient phase measurement with a chirped pulse.....	186
E.1 Description of chirped pulses in time and frequency domains.....	186
E.2 Derivation of temporal resolution associated with direct mapping.....	187

E.3 Direct mapping: simulation.....	188
E.4 Derivation of transient phase shifts using Fourier transform.....	189
Appendix F: Fourier-transform fringe analysis.....	192
F.1 Interferometric fringe analysis with Fourier-transform technique.....	192
Appendix G: Optical material dispersion.....	196
Appendix H: Synchronization of Ti:sapphire and Nd:YAG laser systems.....	199
List of References.....	201
Chapter 1 References.....	201
Chapter 2 References.....	205
Chapter 3 References.....	207
Chapter 4 References.....	210
Chapter 5 References.....	212
Chapter 6 References.....	215
Chapter 7 References.....	218
Appendix A References.....	221
Appendix B References.....	224
Appendix C References.....	226
Appendix D References.....	227
Appendix E References.....	228
Appendix F References.....	228
Appendix G References.....	228

## LIST OF TABLES

Table 5.1: The values of $k_H$ , $r_{WS}$ , and inter-cluster atomic density for noble gases	85
Table G.1: GDD, TOD, 4OD for a variety of optical glasses at 800 nm.	199

## LIST OF FIGURES

Figure 1.1: Focusing of ultrashort high power laser pulses in a small volume for high intensity laser–matter interaction experiments.	17
Figure 1.2: Three different laser-induced ionization mechanisms: (a) multiphoton, (b) tunneling, and (c) over-the-barrier (barrier suppression) ionization.	17
Figure 1.3: Two pump-probe diagnostic schemes: (a) multi-shot and (b) single-shot.	18
Figure 1.4: Interaction of an intense laser pulse with atomic or molecular clusters produces energetic electrons and ions, x-rays, and extreme ultraviolet (EUVs).	19
Figure 1.5: Diagram illustrating the interaction of intense laser fields with clusters.	19
Figure 1.6: Laser wakefield excitation scheme in a preformed plasma waveguide. SSSI can potentially detect the electron density oscillations in the waveguide with one-dimensional (1D) spatio-temporal information in a single-shot.	20
Figure 2.1: (a) Multi-shot spectral interferometry layout. (b) Single-shot chirped spectral interferometry diagnostic layout.	34
Figure 2.2: (a) Schematic of cross phase modulation (XPM) of a probe pulse induced by an intense pump pulse in fused silica glass. (b) XPM experimental setup, showing pump, reference, and probe beams, dispersive window (DW), dichroic splitter (DS), 1-mm-thick fused silica glass (FS), pump removal mirror (M), and imaging spectrometer. Sample spectral interferogram image from optical Kerr-induced XPM in FS is also shown.	35
Figure 2.3: (a) Raw chirped spectral interferogram with XPM. (b) Extracted spectral phase $\Delta\phi(x, \lambda)$ using fast Fourier transform (FFT) phase extraction method shown in (i)-(iii).	36
Figure 2.4: Determination of the chirp parameter of the SC pulse. Two methods [(a) and (b)] are possible. (a-i) Spectral phase plots were extracted for a sequence of incremental delays ( $\Delta t = 66$ fs) of the pump for DW = 22.2 mm BK7. The plots are vertically offset for clarity. (a-ii) Linear least squares fit of the phase peaks versus time delay gave $a_2 = (2.40 \pm 0.03) \times 10^3$ fs <sup>2</sup> for DW = 22.2 mm BK7. (b-i) Raw probe spectral intensity modulations with varying pump-probe delay. (b-ii) Plot of wavelength at modulation peaks vs. pump-probe delay with a linear least squares fit.	37

Figure 2.5: (a) Experimental [(i)-(iii)] and corresponding theoretical [(i')-(iii')] transient phase extracted using direct frequency-to-time mapping for chirp parameters (i) $a_1 = 1.06 \times 10^3 \text{ fs}^2$ , (ii) $a_2 = 2.40 \times 10^3 \text{ fs}^2$ , and (iii) $a_3 = 6.85 \times 10^3 \text{ fs}^2$ . The plots are space-central time line-outs of the full phase images. (b) Full Fourier extraction of transient phase for the three chirps of (a). Experimental results: (i)-(iii). Corresponding simulations: (i')-(iii').	38
Figure 2.6: Full time and one-dimensional (1D) space image of extracted spatio-temporal XPM phase shift $\Delta\Phi(x, t)$ with (a) direct frequency-to-time mapping and (b) full Fourier transform methods for the chirp of $a_3 = 6.85 \times 10^3 \text{ fs}^2$ .	39
Figure 2.7: Simulated transient phase extraction from XPM perturbation with (a) 80 fs, (b) 50 fs, and (c) 20 fs pump pulse durations with probe pulse chirp through cubic term accounted for (solid lines) and with chirp kept only through quadratic term (lines with solid squares). Cubic term are (i) $c = 6.9 \times 10^{-8} \text{ fs}^{-3}$ , (ii) $c = 3.5 \times 10^{-7} \text{ fs}^{-3}$ , and (iii) $c = 6.9 \times 10^{-7} \text{ fs}^{-3}$ .	40
Figure 3.1: Schematic of the 10 Hz repetition rate, 2 TW peak power, 60 fs Ti:sapphire laser system used in the experiments of this dissertation.	57
Figure 3.2: (a) A prism pair compensating GDD and TOD inside the oscillator. (b) A grating pair in the compressor for the pulse recompression.	58
Figure 3.3: (a) Schematic diagram of interferometric autocorrelator using two-photon absorption. (b) Sample autocorrelation trace of oscillator output with a 72 fs full width at half maximum (FWHM).	59
Figure 3.4: Ti:sapphire laser pulse (a) spectra and (b) beam spatial profiles (with the FWHM beam sizes) after each CPA stage: oscillator, stretcher, RGA, and PA1&2, and compressor. The dashed lines in (a) are free-running spectra without the seed beam injection.	60
Figure 3.5: (a) Frequency resolved optical gating (FROG) setup with polarization gating (PG) geometry. (b) Retrieved electric field envelope (thick black line) and phase profiles (red thin lines) retrieved from the sample PG FROG trace (inset) taken after the compressor. Uncompensated TOD is responsible for the oscillatory side lobes.	61
Figure 3.6: (a) The vacuum focal spot profile with (b) the horizontal and vertical line-outs. The peak intensity is $\sim 10^{18} \text{ W/cm}^2$ with the spot size of $12.6 \mu\text{m}$ (FWHM).	62
Figure 4.1: (a) Ionization of a thin helium gas jet irradiated by an intense laser pulse.	75

- Figure 4.2: (a) Theoretical spatio-temporal electron density profile at the laser focus using ADK theory with  $\tau_{FWHM} = 240$  fs,  $r_{FWHM} = 10.3 \mu\text{m}$ , and  $I_{\text{peak}} = 3.8 \times 10^{16}$  W/cm<sup>2</sup>. (b) On-axis electron density evolution (blue line) and pump pulse envelope (red line). (c) Electron density profiles at  $\Delta t = 20$  fs time increments. 75
- Figure 4.3: (a) Experimental setup with pump beam and chirped supercontinuum (SC) reference and probe pulses combined at a beam splitter and focused into a helium gas jet. The pump is dumped and the reference and probe SC pulses are relayed to the imaging spectrometer. (b) A photograph of the helium gas jet irradiated by a Ti:sapphire laser pulse (artificial color) with peak intensity  $I_{\text{peak}} = 3.8 \times 10^{16}$  W/cm<sup>2</sup>. Laser-produced helium plasma is visible at the jet center. 76
- Figure 4.4: Sample spectral interferograms are shown with the helium gas jet (a) off and (b) on. A notable wavelength-dependent fringe shift occurs in (b). 77
- Figure 4.5: (a) Experimental spatio-temporal phase profile  $\Delta\Phi(x, t)$  from optical field ionization of helium at 15 psi jet backing pressure. (b) Central line-outs for jet backing pressures of 5 psi (line with solid triangles) and 15 psi (line with squares). The pump pulse envelope obtained from XPM in glass is also shown (line with circles). The inset shows spatial phase profiles from the 5-psi case at 20 fs increments. 78
- Figure 4.6: (a) Schematic pump-probe diagram. A slice of the probe pulse samples the volume of the helium plasma. (b) Simulated electron density profiles  $N_e(x, z, t' - \tau)$  that a slice of the probe pulse  $\delta_{\text{pr}}(t - \tau)$  samples with  $\tau = 50$  fs time increments. 79
- Figure 4.7: Theoretical 2D spatial refractive index shift profiles  $\Delta n(x, z, t' - \tau)$  of the helium plasma sampled by a slice of the probe pulse  $\delta_{\text{pr}}(t - \tau)$  with (a) 50 fs, (b) 100 fs, (c) 150 fs, (d) 200 fs, (e) 250fs, and (f) 300 fs delays with respect to the pump pulse. 80
- Figure 4.8: Theoretical probe phase profiles  $\Delta\Phi(x, t)$  at the end of the helium plasma with the laser-gas interaction length  $\Delta z$  (a) 0.1 mm, (b) 0.25 mm, (c) 0.5 mm, (d) 0.75 mm, (e) 1 mm, and (f) 2 mm. 81
- Figure 5.1: (a) Free jet condensation source for clusters consists of a solenoid valve and a supersonic conical nozzle ( $d = 0.5$  mm entrance orifice diameter,  $\alpha = 5^\circ$  expansion half angle, 12.7 mm nozzle length, and 3 mm diameter exit orifice) at a valve backing pressure of  $p_0$  and temperature  $T_0$ . (b) Gas jet with an elongated nozzle ( $l = 11.5$  mm length and 0.4 mm width). 100
- Figure 5.2: (a) Experimental layout for 90° Rayleigh scattering. A probe pulse is 101

weekly focused in the cluster jet and scattered into the collecting lens followed by an interference filter and a photomultiplier tube (PMT). The scattered photon energy is registered by the PMT and plotted in (b) as a function of backing pressure with a polynomial least squares fit (red line).

- Figure 5.3: (a) 90° Rayleigh scattering experiment. (b) Rayleigh scattering images on the CCD camera at various backing pressures (images are 50-shot averaged). 102
- Figure 5.4: (a) 1D Rayleigh scattering profiles at various valve backing pressures for the conical gas jet. (b) On-axis Rayleigh scattering signal versus backing pressure with a polynomial least squares fit. 103
- Figure 5.5: 2D Rayleigh scattering imaging profiles at the heights of (b)  $z = 2$  mm, (c) 3 mm, and (d) 4 mm from the nozzle exit orifice obtained by scanning the cluster jet with respect to the probe beam as shown in (a). One line represents one scan position. (e) 1D spatial and temporal Rayleigh scattering profiles at  $z = 2$  mm height from the nozzle. 104
- Figure 5.6: (a) Experimental layout for neutral cluster gas interferometry. The frequency-doubled 532 nm Nd:YAG pulse picks up a phase shift in the cluster gas jet as shown in (b) sample interferogram. (c) Extracted phase shift  $\Delta\phi(x, z)$  using FFT method from the raw interferogram. (d) Line-outs  $\Delta\phi(x)$  at  $z = 2$  mm (triangles), 3 mm (circles), and 4 mm (squares). The  $z = 3$  mm points are shown plotted with a Gaussian least squares fit (red line). 105
- Figure 5.7: The average cluster radius and density across the conical gas jet. (b) On-axis average cluster radius and density as a function of pressure. 106
- Figure 5.8: (a) Picture of the cryogenic elongated cluster source. The elongated gas jet, coolant tube, and heaters are clamped in the copper cryostat. The whole unit is mounted on a xyz stage inside a vacuum chamber. The cryostat temperature is monitored by a T-type thermocouple and controlled by both LN<sub>2</sub> cooling and solid-state cartridge heating. (b) Photograph of Rayleigh scattering of 532 nm probe pulse in the elongated Ar cluster gas jet at  $T = 153$  K. 107
- Figure 5.9: (a) Ar cluster Rayleigh scattering images and (b) 1D line-outs at various backing pressures and temperatures [(i) 24 °C, (ii) -28 °C, (iii) -80 °C, and (iv) -120 °C]. In these images, ND filters with calibrated optical densities (OD) were used to avoid CCD pixel saturation. 108
- Figure 5.10: (a) Ar cluster Rayleigh scattering images and (b) central line-outs for the spatial distribution of Ar clusters in the elongated gas jet at 400 psi and various temperatures. (c) N<sub>2</sub> cluster Rayleigh scattering images and (d) central line-outs at 400 psi and various temperatures. ND filter 109

transmissions are varied to avoid CCD sensitivity saturation in (a) and (c). For the jet conditions explored, scattering was more uniform from Ar than from N<sub>2</sub> sources.

Figure 5.11: 2D Rayleigh scattering spatial profiles of the elongated Ar cluster gas jet at room temperature (T = 297 K) and (b) T = 153 K. 1D Rayleigh scattering profiles of the elongated Ar cluster jet as a function of time at (c) T = 297 K and (d) T = 153 K. The Rayleigh scattering becomes relatively uniform and enhanced by three orders of magnitude at T = 153 K compared to T = 297 K. 110

Figure 5.12: (a) Extracted phase profile  $\Delta\phi(x, z)$  from sample interferogram obtained at room temperature. The nozzle is 90° rotated with respect to the probe pulse, and the jet is viewed end-on. (b) Ar cluster nozzle shadowgrams with jet on and off for the measurement of probe intensity attenuation. The probe transmission line-out is shown at  $z = 1.53$  mm. (c)-(d) On-axis ( $x = 0$ ) phase shifts  $\Delta\phi_0$  at  $z = 1.53$  mm at various pressures and temperatures for argon and nitrogen clusters. 111

Figure 5.13: Average Ar cluster (a) sizes and (b) densities versus backing pressure at various temperatures T = 297 K, 245 K, 193 K, and 153 K at  $z = 1.53$  mm height from the elongated nozzle exit orifice. The temperature dependence of average Ar or N<sub>2</sub> cluster (c) size and (d) density at 400 psi backing pressure. The average cluster size is also estimated from shadowgraphy and Mie scattering at low temperatures  $133 \text{ K} < T < 153 \text{ K}$ . 112

Figure 6.1: (a) Diagram of the hydrodynamic simulation code for intense laser-cluster interaction. It computes the self-consistent electric near field in a single cluster, coupled with 1D radial Lagrangian hydrodynamics. (b) For 1D calculation, the electric field  $E(r, \theta)$  is approximated to  $E_{\text{eff}}(r) = \langle E \cdot E^* \rangle^{1/2}$  averaged over solid angle. 130

Figure 6.2: 1D hydrocode simulation results for the temporal evolution of (a) electron density and (b) electric field (normalized to vacuum value) profiles for an argon cluster of initial radius of 300 Å, irradiated by 800 nm, 300 fs FWHM Gaussian pulse with a peak intensity of  $10^{15} \text{ W/cm}^2$ . The average degree of ionization is also superimposed in (a). 131

Figure 6.3: 1D hydrocode simulation results for the transient (a) real and (b) imaginary polarizability  $\gamma(t)$  of an exploding Ar cluster with 300 Å initial radius, irradiated by 800 nm, 80 fs (FWHM) Gaussian pulse with a peak intensity of  $10^{15} \text{ W/cm}^2$ . 132

Figure 6.4: (a) Experimental setup for 90° Rayleigh scattering of an intense Ti:sapphire laser pulse in a gas of laser-heated clusters. (b) Scattering angular distribution of intense laser pulses interacting with clusters, 133

measured with  $\theta$ -rotation of the linear laser polarization with respect to the CCD axis. A least squares fit of  $\sin^2 \theta$  and representative raw 2D scattering images at  $\theta = 8, 32, 60, \text{ and } 88^\circ$  are overlaid on the plot.

Figure 6.5: (a) Schematic of laser-cluster interaction with the presence of a laser prepulse. The inset shows a photograph of laser-irradiated clustered gas, imaging a segmented plasma recombination emission induced by laser prepulses. The side scattering of intense laser pulse and the corresponding interferograms are shown with a main to prepulse contrast ratio of (b)  $< 10^3$  and (c)  $> 10^4$ . 134

Figure 6.6: Time-resolved 400 nm probe (a) transmission and (b)  $90^\circ$  Rayleigh scattering as a function of pump-probe delay for an argon cluster gas at 200 and 400 psi backing pressures (average cluster radii 200 Å and 350 Å expected from Hagen), irradiated by a 2.5 mJ laser pump pulse. The inset shows the probe and reference intensity profiles imaged on the CCD detector. 135

Figure 6.7: (a) Experimental setup, showing pump beam and chirped supercontinuum (SC) reference and probe pulses combined at a beam splitter and focused by a lens through the edge of a cluster jet. The pump is dumped and the reference and probe SC pulses are relayed by a lens to the imaging spectrometer where they interfere, producing a spectral interferogram. (b) Sample spectral interferogram indicating (+) fringe shifts at early times and (−) later. (c) Perspective plot of the phase shift  $\Delta\Phi$  (proportional to  $n_r - 1$ ) versus transverse coordinate and time at 350 psi. 136

Figure 6.8: (a) Phase shift  $\Delta\phi$  (left scale) and corresponding real index shift  $n_r - 1$  (right scale) extracted from spectral interferograms, for backing pressures (cluster radii) 150 psi (150 Å), 200 psi (200 Å), 250 psi (235 Å), 300 psi (270 Å), and 350 psi (300 Å). (b) Small signal absorption coefficient (left scale) and corresponding imaginary index  $n_i$  (right scale). Plots are 10 shot averages. The error bars shown on the 350-psi plots represent the variance. (c) Calculation of  $\text{Re}(\bar{\gamma}(t))$  for average cluster sizes 150 – 300 Å. The noise at longer times is from the numerical computation. Values for  $\bar{\gamma}_{r, long}$  are shown as dotted lines. The temporal position of the pump laser pulse is shown. (d)  $\text{Im}(\bar{\gamma}(t))$  for the clusters of (c). The very small peaks in  $\text{Im}(\bar{\gamma})$  and steps in  $\text{Re}(\bar{\gamma})$  at  $t \sim 30$  fs are from the  $3N_{cr}$  resonance. 137

Figure 7.1: (a) Conical lens (axicon) and its use to generate a line focus. (b) Generation of a plasma waveguide by focusing Nd:YAG laser through an axicon lens in a backfill gas of 640 torr of helium plus 10 torr of  $N_2O$ . Intense Ti:sapphire laser pulses can be coupled into the waveguide and guided over many Rayleigh lengths. 154

Figure 7.2: Experimental layout for guiding of intense Ti:sapphire laser pulses in a 155

pre-formed plasma channel generated by focusing Nd:YAG laser pulses with an axicon. A plasma funnel is generated at the entrance of the plasma waveguide by focusing part of Nd:YAG laser pulses with the Ti:sapphire pump pulse lens. The funnel generation pulse is independently adjustable in time and space with respect to both the waveguide generation pulse (axicon pulse) and the injected pump pulse. Included are transverse interferometry/shadowgraphy and longitudinal imaging/SSSI diagnostics.

- Figure 7.3: Shadowgrams and interferograms of waveguide end region showing typical taper for case of no funnel pulse, and taper removed for cases of funnel pulse at various delays before and after the waveguide generation pulse. 156
- Figure 7.4: Transverse shadowgrams and interferograms of an injected Ti:sapphire laser pulse (40 mJ, 70 fs, 800 nm) into the entrance of plasma waveguide with the funnel generation beam (a) off and (b) on. 157
- Figure 7.5: Images of (a) pump and (b) probe on the waveguide exit plane when no waveguide present. [(a')-(b')] with presence of waveguide. Single-shot supercontinuum spectral interferograms for case of waveguide (c) off and (c') on. 158
- Figure 7.6: Single-shot supercontinuum spectral interferogram (SSSI) for cases of pump pulse (a) off and (b) on into the plasma waveguide. (c) Extracted transient phase shift of probe pulse by an intense pump pulse injected into the plasma waveguide. 159
- Figure 7.7: (a) Schematic of self-focusing of intense laser pulses in a gas of clusters. (b) Perspective plots of  $\text{Re}(\bar{\gamma})$  and  $\text{Im}(\bar{\gamma})$  versus radius and time calculated for a gas of 300 Å average radius clusters (with a 100% FWHM size distribution) heated by a 100 fs pulse of peak intensity of  $5 \times 10^{15}$  W/cm<sup>2</sup> in a 15 μm FWHM spot. 160
- Figure 7.8: (a) Pump beam root-mean-square (RMS) radius at jet exit and transmission versus pulse width. (b) Transverse shadowgrams of pump beam tracks in cluster jet 10 ps after pump enters from left for selected pump pulse widths. VF: location of vacuum focus. (c) Interferogram corresponding shadowgraph for the 80 fs pump pulse. (d) Transient intensity profile of SC probe. 161
- Figure 7.9: (a) Photograph of cryogenically cooled elongated Ar cluster gas jet irradiated by a 50 mJ, 70 fs Ti:sapphire pump pulse. Shadowgrams and interferograms at T = 153 K (−120 °C) and 400 psi valve backing pressure for the probe delays of (b) 20 ps and (c) 2 ns after the pump beam. 162
- Figure A.1: Increases in peak power and focused intensity of tabletop lasers with 166

year, showing thresholds for various physical phenomena [Adapted and modified from M. D. Perry and G. Mourou, *Science* **264**, 917 (1994); G. A. Mourou, C. P. J. Barty, and M. D. Perry, *Phys. Today* **51**, 22 (January 1998)].

- Figure A.2: Schematic of concept of chirped pulse amplification (CPA) technique. 167
- Figure A.3: Development of terawatt and petawatt subpicosecond lasers with chirped pulse amplification (CPA) technology. 167
- Figure C.1: Electric fields and the corresponding spectra of a Gaussian reference pulse  $E_r(t) = \exp(-4 \ln 2 t^2 / \tau_e^2 - i\omega_0 t)$  and  $\tau_0$ -delayed probe pulse  $E_{pr}(t) = T_0 E_r(t - \tau_0) e^{i\Delta\Phi}$ , upon which a phase shift  $\Delta\Phi$  and amplitude transmission  $T_0$  has been imposed. For (a)-(c),  $T_0^2 = 1$ . For (d),  $T_0^2 < 1$ . 179
- Figure C.2: (a) Diagram showing how two temporally separated pulses, reference  $E_r(t)$  and probe  $E_{pr}(t)$ , can interfere each other in the frequency domain.  $E_r(t)$  and  $E_{pr}(t)$  are stretched in time after the grating diffraction inside a spectrometer, then temporally overlapping and interfering on the imaging plane of spectrometer. (b) Perspective view of an imaging spectrometer, capable of providing spectral intensity modulations  $I(x, \lambda)$  with 1D space information. 180
- Figure C.3: (a) Schematic of general multi-shot spectral interferometry scheme. Here it was applied to the femtosecond ionization of helium. See text for details. (b) Plots of the probe phase shift  $\Delta\phi$  versus pump-probe delay  $\tau$ . The central lineouts of the spectral interferograms are plotted in (iii) with the pump-off (dashed line) and pump-on (solid line) modes. 181
- Figure D.1: Spectra of supercontinuum (SC) light generated by a femtosecond Ti:sapphire laser pulse focused in (a) sapphire window at  $P > P_{cr}$  and (b) atmospheric pressure air. Each inset shows the spectral interferogram, obtained from interference between the SC pulse and a  $\sim$ ps delayed SC twin replica. The spectral fringes in (a) are completely washed out due to the multi-filament SC generation with phase disruptions, whereas a single SC filament with a coherent  $\sim$ 100 nm spectral bandwidth was obtained in (b). 185
- Figure E.1: Simulation results for the retrieved phase  $\Delta\Phi_{ret}(t)$  (solid lines) with the direct mapping method. An external phase modulation (dashed lines)  $\Delta\Phi_{ext}(t) = 0, (\pi/100)(t+50)$ , and  $\pi$  for  $t < -50$  fs,  $-50$  fs  $< t < 50$  fs, and  $t > 50$  fs, respectively, is applied to the probe pulse. The reference and probe spectral bandwidths (FWHM) are (a)  $\Delta\lambda = 4$  nm, (b) 8 nm, and (c) 32 nm at  $\lambda_0 = 400$  nm, and the pulse durations  $\tau_e$  (FWHM) are (i)  $\tau_e = 100$  fs, (ii)  $\tau_e = 200$  fs, and (iii)  $\tau_e = 400$  fs. 191

- Figure F.1: Fourier-transform process showing various stages to extract the envelope intensity and phase profiles. (a) 1-D raw interferometric intensity profile  $g(x, y)$ . (b) Modulus of Fourier transform  $|G(x, y)|$  containing a DC-component  $A(f_x, y)$  and AC-spectra  $C(f_x - f_0, y)$  and  $C^*(f_x + f_0, y)$ .  $C(f_x - f_0, y)$  spectrum is selected with a filter function and shifted toward center by  $f_0$  to make  $C(f_x, y)$ . (c) Modulus  $b(x, y)$  and phase  $\phi(x, y)$  obtained from the inverse Fourier transform of  $C(f_x, y)$ . 195
- Figure G.1: Material dispersion with (a) index of refraction (b) group delay dispersion (GDD) (c) third order dispersion (TOD), and (d) fourth order dispersion (4OD) for various glass in the optical wavelength range. 198
- Figure H.1: Schematic diagram for the electronic signal synchronizations of Ti:sapphire and Nd:YAG laser systems using the rf generator (Coherent 7600 Mode-locker), Delay box (EG&G Model DB463), Lok-to-Clock electronics (Spectra-Physics Model 3930), Medox timer (Medox Electro-Optics), Delay box 1 & 2 (Stanford Research Systems DG535), and Delay box 3 (Berkeley Nucleonics Corporation Model 555). 200

# Chapter 1: Introduction and overview

## 1.1 Overview of intense laser–matter interactions

The interaction of light with matter is one of the fundamental and universal phenomena in nature. The first demonstration of the laser in the early 1960's<sup>1</sup> opened up a path to investigate light-matter interaction with rich applications in many areas of science and technology. The recent development of a new class of ultrahigh intensity lasers has extended such studies to conditions only previously seen in either astrophysical or particle accelerator settings: gigabar pressures, megavolt temperatures, relativistic particle dynamics, and nuclear reactions.

Practically, high intensity laser–matter interactions are performed by focusing ultrashort high-power laser pulses into a small volume where a target is located (see Fig. 1.1). At high laser intensities, the electric field in a laser pulse becomes strong enough to greatly exceed the Coulomb atomic field seen by electrons in the ground state of atoms and many highly charged ions. For hydrogen, the atomic Coulomb field is  $E_{\text{at}} \sim 5 \times 10^9$  V/cm. A laser intensity of  $\sim 3 \times 10^{16}$  W/cm<sup>2</sup> can supply such a field, and such intensities are nowadays considered modest.

The maximum electric  $E$  and magnetic  $B$  fields in vacuum are, in practical units,

$$E_{\text{max}} = 2.75 \times 10^{10} \sqrt{I [10^{18} \text{ W/cm}^2]} \text{ V/cm}, \quad (1.1)$$

$$B_{\text{max}} = 92 \times 10^6 \sqrt{I [10^{18} \text{ W/cm}^2]} \text{ Gauss}, \quad (1.2)$$

where  $I$  is the laser intensity in units of  $10^{18}$  W/cm<sup>2</sup>. For instance, at a laser intensity of  $10^{18}$  W/cm<sup>2</sup>, which is routinely obtained with current tabletop laser technology, the

corresponding electric field is  $E_{\max} \sim 2.8 \times 10^{10}$  V/cm. This is well beyond the Coulomb binding field strength in ground state hydrogen. At such field strengths, the laser can easily ionize the bound electrons of atoms and generate a plasma in which the electrons quiver at velocities close to the speed of light, and their relativistic mass increase strongly changes the plasma refractive index.

At such high intensity ( $10^{18}$  W/cm<sup>2</sup>), the magnetic field strength associated with the laser becomes enormous ( $B \sim 10^4$  Tesla, which cannot be accessed with a conventional source of static magnetic field in the laboratory) and the full Lorentz force  $\mathbf{F} = e[\mathbf{E} + (\mathbf{v} \times \mathbf{B})/c]$  determines the motion of electrons in the laser field, where  $\mathbf{v}$  and  $e$  are the velocity and charge, respectively, of electrons. This leads to relativistic nonlinear effects. The free electrons oscillate in a figure-of-8 pattern, radiating photons at harmonics of the incident laser frequency. This is called relativistic nonlinear Thomson scattering,<sup>2</sup> in which each harmonic has its own unique angular distribution of scattering.<sup>3</sup>

The creation of strong electromagnetic fields, unique with high intensity lasers, has allowed us to reach a new regime inaccessible before in the laboratory (see Appendices A and B for a chart of high intensity laser evolution and relevant physics). The theme of this dissertation is the measurement of ultrafast processes in the interaction of intense laser pulses with gases, clusters, and plasmas. Under high intensity illumination, all neutral materials undergo extremely rapid changes, ultimately transforming to plasma. In this introductory chapter, we review basic high intensity processes, ultrafast measurement techniques, and previous work in the areas of laser-gas, laser-cluster, and laser-plasma interactions.

## 1.2 Laser-driven ionization of gases

### 1.2.1 Ionization mechanisms

The interaction of intense ( $I \geq 10^{13}$  W/cm<sup>2</sup>) laser fields with gases is commonly accompanied by ionization and plasma creation. The intensity of  $10^{13}$  W/cm<sup>2</sup> corresponds to the typical threshold for direct laser ionization of noble gases such as xenon. For very long laser pulses (> few nanoseconds), gas breakdown can occur at lower intensities via the seeding of avalanche ionization by pre-existing free electrons.

Depending on the laser intensity and gas atomic/molecular properties, three regimes of ionization are observed: (a) multiphoton, (b) tunneling, and (c) over-the-barrier (barrier suppression) ionization, as shown in Fig. 1.2. These ionization regimes are typically characterized by the Keldysh parameter  $\gamma_K$ , given by <sup>4</sup>

$$\gamma_K = \sqrt{\frac{U_i}{2U_p}}, \quad (1.3)$$

where  $U_i$  is the ionization potential energy of the atom or ion and  $U_p$  is the laser ponderomotive potential energy (= average kinetic energy of electrons in the oscillating laser field), which is given by

$$U_p = \frac{1}{2} m_e \langle v_{os}^2 \rangle = \frac{e^2 E^2}{4m_e \omega^2}, \quad (1.4)$$

or in practical units  $U_p$  [eV] =  $9.33 \times 10^{-14} I$  [W/cm<sup>2</sup>]  $\lambda^2$  [ $\mu$ m)], where  $v_{os} = \frac{eE}{m_e \omega}$  is the

quiver velocity of an electron, and  $m_e$  and  $e$  are the electron mass and charge. In the semi-classical picture, the Keldysh parameter  $\gamma_K$  represents the ratio of the ionization time to the laser period

$$\gamma_K = \sqrt{\frac{U_i}{2U_p}} \approx \sqrt{\frac{(x_0 / \langle v_{os}^2 \rangle^{1/2})}{T}} = \sqrt{\frac{\text{ionization time}}{\text{laser optical period}}}, \quad (1.5)$$

where  $T = 2\pi/\omega$  is the laser oscillation period and  $x_0 \approx U_i/(eE)$  is the distance from the atomic core where the bound electron is liberated.

For  $\gamma_K \gg 1$ , there are many optical periods during the ionization time. In this regime, multiphoton ionization (MPI), bound electron absorbs  $N$  photons where  $N\hbar\omega > U_i$  [see Fig. 1.2(a)]. The rate for non-resonant MPI is given by

$$w = \sigma_N I^N, \quad (1.6)$$

where  $\sigma_N$  the generalized  $N$ -photon ionization cross section and  $N$  is the minimum number of photons required for ionization.<sup>5</sup>

In the regime of  $\gamma_K < 1$ , where the ionization time is much shorter than a laser period, the Coulomb potential can be viewed as being suppressed by the instantaneous laser field which the electron sees as a DC field. In this regime, the bound electron experiences a combined effective potential as shown in Fig. 1.2(b), and the electron can tunnel out of the new effective barrier. This ionization regime is called optical field ionization (OFI) or tunneling ionization (TI) and the ionization rate  $w$  is discussed in Chapter 4 in detail.

In the strong field limit ( $\gamma_K \ll 1$ ), the laser field completely suppresses the Coulomb potential, so the bound electron can simply escape over the top of the effective potential barrier. This regime is called “over-the-barrier ionization” (OTBI) and shown in Fig. 1.2(c). By equating the maximum of the suppressed atomic potential to the binding (ionization potential) energy, the threshold intensity for OTBI is estimated as

$$I_{\text{th}} = \frac{cU_i^4}{128\pi e^6 Z^2} \quad (1.7)$$

or  $I_{\text{th}} [\text{W}/\text{cm}^2] = 4 \times 10^9 (U_i [\text{eV}])^4 Z^2$ , where  $U_i$  is the ionization potential,  $Z$  is the charge state of the resulting ion.<sup>6,7</sup>

In terms of laser intensity, the ionization is dominated by the MPI process for intensities below  $\sim 10^{12} \text{ W}/\text{cm}^2$  (for laser wavelength  $\lambda \sim 0.8 \mu\text{m}$  and  $\text{Ar} \rightarrow \text{Ar}^{1+}$ ), by the OFI (TI) process for intensities above  $\sim 10^{14} \text{ W}/\text{cm}^2$ , and by OTBI process for intensity in excess of  $\sim 3 \times 10^{14} \text{ W}/\text{cm}^2$ . For higher ion stages, however, the threshold intensities become higher. For example, OFI (TI) dominates for  $I > \sim 10^{16} \text{ W}/\text{cm}^2$  (for  $\text{Ar}^{7+} \rightarrow \text{Ar}^{8+}$ ), whereas OTBI dominates for  $I > \sim 3 \times 10^{16} \text{ W}/\text{cm}^2$ . Since in a pulse, the laser intensity increases with time, for high intensities ( $I_{\text{peak}} > 10^{14} \text{ W}/\text{cm}^2$ ) OFI dominates the ionization process before the laser intensity reaches the OTBI regime.

### 1.2.2 Optical field ionization and collisional ionization

In the intensity regime of  $10^{15} \sim 10^{17} \text{ W}/\text{cm}^2$ , which is of interest in this dissertation, the Keldysh parameters are in the range of  $\gamma_K \sim 0.07 - 0.7$  for  $\text{He}^{1+} \rightarrow \text{He}^{2+}$  and  $\gamma_K \sim 0.1 - 1$  for  $\text{Ar} \rightarrow \text{Ar}^{8+}$ , showing that OFI is the dominant photoionization mechanism for the laser-gas (helium) or laser-cluster (argon) interaction experiments of this dissertation. Even at an intensity of  $10^{15} \text{ W}/\text{cm}^2$ , the OFI rate is  $\sim 10^{-1} \text{ fs}^{-1}$  ( $1 \text{ fs} = 10^{-15} \text{ s}$ ) for ( $\text{He} \rightarrow \text{He}^{1+}$ ) and  $\sim 1 \text{ fs}^{-1}$  for ( $\text{Ar} \rightarrow \text{Ar}^{1+}$ ), indicating that OFI occurs so rapidly under our conditions that the main laser field propagates in plasma while still ionizing atoms.

An initially field-ionized plasma can undergo further ionization through electron-ion collisional process (collisional ionization). For a laser-produced plasma, the electron-

ion collision rate for a thermal electron velocity distribution <sup>8,9</sup> of temperature  $T_e$  in the presence of a laser field <sup>10</sup> is given by <sup>11</sup>

$$\nu_{ei} = \frac{4\sqrt{2\pi}Z^2e^4N_i \ln \Lambda_{ei}}{3\sqrt{m_e}(k_B T_e + 2U_p/3)^{3/2}} \approx 2.9 \times 10^{-6} \frac{Z^2 N_i [\text{cm}^{-3}] \ln \Lambda_{ei}}{(T_{\text{eff}} [\text{eV}])^{3/2}}, \quad (1.8)$$

where  $Z$  is the average degree of ionization,  $N_i$  is the ion density,  $\ln \Lambda_{ei}$  is the Coulomb logarithm, and  $T_{\text{eff}} = k_B T_e + 2U_p/3$  is the effective temperature. In the high intensity limit ( $U_p \gg k_B T_e$ ), where the ponderomotive quiver velocity of electron dominates the mean thermal electron velocity, the collision rate is approximated by  $\nu_{ei} \sim 10^{15} Z^2 N_i [\text{cm}^{-3}] (I[\text{W}/\text{cm}^2])^{-3/2} (\lambda[\mu\text{m}])^{-3}$ . For an initially singly ionized plasma of ion density of  $N_i \sim 2 \times 10^{19} \text{ cm}^{-3}$  (for an ideal gas of approximately atmospheric pressure) and laser intensity of  $10^{15} \text{ W}/\text{cm}^2$  at  $\lambda = 0.8 \mu\text{m}$ , the collision frequency is  $\nu_{ei} \sim 10^{12} \text{ s}^{-1}$ , corresponding to a time between collisions of  $\sim 1$  picosecond ( $1 \text{ ps} = 10^{-12} \text{ s}$ ), which is much longer than the typical pulse length of  $\sim 100$  fs used in the experiments discussed in this dissertation. Additionally, since the collision rate is far smaller than the OFI ionization rate under the same conditions, collisional processes during the laser pulse can often be ignored for most ultrashort (subpicosecond) laser interaction with gases at less than atmospheric pressure. However, for dense plasmas ( $N_i \geq 10^{22} \text{ cm}^{-3}$ ), collisions play a key role, even on femtosecond ( $10^{-15} \text{ s}$ ) time scales. One example is the plasma of laser-heated clusters, described later in this dissertation.

### 1.3 Ultrafast optical diagnostics for high intensity laser–matter interaction

To date, many experiments have examined the issue of laser–matter interaction dynamics by measuring x-ray spectra or fast particles (with time-of-flight spectrometers)

that emerge from the interaction zone long after the interaction has occurred. The interaction scenario is then inferred from this data. Since these diagnostics naturally deal with time-integrated signals, the understanding of *ultrafast evolution dynamics*, which is inherent in ultrashort ( $\sim 100$  fs) pulse interaction, may be limited. Therefore, to investigate the interaction processes on a femtosecond time scale, time-resolved ultrafast diagnostics are strongly demanded. In this section, we present some basic concepts of ultrafast optical diagnostics that play an essential role in the study of intense laser–matter interactions. Further details are described in Chapter 2.

Laser-irradiated targets such as solids, gases, and plasmas can have their macroscopic complex index of refraction significantly altered in time and space. This transient refractive index change can then encode itself on the propagation phase and amplitude envelope of laser pulses. A laser pulse propagating the transient refractive index experiences absorption,  $A$ , and phase shift,  $\Delta\phi$ , given by

$$A(\mathbf{r}_\perp, t) \approx E_{\text{in}} \left\{ 1 - \exp\left(-\frac{2\pi}{\lambda} \int n_i(\mathbf{r}_\perp, z, t) dz\right) \right\}, \quad (1.9)$$

$$\Delta\phi(\mathbf{r}_\perp, t) \approx \frac{2\pi}{\lambda} \int [n_r(\mathbf{r}_\perp, z, t) - 1] dz, \quad (1.10)$$

where  $E_{\text{in}}$  is the incident laser energy,  $z$  is the propagation direction,  $\mathbf{r}_\perp$  is the coordinate normal to  $z$ ,  $\lambda$  is the wavelength of laser in vacuum, and  $n_r$  and  $n_i$  are the transient real and imaginary indices of refraction. Hence, the absorption and phase shift measurements show how the complex refractive index ( $n = n_r + in_i$ ) in the laser-irradiated target evolves in space as well as with time. This, in turn, reveals the details of the laser-target interaction dynamics.

Typically, time-resolved absorption can be measured with a real-time fast detector such as a photodiode or a streak camera. Here, the time resolution which resolves the dynamics is set by the response time of the detector. Typically, ultrafast photodiodes<sup>12</sup> and optical streak cameras<sup>13</sup> provide the fastest response times of  $\sim 10$  ps and  $\sim 0.5$  ps, respectively. To achieve time resolutions of well under 1 ps, a novel diagnostic technique must be employed.

Recently, nonlinear optical diagnostics have been greatly developed to provide femtosecond time resolution. Examples include intensity or interferometric autocorrelation/cross-correlation techniques,<sup>14</sup> FROG (Frequency Resolved Optical Gating)<sup>15-17</sup> and SPIDER (Spectral Phase Interferometry for Direct Electric-field Reconstruction).<sup>18,19</sup> In particular, FROG and SPIDER can characterize the intensity and phase shifts of laser pulses with femtosecond temporal resolution. For example, ultrafast laser-induced ionization dynamics of gases has been investigated using FROG.<sup>20</sup> However, relatively high intensities are needed because of nonlinear signal yield requirements. Furthermore, these diagnostics do not provide any spatial information on the pump-perturbed target, which is necessary for the full understanding of the interaction dynamics. In contrast to nonlinear techniques, some novel linear methods can overcome these limitations, while still providing femtosecond temporal resolution.

To serve these goals, we have developed an ultrafast linear optical diagnostic: *single-shot supercontinuum spectral interferometry* (SSSI). With this diagnostic, we can observe interaction dynamics in a single-shot with femtosecond time resolution and micron 1D spatial resolution. Essentially, SSSI is based on the pump-probe technique, where the

first laser pulse (pump) initiates the interaction dynamics in a target or sample, and the second laser pulse (probe) probes the resulting dynamics.

The concept of pump-probe technique is shown in Fig. 1.3 with two possible operating schemes: (a) multi-shot and (b) single-shot. In case (a), a synchronized short (femtosecond) probe pulse, typically split from the main pump laser, samples the pump-disturbed volume and takes a “snapshot” of pump-induced dynamics at a certain delay after the pump. The pump-induced disturbance – such as absorption, frequency modulation, and phase shifts – can be recorded with a relatively slow detector. By successively varying the pump-probe delay, one can reconstruct the interaction history from a series of time-delayed snapshots. The time resolution is determined by the probe pulse duration, independent of the detector response time. Such optical pulse width can be as short as  $\sim 10 - 20$  fs. For x-rays used as probes,<sup>21-23</sup> it can be of order of  $\sim 1$  fs.

In case (b), shown in Fig. 1.3(b), a long probe pulse records the entire dynamics in a single-shot. To reconstruct the full dynamics, the probe pulse needs to be temporally resolved to extract the absorption and phase shift modulated by the transient refractive index in the pump-irradiated target. SSSI is a subject of method (b) and the detailed descriptions of the diagnostic are provided in Chapter 2.

#### **1.4 Interaction of intense femtosecond laser pulses with gases**

One of the earliest works on optical field ionization (OFI) was the measurement of the peak intensity dependence of ion yields for various gases,<sup>24</sup> over a high dynamic range of laser intensity. Use of similar ion or electron spectroscopy techniques has triggered the discovery of nonsequential ionization in helium ( $\text{He} \rightarrow \text{He}^{+2}$  directly, compared to the

sequential process  $\text{He} \rightarrow \text{He}^+ \rightarrow \text{He}^{+2}$ ).<sup>25</sup> However, these types of measurements, which involve charged particle detection long after the ionization event, do not provide information on the time-resolved ionization dynamics. Hence, it is desirable to employ ultrafast optical diagnostics to probe laser-induced ionization processes with femtosecond temporal resolution.

One earlier example of time-resolved measurement of ionization dynamics is the monitoring of spectral blue shifts. A rapid increase in electron density owing to ionization results in a rapid reduction of  $n$ , which in turn causes a spectral blue shift in either the pump pulse inducing the ionization<sup>26</sup> or in a probe beam co-propagating with the pump.<sup>27</sup> The time-dependent spectral shift is given by  $\Delta\omega(t, \tau) = \omega(t, \tau) - \omega_0$  where  $\omega(t, \tau) = -\partial\phi(t, \tau)/\partial t = \omega_0 - k_0z\partial n(t, \tau)/\partial t$ , where  $\tau$  is the time delay between the pump and probe pulses ( $\tau = 0$  for pump alone). The blue shift method for extraction of ionization dynamics depends on the time derivative of the refractive index,  $\partial n/\partial t$ , which in many practical cases can be small. As a result, the spectral change  $\Delta\omega$  is too small to measure from the ionization of low-density and low- $Z$  gases.

Further investigation was conducted using FROG by measuring the time-domain intensity and phase of an ultrashort pulse interacting with gases.<sup>23</sup> FROG measured the femtosecond ionization processes and ionization rates for several species of noble and diatomic gases. However, due to the lack of spatial information on the laser-gas interaction, the full study of ionization dynamics was quite restricted. We overcome this limitation using our ultrafast SSSI diagnostic, providing a complete picture of laser-produced ionization processes in time and space. For instance, our SSSI could measure the spatio-temporal ionization process of helium in an intense laser field. In particular, we observed

the characteristic double stepwise ionization of helium ( $\text{He} \rightarrow \text{He}^+$  followed by  $\text{He}^+ \rightarrow \text{He}^{2+}$ ). The details are described in Chapter 4.

## 1.5 Interaction of intense laser pulses with clusters

Atoms or molecules exhibit short-range attractions for one another owing to Van der Waals forces. Under a rapid cooling process, such as nozzle ejection of a gas puff into vacuum, hundreds to a few tens of millions of atoms can aggregate together to make nano-scale clusters, typically of diameter less than a few thousand angstroms.

Recently, there has been great interest in the interaction of intense laser pulses with clusters. The first experiments were conducted by McPherson *et al.*,<sup>28–30</sup> who observed what was considered anomalous x-ray emission from high intensity ( $10^{16} - 10^{18} \text{ W/cm}^2$ ) laser-irradiated krypton clusters. McPherson *et al.* attributed the emission to the multiphoton excitation of atoms in clusters (present in their jet) to yield ions with inner-shell vacancies, which then decayed by prompt emission of kilovolt x-rays. To explain their observations, they proposed the “coherent electron motion model”, in which high charge states arise from collisions by coherently moving electrons accelerated by the strong laser field to produce “hollow atoms” (with inner shell vacant while outer shells are still populated, making an inverted electronic configuration).<sup>28</sup> Even though there has been debate about their model, their initial work generated interest in the high intensity physics community, raising interesting questions about the source of the observed highly charged ions and energetic x-ray emission.

Since then, many experiments revealed that if an intense, ultrashort laser pulse is focused in a gas of clusters, the clusters are almost instantaneously heated to temperatures

up to  $\sim 10^7$  K – many times hotter than the sun – and they explode violently. This occurs owing to the near solid density ( $> 10^{22} \text{cm}^{-3}$ ) internal to clusters, which exhibit most characteristics of laser-irradiated solids – high laser energy absorption and the resulting creation of high temperature plasma.<sup>31</sup> Such high plasma temperature indicates that laser-heated clusters are a copious source of x-rays,<sup>28–33</sup> energetic ions<sup>34, 35</sup> and electrons,<sup>35, 36–38</sup> and neutrons.<sup>39–42</sup> The velocities of the particles thrown off by the explosion are high enough that nuclear fusion has been demonstrated from the collisions of deuterium nuclei from nearby explosions.<sup>39–42</sup> Figure 1.4 illustrates the high intensity laser interaction with nano-scale clusters and resulting generation of x-rays, extreme ultraviolet (EUV) emission, and energetic particles, accompanied by strong laser absorption and scattering.

However, exactly how these nano-plasmas explode has been a controversial question, and one of more than just academic interest. For it turns out that the clusters explode so rapidly that the heating laser pulse – even one as short as 100 fs – is still on while they are doing so. The time-dependent details of the ultra-rapidly evolving cluster ion and electron spatial distributions determine the manner in which the laser couples energy to the cluster and with what efficiency.

Recently, several laser-cluster interaction models have been developed.<sup>43–48</sup> For small clusters of a few hundred atoms or less, laser-heated electrons can easily escape the cluster early in the interaction, leaving electrostatic forces between the ions to drive cluster disassembly (“coulomb explosion”).<sup>46</sup> For larger clusters composed of greater than  $\sim 10^3$  atoms, hydrodynamic forces dominate the cluster explosion dynamics.<sup>43, 44, 46, 48</sup> However, Lezius *et al.* have claimed that the Coulomb explosion scenario could still dominate in

clusters as large as  $10^5$  atoms, which has raised questions about the details of cluster dissociation mechanism.<sup>46</sup>

Rose-Petruck *et al.* proposed the “ionization ignition model” to explain the enhanced ionization with high charge states in laser-heated rare gas clusters, based on classical trajectory Monte-Carlo simulations.<sup>45</sup> In their model, the ionization is driven by the combined field of the laser and Coulomb forces arising from neighboring ions in clusters. However, the simulation was limited to treat only small clusters (up to 50 atoms).

The earliest and most often cited plasma hydrodynamic model assumes that a laser-heated cluster expands at uniform density (“uniform density model”).<sup>43, 44</sup> This model qualitatively explains the observation of high ionization stages,<sup>29</sup> energetic electrons and ions,<sup>36, 49</sup> and resonant behavior in the laser-cluster coupling.<sup>43, 44, 50–53</sup> However, this model fails to explain the apparent few hundred femtosecond time scale for strong laser-cluster coupling (for cluster sizes of  $>10^4$  atoms per cluster), inferred from recent absorption/scattering<sup>50, 51</sup> and x-ray<sup>52, 53</sup> measurements.

For a better understanding of the laser-cluster interaction (for cluster sizes of  $>10^3$  atoms per cluster), Milchberg *et al.* have recently developed a one-dimensional (1D) hydrodynamic laser-cluster interaction code, in which the laser field is treated self-consistently (see Chapter 6 for details).<sup>48</sup> The model not only explains the discrepancy on the coupling time scale but also provides additional physical insight into the interaction dynamics which lead to applications. The model predicts that the laser couples resonantly at the critical density region of the expanding clusters (see Fig. 1.5).<sup>48</sup> This implies that clusters explode “layer-by-layer” rather than at uniform density. This determination has significant consequences for the applications of laser-heated clusters such as optical

guiding,<sup>55</sup> high harmonic generation,<sup>56–58</sup> x-ray sources for next generation lithography,<sup>59</sup> EUV and x-ray microscopy,<sup>60</sup> and energetic neutron sources.<sup>39–42</sup>

To overcome certain limitations of the hydrodynamic model (see Chapter 6), a three-dimensional (3D) electrostatic particle-in-cell (PIC) simulation has been developed by Taguchi *et al.* to study the kinetics of energetic electrons in a laser-heated cluster.<sup>61</sup> It shows that energetic electrons are created by a Brunel-type absorption process<sup>62</sup> in the sharp density gradient of the cluster edge and that above a certain intensity threshold related to the cluster size, nonlinear resonant absorption and heating occurs when these electrons are driven in phase with the laser field. In addition, the simulation results also verify the characteristic layer-by-layer expansion feature of our 1D hydrodynamic model.<sup>61</sup>

## 1.6 Interaction of intense laser pulses with plasma waveguides

Without a means for defeating beam diffraction, at best the interaction of high intensity laser fields with matter is practically limited to the laser focal volume, as shown in Fig. 1.1. This is mainly because a focused laser beam naturally diverges (diffraction) immediately after its focus, and hence away from the focal region, and the laser peak intensity decreases dramatically. Typically the high intensity interaction area is given by twice the Rayleigh length of laser beam,  $2z_0 = 2\pi w_0^2 / \lambda$ , where  $w_0$  is the spot size ( $1/e^2$  intensity radius) and  $\lambda$  is the wavelength.

Elongated guiding of high intensity lasers over many Rayleigh lengths is greatly demanded for many intense laser–matter applications. For example, in the scheme of laser-driven plasma electron accelerators (see Appendix B), the electron energy gain is limited to  $\sim 100$  MeV for an interaction length of 1 mm (for electron density  $N_e = 10^{18} \text{ cm}^{-3}$ ), which is

large but far below the requirements for high energy physics-based particle acceleration. To achieve several GeV energy gain, at least a few centimeters of propagation at high intensity is required. This can be realized with the use of plasma waveguides, the details of which are described in Chapter 7.

Since a plasma waveguide is essential for many high intensity laser–matter interaction experiments, how an ultrashort, intense laser pulse interacts with a plasma waveguide must be investigated. Figure 1.6 shows a schematic illustrating laser wakefield acceleration (LWFA) of electrons using a plasma waveguide. Here a preformed plasma waveguide is preferred over the relativistic self-channeling because of several advantages (see Chapter 7 for details). An intense laser pulse excites a wakefield as it propagates in the plasma waveguide. Our SSSI diagnostic beam can probe the wakefield region, potentially revealing the plasma electron density oscillations in the waveguide. The inset in Fig. 1.6 shows a schematic of an electron density oscillation in time and 1D space, which can be probed by with SSSI.

## 1.7 Synopsis

The main theme of this dissertation is the study of time-resolved dynamics of intense laser interactions with gases, clusters, and plasmas. To observe these ultrafast laser-induced dynamics, we first introduce a novel femtosecond optical diagnostic: *single-shot supercontinuum spectral interferometry* (SSSI) in Chapter 2.

Chapter 3 provides a detailed description of our multi-terawatt Ti:sapphire laser system used for the experiments discussed in this dissertation. Presented in Chapter 4 is the time-resolved ionization dynamics of helium in an intense laser field.

Chapter 5 describes the characterization of our nanometer-sized atomic or molecular cluster sources that will be used for our studies of high intensity laser–cluster interactions. The average cluster size and the number of clusters per unit volume – both of which play an essential role in the interaction of intense laser pulses with clustered gases – are measured with an all-optical diagnostic.

Chapter 6 discusses the transient explosion dynamics of intense laser-heated clusters. With the use of ultrafast optical diagnostics, such as time-resolved pump-probe laser absorption/scattering and SSSI, we verify our 1D hydrodynamic laser-cluster interaction model, in which “layer-by-layer” cluster explosion occurs, resulting in resonant coupling durations of several hundred femtoseconds. These results directly lead to the demonstration of self-focusing of intense laser pulses in clustered gases, discussed later in Chapter 7.

Chapter 7 also deals with the interaction of intense ultrashort laser pulses with plasma waveguides. Our SSSI diagnostic reveals the presence of pump-induced ionization distortions in the plasma waveguide. In this chapter, a novel plasma waveguide generation method is also demonstrated, which uses the unique features of the laser interaction with clustered gases – self-focusing and strong absorption.

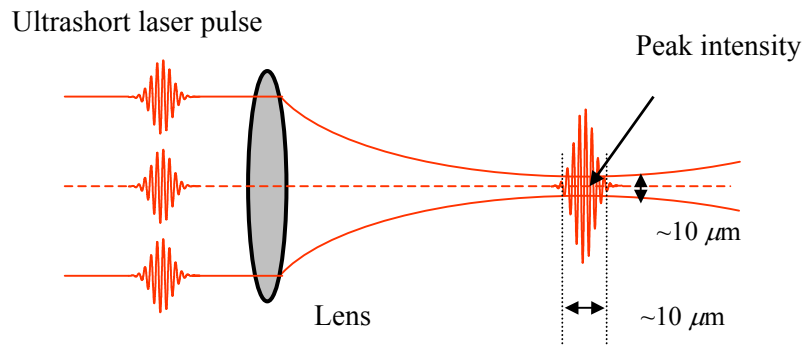


Figure 1.1: Focusing of ultrashort high power laser pulses in a small volume for high intensity laser–matter interaction experiments.

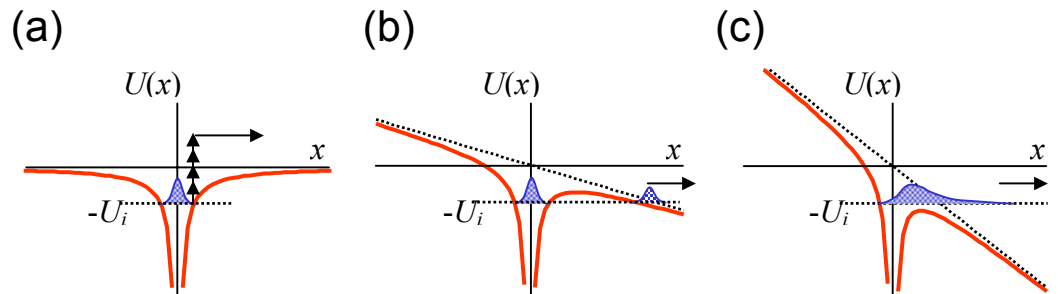


Figure 1.2: Three different laser-induced ionization mechanisms: (a) multiphoton, (b) tunneling, and (c) over-the-barrier (barrier suppression) ionization.

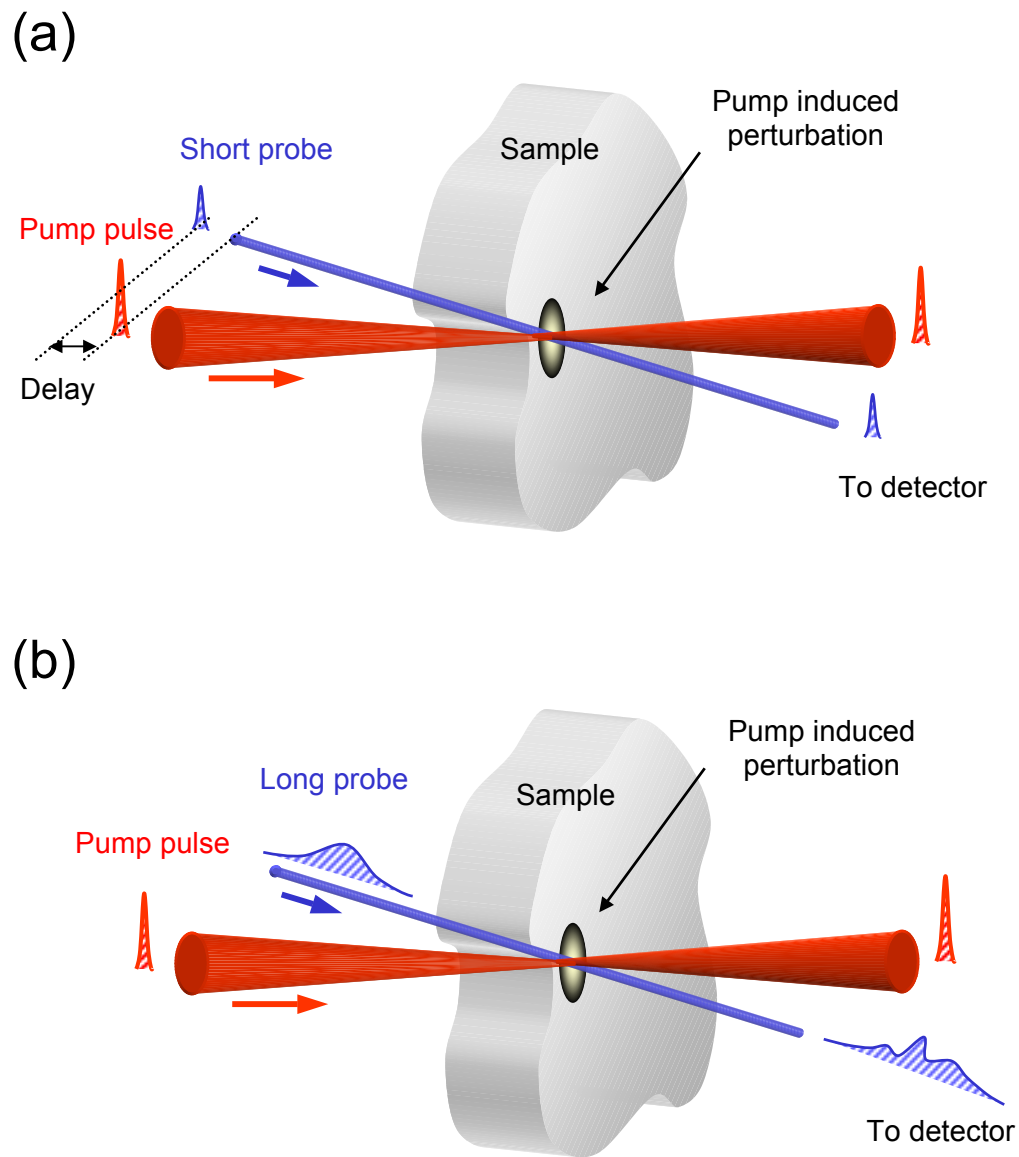


Figure 1.3: Two pump-probe diagnostic schemes: (a) multi-shot and (b) single-shot.

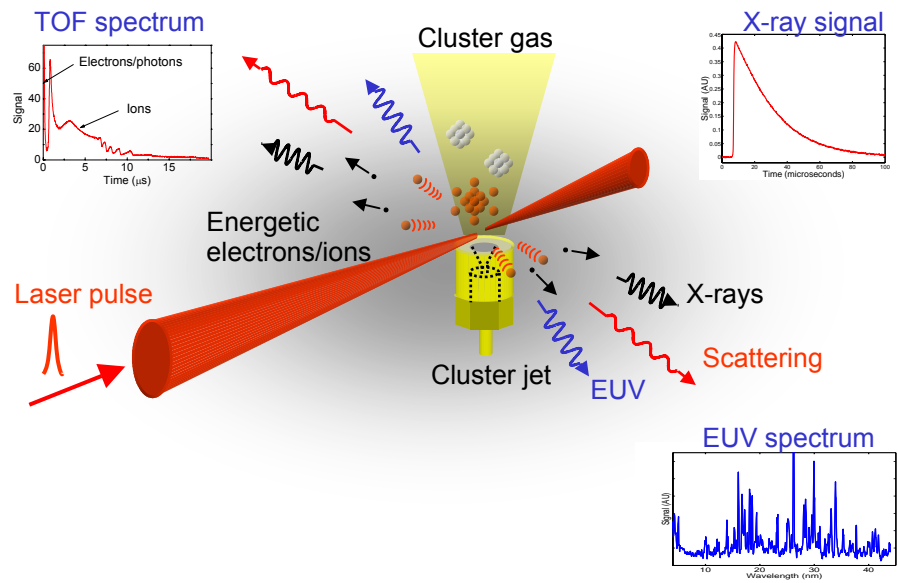


Figure 1.4: Interaction of an intense laser pulse with atomic or molecular clusters produces energetic electrons and ions, x-rays, and extreme ultraviolets (EUVs).

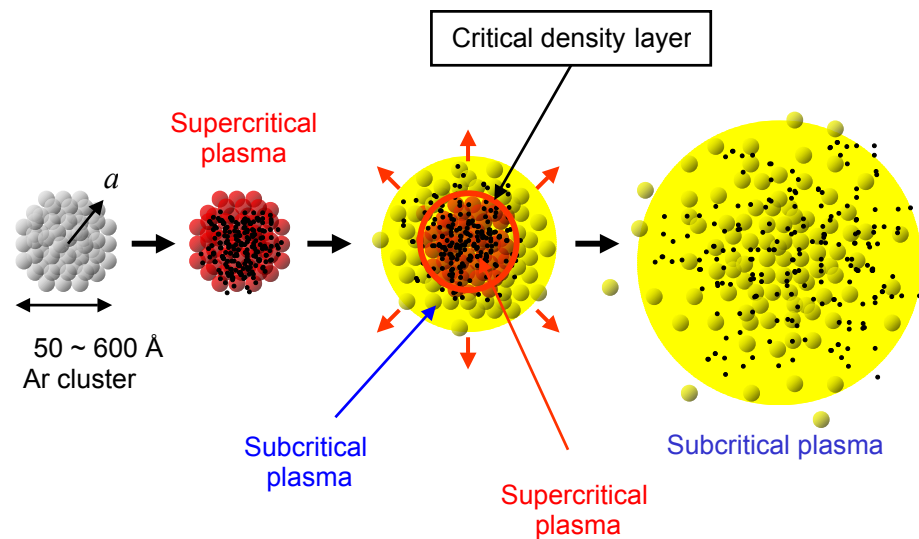


Figure 1.5: Diagram illustrating the interaction of intense laser fields with clusters.

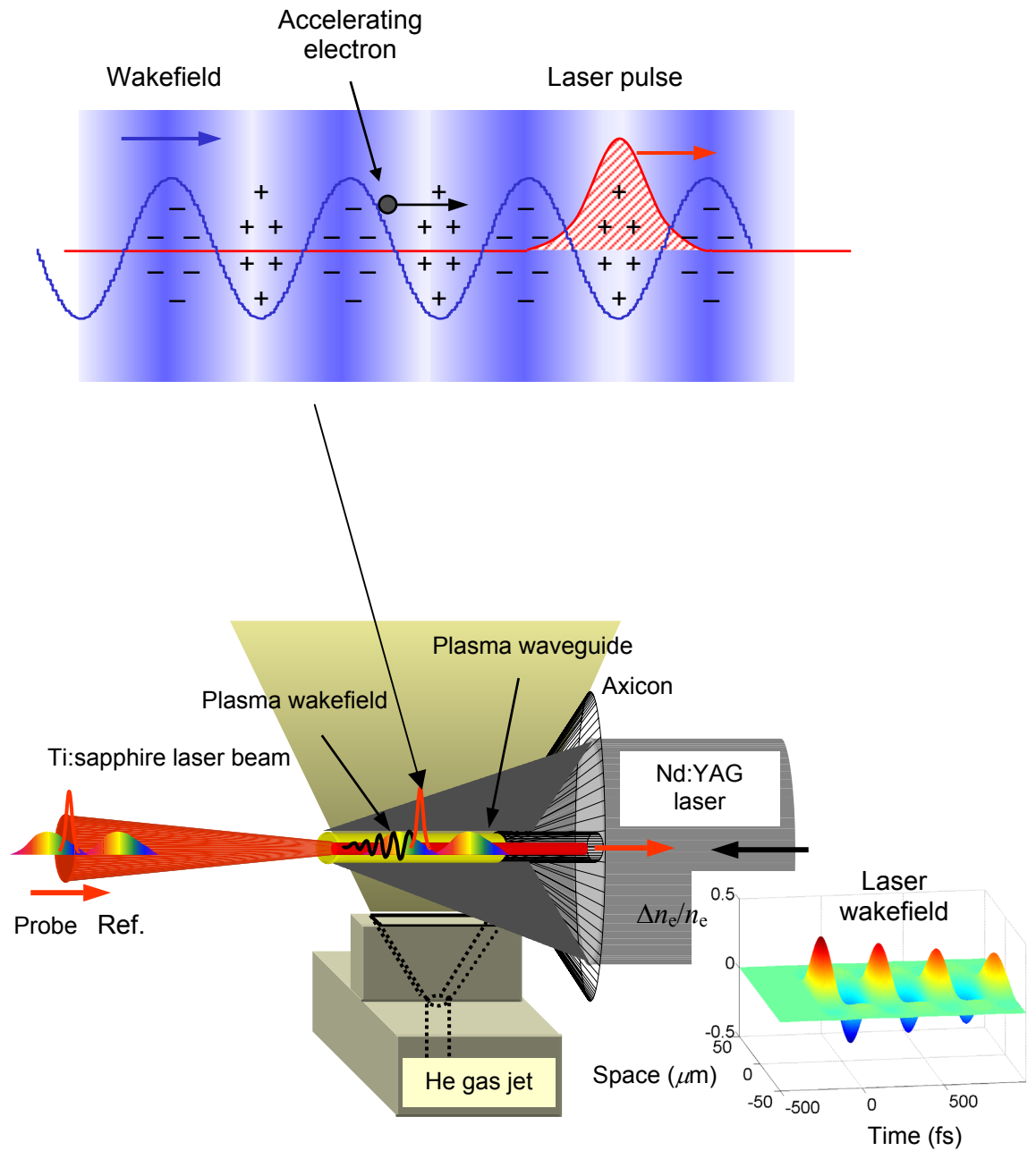


Figure 1.6: Laser wakefield excitation scheme in a preformed plasma waveguide. SSSI can potentially detect the electron density oscillations in the waveguide with one-dimensional (1D) spatio-temporal information in a single-shot.

## **Chapter 2: Single-shot supercontinuum spectral interferometry**

### **2.1 Introduction**

As described in Chapter 1, ultrafast optical diagnostics play an important role in studying femtosecond laser-matter interactions. In this chapter, we present single-shot supercontinuum spectral interferometry (SSSI). SSSI measures laser-induced refractive index transients using an ultrafast optical probe pulse, enabling the study of the evolution dynamics of laser-irradiated targets with femtosecond time resolution. In this dissertation, SSSI has been used as an essential diagnostic in investigating the time-resolved interaction dynamics of laser pulses with atomic gases, clusters, and plasma waveguides.

To understand SSSI, we first introduce spectral interferometry (SI) with its main application to time-resolved laser spectroscopy. In addition, multi-shot and single-shot SI (SSI) schemes are described, with an emphasis on the ultimate achievable temporal resolution. After the overview of SI and SSI, the theoretical framework and experimental demonstration of SSSI are presented.

### **2.2 Spectral interferometry**

Spectral interferometry (SI),<sup>1</sup> also known as frequency domain interferometry (FDI), is a phase-sensitive linear diagnostic which has been widely used in many experiments to measure refractive index transients. In this technique, a pump pulse induces an index transient in a medium, and a reference pulse and a time delayed replica (probe) pulse, upon which the pump-pulse-induced phase shift has been imposed, are interfered in

the frequency domain by combining them in a spectrometer [see Fig. 2.1(a)].<sup>2</sup> The interference allows even small phase shifts to be detected. In early applications of this technique,<sup>2,3</sup> the index transient was reconstructed by probing, at a succession of delays, with a pulse much shorter than the transient. This version of SI is sensitive to shot-to-shot variations in the laser pulse properties and in the sample response, which can result in degradation of the acquired phase information upon its step-delayed reconstruction. Nevertheless, SI diagnostics have been successfully used for the measurements of induced phase modulation in solids,<sup>2,4,5</sup> time evolution of femtosecond laser-plasmas,<sup>3,6,7</sup> shock waves,<sup>8</sup> and laser-driven plasma electron density oscillations.<sup>9-13</sup> A more detailed description of SI is provided in Appendix C.

Recently, single-shot SI (SSI) was developed in order to avoid the need for step-delayed reconstruction of pump-induced index transients. This was realized by linearly chirping the reference and a probe beams so that each temporal slice of the refractive index variation was projected onto a different frequency component [see Fig. 2.1(b)].<sup>14-16</sup> The temporal phase variation was then obtained from considering a direct mapping between the frequency and time. However, temporal resolution can be severely limited by using direct mapping. In recent work, this limitation has not been considered<sup>14,15</sup> or has been incompletely analyzed, neglecting the effect of the phase modulation itself on the achievable resolution.<sup>16,17</sup>

## **2.3 Single-shot supercontinuum spectral interferometry (SSSI)**

### **2.3.1 Introduction**

Recently, we have developed a novel single-shot spectral interferometry (SSI) diagnostic which uses a chirped probe pulse having an extremely broad spectral bandwidth. We have called the method Single-shot Supercontinuum Spectral Interferometry (SSSI).<sup>5</sup> It uses a probe of bandwidth in excess of 100 nm generated by the self-focusing of an intense laser pulse in atmospheric pressure air (see Appendix D). This large bandwidth allows temporal resolution of  $\sim 10$  fs, which is up to an order of magnitude better than in previous work.<sup>14-16</sup> The use of air as the nonlinear medium provides, in a single self-focused filament, probe light at almost three orders of magnitude greater brightness compared to the SC generated in solids (see Appendix D). We note that the proximity of the SC spectrum to the pump wavelength reduces group velocity walk-off effects, which can be present in spectral interferometry schemes using frequency-doubled probe pulses.<sup>18</sup> In addition, the temporal field of view can be arbitrarily adjusted (up to a few picoseconds) by chirping the probe beam with an appropriate thickness of dispersive material, which is easier than pulse stretching by limiting the phase-matching bandwidth.<sup>18</sup> The very large bandwidth of our SSI probe pulses demands that a detailed analysis be performed in order to determine the method's ultimate temporal resolution. To this end, we have examined, experimentally and theoretically, the dependence of the temporal resolution of this diagnostic on the SC pulse bandwidth and chirp.

Our SSSI diagnostic has been successfully applied to measurements of the femtosecond transients of laser-induced nonlinear Kerr effect in glass,<sup>5</sup> optical field

ionization (OFI) of helium gas,<sup>19</sup> and the dynamics of exploding laser-heated argon clusters.<sup>20</sup>

### 2.3.2 Principle of SSSI

In our SSSI scheme, a reference SC pulse  $E_r(t)$  and a  $\tau_0$ -delayed probe pulse  $E_{pr}(t) = E_r(t - \tau_0)e^{i\Delta\Phi(t-\tau_0)}$ , upon which a time-dependent phase shift  $\Delta\Phi(t)$  has been imposed, interfere in the frequency domain according to

$$\left| \tilde{E}_r(\omega) + \tilde{E}_{pr}(\omega) \right|^2 = \left| \tilde{E}_{r0}(\omega) \right|^2 + \left| \tilde{E}_{pr0}(\omega) \right|^2 + 2\left| \tilde{E}_{r0}(\omega) \right| \left| \tilde{E}_{pr0}(\omega) \right| \cos[\Delta\phi(\omega)], \quad (2.3)$$

where  $\tilde{E}_r(\omega) = \tilde{E}_{r0}(\omega)e^{i\phi_r(\omega)}$  and  $\tilde{E}_{pr}(\omega) = \tilde{E}_{pr0}(\omega)e^{i\phi_{pr}(\omega)}$  are the Fourier transforms of  $E_r(t)$  and  $E_{pr}(t)$ , respectively, the spectral amplitudes  $\tilde{E}_{r0,pr0}$  and phases  $\phi_{r,pr}$  are real, and  $\Delta\phi(\omega) = \phi_{pr}(\omega) - \phi_r(\omega) + \omega\tau_0$  is the spectral phase difference between the probe and reference pulses. The temporal phase shift  $\Delta\Phi(t - \tau_0)$  is determined by (see Appendix E)

$$\Delta\Phi(t - \tau_0) = \text{Im} \left[ \ln \left( \frac{\int \tilde{E}_{pr0}(\omega) e^{i\phi_{pr}(\omega) + i\Delta\phi(\omega)} e^{-i\omega(t-\tau_0)} d\omega}{\int \tilde{E}_{r0}(\omega) e^{i\phi_r(\omega)} e^{-i\omega(t-\tau_0)} d\omega} \right) \right], \quad (2.4)$$

where  $\Delta\phi(\omega)$  and  $\tilde{E}_{pr0}(\omega)$  are extracted from the interferogram,<sup>21</sup>  $\tilde{E}_{r0}(\omega)$  is the square root of the measured reference pulse spectrum, and  $\phi_r$  is measured through cross-phase modulation (XPM) of the SC pulse with a short pump pulse in fused silica.

A simpler and more direct approach which avoids Eq. (2.4) uses the nearly linear mapping between frequency and time to extract the transient phase shift as

$$\Delta\Phi(t(\omega)) = \Delta\phi(a(\omega - \omega_0)). \quad (2.5)$$

Here

$$a = 2\beta_2(1 + \beta_2^{-2}(\Delta\omega)^{-4}) \quad (2.6)$$

is the linear chirp coefficient for a Gaussian pulse (see Appendix C), where  $\Delta\omega$  is the full width at half maximum (FWHM) of the probe spectrum and  $\beta_2 = \frac{1}{2}(\partial^2\phi / \partial\omega^2)_{\omega_0}$  is the group delay dispersion. With this method, however, the temporal resolution of the extracted phase transient can be shown to be limited to

$$\Delta t_{\text{resol}} \sim (\Delta\omega)^{-1}[1 + \beta_2^2(\Delta\omega)^4]^{1/2}, \quad (2.7)$$

(see Appendix E for derivation). Shortly,  $\Delta t_{\text{resol}}$  is the minimum temporal interval that contributes to the phase shift at a fixed probe frequency, and is obtained by examining the decay with  $t'$  of  $\Delta\phi(\omega, t')$  as a result of an impulse perturbation applied at  $t' = 0$ . Equation (2.7) implies that for a large chirp ( $\beta_2 \gg \Delta\omega^{-2}$ ), the resolution is  $\Delta t_{\text{resol}} \sim \beta_2 \Delta\omega$ , indicating that excessive chirp (large  $\beta_2$ ) can degrade the resolution. With a small chirp ( $\beta_2 \ll \Delta\omega^{-2}$ ),  $\Delta t_{\text{resol}}$  approaches the fundamental limit of transform-limited pulse duration  $\Delta\omega^{-1}$  at the sacrifice of temporal field of view. Nevertheless, the utility of the direct mapping technique is that it allows one to see the temporal phase variations intuitively from a raw interferogram, tracing the relative fringe shift with respect to the frequency axis.

## 2.4 Experimental demonstration of SSSI – cross phase modulation in glass

In this section, we present proof-of-principle demonstration of our SSSI diagnostic, with an emphasis on the limitations of direct mapping and on the ultimate temporal resolution. As shown in Fig. 2.2(a), Kerr-induced cross phase modulation (XPM) in fused silica glass was used to shift the probe phase on a femtosecond time scale. An optical pump pulse modulates the refractive index of the fused silica glass as  $n = n_0 + n_2 I_p(t)$  where  $I_p(t)$

is the instantaneous pump intensity and  $n_2 = 3.2 \times 10^{-16} \text{ cm}^2/\text{W}$  is the nonlinear index of refraction of fused silica.<sup>22</sup> This transient refractive index, in turn, perturbs the probe pulse with a temporal phase shift of  $\Delta\Phi(t) = \omega_0 n_2 I_p(t) L / c$  where  $L$  is the material length. Using SSSI, we measured the spectral shift  $\Delta\phi(\omega)$  of the probe with various chirps at a fixed broad spectral bandwidth. Both direct mapping and Fourier transform techniques were used to extract  $\Delta\Phi(t)$ .

### 2.4.1 Experimental setup

The experimental setup is shown in Fig. 2.2(b). The SC pulse is generated as broadband conical emission from  $f/8$  focusing of a  $\sim 1$  mJ, 80 fs pulse in atmospheric pressure air. Although it is possible to generate SC in a sapphire window,<sup>23</sup> the pump power is limited to the critical power for self-focusing ( $P_{\text{cr}} \approx 3\text{MW}$ ) to avoid multiple filament formation,<sup>24</sup> which leads to significant spatio-temporal phase distortions. This limits maximum useable pump energies in bulk media to the microjoule range (see Appendix D for details).

Imaging of our air SC source shows that it originates from a single filament in the focal region. The conical emission spectrum is increasingly blue-shifted with radius.<sup>25, 26</sup> The SC beam is collimated and split into collinear twin pulses (reference and probe pulses) with delay  $\tau_0$  by a Michelson interferometer delay line. The twin pulse beam is sent through a  $\sim 250 \mu\text{m}$  diameter aperture to clean the spatial profile and reduce the spatial chirp (see Appendix D). Temporal chirp, in addition to that imposed by the intrinsic system optics, was added with an additional dispersive glass window DW, either 22.2 mm thick BK7 or 25.4 mm thick SF4 glass.

The time-dependent refractive index variation used to test the diagnostic was generated by a 0.12  $\mu\text{J}$ , 800 nm, 80 fs pump pulse focused at  $f/50$  by a  $\text{MgF}_2$  lens into a 1-mm-thick fused silica window (FS) with a FWHM spot size of 40  $\mu\text{m}$ . The pulse width was measured independently by frequency resolved optical gating (FROG)<sup>27</sup>. The twin chirped SC pulses were directed through the pump mirror (dichroic splitter DS), and collinearly focused into the FS window with the pump to a FWHM spot size of 170  $\mu\text{m}$ , overfilling the pump spot. The pulse timing was arranged so that the reference pulse preceded the probe pulse, and the pump pulse was overlapped with the probe, generating a time- and space-dependent phase variation due to the Kerr-induced XPM. The pump was removed from the beam path by mirror M with a  $\sim 60$  nm-bandwidth high reflectivity coating at 800 nm, leaving the SC pulses with a FWHM bandwidth of  $\sim 65$  nm. The coherence time corresponding to this bandwidth is  $\tau_c = 2.77/\Delta\omega \sim 11$  fs. The twin pulses were then imaged with  $15\times$  magnification onto the spectrometer entrance slit, producing a spectral interferogram on the spectrometer CCD with 1D spatial resolution along the slit. The spectral and spatial resolutions of the imaging spectrometer were 0.5 nm and 7  $\mu\text{m}$ , respectively.

#### 2.4.2 Spectral phase extraction and chirp characterization

Once a spectral interferogram is obtained experimentally, the spectral phase difference  $\Delta\phi(x, \omega) = \phi_{\text{pr}}(x, \omega) - \phi(x, \omega) + \omega\tau_0$  is extracted first. The simplest method is tracing the shifts of fringe peaks or valleys as demonstrated in references.<sup>2, 4, 15</sup> This technique, however, depends on the criterion used for fringe location, and requires a great deal of time for data processing. Moreover, the finite number of fringes substantially limits

the extractable data points. To extract  $\Delta\phi(\omega)$  more accurately, we used the Fourier transform method developed by Takeda *et al.*<sup>21</sup> (see Appendix F). This method can extract  $\left| \tilde{E}_{\tau_0}(x, \omega) \tilde{E}_{\text{pr}0}(x, \omega) \right|$  and  $\Delta\phi(x, \omega)$  from a two-dimensional (2D) spectral interferogram  $I(x, \omega)$ . For more detailed descriptions, see Appendix F. Figure 2.3 shows (a) a sample experimental 2D spectral interferogram  $I(x, \lambda)$  and (i)-(iii) show the steps in the Fourier transform method to extract the phase difference  $\Delta\phi(x, \lambda)$ . Shown in Figure 2.3(b) is  $\Delta\phi_{\text{pr}}(x, \lambda)$  obtained from  $\Delta\phi_{\text{pump-on}}(x, \omega)$  by subtracting  $\Delta\phi_{\text{pump-off}}(x, \omega)$  where  $\Delta\phi_{\text{pump-on, pump-off}}(x, \omega)$  are the probe-reference phase differences with the pump on and off, respectively. This method bypasses the need for measuring  $\tau_0$ , and it potentially reduces the unwanted spatial phase distortion arising from irregularities in the spectrometer slit or beam spatial chirp.

To determine the temporal probe phase shift  $\Delta\Phi_{\text{pr}}(t)$  from the spectral phase shift  $\Delta\phi_{\text{pr}}(x, \omega)$  measurement, the spectral phase  $\phi_{\text{r}}(\omega)$  of the reference pulse must be well characterized. In this section, we present a method to measure the linear chirp coefficient  $a$ , defined in Eq. (2.6), which will give us the spectral phase through second order in  $\omega$ .<sup>4</sup> This was experimentally implemented by tracing the translation of  $\Delta\phi(\omega)$  along the  $\omega$ -axis as the pump-probe separation  $\tau$  was varied. Figure 2.4(a) shows the results of the XPM procedure for determining the chirp parameter  $a$  of the SC pulse. Spectral phase plots  $\Delta\phi(\omega)$  on the beam axis were extracted for a sequence of incremental delays ( $\Delta t = 66$  fs) of the pump [Fig. 2.4(a-i)]. A linear least squares fit of the phase peaks versus time delay gave  $a_1 = (1.06 \pm 0.08) \times 10^3 \text{ fs}^2$  (no chirping window W),  $a_2 = (2.40 \pm 0.03) \times 10^3 \text{ fs}^2$  [22.2

mm BK7, shown in Fig. 2.4(a-ii)], and  $a_3 = (6.85 \pm 0.05) \times 10^3 \text{ fs}^2$  (25.4 mm SF4). The quoted errors represent the variance of the data points from the fits.

The second approach, which is similar but even simpler than the first method, was to monitor the probe (or reference) XPM spectrum without the presence of the other replica pulse. Figure 2.4(b-i) shows raw probe spectra under the variation of the pump-probe delay  $\tau$ . The wavelength shifts of perturbed probe spectra are plotted in Fig. 2.4(b-ii) as a function of delay  $\tau$ . Co-plotted is a linear least squares fit of the data points, from which the chirp coefficient  $a$  can be extracted. Similar results were obtained with this method.

To characterize the linear chirp of probe (or reference), we ignored higher-order dispersions (TOD, 4OD, and etc.; see Appendix C) arising from the SC generation process and the intrinsic material dispersion of the optics (see Appendix D). Even though the probe pulse is mostly linearly chirped as shown in Fig. 2.4, unknown higher order dispersion may cause an imperfect retrieval of the temporal phase variation  $\Delta\Phi(t)$ , particularly with the Fourier transform method. This will be addressed in Section 2.5 in detail.

### 2.4.3 Experimental results

We first examined the effect of increasing chirp at fixed SC bandwidth on results obtained using the direct mapping method. Figure 2.5(a) shows the measured and simulated time dependent phases for (i)  $a_1 = (1.06 \pm 0.08) \times 10^3 \text{ fs}^2$ , (ii)  $a_2 = (2.40 \pm 0.03) \times 10^3 \text{ fs}^2$ , and (iii)  $a_3 = (6.85 \pm 0.05) \times 10^3 \text{ fs}^2$ , for which Eq. (2.6) gives the expected time resolutions  $\Delta t_{\text{res}}$  of  $\sim 140 \text{ fs}$ ,  $\sim 300 \text{ fs}$ , and  $\sim 870 \text{ fs}$ , respectively. As predicted by Eq. (2.7), the phase recovered from direct mapping becomes increasingly distorted as the chirp increases for a fixed pulse bandwidth. Even for the case of smallest chirp, panel (i) of Fig.

2.5(a), the associated time resolution of 140 fs is still insufficient to track the index variation induced by the 80 fs pump.

The theoretical simulations of Fig. 2.5(a)(i')-(iii') were performed by assuming Gaussian probe and reference pulses using the measured values of bandwidth and chirp and separated by delay  $\tau_0$ . The pump pulse perturbed the probe via XPM according to

$E_{\text{pr}}(t) = E_r(t - \tau_0)e^{i\Delta\Phi(t-\tau_0)}$ , where  $\Delta\Phi(t) = \Delta\Phi_{\text{peak}} \exp(-4 \ln 2 t^2 / \tau_p^2)$  and  $\Delta\Phi_{\text{peak}} = \omega_0 n_2 I_{\text{peak}} L / c = 3.45$  rad is the peak nonlinear phase shift, using peak laser intensity  $I_{\text{peak}} = 1.2 \times 10^{12}$  W/cm<sup>2</sup>, pump FWHM pulsewidth  $\tau_p = 80$  fs, interaction length  $L = 1$  mm, and central probe frequency  $\omega_0 = 2.72 \times 10^{15}$  Hz. Transforming into the frequency domain yielded a spectral interferogram via Eq. (2.3), from which the transient phase was calculated as  $\Delta\Phi[t(\omega)] = \Delta\phi[a(\omega - \omega_0)]$ . The simulations are in excellent agreement with the experimental results: increasing distortion with chirp in the recovery of  $\Delta\Phi(t)$ .

Applying the full Fourier transformation to determine  $\Delta\Phi(t)$  via Eq. (2.4) requires knowledge of  $\phi_t(\omega)$ . This was determined through second order  $\phi_t(\omega) \approx \beta_2(\omega - \omega_0)^2$  from the XPM calibration shown in Fig. 2.4. The results for increasing chirp (and increasing temporal observation window) are shown in Fig. 2.5(b), where the chirp-induced distortions are largely eliminated. Figure 2.6 compares the direct mapping and Fourier transform methods in a 2D plot, corresponding to Fig. 2.5(a-iii) and 2.6(b-iii). Distortion is seen in Fig. 2.6(a) with direct frequency-to-time mapping, while the full Fourier transform shows little distortion in Fig. 2.6(b).

## 2.5 Limitations of SSSI

In this section, we investigate the limitations of the SSSI diagnostic. First, we examine the effect of higher order dispersion on the ultimate achievable temporal resolution. In addition, the issue of temporal field of view is addressed in comparison with other femtosecond optical diagnostics.

As noted before, we assumed that the reference pulse was linearly chirped, ignoring higher order dispersions (3OD, 4OD, and etc.) that may exist. Here a question arises: does neglect of higher order dispersion corrections to  $\phi_r(\omega)$  affect the ultimate temporal resolution of this technique? Additional  $n \geq 3$  terms  $\beta_n(\omega - \omega_0)^n$  would have the effect of extending the fit in Fig. 2.4(a)-(b) to the nonlinear terms in  $\omega(t) = \omega_0 + bt + ct^2 + dt^3 + \dots$ , where  $b = 1/a$  is the linear chirp rate, and  $c$  and the higher order coefficients are functions of  $\Delta\omega$  and  $\beta_n$ .

To examine the effect of higher order chirp contributions that were neglected by the linear fit of Fig. 2.4(a)-(b), we simulated the extraction of  $\Delta\Phi(t)$  for XPM pump durations  $\tau_p$  of (a) 80 fs, (b) 50 fs, and (c) 20 fs for fixed  $\Delta\Phi_{\text{peak}} = 3.45$  rad. We assumed nonlinearly chirped reference and probe pulses of the form  $E_0 \exp\left(-4 \ln 2 t^2 / \tau_0^2\right) \exp\left[-i\left(\omega_0 t + bt^2/2 + ct^3/3\right)\right]$ , where  $b = 1/a_1 = 9.4 \times 10^{-4} \text{ fs}^{-2}$  and  $\Delta\omega = 4 \ln 2 / \tau_c \sim 0.255 \text{ fs}^{-1}$  (measured values of chirp and bandwidth were used),  $\tau_0 = \Delta\omega/b \sim 270$  fs is the FWHM of the chirped pulse, and  $c$  is the non-zero cubic chirp coefficient. Here the uncertainty in  $b$ , i.e.,  $\Delta b/b$  limits the maximum possible value of the coefficient  $c$  to  $\sim 2\Delta b/\tau_0$ . The results are shown in Fig. 2.7. There, we considered three cases: (i)  $\Delta b/b = 0.01$ , (ii)  $\Delta b/b = 0.05$ , and (iii)  $\Delta b/b = 0.1$ . The corresponding  $c$  values are (i)  $c = 6.9 \times 10^{-8} \text{ fs}^{-3}$ , (ii),  $c = 3.5 \times 10^{-7} \text{ fs}^{-3}$ ,

and (iii)  $c = 6.9 \times 10^{-7} \text{ fs}^{-3}$ . The XPM perturbation was imposed on the probe and the sum of the reference and perturbed probe was transformed to the frequency domain, generating a spectral interferogram from which  $\Delta\phi(\omega)$  was extracted. The absolute probe phase was then constructed as  $\phi_{\text{pr}}(\omega) = \Delta\phi(\omega) + \beta_2(\omega - \omega_0)^2$ , purposely neglecting the higher order dispersion terms which should have been included by virtue of  $c \neq 0$ . Finally,  $\Delta\Phi(t)$  was extracted via Eq. (2.4). It is seen that neglect of higher order terms in  $\phi_{\text{pr}}(\omega)$  is most significant for the shortest ( $\tau_p = 20 \text{ fs}$ ) pump pulse and the largest uncertainty in  $\Delta b/b$ . Our estimated uncertainty in  $b$  from the linear least squares fit in Fig. 2.4(b-ii) is  $\Delta b/b \sim 0.01$ , which is consistent with the onset of retrieval distortion for a 20 fs pump pulse.

We note another restriction on the ultimate temporal resolution. Short intense pump pulses can add additional frequency wings  $\delta\omega$  to the probe spectrum owing to XPM, whereas the reference spectrum remains unchanged. This frequency mismatch leads to distorted spectral interference between the reference and probe. As a result, the retrieval of the transient refractive index becomes incomplete, effectively increasing the temporal resolution. This can be seen analytically: if frequency wings  $\delta\omega \sim \Delta\Phi_{\text{peak}}/\tau_p$  are added by the XPM perturbation  $\Delta\Phi(t) = \Delta\Phi_{\text{peak}} \exp(-4 \ln 2 t^2 / \tau_p^2)$ , then the distortion of spectral interference is negligible if  $\delta\omega \ll \Delta\omega$  or  $\tau_p \gg \Delta\Phi_{\text{peak}} \tau_c$ . Thus  $\Delta\Phi_{\text{peak}}$  sets the ultimate temporal resolution through  $\Delta t_{\text{resol}} \sim \Delta\Phi_{\text{peak}} \tau_c$  for  $|\Delta\Phi_{\text{peak}}| > 1$ . In general, the time resolution  $\Delta t_{\text{resol}}$  is determined by the spectral bandwidth ( $\Delta\omega \sim 1/\tau_c$ ) and the smallest measurable phase shift  $\Delta\Phi_{\text{peak}}$ .

The temporal field of view is an important consideration in a single-shot diagnostic. With SSSI, the temporal observation window is determined from the probe pulse duration,

and it is easily controlled by the thickness of dispersive material (DW). There is, however, a fundamental limit on the probe pulse duration  $\tau_{\text{pr}}$ : the probe and reference separation  $\tau_0$  must be larger than the pulse duration, i.e.,  $\tau_0 > \tau_{\text{pr}}$ . Otherwise, the reference and probe pulses overlap in time, and the pump-induced modulation can perturb both of these pulses, consequently making the reference pulse useless. However, too large a  $\tau_0$  causes fringe visibility to become poor as the spectral modulation period shrinks according to  $\delta\omega = 2\pi/\tau_0$  or  $\delta\lambda = -\lambda^2(c\tau_0)^{-1}$  from Eq. (2.3). From our spectrometer resolution of  $\delta\lambda = 0.5$  nm, the maximal reference-probe separation is  $\tau_0 = 3$  ps, which sets the maximum observation window in our implementation of SSSI.

## 2.6 Conclusions

We have reviewed the principles of SI and SSI diagnostics and their applications for time-resolved phase and amplitude spectroscopy. More importantly, we have developed a SSI method using sub-mJ-level supercontinuum pulses generated by self-focusing in air: single-shot supercontinuum spectral interferometry (SSSI). It was theoretically and experimentally shown that the direct frequency-to-time mapping method of transient phase extraction has its time resolution strongly limited by the pulse chirp. In addition, with a full Fourier transformation, the complete phase transient can in principle be extracted with temporal resolution limited mainly by the accuracy of the chirp measurement to

$$\sim \Delta\Phi_{\text{peak}} \tau_c / 2.$$

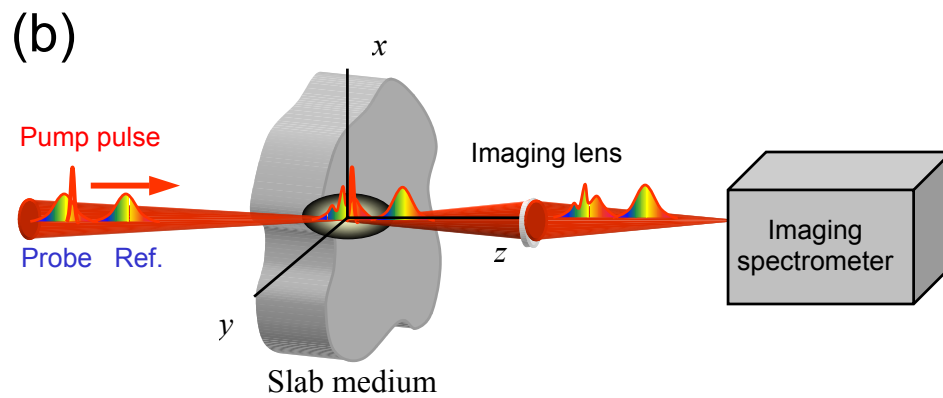
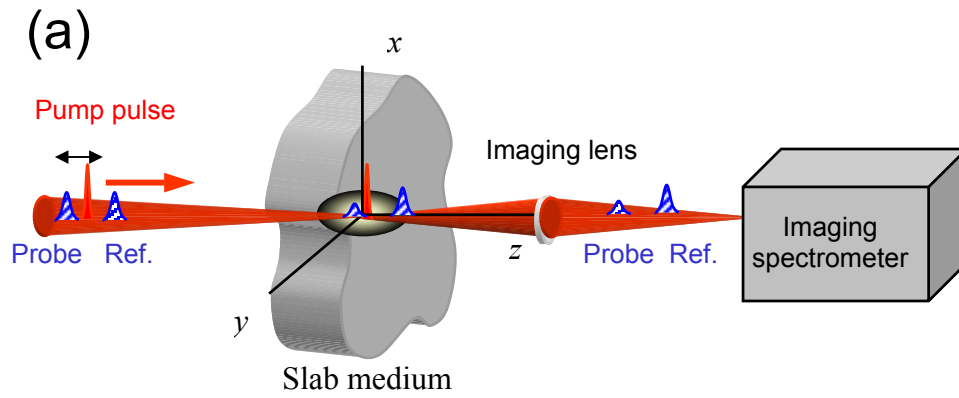


Figure 2.1: (a) Multi-shot spectral interferometry layout. (b) Single-shot chirped spectral interferometry diagnostic layout.

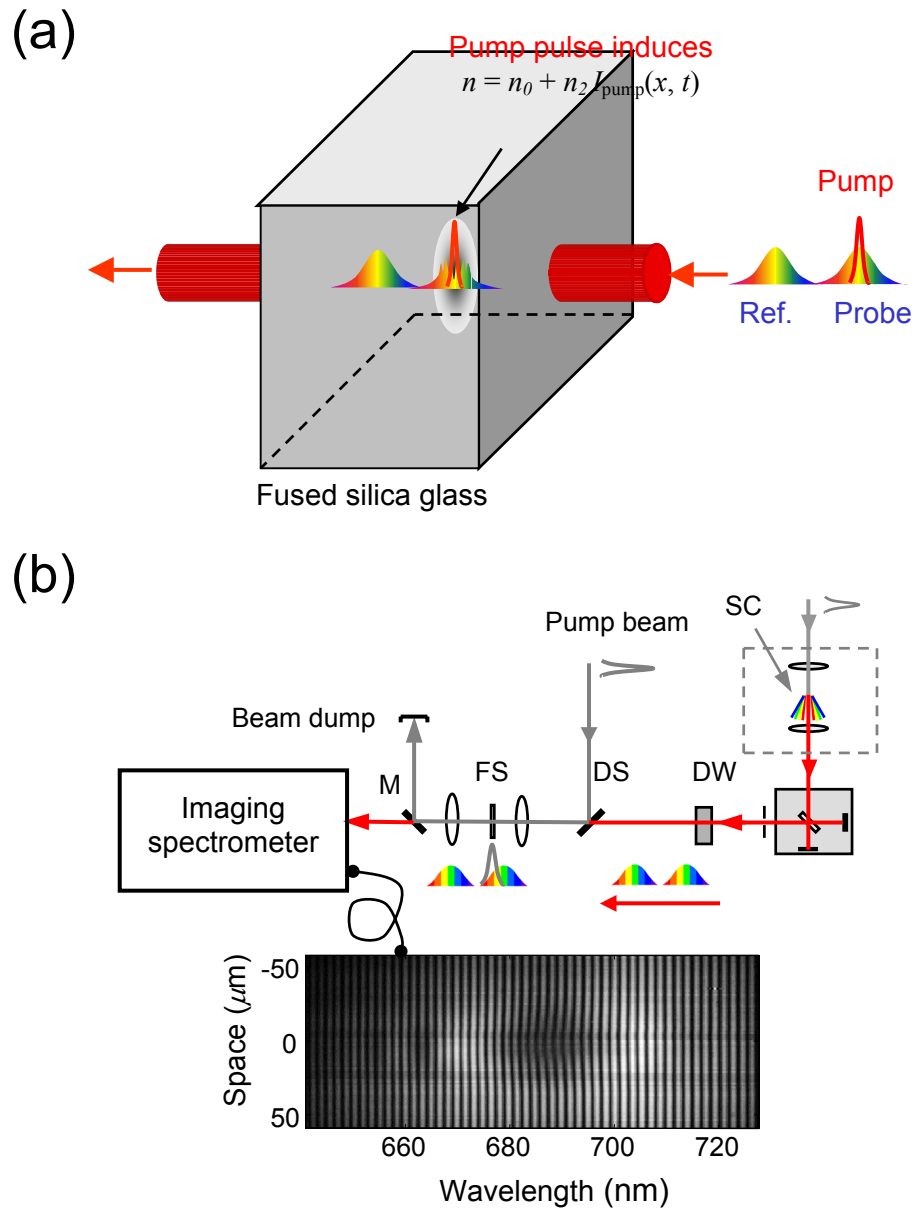


Figure 2.2: (a) Schematic of cross phase modulation (XPM) of a probe pulse induced by an intense pump pulse in fused silica glass. (b) XPM experimental setup, showing pump, reference, and probe beams, dispersive window (DW), dichroic splitter (DS), 1-mm-thick fused silica glass (FS), pump removal mirror (M), and imaging spectrometer. Sample spectral interferogram image from optical Kerr-induced XPM in FS is also shown.

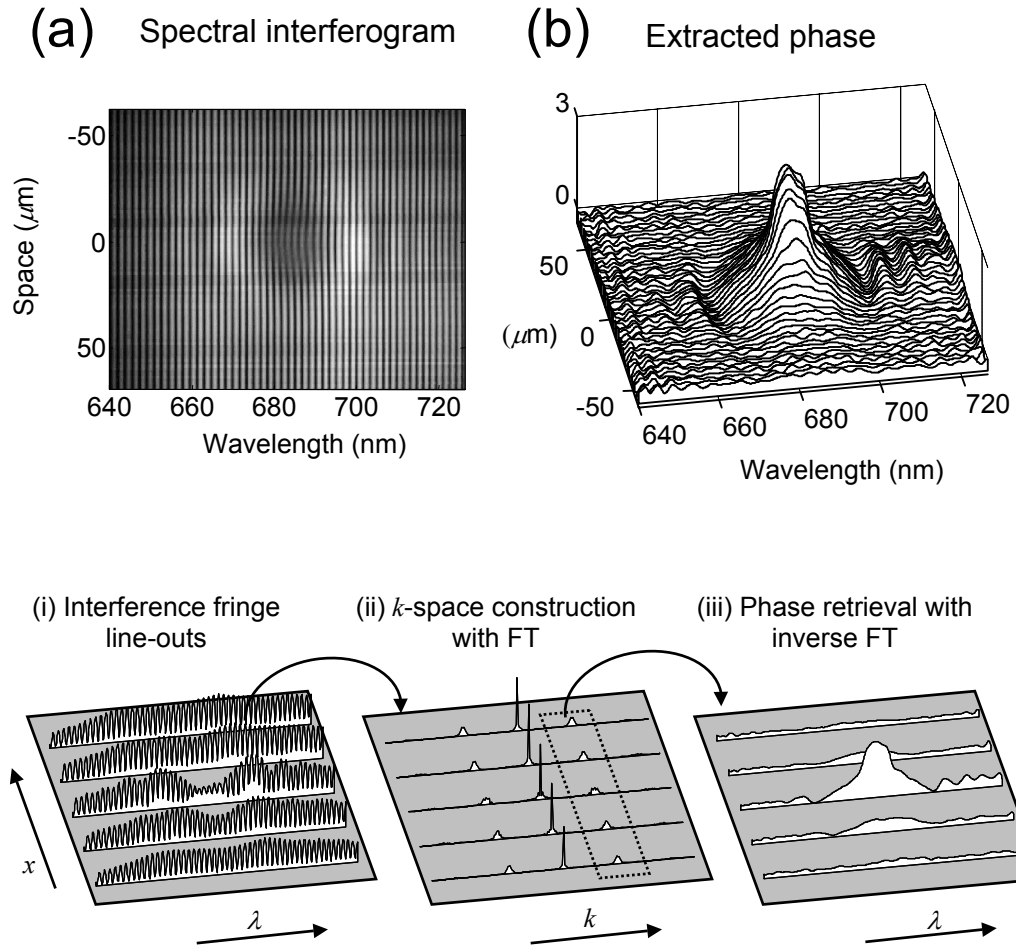


Figure 2.3: (a) Raw chirped spectral interferogram with XPM. (b) Extracted spectral phase  $\Delta\phi(x, \lambda)$  using fast Fourier transform (FFT) phase extraction method shown in (i)-(iii).

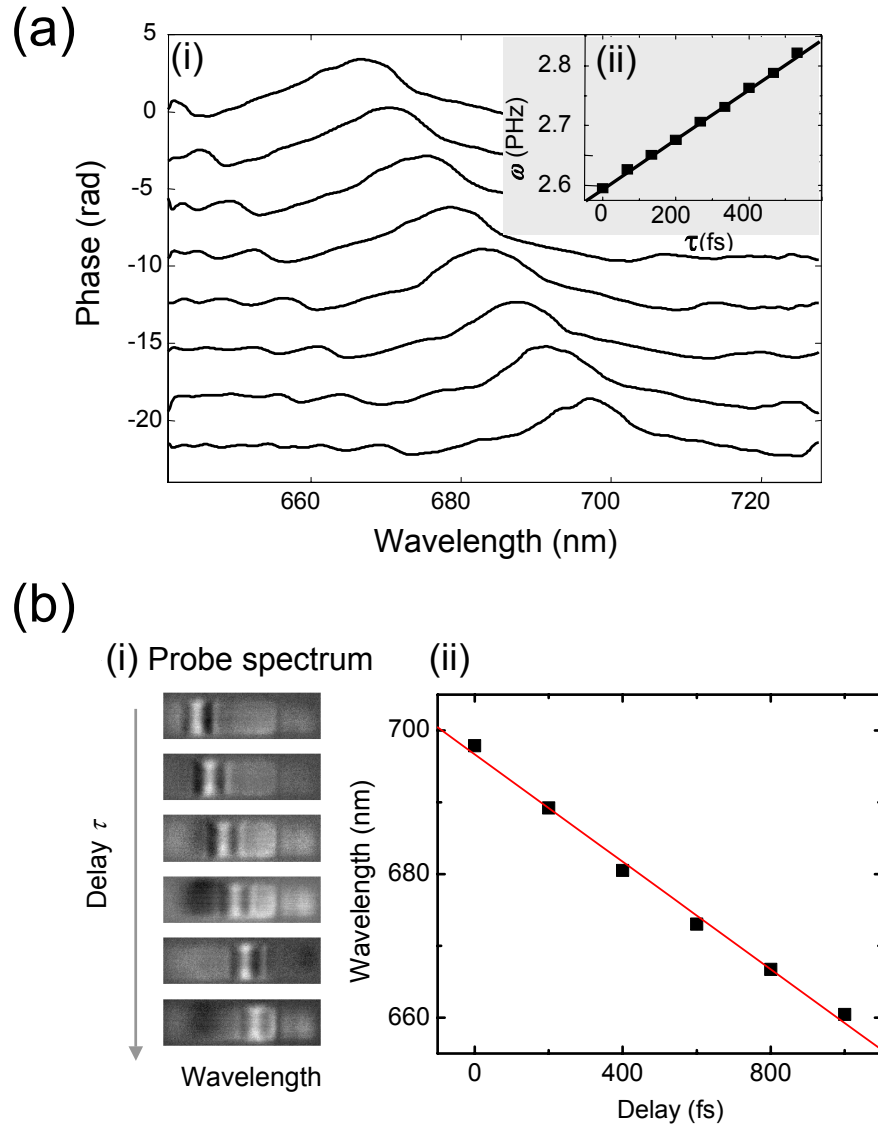


Figure 2.4: Determination of the chirp parameter of the SC pulse. Two methods [(a) and (b)] are possible. (a-i) Spectral phase plots were extracted for a sequence of incremental delays ( $\Delta t = 66$  fs) of the pump for DW = 22.2 mm BK7. The plots are vertically offset for clarity. (a-ii) Linear least squares fit of the phase peaks versus time delay gave  $a_2 = (2.40 \pm 0.03) \times 10^3$  fs<sup>2</sup> for DW = 22.2 mm BK7. (b-i) Raw probe spectral intensity modulations with varying pump-probe delay. (b-ii) Plot of wavelength at modulation peaks vs. pump-probe delay with a linear least squares fit.

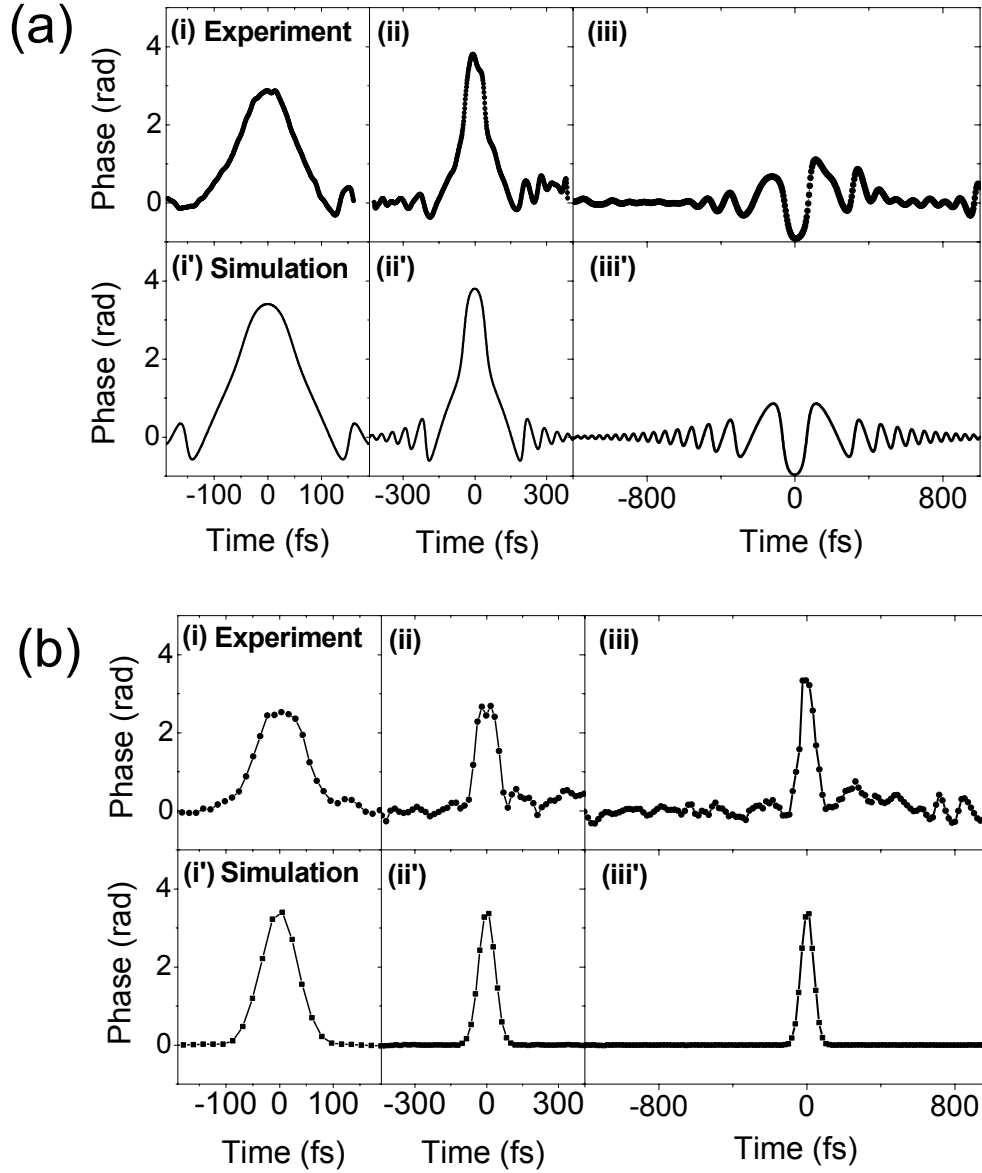
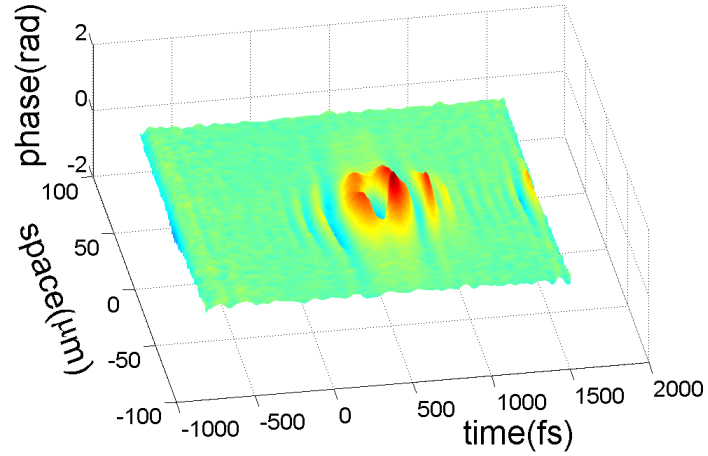


Figure 2.5: (a) Experimental [(i)-(iii)] and corresponding theoretical [(i')-(iii')] transient phase extracted using direct frequency-to-time mapping for chirp parameters (i)  $a_1 = 1.06 \times 10^3 \text{ fs}^2$ , (ii)  $a_2 = 2.40 \times 10^3 \text{ fs}^2$ , and (iii)  $a_3 = 6.85 \times 10^3 \text{ fs}^2$ . The plots are space-central time line-outs of the full phase images. (b) Full Fourier extraction of transient phase for the three chirps of (a). Experimental results: (i)-(iii). Corresponding simulations: (i')-(iii').

(a)  $\Delta\Phi(x,t)$  extraction with direct mapping



(b)  $\Delta\Phi(x,t)$  extraction with Fourier transform

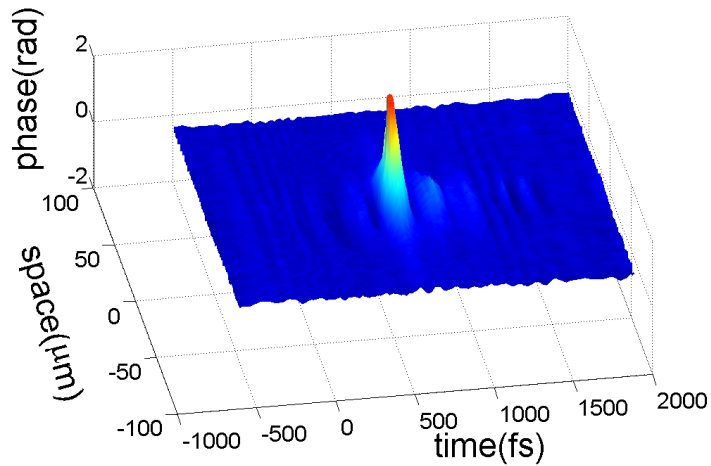


Figure 2.6: Full time and one-dimensional (1D) space image of extracted spatio-temporal XPM phase shift  $\Delta\Phi(x, t)$  with (a) direct frequency-to-time mapping and (b) full Fourier transform methods for the chirp of  $a_3 = 6.85 \times 10^3 \text{ fs}^2$ .

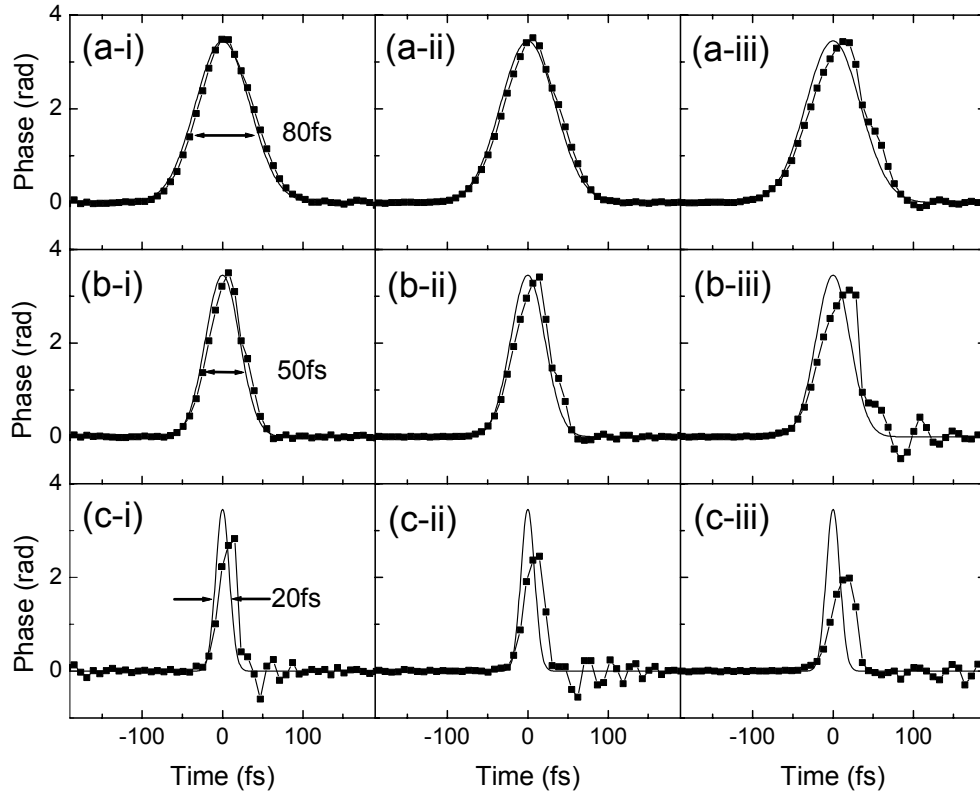


Figure 2.7: Simulated transient phase extraction from XPM perturbation with (a) 80 fs, (b) 50 fs, and (c) 20 fs pump pulse durations with probe pulse chirp through cubic term accounted for (solid lines) and with chirp kept only through quadratic term (lines with solid squares). Cubic term are (i)  $c = 6.9 \times 10^{-8} \text{ fs}^{-3}$ , (ii)  $c = 3.5 \times 10^{-7} \text{ fs}^{-3}$ , and (iii)  $c = 6.9 \times 10^{-7} \text{ fs}^{-3}$ .

## Chapter 3: Femtosecond multi-terawatt Ti:sapphire laser system

### 3.1 CPA technique and Ti:sapphire laser

The chirped pulse amplification (CPA) technique<sup>1,2</sup> described in Appendix A opened a new path for the generation of ultrahigh power laser pulses. It directly led to the advent of high-repetition-rate tabletop multi-terawatt pulsed lasers with an adoption of titanium-doped sapphire (Ti:Al<sub>2</sub>O<sub>3</sub> or Ti:sapphire) crystals as the gain medium. The first use of Ti:sapphire in a solid state laser was demonstrated by Moulton in 1982.<sup>3,4</sup> Since then, Ti:sapphire has been the most popular gain medium for ultrashort high power solid state lasers due to the following spectroscopic and material characteristics: large peak emission cross section of  $\sigma = 30 \times 10^{-20} \text{ cm}^2$ , relatively long upper state lifetime of 3.2  $\mu\text{s}$ , broad gain bandwidth from 700 nm to 1100 nm, high thermal conductivity of 46 W/m·K at 300 K, high optical damage threshold of 8 ~ 10 J/cm<sup>2</sup>, and high energy storage density of 1 J/cm<sup>2</sup>.<sup>3-6</sup> Other solid state crystal such as Cr:LiSAF (Cr:LiSrAlF<sub>6</sub>) and Cr:Forsterite also have been used as gain media to generate femtosecond terawatt laser pulses, but laser rods of these materials have not been manufactured to the same optical quality as with Ti:sapphire. Therefore, the Ti:sapphire crystal is still the most popular active medium for the majority of high-repetition-rate, multi-terawatt laser facilities around the world. The general features of femtosecond multi-terawatt Ti:sapphire laser systems can be found in review papers<sup>6-9</sup> and dissertations.<sup>10,11</sup>

In this chapter, our home-made multi-terawatt Ti:sapphire laser system, used for most of the experiments of this dissertation, is described. Figure 3.1 is a schematic of our

10 Hz repetition rate, 2 TW peak power, 60 fs Ti:sapphire laser system. The system consists of an oscillator, a pulse stretcher, a regenerative amplifier, and two multi-pass amplifiers followed by a pulse compressor. First, a 50 fs pulse train at 76.3 MHz is generated from the Kerr-lens mode-locked Ti:sapphire oscillator. The pulse is temporally stretched in the pulse stretcher, and then amplified in the regenerative amplifier followed by two additional multi-pass amplifiers. Finally, the amplified pulse is compressed back to nearly the original pulse duration in the compressor to produce 60 fs, 100 mJ pulses at 10 Hz repetition rate.

### **3.2 Femtosecond pulse train generation (oscillator)**

Femtosecond pulse generation in our Ti:sapphire oscillator is based on the Kerr lens mode-locking (KLM) mechanism. The first operation of KLM or self-mode-locking using Ti:sapphire was demonstrated by Sibbett and his group in 1991.<sup>12, 13</sup> After that, a number of experimental<sup>14–19</sup> and theoretical<sup>20–23</sup> works on KLM have been reported. The basic concept of KLM is that the gain crystal behaves like a fast saturable nonlinearity under the onset of Kerr lens focusing, resulting in passive mode locking to generate a femtosecond pulse train. In the nonlinear regime of KLM, the Kerr effect occurs when the refractive index of the gain medium becomes intensity-dependent according to  $n = n_0 + n_2I$ , where  $n_0$  is the normal refractive index and  $n_2$  is called the “nonlinear index of refraction”. This effect results in an intensity-dependent graded-index lens, which causes the laser crystal to act as a lens with an intensity-dependent focal length. With the employment of a hard or soft aperture in the resonator, the Kerr lens can introduce a low loss for high intensity and high loss for low intensity. Ultimately, this gives rise to pulse sharpening in the time

domain, as only the most intense pulses survive the losses. Because of the extremely fast electronic response time of  $\sim 1$  fs in solid media,<sup>24</sup> KLM is preferred over other mode-locking methods for the generation of stable femtosecond laser pulses. To date, sub-6-fs pulses ( $\sim 2$  optical cycles) are the shortest pulses to be directly produced using KLM.<sup>25</sup> More details on KLM and femtosecond pulse generation are found in references.<sup>5, 26</sup>

Our home-made Ti:sapphire oscillator is shown in Figure 3.1. It consists of an astigmatically compensated cavity,<sup>18</sup> a Brewster cut 9 mm long Ti:sapphire crystal rod, two concave mirrors with dichroic coatings, a flat output coupler (OC), a flat high-reflection cavity mirror, a mirror mounted on a piezo-electric transducer (PZT) stage, one folding mirror, and fused silica prism pair. The Ti:sapphire crystal is pumped by a frequency-doubled diode pumped Nd:YVO<sub>4</sub> (vanadate) laser (Spectra-Physics Millennia Classic) delivering 4.75 W at 528 nm. The repetition rate of the oscillator is  $f = c/2L_{\text{cavity}} = 76.3$  MHz where  $L_{\text{cavity}} = 1.97$  m is the cavity length. The average power is 300 mW. Since the Kerr nonlinearity is not strong enough for the self-starting of KLM from quiescent oscillator noise, in order to initiate KLM one needs to translate the second prism rapidly to generate strong amplitude modulations.

In general, dispersion in the oscillator – induced by self phase modulation (SPM) and material dispersion (see Appendix G) in the crystal and multilayer dielectric mirrors – distorts the spectral phase and leads to pulse broadening. Hence, to generate ultrashort optical pulses, phase distortion should be minimized. To compensate group delay dispersion (GDD) and third order dispersion (TOD) in the oscillator, a pair of prisms is introduced inside the cavity to produce negative GDD and TOD (see Appendix C for GDD and TOD). This was first proposed by Fork and *et al.*<sup>27</sup> and demonstrated by many groups.

A diagram of the prism pair geometry is shown in Figure 3.1 and 3.2 (a). The GDD and TOD for a prism pair are given as follows<sup>28, 29</sup>

$$\phi'' = \frac{\lambda^3}{2\pi c^2} \frac{d^2 P}{d\lambda^2} \quad \text{and} \quad \phi''' = -\frac{\lambda^4}{4\pi^2 c^3} \left( 3 \frac{d^2 P}{d\lambda^2} + \lambda \frac{d^3 P}{d\lambda^3} \right), \quad (3.1.1)$$

where

$$\frac{d^2 P}{d\lambda^2} = 4 \left[ \frac{d^2 n}{d\lambda^2} + (2n - n^{-3}) \left( \frac{dn}{d\lambda} \right)^2 \right] l_p \sin \beta - 8 \left( \frac{dn}{d\lambda} \right)^2 l_p \cos \beta, \quad (3.1.2)$$

$$\frac{d^3 P}{d\lambda^3} = 4 \frac{d^3 n}{d\lambda^3} l_p \sin \beta - 24 \frac{dn}{d\lambda} \frac{d^2 n}{d\lambda^2} l_p \cos \beta, \quad (3.1.3)$$

where  $P = 2l_p \cos \beta$  is the optical path length that contributes to dispersion,  $l_p$  is the distance between the two prisms,  $\beta$  is the angle between the ray at wavelength  $\lambda$  and the reference ray which connects the prism apexes, and  $n$  is the refractive index of the prism. For fused silica glass prisms in our geometry,  $\cos \beta \approx 1$ ,  $l_p \approx 1$  m,  $l_p \sin \beta \approx 2$  mm,  $n = 1.711$ ,  $dn/d\lambda = -0.01726 \mu\text{m}^{-1}$ ,  $d^2 n/d\lambda^2 = 0.03965 \mu\text{m}^{-2}$ , and  $d^3 n/d\lambda^3 = -0.2365 \mu\text{m}^{-3}$  at 800 nm (see Appendix G). We get  $\phi'' = -6.2 \times 10^3 \text{ fs}^2$  and  $\phi''' = -2.1 \times 10^3 \text{ fs}^3$  for GDD and TOD. Prism 2 is mounted on a 2D translation stage so that one can easily adjust  $l_p$  and  $d_2$  independently to eliminate GDD and TOD [see Fig. 3.2(a)]. In addition, the stage for prism 2 makes possible the rapid motion of this prism to initiate KLM.

The maximum spectral bandwidth of 48 nm (FWHM) is produced with good oscillator alignment. It supports an approximate 20 fs Fourier-transform-limited pulse width assuming a Gaussian pulse shape. The autocorrelation trace of the oscillator output was measured to be 72 fs (FWHM) with our interferometric autocorrelator using two-photon absorption<sup>30, 31</sup> in GaAsP, shown in Fig. 3.3(a) with a sample autocorrelation trace in Fig. 3.3(b). Assuming a Gaussian pulse envelope, the estimated pulse width is 50 fs. It is

larger than the Fourier-transform-limited value because the pulse acquires a strong chirp due to the material dispersion in the output coupler and in the autocorrelator optics.

However, the ultimate pulse duration at the output of the full laser system can be less than 50 fs because much of the chirp can be compensated by compressor adjustments.

Our oscillator is sensitive to temperature variations in the room. Due to the thermal expansion of the optical table and in the metallic optical mounts in the oscillator, the cavity length (repetition rate) changes with temperature at a rate of  $31 \mu\text{m}/\text{C}^\circ$  ( $-1.2 \text{ kHz}/\text{C}^\circ$ ). In addition, the central wavelength drifts with temperature at a rate of  $1.85 \text{ nm}/\text{C}^\circ$ . To stabilize the temperature of the optical table surface and in the optical mounts, a heater tape was laid out surrounding the footprint of the oscillator. The table surface temperature is monitored and controlled by a thermocouple and controller (Omega Engineering, CN77324). This arrangement greatly improves oscillator stability. Additionally, the PZT-mounted mirror is controlled by a Lock-to-Clock (LTC) phase-locked loop (Spectra-Physics), originally installed for the synchronization of Ti:sapphire and Nd:YAG laser systems (see Appendix H). This is used to fix the mode-locked pulse repetition rate at 76.3 MHz.

### **3.3 Pulse stretcher**

In many CPA laser systems, a pair of anti-parallel diffraction gratings with two lenses is commonly used to stretch pulses of large bandwidth by typically 1000 times their original pulse duration.<sup>32</sup> Between the two anti-parallel gratings, two lenses form a telescope, which inverts the angular dispersion and results in a net positive GVD provided that the gratings lie inside the focal planes of the lenses.<sup>33</sup> However, for pulse durations

below 100 fs, as in our system, the lens-based telescope introduces strong chromatic aberrations. To avoid the chromatic aberration and on-axis coma due to the refractive elements, an aberration-free stretcher using a single grating and two spherical concentric mirrors in an Öffner Triplet<sup>34</sup> design was adapted for our stretcher.<sup>35</sup> Additionally, the single grating design eliminated the possibility of misaligning two separate gratings. The layout for our stretcher is shown in Fig. 3.1. A grating of 1200 grooves/mm is placed 450 mm away from the center of the concave mirror with curvature radius of  $R_1 = 900$  mm and the convex mirror of  $R_2 = 1800$  mm. With a grating separation of  $L = 900$  mm, injection angle  $\theta_{in} = 36^\circ$ , grating groove spacing  $d = 0.830 \mu\text{m}$ , and  $\lambda = 805$  nm, GDD and TOD are  $\phi''_{\text{stretcher}} = 3.02 \times 10^6 \text{ fs}^2$  and  $\phi'''_{\text{stretcher}} = -2.18 \times 10^8 \text{ fs}^3$ , respectively, from Eq. (3.1). This gives a stretching ratio of  $\sim 9$  ps/nm at 800 nm. For a spectral bandwidth of  $\Delta\lambda = 32$  nm (FWHM) input, the stretched output pulse duration is  $\sim 300$  ps (FWHM). Since the same expression Eq. (3.2) for compressor dispersion can be applied to the stretcher, see Section 3.5 for more details.

### 3.4 Laser pulse energy amplification

#### 3.4.1 Regenerative pulse energy amplification

The regenerative amplifier (RGA) gain medium is a Brewster-cut Ti:sapphire crystal (6.25 mm diameter and 20 mm length, absorption coefficient  $\alpha = 1.31$  at 514 nm, Crystal Systems) pumped by a 10 Hz repetition rate, 35 mJ frequency doubled 532 nm Nd:YAG laser pulse (Spectra-Physics, Quantra-Ray INDI-30). The RGA cavity consists of two cavity mirrors (one concave with  $f = 3$  m and one convex with  $f = -3$  m) and one folding dichroic mirror for pump pulse transmission.

After passing through the pulse stretcher, the temporally stretched pulse is amplified in the RGA. First, the pulse propagates through a thin film polarizer (TFP) with a horizontal polarization (P-polarization) as shown in Fig. 3.1. Then, it travels through a half-wave plate ( $\lambda/2$ ) followed by a Faraday rotator (FR) with a net  $90^\circ$  polarization changes (from P to S). The S-polarized pulse is reflected from the second TFP and goes through a KDP Pockels cell PC1 (Medox Electro-Optics, Model 700-KD\*P) with a 25-mm long 10-mm aperture KD\*P crystal. The Pockels cell angle is adjusted to provide quarter-wave ( $\lambda/4$ ) retardation without any applied voltage to the birefringent KD\*P crystal. After a double pass through the Pockels cell with a net half-wave retardation, the polarization is changed from S to P. The pulse then propagates through TFP2 and remains in the RGA cavity. After it again double passes the Pockels cell, it leaves the cavity with a negligible amount of amplification. However, the optical pulse can be trapped in the cavity for many round trips and significant energy amplification by applying a half-wave high voltage pulse (with a rise time of 3.6 ns) from a pulse driver (Electro-Optics, Medox DR 85-A) to the Pockels cell to induce a half-wave ( $\lambda/2$ ) retardation. The optical pulse energy then grows from the nanojoule level up to the millijoule level after  $\sim 28$  times round trips in the RGA cavity, constituting an energy gain of  $\sim 10^6$ . The pulse is ejected from the cavity by applying an additional high voltage pulse (with a rise time of 3.9 ns) to make  $\frac{3}{4}\lambda$  retardation in the Pockels cell, changing the polarization from P to S. The S-polarized pulse goes through the FR and TFP without polarization change and leaves RGA. The Medox timer/driver sets the repetition rate in the RGA at 10 Hz, with synchronization ensured to individual oscillator pulses from the 76.3 MHz pulse train (see Appendix H).

Two major effects – gain narrowing<sup>36,37</sup> and gain shifting<sup>37</sup> – must be considered in the CPA amplification system in order not to distort the spectrum during power amplification. As the RGA stage contributes the largest portion of the system amplification, gain narrowing must be considered most carefully there. For instance, for the case of gain narrowing, if a seed beam with an infinite spectral bandwidth is injected into a Ti:sapphire amplification chain with a gain of  $10^7$ , even though the Ti:sapphire crystal has a broad gain bandwidth of 230 nm (FWHM), the spectrum of the amplified pulse is reduced to 47 nm (FWHM).<sup>7,38</sup> It can then only support the minimal transform-limited pulse duration of 18 fs at a millijoule energy level. In addition, the finite reflection or transmission bandwidth of the mirrors and TFPs in the RGA results in further narrowing of the pulse spectrum. It is shown in Fig. 3.4 that the spectral bandwidth is reduced from 32 nm at the oscillator output to 27.7 nm after power amplification.

The other effect, gain shifting, happens when the leading part of the stretched seed pulse – positively chirped and thus with red spectral components arriving earliest – experiences more gain, owing to gain saturation, compared to the blue components which come later. This gain shifting is not serious in our RGA, but it becomes more serious after the two power amplifiers (PA1 and PA2) as shown in Fig. 3.4(a).

Typically, the pulse output from the RGA has multiple pre-pulses and post-pulses superimposed on a long plateau. The pre- and post-pulses are generated due to the finite S- vs. P-polarization extinction ratio of the TFPs (1:100) in the RGA cavity. Therefore, at each round trip, ~1 % of the pulse energy leaks out of RGA to produce multiple pre- and post-pulses. To enhance the contrast ratio between the main pulse and the unwanted pre- and post-pulses, an external Pockels cell PC2 (rise time 2 ~ 3 ns, Cleveland Crystals

IPD2545) is introduced after the RGA (see Fig. 3.1). The pulse ejected from the RGA is reflected from an external thin film polarizer (TFP3) with S-polarization. Then, it double-passes through the external Pockels PC2 with a net  $\lambda/2$  retardation when a high voltage is applied to PC2. The high voltage pulse is applied right before the main pulse enters PC2 so that there is no polarization shift for the pre-pulses. Hence, only the P-polarized main pulse with a PC2-induced retardation can propagate through TFP3 and enter the next amplification stage PA1. In this arrangement, the post-pulses are not filtered out because they acquire the same phase retardation in PC2 (PC2 has a relaxation time of  $2 \sim 3 \mu\text{s}$  to decay to zero voltage). Before PC2, the contrast ratio is  $10^{-2}:1$ . However, after PC2, the pre-to-main pulse extinction ratio is  $10^{-4}:1$ .

### 3.4.2 Multi-pass power amplification

The pulse from the RGA is amplified further in a 3-pass amplifier PA1 and a 4-pass amplifier PA2. The beam paths and pumping geometry for these stages are shown in Fig. 3.1. In PA1, a Brewster cut Ti:sapphire crystal (10 mm diameter  $\times$  12 mm length, Crystal Systems) is pumped by 350 mJ frequency doubled (532 nm) Nd:YAG pulses at a repetition rate of 10 Hz. The pump beams are relay-imaged to the amplifier crystal by  $f_1 = 1500$  mm and  $f_2 = 800$  mm lenses. With a demagnification of 2, the pump beam diameter at the crystal face is 4 mm with a flat-top profile. The Ti:sapphire pulse propagates through the crystal in a 3-pass bow-tie amplification geometry. The overall energy gain of 20 is achieved, agreeing with the theoretical expectation based on the Frantz-Nodvic equation.<sup>39</sup> The normal-cut Ti:sapphire crystal ( $\alpha = 2.70 \text{ cm}^{-1}$  at 514 nm, Crystal Systems) in PA2 has a 10 mm diameter and 12 mm length with anti-reflection broad-band coatings of 650  $\sim$  950

nm. The crystal is pumped on both sides by  $\sim 300$  mJ and  $\sim 200$  mJ frequency doubled 532 nm Nd:YAG pulses. The flat-top pump beam diameter is 6 mm on the two crystal faces with dual lens relay imaging system ( $f_1 = 1500$  mm,  $f_2 = 1000$  mm). The maximum output energy after PA2 is 220 mJ with a net gain of 4.4. The pre-compression pump-to-laser energy conversion efficiency of our Ti:sapphire laser system is 0.21.

In designing high power amplifiers, thermal lensing<sup>5,8</sup> – induced by the heat load due to the large pump energy fluence on the laser crystal – is a major concern. Since the quantum efficiency of Ti:sapphire pumped at 527 nm is approximately 0.6, at least 40% of the absorbed light is released as heat.<sup>8</sup> The radial thermal gradient and the thermo-mechanical stress in the pumping zone produce a positive lens-like index of refraction profile in the crystal rod. Hence, as the beam repeatedly passes through the heated crystal, it undergoes unfavorable focusing in the amplification chain and develops a dramatically deteriorated transverse phase profile, which could lead to optical damage. To reduce the thermal lensing in PA1 and PA2, the laser rods are water-cooled at room temperature. In addition, a plano-concave lens L1 with a focal length  $f = -1500$  mm is placed in the beam path of PA1. The lens overwhelms the thermal lensing with a moderate beam divergence. In addition, a telescope with 150 mm (L2) and  $-100$  mm (L3) lenses is placed between PA1 and PA2 as shown in Fig. 3.1. The telescope divergence is adjusted so that the thermal lensing in PA2 is also pre-compensated. However, in general it is not easy to cancel out exactly the thermal lensing because of alignment difficulty and the variation of the effective focal length of the thermal lens with pump energy. For even higher pump energies than used in our system, cryogenic cooling of the Ti:sapphire crystal rod with liquid nitrogen is preferable for minimizing thermal lensing, because the Ti:sapphire

material develops a very high thermal conductivity at low temperatures (2000 W/m·K at 77 K).<sup>8</sup>

In high intensity amplification systems, self-phase modulation (SPM) occurs due to the nonlinear index of refraction of a material induced by the beam itself. Typically, the effect on laser beams of SPM is described by the so-called  $B$ -integral,  $\mathbf{B}(r, t) =$

$\frac{2\pi n_2}{\lambda} \int_0^L I(r, z, t) dz$ , where  $n_2$  is the nonlinear index of refraction of the material through which the intense beam propagates,  $\lambda$  is the vacuum wavelength, and  $L$  is the propagation length in the material.<sup>40</sup> The  $B$ -integral is simply the additional phase accumulated by the nonlinear propagation. In general, linear phase distortion components such as GDD and TOD from the amplification system can be compensated in the final pulse compression stage. However, the intensity dependence of the  $B$ -integral makes it impossible to exactly compensate the phase shift over the entire beam profile. Hence, SPM in the amplification chain should be minimized to keep the  $B$ -integral small. Otherwise, SPM degrades the contrast of the compressed pulse, thereby reducing the peak intensity significantly.<sup>41</sup> The overall estimated  $B$ -integral in our Ti:sapphire laser system is far less than unity.

### 3.5 Pulse compressor

To compress the stretched pulse back to near the original pulse width, two parallel gratings (120 × 140 mm, 1200 grooves/mm) were used to produce negative GDD.<sup>42</sup> The schematic of our compressor is shown in Figs. 3.1 and 3.2(b). The GDD and TOD in the double-pass compressor are given by<sup>29</sup> (see Appendix C for GDD and TOD)

$$\phi''_{\text{compressor}} = -\frac{\lambda^3 L}{\pi c^2 d^2} \left[ 1 - \left( \frac{\lambda}{d} - \sin \theta_{in} \right)^2 \right]^{-3/2}, \quad (3.2.1)$$

$$\phi'''_{\text{compressor}} = -\phi''_{\text{compressor}} \frac{6\pi\lambda \left[ 1 + \sin \theta_{in} \left( \frac{\lambda}{d} - \sin \theta_{in} \right) \right]}{c \left[ 1 - \left( \frac{\lambda}{d} - \sin \theta_{in} \right)^2 \right]}, \quad (3.2.2)$$

where  $L$  is the perpendicular separation between the two parallel gratings,  $\theta_{in}$  is the incident angle, and  $d$  is the grating groove spacing, and  $\lambda$  is the central wavelength. Under our conditions [ $L = 940 \text{ mm} \times \cos(33.7^\circ) = 782 \text{ mm}$ ,  $\theta_{in} = 24.4^\circ$ ,  $d = 0.830 \mu\text{m}$ , and  $\lambda = 793 \text{ nm}$ ], the estimated GDD and TOD are  $\phi''_{\text{compressor}} = -3.10 \times 10^6 \text{ fs}^2$  and  $\phi'''_{\text{compressor}} = 2.56 \times 10^8 \text{ fs}^3$ , respectively. As shown in Eqs. (3.2.1) and (3.2.2), by adjusting  $L$  and  $\theta_{in}$ , GDD and TOD can be arbitrarily adjusted at a fixed wavelength. In general, to compensate GDD, TOD, 4OD, and so forth in the compressor, one needs to satisfy the following equations.

$$\phi''_{\text{stretcher}} + \phi''_{\text{amp}} + \phi''_{\text{compressor}}(L, \theta_{in}) = 0, \quad (3.3.1)$$

$$\phi'''_{\text{stretcher}} + \phi'''_{\text{amp}} + \phi'''_{\text{compressor}}(L, \theta_{in}) = 0, \quad (3.3.2)$$

...

$$\phi^{(n)}_{\text{stretcher}} + \phi^{(n)}_{\text{amp}} + \phi^{(n)}_{\text{compressor}}(L, \theta_{in}) = 0. \quad (3.3.3)$$

However, since the grating-based compressor has only two degrees of freedom – the incidence angle  $\theta_{in}$  and the grating distance  $L$  – one can eliminate dispersion only up to third order, leaving the higher order dispersion terms uncompensated. To compensate these higher order dispersions, more degrees of freedom are needed. For instance, adding additional material in the amplification chain<sup>43</sup> or using an adjustable air-spaced doublet lens in the stretcher,<sup>44</sup> dispersion compensation up to 4OD was achieved. In our case, the

accumulated GDD and TOD in the stretcher and the amplifier chains are almost fully compensated in the compressor.

The overall compressor energy transmission efficiency of 50% is mostly determined by the grating diffraction efficiency (90% near the Littrow angle, 4 grating reflections) and the gold mirror reflection efficiency (~96% at 800 nm, 6 mirror reflections). Before the amplified chirped pulse enters the compressor, the beam size is expanded to ~12 mm (FWHM). Otherwise, the compressed pulse could damage the last compressor grating because of its high peak intensity  $\sim 9.6 \times 10^{11}$  W/cm<sup>2</sup>.

One also needs to consider the self-focusing of the compressed pulse in air after it exits the compressor. With the nonlinear refractive index of air  $n_2 = 5 \times 10^{-19}$  cm<sup>2</sup>/W,<sup>45</sup> the *B*-integral accumulates at a rate of 0.008 cm<sup>-1</sup>. For the air propagation length  $L = 1$  m, the *B*-integral of 0.8 is still less than unity. However, if the energy exceeds twice more than our current 100 mJ after the compressor, strong SPM in air would require the entire compressor and the path from the compressor to the interaction chamber to be enclosed in vacuum. The equivalent self-focusing length in air  $z_f$  for the current system output energy

of 100 mJ is approximately  $z_f = \frac{\frac{1}{2}kw^2}{(P/P_c - 1)^{1/2}} \approx 14$  m where  $k = 2\pi/\lambda$  is the wavenumber in

vacuum,  $w = 10.2$  mm is the compressor output beam radius at  $1/e^2$ ,  $P \approx 1.7$  TW is the peak

power, and  $P_c = \frac{\lambda^2}{2\pi n_0 n_2} = 2$  GW is the critical power for self-focusing in air.<sup>46</sup>

### 3.6 Femtosecond laser pulse characterization

The spatial, temporal, and spectral characteristics of intense pulses should be well diagnosed before any experiments. Figure 3.4(a)-(b) show the pulse spectra and spatial profiles after each CPA stage: oscillator, stretcher, RGA, PA2, and compressor. The central wavelengths and spectral full width at half maxima (FWHM) after each stage are marked in Fig. 3.4(a). It is notable that the spectral bandwidth decreases gradually as the pulse propagates through our CPA system. First, physical spectrum clipping occurs due to the finite transverse size of the grating in the stretcher, which reduces the FWHM spectrum from 48 nm to 32 nm. Additionally, gain narrowing in the amplifiers – mainly in the RGA and also in PA1 and PA2 – further limits the spectral bandwidth. Finally, the spectral bandwidth reduces further down to ~23 nm in the compressor because the grating has a maximum diffraction efficiency near 790 nm, whereas the central wavelength of the pulse after PA2 is 811.3 nm. To take the full advantage of the broad oscillator spectrum of 48 nm, whose transform-limited pulse duration is 20 fs, spectral narrowing and clipping should be avoided.

In the future, to preserve the broad oscillator broad bandwidth throughout the laser system, it would be desirable to inject more bluer (795 ~ 790 nm) seed pulses into the RGA to solve four problems simultaneously<sup>47</sup>: spectral clipping, gain narrowing, gain shifting, and the wavelength mismatch in the compressor. In addition, spectral beam shaping techniques<sup>48</sup> can be employed in the system to increase the spectral bandwidth. One well-known solution is to use a thin angle-tuned étalon as a frequency-dependent attenuator (or spectrum flattener) in the RGA for regenerative pulse shaping.<sup>49</sup> With this technique, it was reported that the spectral bandwidth was broadened to ~100 nm, which is nearly three

times wider than the gain-narrowing limit.<sup>47</sup> However, this technique requires careful pulse recompression with compensation of higher order dispersion necessitated by the spectral broadening. Another pulse shaping technique, the acousto-optic programmable dispersive filter (AOPDF)<sup>50, 51</sup> method can be used not only to modulate the spectral shape but also to adaptively compensate the dispersion in the laser system, enabling reshaping of the output pulse envelope and phase.

The temporal pulse envelope and time-dependent phase of the Ti:sapphire laser pulse after the compressor is characterized by polarization gating (PG) frequency resolved optical gating (FROG). Figure 3.5(a)-(b) show our PG FROG setup and a sample of FROG trace taken after the compressor. The retrieved temporal pulse envelope and its phase are shown in Fig. 3.5(b). The FWHM pulse duration is  $\sim 70$  fs. It has modulated wings because of the incomplete compensation of TOD in the compressor. With a careful adjustment of the compressor, the pulse width is measured to be as short as 60 fs.

The spatial profiles of beams are shown in Fig. 3.4(b) with the beam radii (FWHM) in the parenthesis after each CPA stage. The beam radius after the compressor is 12 mm (FWHM) with a Gaussian profile. The typical peak intensity is  $I_{\text{peak}} = 10^{18}$  W/cm<sup>2</sup> with a spot-size of  $\sim 12.6$   $\mu\text{m}$  (FWHM) using plano-convex lens focusing (see Fig. 3.6). Higher peak intensity  $I_{\text{peak}} = 2.3 \times 10^{18}$  W/cm<sup>2</sup> can be achieved with a spot-size of  $\sim 8$   $\mu\text{m}$  by focusing with an off-axis parabola.

### **3.7 Conclusions and future upgrade**

In this chapter, our 2-TW Ti:sapphire laser system was described. A future laser upgrade is planned to increase the peak power up to  $\sim 6$  TW with a high contrast ratio. The

pulse duration can be reduced to sub-35 fs by limiting the spectral narrowing and optimizing the phase compensation in the compressor. In addition, the pulse energy will be further amplified with an additional pump laser source. With the overall pump laser energy of 1.8 J and compressor efficiency improvements, the expected Ti:sapphire pulse energy is ~300 mJ after the compressor. Here, a vacuum compressor must be employed to avoid any nonlinear effects owing to the intensity-dependent refractive index of air.

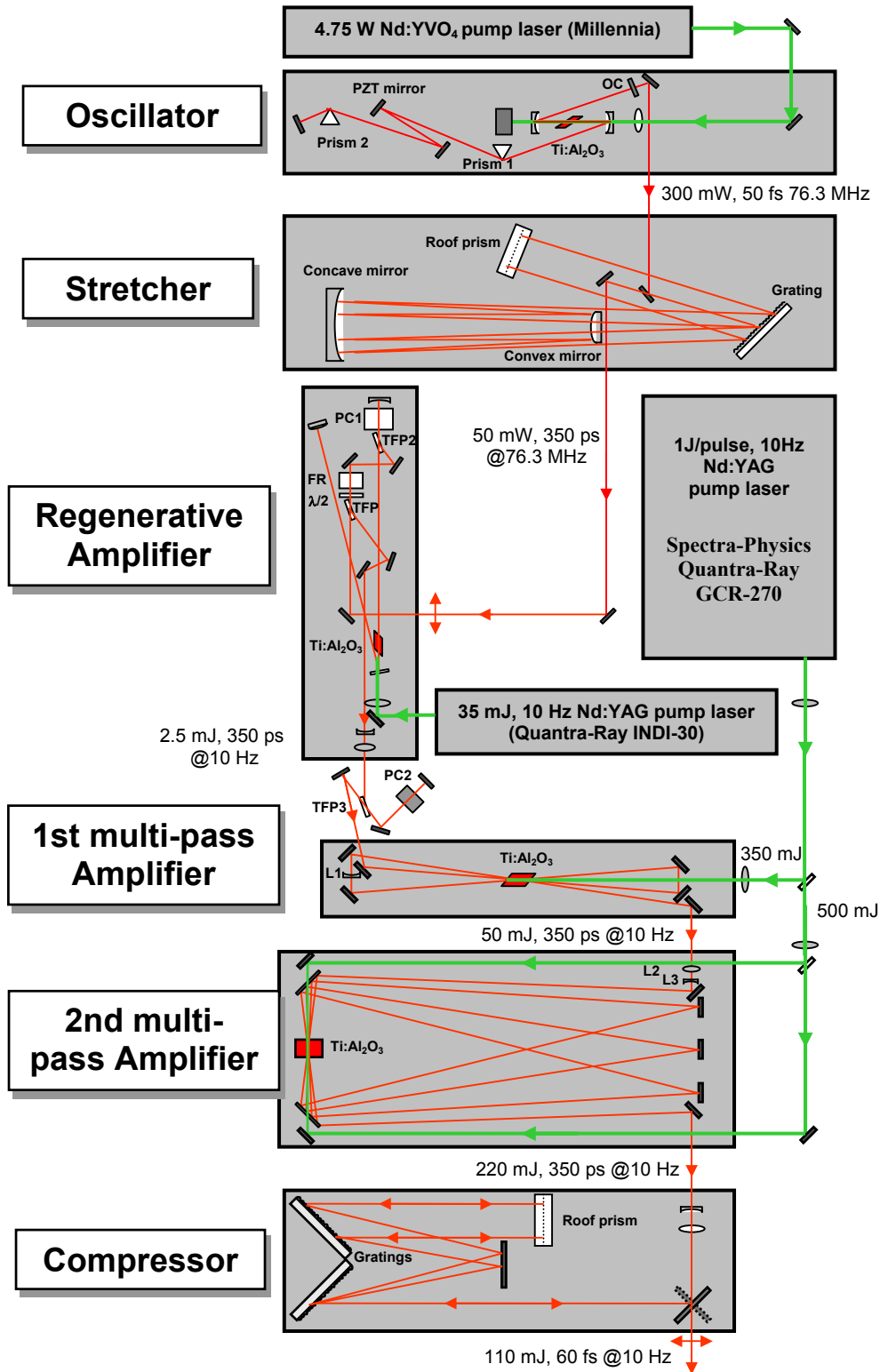


Figure 3.1: Schematic of the 10 Hz repetition rate, 2 TW peak power, 60 fs Ti:sapphire laser system used in the experiments of this dissertation.

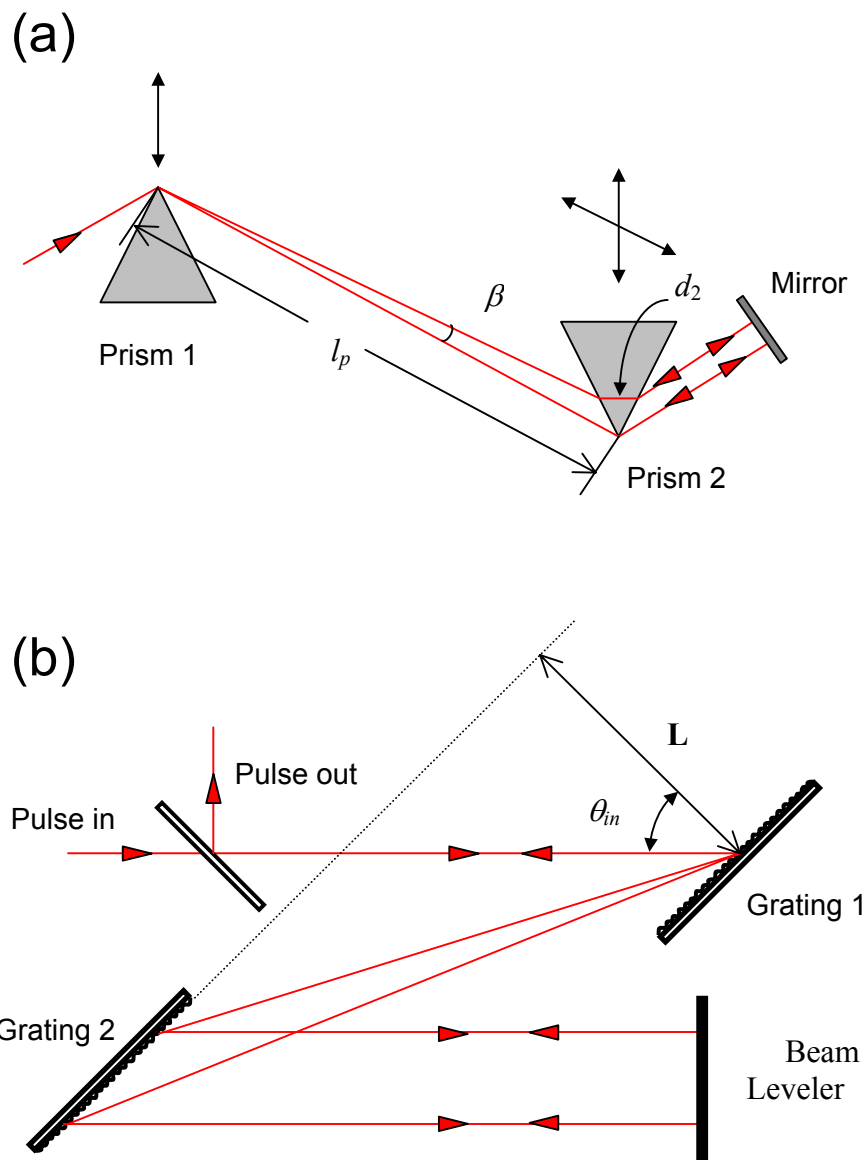


Figure 3.2: (a) A prism pair compensating GDD and TOD inside the oscillator. (b) A grating pair in the compressor for the pulse recompression.

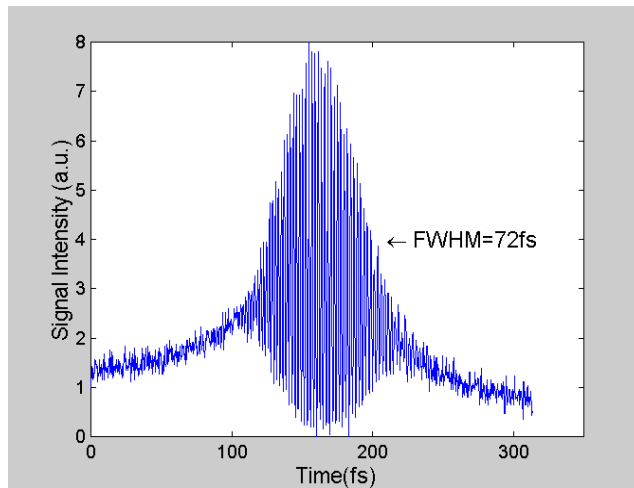
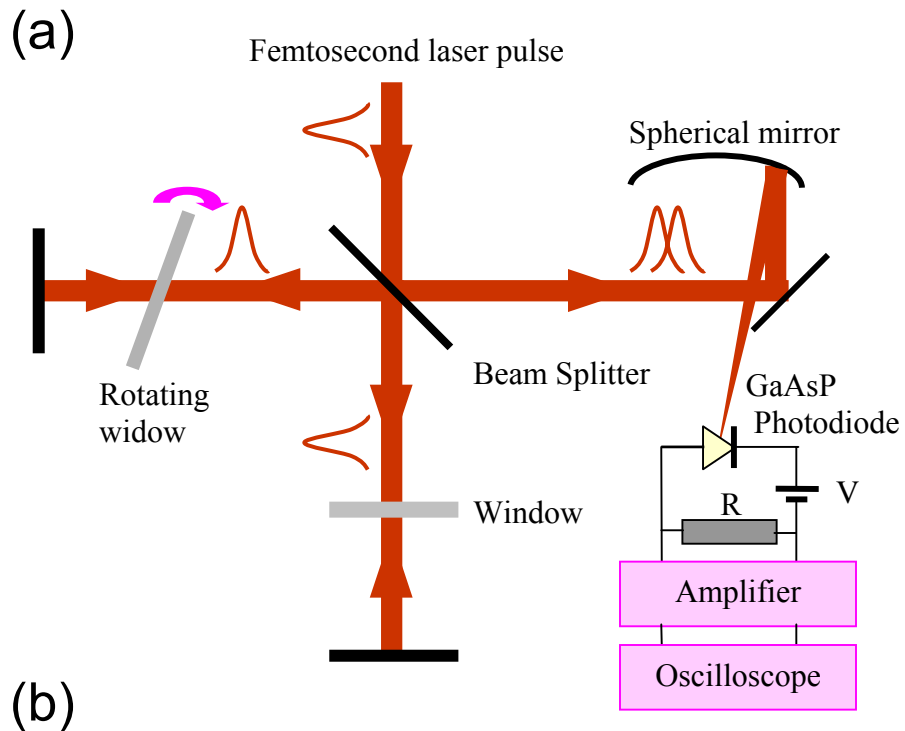


Figure 3.3: (a) Schematic diagram of interferometric autocorrelator using two-photon absorption. (b) Sample autocorrelation trace of oscillator output with a 72 fs full width at half maximum (FWHM).

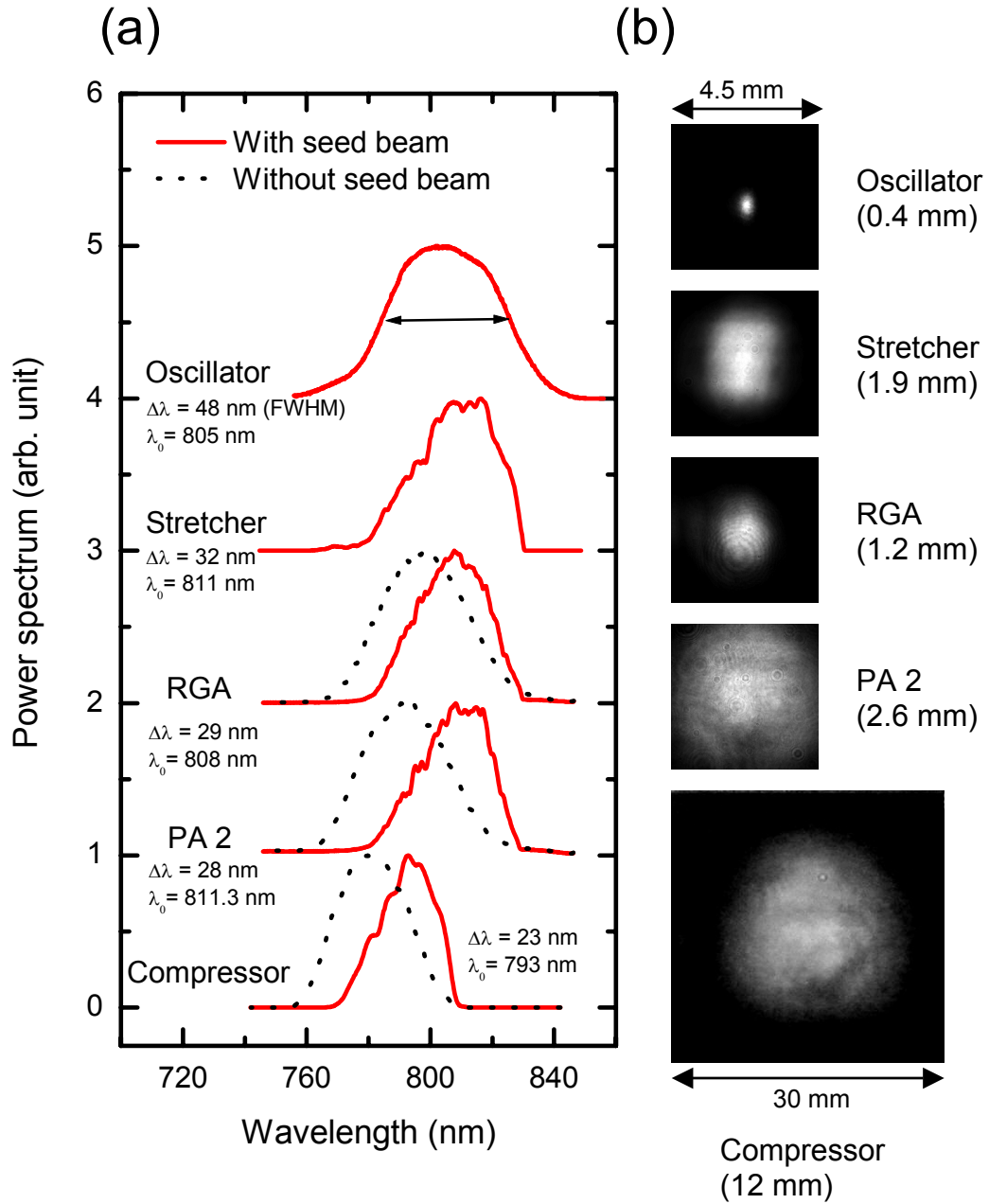


Figure 3.4: Ti:sapphire laser pulse (a) spectra and (b) beam spatial profiles (with the FWHM beam sizes) after each CPA stage: oscillator, stretcher, RGA, and PA1&2, and compressor. The dashed lines in (a) are free-running spectra without the seed beam injection.

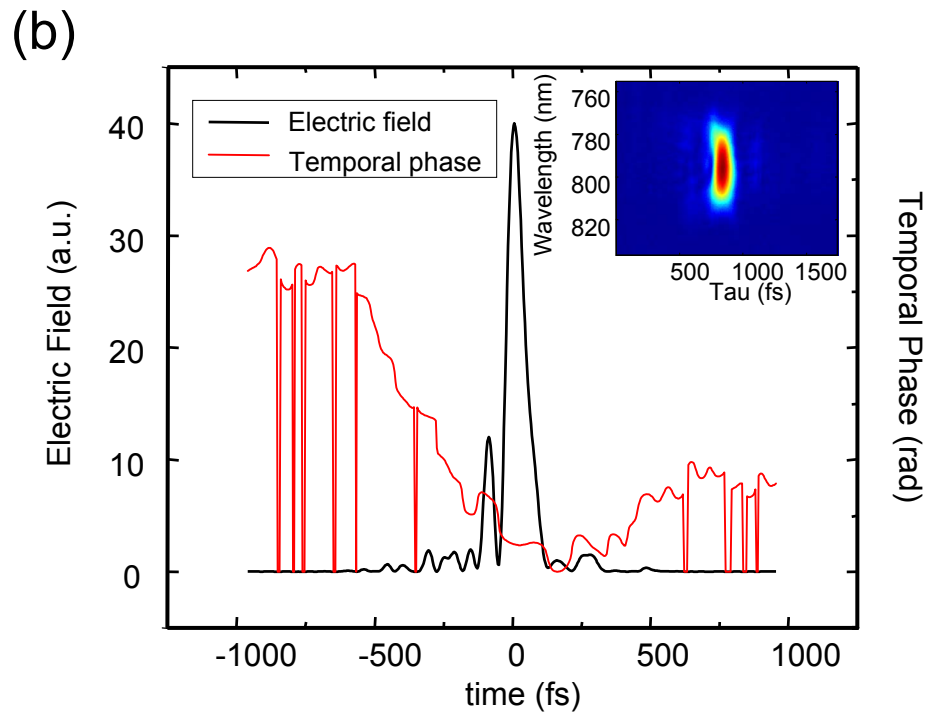
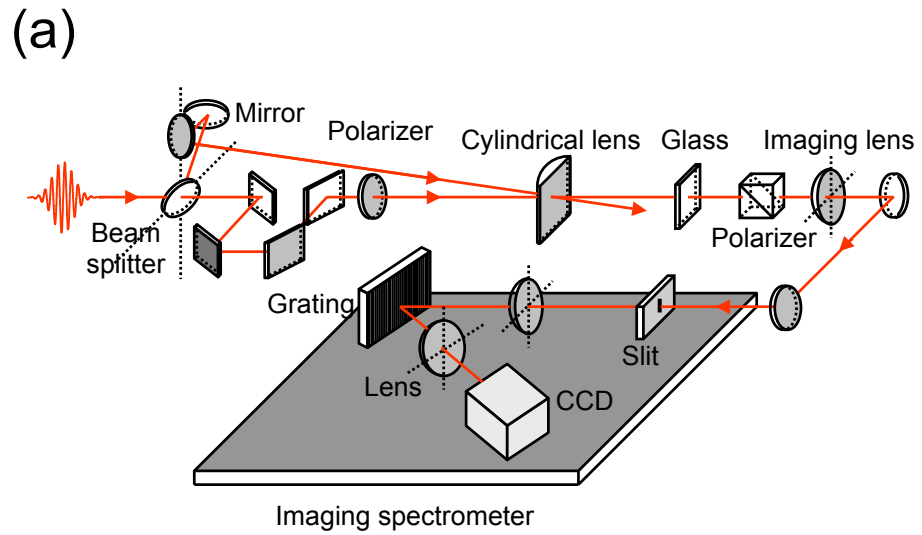
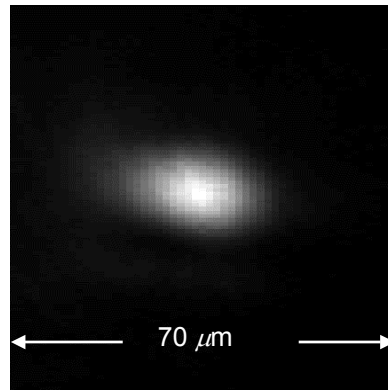


Figure 3.5: (a) Frequency resolved optical gating (FROG) setup with polarization gating (PG) geometry. (b) Retrieved electric field envelope (thick black line) and phase profiles (red thin lines) retrieved from the sample PG FROG trace (inset) taken after the compressor. Uncompensated TOD is responsible for the oscillatory side lobes.

(a)



(b)

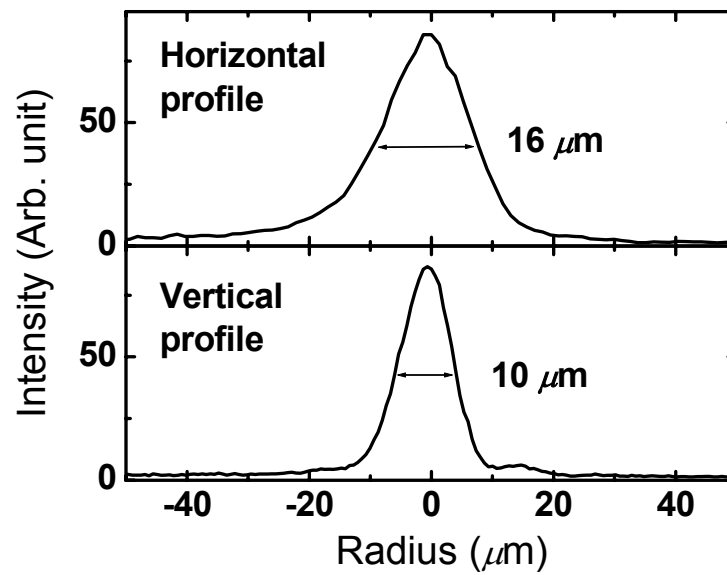


Figure 3.6: (a) The vacuum focal spot profile with (b) the horizontal and vertical line-outs. The peak intensity is  $\sim 10^{18}\ \text{W}/\text{cm}^2$  with the spot size of  $12.6\ \mu\text{m}$  (FWHM).

## Chapter 4: Femtosecond laser-induced ionization of helium

### 4.1 Introduction

The interaction of high intensity ultrashort pulses with low density gases and plasmas is rich in fundamental phenomena and applications including optical field ionization,<sup>1-3</sup> high harmonic generation,<sup>4,5</sup> relativistic self-channeling,<sup>6,7</sup> and laser-induced wake-fields in plasmas.<sup>8</sup> In particular, optical field ionization is a fundamental and universal process that occurs in a wide range of media under high intensity femtosecond laser irradiation  $I_{\text{peak}} \geq 10^{15}$  W/cm<sup>2</sup> where the Keldysh parameter  $\gamma_K < 1$ .

In this chapter, we use our single-shot supercontinuum spectral interferometry (SSSI) diagnostic to characterize the laser-induced optical field ionization (OFI) dynamics of helium gas. Helium was chosen as a target because of the atom's relatively simple electronic structure, with two bound electrons. Using SSSI, we directly observe the liberation process of bound electrons by an intense laser field. The diagnostic directly reveals that the rising edge of the laser field liberates the first bound electron in helium atoms via the OFI process ( $\text{He} \rightarrow \text{He}^+$ ), and once the first electron is removed, it takes time for the laser field to strip the second electron from  $\text{He}^+$  because it requires an even stronger electric field to remove it. As the laser field increases with time, the second electron is finally liberated through OFI ( $\text{He}^+ \rightarrow \text{He}^{2+}$ ), ultimately producing completely stripped helium ions ( $\text{He}^{2+}$ ) and free electrons. Experimentally, we observe the time-resolved stepwise ionization process  $\text{He} \rightarrow \text{He}^+$  followed by  $\text{He}^+ \rightarrow \text{He}^{2+}$  by measuring the refractive index evolution in a helium gas jet induced by intense femtosecond field ionization. The

index transient is attributed to the rapid stepwise onset of free electron density. As emphasized earlier, the SSSI diagnostic measures the refractive index transient in a single-shot. Also in this chapter, we discuss the importance of using a thin interaction region for all such spectral interferometry measurements of refractive index transients.

## 4.2 ADK tunneling ionization model of helium

For sub-atmospheric pressure gases exposed to intense femtosecond laser pulses, the dominant ionization mechanism is optical field ionization or tunneling ionization for cases where the Keldysh parameter  $\gamma_K < 1$  (see Chapter 1).<sup>1</sup> For our experimental pump pulses with  $\lambda = 800$  nm and peak intensity  $I_{\text{peak}} = 3.8 \times 10^{16}$  W/cm<sup>2</sup>,  $\gamma_K \sim 0.07$ . We use the tunneling ionization rate calculated by Ammosov, Delone, and Krainov (ADK).<sup>9, 10</sup> The static-field ADK ionization rate is

$$w_{st} = \frac{\omega_{\text{at}}}{2} C_{n^*}^2 \left( \frac{U_i}{U_h} \right) \frac{(2l+1)(l+|m|)!}{2^{|m|} |m|! (l-|m|)!} \left( 2 \left( \frac{U_i}{U_h} \right)^{3/2} \frac{E_{\text{at}}}{E} \right)^{2n^* - |m| - 1} \exp \left( - \frac{2}{3} \left( \frac{U_i}{U_h} \right)^{3/2} \frac{E_{\text{at}}}{E} \right), \quad (4.1)$$

where  $\omega_{\text{at}} = me^4/\hbar^3 \approx 4.134 \times 10^{16}$  s<sup>-1</sup> is the atomic unit of frequency,  $C_{n^*} \approx (2e/n^*)^{n^*} \cdot$

$(2\pi n^*)^{-1/2}$  is a constant approximately equal to 2,  $U_i$  is the ionization potential for the atom of interest,  $U_h = 13.598$  eV is the ionization potential for hydrogen,  $E$  is the laser electric field,  $E_{\text{at}} = m_e^2 e^5/\hbar^4 \approx 5.142 \times 10^9$  V/cm is the atomic field seen by the ground state electron in hydrogen,  $n^* = Z(U_i/U_h)^{-1/2}$  is the effective principal quantum number,  $l$  is the orbital angular momentum quantum number,  $m$  is the magnetic quantum number, and  $Z$  is the resulting ion charge. The ADK ionization rate  $w$ , averaged over a laser period for a linearly polarized laser, is

$$w = \left( \frac{3}{\pi} \left( \frac{E}{E_{\text{at}}} \right) \left( \frac{U_h}{U_i} \right)^{3/2} \right)^{1/2} w_{\text{st}}, \quad (4.2)$$

where  $w_{\text{st}}$  is the static-field ionization rate shown in Eq. (4.1).

The ADK ionization rate for each state of helium (He and He<sup>+</sup>), averaged over a laser period, is

$$w = \omega_{\text{at}} \left( \frac{3e}{\pi} \right)^{3/2} \frac{Z^2}{3n_{\text{eff}}^{9/2}} \left( \frac{4eZ^3}{n_{\text{eff}}^4 E_H} \right)^{2n_{\text{eff}}-3/2} \exp\left( -\frac{2Z^3}{3n_{\text{eff}}^3 E_H} \right), \quad (4.3)$$

where  $E_H$  is the laser field normalized to the atomic field seen by the ground state electron in hydrogen,  $\chi_H$  is the ionization potential normalized to that of hydrogen,  $n_{\text{eff}} = Z\chi_H^{-1/2}$  is the effective principal quantum number, and  $Z$  is the resulting ion charge.

First, we simulate the spatio-temporal evolution of the electron density for the case of a low-pressure helium gas jet irradiated by a femtosecond laser pulse. The full simulation code includes optical field ionization, collisional ionization, thermal transport, and hydrodynamics.<sup>11</sup> Figure 4.1 shows a thin helium gas sheet irradiated by an intense laser pulse. The results of a simulation of the spatio-temporal electron density variation on the gas sheet plane is shown in Fig. 4.2 for a spatial and temporal Gaussian pump pulse

$$I_{\text{pump}}(r, t) = I_{\text{peak}} e^{-4 \ln 2 (t - t_{\text{peak}})^2 / \tau_{FWHM}^2} \cdot e^{-4 \ln 2 (r / r_{FWHM})^2}, \quad (4.4)$$

where  $\tau_{FWHM} = 240$  fs is the pump pulse full width at half maximum (FWHM),  $t_{\text{peak}} = 288.3$  fs is the time at which peak intensity of  $I_{\text{peak}} \sim 3.8 \times 10^{16}$  W/cm<sup>2</sup> is achieved, and  $r_{FWHM} = 10.3$   $\mu\text{m}$  is the pump spot radius. The neutral helium gas density was taken to be  $N_{\text{He}} = 1.7 \times 10^{17}$  cm<sup>-3</sup> to correspond with the experimental value (see below). The two-step ionization (He  $\rightarrow$  He<sup>+</sup>  $\rightarrow$  He<sup>2+</sup>) in space and time is clearly seen in Fig. 4.2(a). The simulation confirms that optical field ionization is by far the dominant effect. Collisional ionization

plays no role here: increasing the initial neutral He density by more than a factor of 50 increases the spatio-temporal electron density profile only proportionally. The effects of thermal transport and hydrodynamics are similarly negligible at these densities and time scales. The distinctiveness of the field ionization steps in space and time results from the large ionization potential (I.P.) gaps for  $\text{He} \rightarrow \text{He}^+$  (I.P. = 24.58741 eV) and  $\text{He}^+ \rightarrow \text{He}^{2+}$  (I.P. = 54.41778 eV).<sup>12</sup> Figure 4.2(b) shows the on-axis ( $r = 0$ ) transient electron density evolution and the pump pulse envelope. The temporal step is clearly seen. The time evolution of the spatial steps in electron density is seen in Fig. 4.2(c), which shows a sequence of electron density profiles at 20 fs increments.

### 4.3 Experimental results

The experimental setup is shown in Fig. 4.3(a). A 20 mJ,  $\lambda = 800$  nm, 240 fs FWHM pump pulse from a Ti:sapphire laser system is focused at  $f/4$  by a BK7 lens into a helium gas jet. The focal spot is elliptical with FWHM dimensions  $10.3\ \mu\text{m} \times 16.1\ \mu\text{m}$ . This corresponds to a peak vacuum intensity  $I_{\text{peak}} = 3.8 \times 10^{16}$  W/cm<sup>2</sup>. The pump beam confocal parameter is  $2z_0 \sim 0.6$  mm. The thin sheet of helium gas, produced by a nozzle with a  $10\ \text{mm} \times 0.4\ \text{mm}$  exit orifice, is also shown in Fig. 4.1(a). The pump laser beam was incident normal to the gas sheet and 0.5 mm above the nozzle mouth, with a resulting laser-gas interaction length of 0.5 mm. The setup of our SSSI diagnostic was previously described in Chapter 2. Here, the reference and probe pulses were sent through a 1" thick SF4 glass window and positively chirped to  $\sim 1.5$  ps. This sets the maximum temporal window for the single-shot observation of ionization dynamics. Figure 4.3(b) shows an image of the helium gas jet irradiated by the Ti:sapphire laser pulse (artificial color). The laser-produced

helium plasma is clearly visible at the center of the gas jet. Sample spectral interferograms are shown in Fig. 4.4(a)-(b) with the gas jet off (a) and on (b), where a wavelength-dependent fringe shift is seen only in (b).

An experimental spatio-temporal phase profile  $\Delta\Phi(x, t)$  at 15 psi jet backing pressure is shown in Fig. 4.5(a). This profile was extracted using the procedure embodied by Eq. (2.4).  $\Delta\Phi(x, t)$  is proportional to the transient electron density variation across the pump beam profile at the jet. The transient phase at the profile center [ $\Delta\Phi(x = 0, t)$ ] is plotted in Fig. 4.5(b) for 5 psi jet backing pressure (line with triangles) and 15 psi (line with squares). For the laser-gas interaction length of 0.5 mm, the maximum phase shift in the 5 psi case implies an electron density of  $3.4 \times 10^{17} \text{ cm}^{-3}$ , which, for 2 free electrons per atom, implies a neutral helium density of  $N_{\text{He}} = 1.7 \times 10^{17} \text{ cm}^{-3}$ . This number was used in the simulations of Fig. 4.2. The on-axis pump temporal envelope is also shown (line with circles) in Fig. 4.5(b). The pump pulse envelope was measured from cross-phase modulation (XPM) between the pump and probe pulses in a thin glass slide (see Chapter 2).

The plots in Fig. 4.5(b) show that the helium gas is ionized in two sequential steps. The phase rises rapidly, and then slightly jogs near  $-250 \text{ fs}$  for both the 5-psi and 15-psi cases. The phase then rises again, saturating near  $-200 \text{ fs}$  for both cases. The coincidence of these temporal features implies that the ionization dynamics are independent of gas density. This in turn implies that collisional ionization is negligible, as predicted by the simulation in Section 4.2. The phase jogs near  $-250 \text{ fs}$  are also seen in the inset to Fig. 4.5(b), which shows the radial phase profile at a sequence of 20 fs incremental delays. Initially the phase profile grows at a constant rate, but it lingers near its half maximum

value, after which it grows again. We interpret the jogs, or steps, as the temporal pause that occurs between the pump achieving ionization saturation to  $\text{He}^+$  and the early stages of ionization to  $\text{He}^{2+}$ . The measured steps, however, are less distinct than predicted in the simulation of Fig. 4.2(b). In addition, the step in the 15-psi result is less distinct than the 5-psi step. These observations are explained by considering the finite interaction length of the laser pulses in the gas jet, as will be discussed in the following section.

#### **4.4 Simulation of probe propagation in helium plasma: beam propagation method**

To examine how the finite laser-gas interaction length affects the probe phase profiles observed at the exit of the helium gas sheet, we simulated probe pulse propagation through refractive index profiles generated by the co-propagating pump pulse. There are three main effects that can result in sufficient probe pulse phase distortion to mask the index transient we wish to uncover. The simulation covers all three. The first is caused by mismatch between the natural divergences of the pump and probe beams. In our experimental geometry, the probe beam overfills the pump at the focus, so the beam divergences are different. Under such conditions, a probe ray would sample a range of radial electron densities along its propagation path. Thus, the transverse phase dependence of the probe beam at the jet exit would differ from the desired transverse phase profile  $\Delta\Phi(x, t)$ , which should be proportional to the axially integrated electron density. This phase distortion effect is mitigated by making the pump and probe beams as planar as possible with respect to the gas jet. This was achieved in practice by ensuring that the confocal parameters of the pump and probe beams ( $2z_0 \sim 0.6$  mm and 65 mm, respectively) were greater than the gas sheet thickness (here 0.5 mm).

The second, and more significant phase distortion effect is described as follows. The pump intensity varies along the propagation axis  $z$ , so the degree of ionization can change along that axis if the gas jet is sufficiently extended along  $z$ . For example, for a sufficiently extended gas jet, helium can be found completely doubly ionized around the pump focus but singly ionized axially away from it. Hence, when the probe pulse propagates along  $z$  with the pump beam, it acquires a phase shift through the  $\text{He}^+$  plasma well before it reaches the pump focal region near  $z = 0$ , whereupon it picks up an additional phase shift due to the  $\text{He}^{2+}$  plasma there. Hence, the accumulated probe phase may not reveal a sharp transition from  $\text{He}^+$  to  $\text{He}^{2+}$ . In general, for thick jets, or even worse, for backfill gas targets,<sup>13–15</sup> pump intensity variation along the propagation axis within the gas volume can significantly degrade transient phase shift measurements. A diagram showing how the chirped probe samples the transient refractive index profile generated by the co-propagating pump pulse is shown in Fig. 4.6(a). Here, the reference pulse is not shown. The chirped probe pulse can be decomposed into a series of temporal slices  $\delta_{\text{pr}}(t - \tau)$  with delays  $\tau$  with respect to the pump. Each slice of the probe  $\delta_{\text{pr}}(t - \tau)$  propagates in an electron density disturbance  $N_e(x, z, t' - \tau)$  generated by the co-propagating pump pulse  $E_p(t)$  where  $N_e(x, z, t)$  is the electron density in the lab frame and  $t' = t - z/v_g$  is a time coordinate local to the pump pulse. The electron density disturbance and the probe pulse are assumed to move at the pump group velocity  $v_g$ . Figure 4.6(b) shows electron density profiles  $N_e(x, z, t' - \tau)$  left in a helium gas volume at 50 fs intervals by a Gaussian pump pulse propagating along the  $z$ -axis. The pulse was modeled to correspond to the experimental one: peak intensity  $I_{\text{peak}} \sim 3.8 \times 10^{16} \text{ W/cm}^2$ ,  $\lambda_{\text{pump}} = 800 \text{ nm}$ , FWHM pulse width  $\tau_{\text{FWHM}} = 240 \text{ fs}$ , and focal radius  $x_{\text{FWHM}} = 10.3 \mu\text{m}$ , corresponding to a confocal

parameter of  $2z_0 \sim 0.6$  mm. The neutral helium target was taken to be of density  $N_{\text{He}} = 1.7 \times 10^{17} \text{ cm}^{-3}$ , corresponding to the 5 psi experiment, but with a jet thickness of 2 mm. A boundary box in the figure shows the actual extent of our helium gas sheet. This calculation of pump pulse propagation ignores ionization-induced refraction.<sup>16, 17</sup> For  $\tau = 50$  and 100 fs delays between the pump  $E_p(t)$  and the probe slice  $\delta_{\text{pr}}(t - \tau)$ , the probe slice samples only a singly ionized helium plasma, but with  $\tau = 150, 200, 250,$  and 300 fs, the probe samples both  $\text{He}^+$  plasma away from the pump focus and  $\text{He}^{2+}$  plasma around the focus. This results in smearing out of the temporal step from  $\text{He}^+$  to  $\text{He}^{2+}$ . However, with the thin 0.5 mm gas jet actually used, which is less than the pump beam confocal parameter  $2z_0 = 0.6$  mm, distortion of the measured is minimized.

The third distortion effect is the refraction of the probe beam owing to the radial distribution of electron density induced by the pump. To simulate the spatio-temporal phase profiles  $\Delta\Phi(x, t - \tau)$  of the probe pulse at the exit of the helium gas sheet, we first compute the refractive index profiles  $\Delta n(x, z, t' - \tau)$  from the corresponding electron density profiles  $N_e(x, z, t' - \tau)$ . Figure 4.7 shows calculated 2D spatial refractive index shift profiles  $\Delta n(x, z, t' - \tau)$  of the helium plasma that a series of probe slices  $\delta_{\text{pr}}(t - \tau)$  propagate through with (a) 50 fs, (b) 100 fs, (c) 150 fs, (d) 200 fs, (e) 250fs, and (f) 300 fs delays with respect to the pump pulse. Once a time-invariant refractive index profile is given for a probe slice  $\delta_{\text{pr}}(t - \tau)$ , the beam propagation method (BPM)<sup>18</sup> is used to achieve the spatio-temporal phase profiles  $\Delta\Phi(x, z, t - \tau)$ . Each  $\tau$ -delayed temporal slice of the probe  $\delta_{\text{pr}}(r, z, t - \tau) = \delta_{\text{pr0}}(r, z, t - \tau) \exp[i\Phi_{\text{pr}}(r, z, t - \tau)]$  with an initial Gaussian transverse spatial profile propagates through the helium jet through the time-invariant refractive index  $n(r, z, t' - \tau) = [1 - N_e(x, z, t' - \tau)/N_{\text{cr}}]^{1/2}$  along the z-axis. Each reference pulse  $\delta(r, z, t -$

$\tau) = \delta_{t_0}(r, z, t - \tau) \exp[i\Phi_r(r, z, t - \tau)]$  propagates in neutral helium gas. At each grid point along  $z$ , the electric fields of the reference and probe slices are decomposed into a superposition of plane waves via a discrete Fourier transform (DFT), and the plane waves propagate a distance  $\delta z$  through the refractive index profile  $\langle n \rangle$  locally averaged along  $\delta z$ . At  $z + \delta z$ , a phase correction term  $\exp[ik_0(n(r, z, t' - \tau) - \langle n \rangle)\delta z]$  is added to take into account the local space variation of the refractive index profile. Finally, an inverse DFT converts the superposition of the plane waves into the electric fields of the reference and probe  $\delta_{r, pr}(r, z + \delta z, t - \tau)$  at  $z + \delta z$ . The transverse fields give the reference and probe phases  $\Phi_{r, pr}(r, z, t - \tau)$  at  $z + \delta z$ . This process is repeated until the waves reach the end of the plasma  $\Delta z$ . At each  $z$ , the phase difference between the reference and probe beams  $\Delta\Phi(r, z, t - \tau) = \Phi_{pr}(r, z, t - \tau) - \Phi_r(r, z, t - \tau)$  can be obtained. At the end of the helium plasma, the phase difference  $\Delta\Phi(r, z = \Delta z, t - \tau) = \Delta\Phi(r, t - \tau)$  simulates the experimentally measured probe phase shift owing to the ionization-induced transient refractive index. In the BPM calculation, the propagation step length is taken to  $\delta z = 10 \mu\text{m}$  for the reference and probe beams, which is much less than  $z_0$  for both. The reference and probe beams have  $\lambda_{\text{probe}} = 700 \text{ nm}$  and focal spot radii  $x_{FWHM} = 100 \mu\text{m}$ , corresponding to the experimental values. The simulation implicitly accounts for distortions owing to the second effect (axial pump variation) and the third effect (ionization-induced refraction).

Figure 4.8 shows a sequence of calculated probe phase profiles  $\Delta\Phi(x, t - \tau)$  at the jet exit for laser-gas interaction lengths  $\Delta z$  of (a) 0.1 mm, (b) 0.25 mm, (c) 0.5 mm, (d) 0.75 mm, (e) 1 mm, and (f) 2 mm. With the shortest interaction length,  $\Delta z = 0.1 \text{ mm}$ , the double-step ionization feature is prominent. However, as the interaction length  $\Delta z$  increases, the step gradually smears out. Also, radial phase oscillations develop due to

increasing probe refraction with interaction length. With  $\Delta z = 0.5$  mm, which corresponds to the gas sheet of our experiment, the temporal double-step in the phase is still discernable. However, both the radial flat-top near the beam center and the step on the beam edge predicted by Fig. 4.2 are substantially smoothed owing to the probe refraction. This agrees with the experimentally measured phase shown in the inset of Fig. 4.5(b). By  $\Delta z = 1$  mm [Fig. 4.8(e)], the temporal step has washed out as well. The washing out of the temporal step is mostly caused by the second distortion effect: axial pump intensity variation within the laser-gas interaction volume. Consequently, it is vitally important to keep the laser-gas interaction length as small as possible. In our case, it appears that a gas sheet not too much thicker than the 0.5 mm of our experiment would have ended up washing out the temporal effects we were trying to uncover.

To summarize, the results of our simulations show that a short laser-gas interaction length must be used to localize the electron density measurement in space and time. Otherwise, the measured spatio-temporal phase at the jet exit is significantly affected by (a) the divergence mismatch of the pump and probe pulses, (b) axial variation of the pump intensity in the interaction volume, and (c) probe beam refraction. A short interaction length mitigates all three effects.

## 4.5 Conclusions

We have observed laser-driven double-step optical field ionization of helium ( $\text{He} \rightarrow \text{He}^+ \rightarrow \text{He}^{2+}$ ) with single-shot supercontinuum spectral interferometry (SSSI). SSSI provides  $\sim 10$  fs resolution and a  $\sim 2$  ps observation window to observe the ionization dynamics. The experimental measurements of electron density evolution  $N_e(x, t)$  are in

good agreement with the tunneling ionization model. The large spectral bandwidth of the supercontinuum probe pulse, the single-shot pump-probe operation, and the minimal laser-gas interaction length of  $\sim 0.5$  mm made it possible to observe the double-step transient.

It was also emphasized that the laser-target interaction length should be minimized to avoid degradation of transient spatio-temporal phase or refractive index measurements. This applies not only to the various versions of spectral interferometry, but to FROG-related measurements as well.<sup>19</sup> In recent SI-based measurements of laser-driven electron density wakefields<sup>13-15</sup> in a static-filled helium gas volume (with laser-gas interaction length  $L \gg z_0$  at densities  $N_e \sim 10^{17}$  cm<sup>-3</sup> similar to those of our experiment), both temporal<sup>14</sup> and spatio-temporal<sup>13, 15</sup> phases  $\Delta\Phi$  were extracted, from which were inferred axial and axial/radial plasma oscillations, respectively. Our calculation cautions that all such measurements where  $L > z_0$  *must* be accompanied by a careful analysis of probe beam propagation.

In summary, our helium ionization experiment not only shows the ultrashort measurement capability of our SSSI diagnostic, but it also strongly illustrates the limitations inherent in any SI-based measurement. In that regard, it is worth emphasizing again that a minimal laser-target interaction length is essential for clear measurements of refractive index profile transients. Otherwise, three effects can act to mask the true index profile transient. First, any difference in divergence between the pump and probe beams can result in transverse spatial mixing of temporal information encoded on the probe beam. Second, the axial pump intensity variation within the interaction volume can act to smear out any temporal phase structure picked up by the probe. Finally, probe beam refraction from the pump-induced index profile can smear out temporal and spatial phase structure.

These three effects can be greatly suppressed with a short laser-target interaction length. Otherwise, all such measurements must be accompanied by a careful analysis of probe beam propagation.

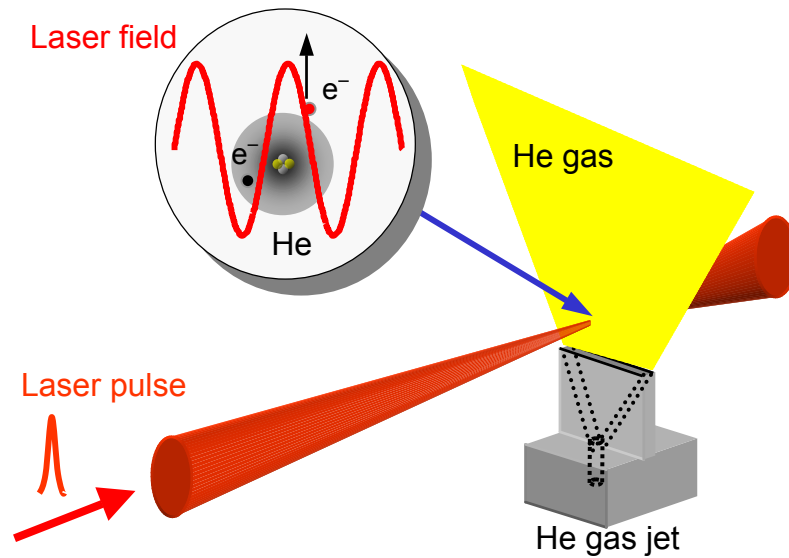


Figure 4.1: (a) Ionization of a thin helium gas jet irradiated by an intense laser pulse.

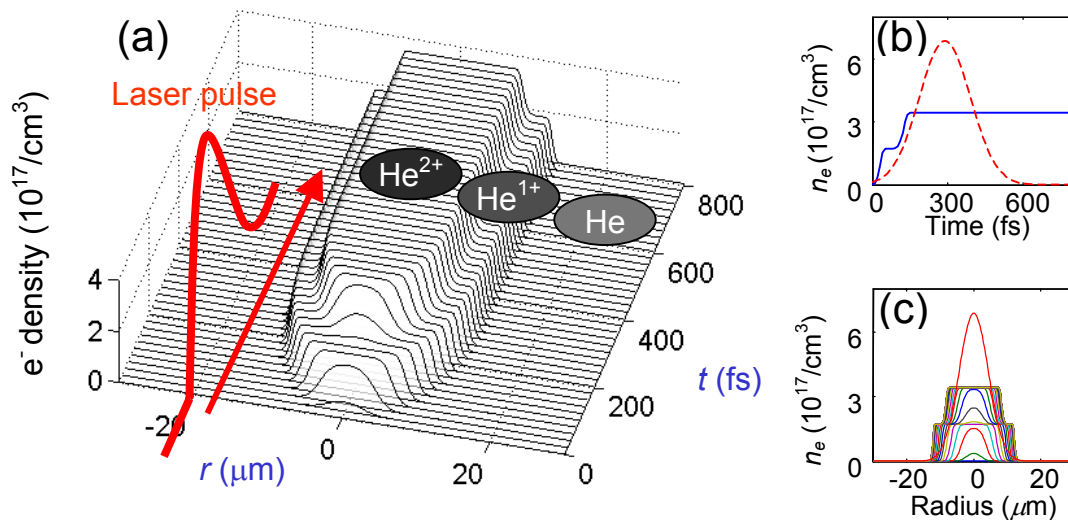


Figure 4.2: (a) Theoretical spatio-temporal electron density profile at the laser focus using ADK theory with  $\tau_{FWHM} = 240$  fs,  $r_{FWHM} = 10.3 \mu\text{m}$ , and  $I_{\text{peak}} = 3.8 \times 10^{16} \text{ W/cm}^2$ . (b) On-axis electron density evolution (solid line) and pump pulse envelope (dashed line). (c) Electron density profiles at  $\Delta t = 20$  fs time increments.

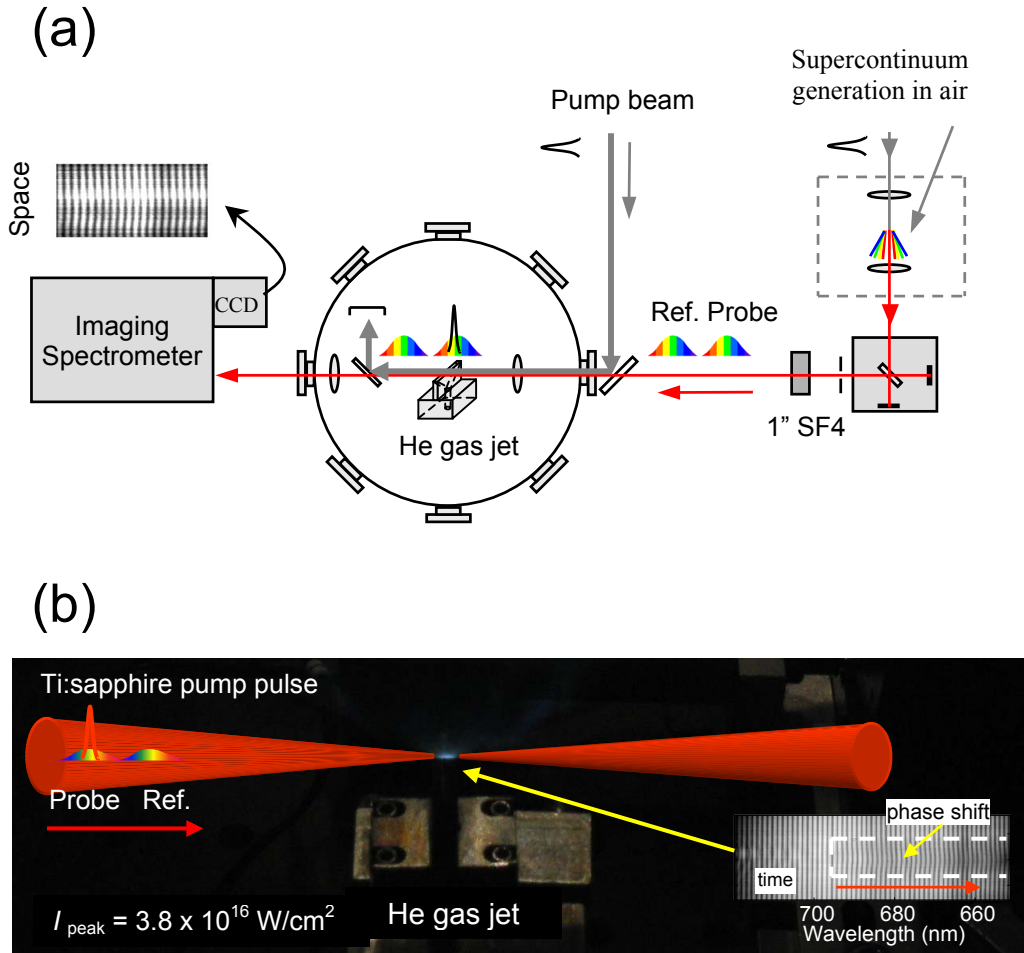


Figure 4.3: (a) Experimental setup with pump beam and chirped supercontinuum (SC) reference and probe pulses combined at a beam splitter and focused into a helium gas jet. The pump is dumped and the reference and probe SC pulses are relayed to the imaging spectrometer. (b) A photograph of the helium gas jet irradiated by a Ti:sapphire laser pulse (artificial color) with peak intensity  $I_{\text{peak}} = 3.8 \times 10^{16} \text{ W/cm}^2$ . Laser-produced helium plasma is visible at the jet center.

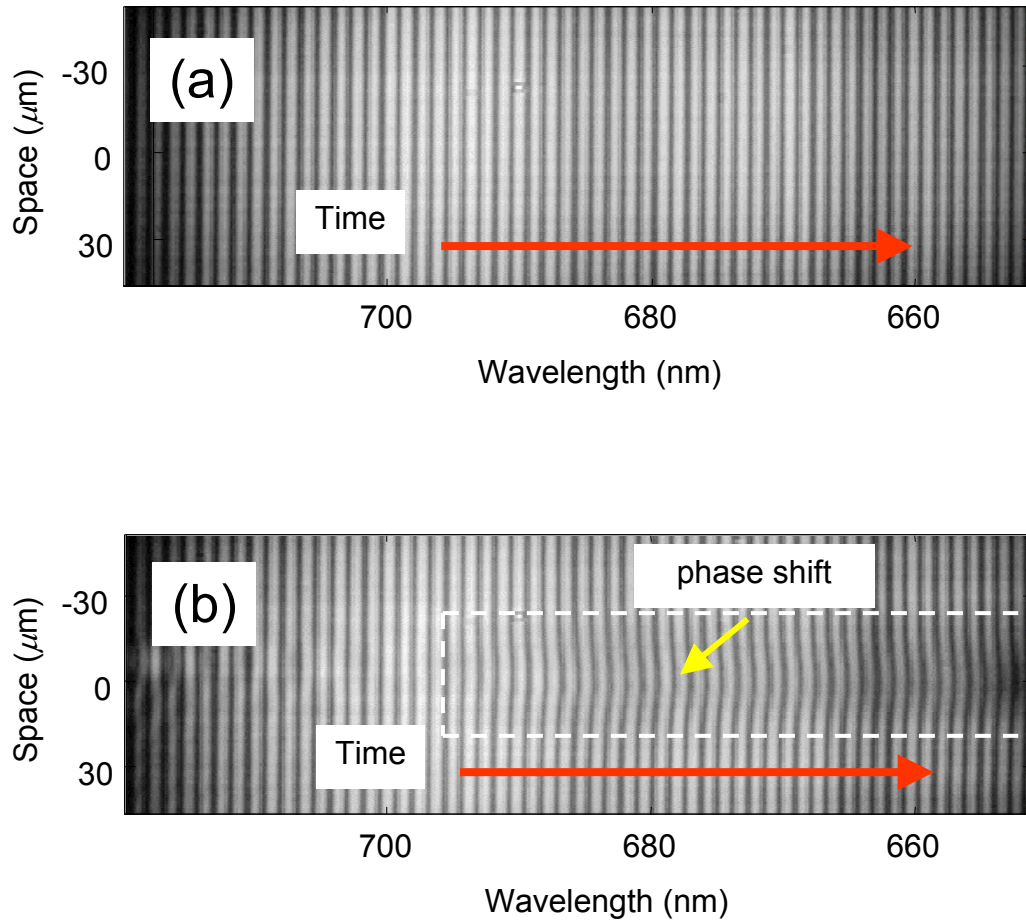


Figure 4.4: Sample spectral interferograms are shown with the helium gas jet (a) off and (b) on. A notable wavelength-dependent fringe shift occurs in (b).

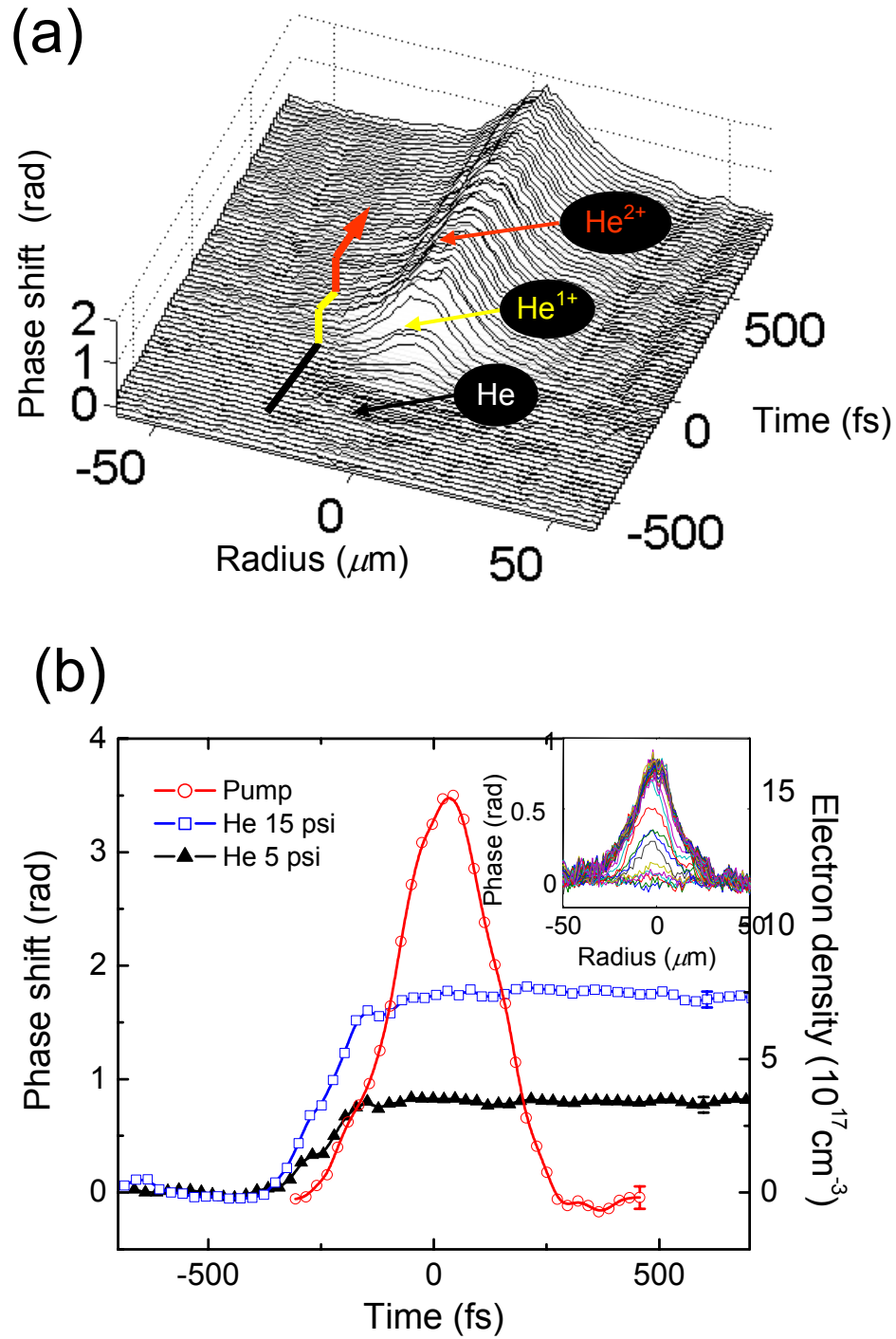


Figure 4.5: (a) Experimental spatio-temporal phase profile  $\Delta\Phi(x, t)$  from optical field ionization of helium at 15 psi jet backing pressure. (b) Central line-outs for jet backing pressures of 5 psi (line with solid triangles) and 15 psi (line with squares). The pump pulse envelope obtained from XPM in glass is also shown (line with circles). The inset shows spatial phase profiles from the 5-psi case at 20 fs increments.

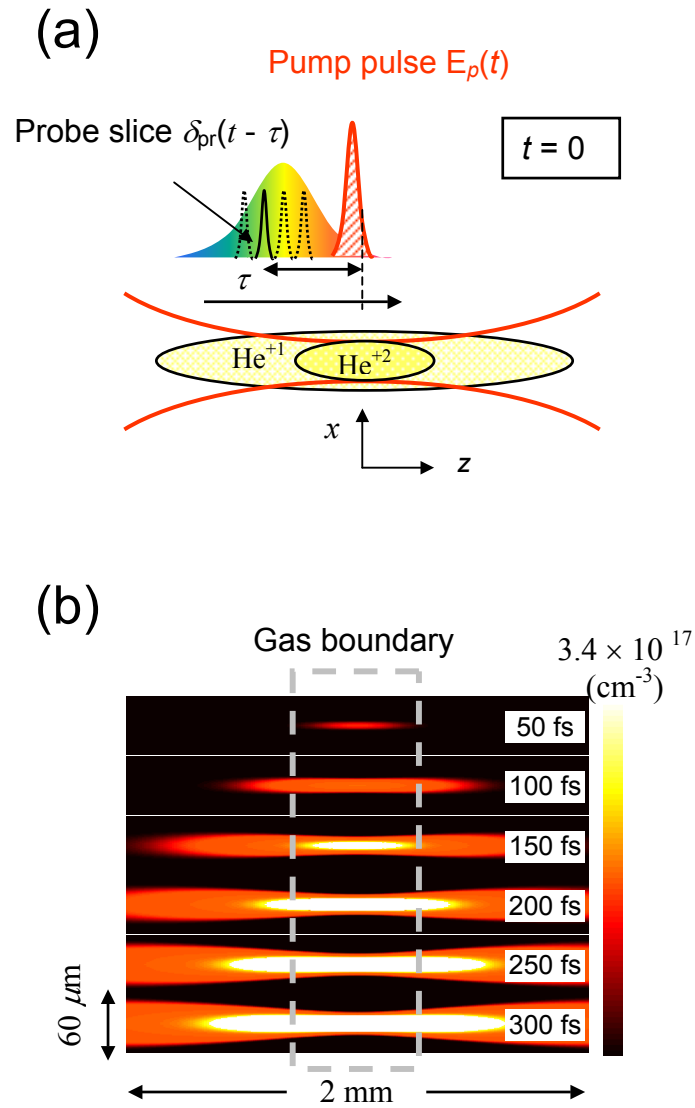


Figure 4.6: (a) Schematic pump-probe diagram. A slice of the probe pulse samples the volume of the helium plasma. (b) Simulated electron density profiles  $N_e(x, z, t' - \tau)$  that a slice of the probe pulse  $\delta_{pr}(t - \tau)$  samples with  $\tau = 50$  fs time increments.

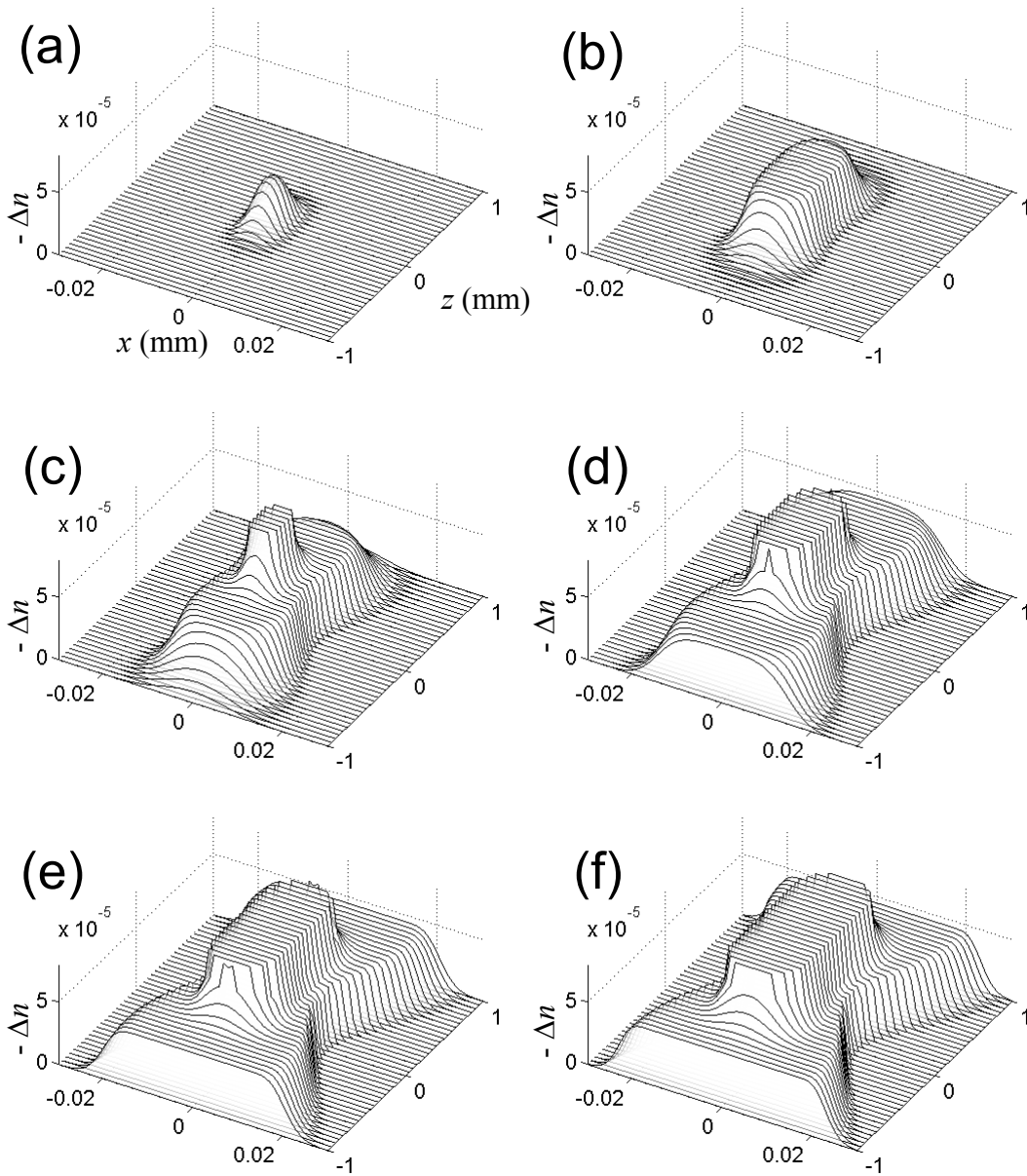


Figure 4.7: Theoretical 2D spatial refractive index shift profiles  $\Delta n(x, z, t' - \tau)$  of the helium plasma sampled by a slice of the probe pulse  $\delta_{\text{pr}}(t - \tau)$  with (a) 50 fs, (b) 100 fs, (c) 150 fs, (d) 200 fs, (e) 250fs, and (f) 300 fs delays with respect to the pump pulse.

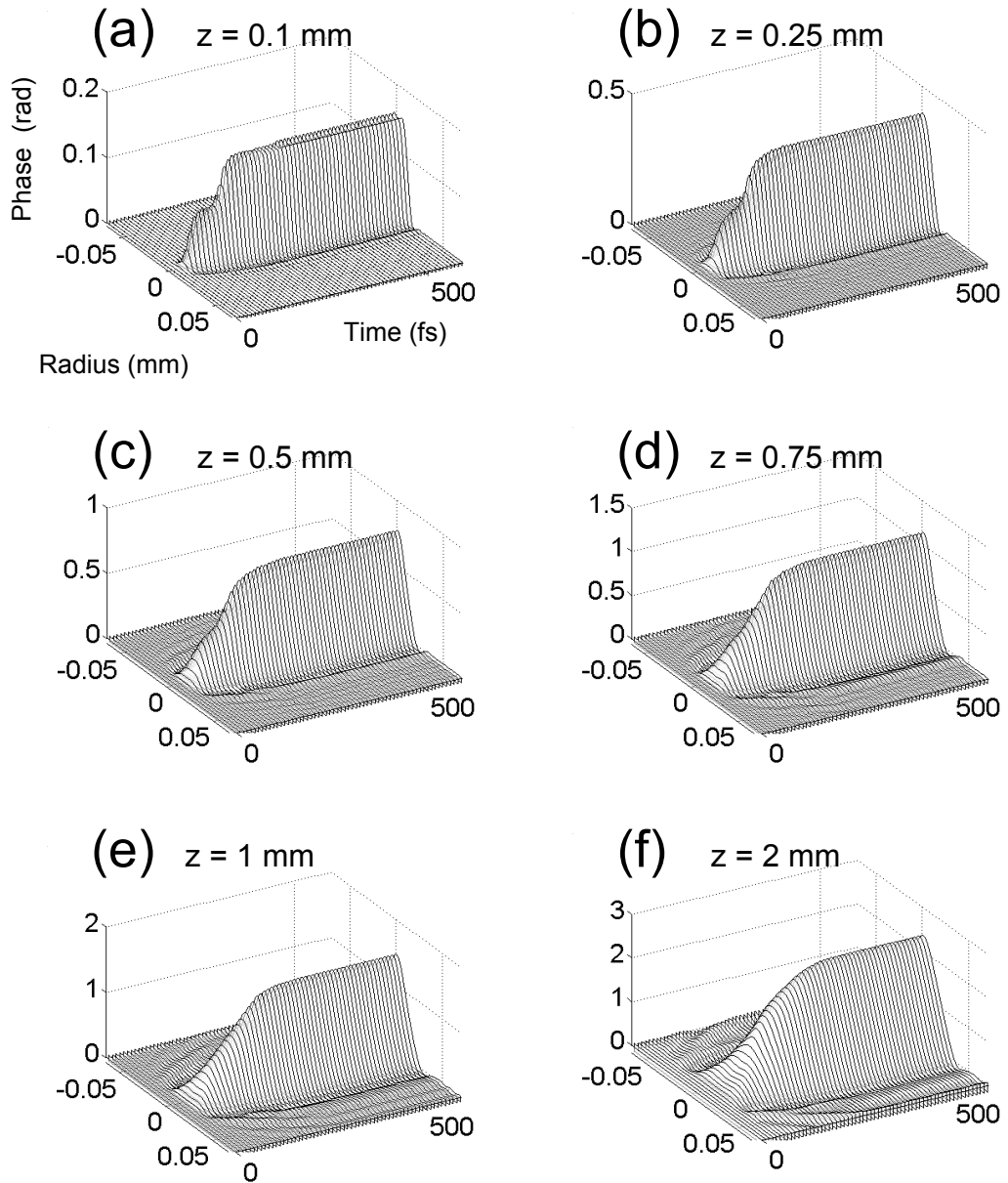


Figure 4.8: Theoretical probe phase profiles  $\Delta\Phi(x, t)$  at the end of the helium plasma with the laser-gas interaction length  $\Delta z$  (a) 0.1 mm, (b) 0.25 mm, (c) 0.5 mm, (d) 0.75 mm, (e) 1 mm, and (f) 2 mm.

## **Chapter 5: Characterization of cluster sources**

In the interaction of intense laser pulses with clusters, van der Waals-bonded aggregates of up to  $\sim 10^7$  atoms, the average cluster size and density play a crucial role in determining the dynamics of the laser-cluster coupling and the resulting explosive dynamics of the super-hot cluster plasma. For proper interpretation of experiments, the cluster source needs to be well characterized. However, the determination of the mean cluster size and number of clusters per unit volume (cluster density) has not been previously performed. Most, if not all, earlier laser-cluster interaction experiments have depended on the use of semi-empirical scaling formulas for cluster size and density estimation.

In this chapter, two different cluster sources are characterized using a simple all-optical technique which enables measurement of the average cluster size and density. The technique employs Rayleigh scattering imaging combined with interferometry. A conical nozzle gas jet and an elongated gas jet were characterized. It will be shown that our elongated gas jet can produce a cm-length plume of clusters (with average cluster size controllable from 20 Å to 1000 Å in radius) with a highly uniform spatial distribution under cryogenic cooling of the gas jet body.

### **5.1 Atomic and molecular cluster source**

Supersonic nozzle or free jet sources are currently widely used for the generation of rare gas, molecular, and low-boiling point metal clusters. Historically, Becker, Bier, and Henkes first reported on the formation of cluster beams – aggregates of atoms or

molecules, bonded via interatomic (or intermolecular) forces such as van der Waals force, ranging in size from dimers to nano-droplets of few million atoms – in a condensing supersonic nozzle flow into vacuum.<sup>1</sup> Since then, formation of clusters in free jets has been well understood and documented in the literature.<sup>2-6</sup>

The mechanism for cluster formation in an expanding nozzle flow is as follows. At high valve backing pressure, atoms or molecules experience many collisions in the initial expanding phase where the collisional mean free path is much smaller than the nozzle diameter. The expansion, which is adiabatic and isenthalpic, cools the gas, resulting in the generation of dimers through collisions mediated by van der Waals forces. Dimers seed the initial cluster nucleation and further cluster growth occurs via collisions. Clusters reach quasi-equilibrium with radii ranging from few Å to ~1000 Å depending on gas species, gas valve backing pressure, valve temperature, and nozzle geometry.

Traditionally, atomic clusters generated by jet expansion have been characterized by the semi-empirical parameter  $\Gamma^*$  introduced by Hagena, expressed as<sup>2-4</sup>

$$\Gamma^* = k_H \frac{d^{0.85} p_0}{T_0^{2.29}}, \quad (5.1)$$

where  $k_H$  is a gas dependent constant ( $k_H \sim 1650$  for Ar and 2890 for Kr,<sup>4</sup> see Table 5.1),  $d$  is the orifice diameter in  $\mu\text{m}$ ,  $p_0$  is nozzle backing pressure in mbar, and  $T_0$  is temperature in Kelvin. For a supersonic nozzle with a jet expansion half angle  $\alpha$ , the throat diameter can be replaced by an equivalent diameter  $d_{\text{eq}} = 0.74d/\tan\alpha$ .<sup>5</sup>

A scaling for the average number of atoms per cluster  $n_c$ ,

$$\langle n_c \rangle = 33 \left( \frac{\Gamma^*}{1000} \right)^{2.35}, \quad (5.2)$$

was verified in the regime  $1000 < \Gamma^* < 7300$  by Hagena using time-of-flight of mass spectrometry.<sup>5</sup> From Eqs. (5.1) and (5.2),  $n_c$  scales with  $p_0$  and the inverse of  $T_0$  ( $\langle n_c \rangle \propto \Gamma^{*2.35} \propto p_0^{2.35} T_0^{-5.38}$ ). Hence, to vary the average cluster size, one can vary the valve backing pressure  $p_0$  and temperature  $T_0$ . In addition, large values of  $k_H$  (i.e. heavier atoms with larger polarizability) are favored for the generation of bigger clusters. Here, the average cluster size  $a$  is related to  $n_c$  by

$$a = r_{WS} n_c^{1/3}, \quad (5.3)$$

in the frame of liquid drop model, where  $r_{WS}$  is the Wigner-Seitz radius  $r_{WS} = (3m/4\pi\rho)^{1/3}$ ,  $m$  is the mass, and  $\rho$  is the atom bulk density in the liquid state at the melting point.<sup>7</sup> The Wigner-Seitz radii of various noble gases are listed in Table 5.1.

Table 5.1 The values of  $k_H$ ,  $r_{WS}$ , and inter-cluster atomic density for noble gases.

	He	Ne	Ar	Kr	Xe
$k_H$ <sup>ref. 4</sup>	3.85	185	1650	2890	5500
$r_{WS}$ <sup>ref. 7</sup> [ $\text{\AA}$ ]	–	1.858	2.231	2.387	2.572
Density ( $\times 10^{22} \text{cm}^{-3}$ )	–	3.72	2.15	1.76	1.40

For the intense laser-cluster interaction studies of this dissertation, gas jets with two types of nozzle are used. The first jet source consists of a stainless solenoid valve (General Valve Corporation series 9) and a supersonic conical expansion nozzle ( $d = 0.5$  mm,  $\alpha = 5^\circ$ , and 12.7 mm nozzle length) as shown in Fig. 5.1(a). The cluster source is placed in a vacuum chamber equipped with a 164 cfm displacement roots pump (Leybold RUVAC WS 251). The solenoid operates at 10 Hz with a valve opening time of 450  $\mu\text{s}$ . A Kel-F poppet, mounted on an armature in the solenoid valve, is actuated with a high-voltage electric pulse in the solenoid coil surrounding the armature. The sudden poppet actuation,

driven by a 300-volt pulse from a high voltage pulse driver (General Valve IOTA ONE), opens the pressurized valve rapidly, resulting in the supersonic expanding nozzle flow, which promotes clustering of the gas atoms. The valve gas pressure  $p_0$  is controlled with a commercial gas regulator, and the chamber background pressure of  $\sim 0.1$  torr is measured with a Baratron absolute pressure transducer (MKS Instruments Model 626A). The conical nozzle jet is typically operated at room temperature whereas the second cluster source, the elongated nozzle shown in Fig. 5.1(b), is cryogenically cooled and its operation is described in Section 5.4 in detail.

## 5.2 Rayleigh scattering by neutral clusters

Rayleigh scattering has been widely used as a simple method to verify the presence of clusters in a jet expansion source.<sup>8-11</sup> The Rayleigh scattering cross section for  $ka \ll 1$  is given by<sup>12</sup>

$$\sigma_{\text{scatt.}} = \frac{8\pi}{3} k^4 |\gamma|^2 = \frac{8\pi}{3} k^4 a^6 \left| \frac{\varepsilon - 1}{\varepsilon + 2} \right|^2, \quad (5.4)$$

where  $k = 2\pi/\lambda$  is the wavenumber,  $\gamma = a^3(\varepsilon - 1)/(\varepsilon + 2)$  is the cluster polarizability,  $a$  is the cluster radius, and  $\varepsilon$  is the dielectric function of the material internal to the cluster.

With an ensemble of uniform sized clusters, the Rayleigh scattering signal  $S_{\text{Rayleigh}} \propto N_c \sigma_{\text{scatt}}$  where  $N_c$  is the cluster density (the number of clusters per unit volume). The cluster density  $N_c \propto N_0/n_c$  where  $N_0$  is the overall atomic density and  $n_c$  is the average number of atoms per cluster. The scattering cross section  $\sigma_{\text{scatt}} \propto a^6$  from Eq. (5.4), and  $\sigma_{\text{scatt}} \propto a^6 \propto n_c^{-2}$  from Eq. (5.3). From Eqs. (5.1) and (5.2), we get  $n_c \propto \Gamma^{*2.35} \propto p_0^{2.35}$ . Since, the overall

atomic density  $N_0$  increases linearly with the gas jet backing pressure  $p_0$ , the Rayleigh scattering signal is proportional to

$$S_{\text{Rayleigh}} \propto N_c \sigma_{\text{scatt.}} \propto (N_0/n_c)(n_c^2) \propto p_0^{3.35}. \quad (5.5)$$

This pressure-dependent Rayleigh scattering yield ( $S_{\text{Rayleigh}} \propto p_0^{3.35}$ ) can be checked experimentally as shown in Fig. 5.2(a). A 7 ns vertically polarized Nd:YAG probe pulse at 532 nm is weakly focused in the conical gas jet at  $f/100$ . The probe is dominantly scattered by the argon clusters formed in the gas jet. The  $90^\circ$  scattered probe pulse is collected by a  $f = 100$  mm collecting lens and focused to a photomultiplier tube (PMT) through an interference filter at 532 nm and 2 mm aperture before the PMT. The relative scattered energy is plotted in Fig. 5.2(b) as a function of gas jet backing pressure. A least squares fit to the data points gives a pressure-dependent scattering yield of  $p_0^{2.54 \pm 0.08}$ . The scaling power of 2.54 indicates the presence of clusters in the gas jet because if monomers alone were present in the scattering volume, we would have simply  $S_{\text{Rayleigh}} \propto N_0 \sigma_{\text{m scatt}} \propto p_0$  where  $\sigma_{\text{m scatt}}$  is the monomer Rayleigh scattering cross-section. However, the scattering yield of  $p_0^{2.54}$  is weaker than  $p_0^{3.35}$  from Eq. (5.5) based on Hagena's scaling law, which implies that Hagena's scaling law overestimates  $n_c$  for the large clusters under our conditions.

Rayleigh scattering is a simple and nondestructive technique to check the presence of clusters and relative cluster sizes, but it cannot on its own be used to absolutely estimate the average cluster size. It is, however, notable that some experimental groups have estimated the average cluster size by assigning a threshold cluster size for the onset of measurable optical scattering.<sup>10, 13</sup> The justification for such a procedure is not clear.

### 5.3 Measurement of the average cluster size and density

Determination of the average cluster size  $a$  and density is a task which up till now had not found a reliable solution. Numerous experimental approaches – mass spectroscopy with electron impact ionization,<sup>2, 3, 5, 6</sup> fragmentation-corrected time-of-flight mass spectroscopic analysis,<sup>14</sup> high-energy electron diffraction,<sup>15, 16</sup> atom scattering,<sup>17–21</sup> water-capture with mass spectroscopy,<sup>22</sup> Mie scattering for large clusters,<sup>23</sup> fluorescence excitation spectra for small clusters,<sup>4</sup> EUV Rayleigh scattering and absorption,<sup>24</sup> Rayleigh scattering with auxiliary mass flux estimation,<sup>25, 26</sup> and Rayleigh scattering with mass-spectroscopy<sup>9</sup> – have been used to measure the average cluster size. Most of these techniques require sophisticated additional setups which may differ considerably from the main experiment of interest. Moreover, some of these methods involve cluster fragmentation due to photoionization or electron impact ionization, and these processes require detailed consideration and subsidiary modeling in the data analysis.<sup>14</sup>

In this section, a simple all-optical technique is presented for the measurement of the spatial distribution of the average cluster size and number of clusters per unit volume (density). This technique uses a combination of Rayleigh scattering imaging and neutral cluster gas interferometry. We first show how Rayleigh scattering and interferometry can be used to determine the cluster size and density.

#### 5.3.1 Theory of Rayleigh scattering and neutral cluster gas interferometry

For a laser beam propagating from  $x$  to  $x + \Delta x$  in an ensemble of clusters, the energy scattered by the clusters at  $90^\circ$  into a collecting lens is given by

$$\Delta E_{\text{lens}}(x) \approx E_{\text{in}} \bar{\sigma}_{\text{lens}}(x) N_c(x) \Delta x, \quad (5.6)$$

where  $E_{\text{in}}$  is the laser energy incident on the scattering volume,  $\bar{\sigma}_{\text{lens}}$  is the cluster size distribution-averaged Rayleigh scattering cross section into the collecting lens, and  $N_c$  is the average number of clusters per unit volume. Since the clusters are randomly distributed in the scattering volume, Eq. (5.6) represents an incoherent sum of individual scatterings. Here, single scattering, in contrast to multiple scattering, is assumed in the scattering volume. For  $90^\circ$  scattering and  $ka \ll 1$ ,  $\bar{\sigma}_{\text{lens}}$  is given by

$$\bar{\sigma}_{\text{lens}} = \int_{\text{lens}} \left( \frac{d\bar{\sigma}}{d\Omega} \right) d\Omega \approx \pi k^4 |\bar{\gamma}|^2 (\alpha^2 - \alpha^4/4), \quad (5.7)$$

where the bar represents an ensemble average over the cluster size distribution,  $\alpha = \tan^{-1}(R_0/h) \approx R_0/h$  is the scattering collection half angle into the lens,  $R_0$  is the collection lens radius, and  $h$  is the distance between the cluster jet and the lens. From Eqs. (5.4) and (5.6), we obtain

$$\bar{a}^6 N_c = \frac{1}{\pi k^4} \left| \frac{\varepsilon + 2}{\varepsilon - 1} \right|^2 \frac{\Delta E_{\text{lens}}}{E_{\text{in}} \Delta x} \frac{1}{(\alpha^2 - \alpha^4/4)}. \quad (5.8)$$

The relative contribution to the measured Rayleigh scattering of any monomers in the cluster jet is negligible.

In addition, neutral cluster gas interferometry can be employed to measure the real radial refractive index shift  $\Delta n_r(\rho)$  induced by the cluster gas, where  $\rho = (x^2 + y^2)^{1/2}$  [see Fig.5.2(a)]. Here, first a probe phase shift  $\Delta\phi(x)$  is measured experimentally, and then  $\Delta n_r(\rho)$  can be extracted from  $\Delta\phi(x)$  using an Abel inversion assuming radial symmetry.<sup>27</sup>  $\Delta\phi(x)$  and  $\Delta n_r(\rho)$  are expressed as

$$\Delta\phi(x) = \int_{-y}^y k \Delta n_r(\rho) dy = \int_{-\sqrt{\rho_0^2 - x^2}}^{\sqrt{\rho_0^2 - x^2}} \frac{k \Delta n_r(\rho)}{\sqrt{\rho^2 - x^2}} \rho d\rho \quad (5.9.1)$$

and

$$\Delta n_r(\rho) = -\frac{1}{k\pi} \int_{\rho}^{\rho_0} \left( \frac{d\Delta\phi(x)}{dx} \right) \frac{dx}{\sqrt{x^2 - \rho^2}}, \quad (5.9.2)$$

where  $\rho_0$  is the radius of the cluster gas-vacuum boundary ( $\Delta n_r(\rho_0) = 0$ ). The index of refraction shift is  $\Delta n_r(\rho) = n_r(\rho) - 1 = 2\pi N_c \bar{\gamma}_r + \delta n_m$  where  $\bar{\gamma}_r = \text{Re}(\bar{\gamma})$  and  $\delta n_m = 2\pi N_m \gamma_m$  is the additional index contribution of monomers of density  $N_m$  and polarizability  $\gamma_m$ . Assuming  $\delta n_m = 0$  for now, we get

$$\bar{a}^3 N_c = \frac{\Delta n_r(\rho)}{2\pi} \left( \frac{\varepsilon + 2}{\varepsilon - 1} \right). \quad (5.10)$$

Combining Eqs. (5.8) and (5.10), one then obtains the effective radius  $a_{\text{eff}}(x) \equiv$

$\left( \overline{a^6(x)} / \overline{a^3(x)} \right)^{1/3}$  and average cluster density  $N_c(x)$  of the ensemble of clusters by measuring  $\Delta E_{\text{lens}}/E_{\text{in}}$  and  $\Delta\phi(x)$ .

### 5.3.2 Experimental measurement of cluster size and density

The experimental layout for 90° Rayleigh scattering is shown in Fig. 5.3(a). A 532 nm, 7 ns, 0.06 mJ frequency-doubled Nd:YAG probe laser pulse synchronized with the gas puff was focused into the conical jet at  $f/100$  with vertical polarization. The estimated peak intensity was  $5.5 \times 10^7 \text{ W/cm}^2$  – sufficiently low so as not to disturb the neutral clusters – with a FWHM spot size of 110  $\mu\text{m}$ . The scattered energy was collected by a BK7 lens of diameter  $2R_0 = 50.8 \text{ mm}$  at a distance  $h = 192.5 \text{ mm}$  from the gas jet. The scattering half angle was  $\alpha = \tan^{-1}(R_0/h) = 0.13$ . The Rayleigh scattering zone in the cluster jet was imaged by the lens onto a CCD camera. 50-shot averaged sample images are shown in Fig.

5.3(b) at a jet backing pressure range of 200 ~ 600 psi. One dimensional (1D) central lineouts of these profiles for increasing valve-backing pressure are plotted in Fig. 5.4(a). Figure 5.4(b) shows the on-axis ( $x = 0$ ) Rayleigh scattering yields as a function of pressure. A polynomial least squares fit gives a pressure-dependent scattering yield of  $p_0^{2.61 \pm 0.07}$ , which is in good agreement with the scaling result of  $p_0^{2.54 \pm 0.08}$  ( $n_c \propto P_0^{1.61}$ ) obtained with the photomultiplier tube as described in Section 5.2. As before, the scattering yield is weaker than the  $p_0^{3.35}$  scaling ( $n_c \propto P_0^{2.35}$ ) predicted by Hagena. A number of experiments by other groups also show that the pressure scaling exponent for  $n_c$  lies in the 1.5 ~ 2 range depending on experimental conditions.<sup>22</sup> This indicates that for larger clusters ( $\Gamma^* > 15,000$ ), Hagena's scaling law overestimates the average cluster size.

Figure 5.5(b)-(d) shows composite 2D Rayleigh scattering profiles at  $z = 2, 3,$  and  $4$  mm heights from the nozzle orifice, obtained by scanning the cluster jet transversely with respect to the probe beam, as shown in Fig. 5.5(a). The cluster jet is mounted on a 3D translation stage driven by closed-loop motorized actuators (Newport CMA-25CCLL with motion controller Newport ESP300). In general, the 2D profiles verify the good cylindrical symmetry of the gas flow (justifying the use of Abel inversion with the interferometric data) and its sharp boundary ( $\sim 500 \mu\text{m}$ ) with vacuum. At (a)  $z = 2$  mm, the profile appears slightly asymmetric, possibly due to an unknown irregularity in the nozzle or poppet. As the height  $z$  increases, the gas flow becomes more symmetric as shown in (c) and (d).

Additionally, the temporal evolution of the cluster gas jet is characterized using Rayleigh scattering. Figure 5.5(e) shows the time history of 1D scattering profiles at  $z = 2$  mm distance from the nozzle orifice, obtained by adjusting the onset of the gas puff with respect to the probe pulse arrival. The scan shows that the jet opening duration is  $750 \mu\text{s}$

(FWHM) whereas the duration of the high voltage pulse in the solenoid coil is set at 450  $\mu\text{s}$ . Each 1D curve is spatially integrated and the result is shown in the panel to the right in Fig. 5.5(e). There is a secondary peak around  $t = 1000 \mu\text{s}$  due to the slight bouncing of the poppet as it returns to seal the nozzle entrance orifice.<sup>28</sup>

To absolutely calibrate the Rayleigh scattering imaging in order to determine  $\Delta E_{\text{lens}}$ , a 45° mirror was placed above the jet to re-direct the Nd:YAG pulse into the CCD camera through the collecting lens, chamber window, and a series of calibrated neutral density (ND) filters. With a measurement of pulse energy before the lens, we can calibrate the scattering source energy sensitivity per pixel of the CCD camera at 532 nm.

For the interferometry experiment, the same Nd:YAG probe pulse, but with an expanded beam size, was directed through the Ar cluster jet along the  $y$ -direction [see Fig. 5.6(a)]. The probe acquires a phase shift  $\Delta\phi(x)$  due to the cluster jet, and it was relay-imaged with a dual lens system from the jet exit through a modified Mach-Zehnder interferometer onto a CCD camera, generating 2D interferograms. Figure 5.6(b) shows a sample interferogram at a jet backing pressure of 800 psi. The phase shift  $\Delta\phi(x, z)$  (where  $z$  is along the nozzle axis) was extracted from the raw interferogram using a fast-Fourier transform (FFT) phase extraction technique<sup>29</sup> and plotted in Fig. 5.6(c). Then, the radial refractive index shift  $\Delta n_r(\rho)$  was obtained from  $\Delta\phi(x)$  using an Abel inversion algorithm.<sup>30-32</sup> To reduce the Abel inversion noise,  $\Delta\phi(x)$  was first fitted to a Gaussian profile  $\Delta\phi_{\text{fit}}(x) = \Delta\phi_0 \exp(-4 \ln 2 x^2/x_0^2)$  where  $x_0$  is FWHM radius.<sup>31</sup> The assumption of Gaussian phase shifts is very reasonable as shown in Fig. 5.6(d), where the phase shift line-outs  $\Delta\phi(x)$  at  $z = 2, 3,$  and  $4$  mm are plotted, and a Gaussian least squares fit is applied to the  $z = 3$  mm curve. The Abel inversion gives the radial refractive index shift  $\Delta n_r(\rho) =$

$\Delta\phi_0(kx_0)^{-1}\sqrt{4\ln 2/\pi}\exp(-4\ln 2\rho^2/x_0^2)$ . This measurement, combined with that of  $\Delta E_{\text{lens}}(x)/E_{\text{in}}$ , is sufficient to determine  $a_{\text{eff}}$  and  $N_c(x)$  from Eqs. (5.8) and (5.10).

Subsidiary information used is  $\text{Re}(\varepsilon)=1.68$  and  $\text{Im}(\varepsilon)=0$  for solid Ar at 532 nm.<sup>33–34</sup>

Figure 5.7(a) plots the cluster effective radius  $a_{\text{eff}}(x)$  (solid squares) and density  $N_c(x)$  (open circles) at 400 psi backing pressure and 3 mm from the nozzle orifice. Figure 5.7(b) shows the on-axis  $a_{\text{eff}}$  and  $N_c$  versus backing pressure.

### 5.3.3 Consideration of cluster size distribution and cluster-monomer ratio

The size distribution of clusters formed in a gas jet is not uniform but represents a distribution.<sup>14, 20, 35</sup> In addition, the cluster beam in the supersonic nozzle consists of two phases – condensed (clusters) and uncondensed (single atoms/molecules or monomers). The details of the cluster size distribution and the monomer fractional density can affect the values of  $a_{\text{eff}}$  and density  $N_c$  estimated from Eqs. (5.8) and (5.10). If the cluster size

distribution is explicitly considered, we note that  $\overline{a^6} = \int_0^\infty a^6 f(n_c) dn_c$  and

$\overline{a^3} = \int_0^\infty a^3 f(n_c) dn_c$ , where  $f(n_c)$  is the normalized density of clusters having  $n_c$  atoms or

molecules and  $a = r_{\text{WS}} n_c^{1/3}$  from Eq. (5.3). For a Gaussian or log-normal cluster size

distribution having a mean atom number  $\bar{n}_c$  and a distribution width  $\sigma$ , we obtain  $a_{\text{eff}}/\bar{a} =$

$(1 + \sigma^2/\bar{n}_c^2)^{1/3}$ . Even for a broad distribution width  $\sigma = \bar{n}_c/2$ , we get  $a_{\text{eff}}/\bar{a} = 1.08$ , which

indicates that the values of  $a_{\text{eff}}$  extracted by the measurement exceeds the mean cluster size

by only 8%. Thus, for non-pathological cluster size distributions,  $a_{\text{eff}}$  is a good

representation of the mean cluster radius.

In any cluster jet flow, there is a non-zero density  $N_m$  of monomers. In general, the monomers contribute negligibly to the collected Rayleigh scattered light, but can have a measurable effect on the interferometric phase shift. As it is difficult to independently determine  $N_m$ , the usual case of non-accounting for monomers in the application of Eqs. (5.8) and (5.10) results in an underestimation for  $a_{\text{eff}}$  by a factor  $(1 - \delta_m)^{-1/3}$ , where  $\delta_m = N_m / (N_m + N_c \bar{n}_c)$  is the relative concentration of monomers. However, this factor's cube root dependence greatly mitigates the effects of the uncertainty in  $\delta_m$ . As an example, for our results at 600 psi, even for  $\delta_m$  in the very wide range of 0% to 80%, the effective cluster size lies in the much more restricted range of  $70 \text{ \AA} < a_{\text{eff}} < 120 \text{ \AA}$ .

#### **5.4 Elongated cluster gas jet and its characterization**

For the generation of a long plasma channel, either preformed or self-guided, we have used a slot gas jet nozzle to produce an elongated thin gas plume as a target of intense laser pulse irradiation.<sup>36</sup> In order to ensure dominant cluster phase generation in the slot jet expansion, our elongated gas jet was cryogenically cooled. This greatly enhanced the cluster yield in the flow, and also improved the flow uniformity.

In this section, our elongated cluster source is described and the source is characterized with the Rayleigh scattering/interferometry diagnostic described in Section 5.3.

##### **5.4.1 Elongated cluster source**

The elongated cluster source consists of a solenoid valve (General Valve Corporation series 9) and an elongated nozzle (11.5 mm length and 0.4 mm width of the

nozzle opening) as shown in Fig. 5.1(b). Teflon spacers (0.4 mm thick and 19 mm long) are placed in between two nozzle jaws to guide the gas flow in the nozzle.

To enhance clustering in the nozzle, the jet valve is cryogenically cooled with liquid nitrogen (LN<sub>2</sub>). Figure 5.8(a) shows the picture of the jet valve (below the elongated nozzle) enclosed in a copper cooling jacket (cryostat). The stainless steel LN<sub>2</sub> feed tube and two solid-state cartridge heaters (Omega Engineering, CSS-10150) are clamped inside the cooling jacket. The gas jet and cooling jacket are mounted as a unit on a motor-driven 3D stage enabling remote positioning of the jet in real time during experiments. Liquid nitrogen, dispensed from a dewar at a backing pressure of 10 psi, flows through the feed tube to the cooling jacket. To control the cryostat temperature, the cartridge heaters are adjusted to vary the temperature from  $-150\text{ C}^\circ$  (123 K) up to room temperature. The temperature measurement and control are conducted with a type T thermocouple embedded inside the cooling jacket and a temperature controller (Omega Engineering, CN77324) which turns the heaters on or off as needed. With this system, the cryostat temperature can be maintained at a user-selected set point to within a temperature range of  $\pm 1.5^\circ$ .

In experiments thus far, argon or nitrogen gas has been used at backing pressures in the range of 200 ~ 600 psi, forming Ar or N<sub>2</sub> clusters. The nucleation and growth of Ar or N<sub>2</sub> clusters are greatly enhanced under cryogenic operation of the jet. At 10 Hz pulse repetition rate of the valve, a background pressure of  $\sim 100$  mTorr is measured at  $T = 123$  K. In general, the background pressure is higher at low temperature because of increasing leakage through the closed valve poppet between gas pulses.

If the valve temperature is lower than the boiling temperature  $T_b$  of Ar or N<sub>2</sub> gases at a pressure  $p_0$ , large-scale ( $\sim \mu\text{m}$ ) liquid fragments or droplets are formed, resulting from

the fragmentation of liquid injected into vacuum.<sup>37</sup> Since we are interested in producing and characterizing nanometer scale clusters for the experiments of this dissertation, the jet operation is limited to the cluster regime, with valve temperature higher than  $T_b$ .

#### 5.4.2 Rayleigh scattering experiment

The experimental setup for Rayleigh scattering in the elongated gas jet is similar to that in Fig. 5.3(a). Here, the conical gas jet is replaced with the elongated cluster gas jet. A 7 ns Nd:YAG probe pulse at 532 nm with vertical polarization was weakly focused ( $f/100$ ) at  $z = 1.53$  mm height from the elongated nozzle orifice. The probe was scattered by the argon or nitrogen cluster flows exiting the orifice. The  $90^\circ$  scattered beam was relay-imaged (with  $3\times$  demagnification) by a collecting lens ( $f = 100$  mm), located  $h = 447$  mm away from the nozzle, to a CCD camera.

Rayleigh scattering by Ar clusters was visible to the unaided eye at  $T = 153$  K as shown in Fig. 5.8(b). Figure 5.9(a) shows CCD images of Rayleigh scattering at various backing pressures and temperatures. The central line-outs of the Rayleigh scattering signals are plotted in Fig. 5.9(b). As predicted, large clusters and resulting strong Rayleigh scattering is favored at high gas jet backing pressures and low temperatures. As seen in Fig. 5.9, scattering is more strongly dependent on temperature than pressure, which is consistent with the greater sensitivity of cluster size to temperature rather than pressure.<sup>2, 5</sup> Rayleigh scattering was measured to be enhanced by three orders of magnitude at  $T = 153$  K compared to room temperature. In addition, the scattering images show that the spatial cluster distribution is non-uniform at relatively high temperatures and low valve backing pressures. For instance, at room temperature, the scattering profile shows two humps up to

600 psi backing pressure, indicating suppressed yields of Ar clusters in the middle of the jet. However, relatively uniform cluster distributions along the nozzle length were observed below  $T = 153$  K even at as low a pressure as 200 psi.

Figure 5.10 shows the temperature-dependent Rayleigh scattering spatial distributions for (a) Ar and (b)  $N_2$  clusters at 400-psi backing pressure. The spatial uniformity of Ar clusters along the jet slot orifice is greatly improved below  $T = 193$  K. In case of  $N_2$ , no measurable Rayleigh scattering was detected above  $T = 202$  K ( $-70$  C°). This is consistent with the lower  $k_H$  value for  $N_2$  ( $k_H = 528$  for  $N_2$  and  $k_H = 1650$  for Ar).<sup>38</sup> Only below  $\sim 140$  K was the scattering uniform. In general, laser scattering imaging explicitly shows that the elongated gas jet can produce a spatially uniform cluster gas.

A 2D laser scattering profile for the elongated gas jet was obtained by mechanically scanning the jet position with respect to the probe beam. Figure 5.11(a)-(b) shows 2D scattering profiles for an Ar cluster jet at  $T = 297$  K (room temperature) and  $T = 153$  K (cryogenic temperature), at  $z = 1.53$  mm from the nozzle exit orifice. At room temperature, a double hump structure appears, which is eliminated at 153 K.

Figure 5.11(c)-(d) shows the temporal evolution of the 1D laser scattering profile at the slot center at (a)  $T = 297$  K and (b)  $T = 153$  K. Notably, at  $T = 297$  K, the double hump cluster distribution structure persists throughout the entire gas pulse history. However, at  $T = 153$  K, the scattering profile starts with a uniform structure and becomes somewhat less uniform at later times. This implies that the jet timing can be properly synchronized with the arrival of an intense laser pulse in order to provide the most uniform cluster size/density distribution. Superimposed on Fig. 5.11(c)-(d) are the results of spatially integrating those plots. It is seen that the valve opening duration of  $530 \mu\text{s}$  is significantly

increased at  $T = 153$  K compared to the  $300 \mu\text{s}$  measured at  $T = 297$  K. This is mainly due to the slower response of the valve poppet at low temperatures.

### 5.4.3 Interferometry and shadowgraphy of elongated cluster jet

Neutral cluster gas interferometry was also performed, as described in Section 5.3, on our elongated gas jet. The experimental layout was similar to that in Fig. 5.6(a), except that here the interferometric probe beam was directed along the jet slot (the long axis of the jet). For the case of the probe beam propagating across the slot, the interferometric phase shift was too small to extract with reasonably good accuracy.

A sample interferogram at 600 psi and room temperature, viewed at the end of the jet, is shown in Fig. 5.12(a), superimposed on an extracted phase shift profile  $\Delta\phi(x, z)$ . Figure 5.12(c) shows the phase shift  $\Delta\phi(x_0, z_0)$  at  $x_0 = 0$  and  $z_0 = 1.53$  mm as a function of pressure at  $T = 297, 245, 193,$  and  $153$  K. The temperature dependence of the phase shift for Ar and  $\text{N}_2$  at 400 psi is plotted in Fig. 5.12(d). As temperature decreases, the phase shift increases mainly due to the result of an increased average gas density  $N_0$  in the valve at constant pressure.

Figure 5.12(b) shows sample probe shadowgrams, obtained by blocking the reference beam in the Mach-Zehnder interferometer [see Fig 5.6(a)], with the jet on and off at 400 psi and 143 K. At low temperatures ( $133$  K  $\sim$   $153$  K), there was measurable probe intensity attenuation due to its scattering loss. The probe transmission line-out at  $z = 1.53$  mm is also plotted, showing more than 50% scattering loss along the jet slot. The cluster average size and density can be determined using such scattering attenuation measurements, by considering the transmission factor  $T = \exp(-N_c \sigma_{\text{scatt}} L)$  for a jet length

of  $L$ , where  $\sigma_{scatt}$  is related to cluster radius [see Eq. (5.4)]. This measurement is combined with additional information obtained from interferometry [see Eq. (5.10)]. The experimental result is presented in next section in comparison with that of scattering/interferometry technique.

#### 5.4.4 Measurement of the average cluster size and density

The average cluster size  $a$  and density  $N_c$  in the elongated gas jet can be estimated from Eqs. (5.8) and (5.10) as described in Section 5.3. Figure 5.13(a)-(b) shows the average radius and density of Ar clusters at  $z = 1.53$  mm as a function of pressure at  $T = 297, 245$  K, 193 K, and 153 K. Figure 5.13(c)-(d) shows the temperature-dependent average radius and density of Ar and  $N_2$  clusters in the jet at 400 psi. It shows that cryogenic cooling provides a means to control the average Ar cluster size in the range  $20 \text{ \AA} - 1000 \text{ \AA}$ . The mean  $N_2$  cluster radius, estimated with  $\text{Re}(\varepsilon) = 1.436$ , is always smaller than that of Ar under the same jet conditions because of its lower value of  $k_H$ .<sup>38</sup>

As temperature drops and the cluster size increases, our scattering/interferometry technique begins to go outside its range of validity because the dipole approximation to the scattering cross section [in Eq. (5.7)] is less accurate for  $a/\lambda \geq 0.05$  (or  $ka \geq 0.31$  or  $a \geq 250 \text{ \AA}$  for  $\lambda = 532 \text{ nm}$ ).<sup>39</sup> As a result, the scattering/interferometry results (line with squares) underestimate the average cluster size in the Mie regime ( $a \geq 250 \text{ \AA}$  for  $\lambda = 532 \text{ nm}$ ). Figure 5.13(c) shows the results of both scattering/interferometry and shadowgraphy/interferometry experiments. The shadowgraphy/interferometry technique provides more reliable values for the average cluster size and density in the near-Mie regime because it is relatively unaffected by the transition from Rayleigh to Mie regimes.

For large clusters at low temperatures (133 K ~ 143 K), we performed 90° Mie scattering measurements as a complementary experiment for comparison with the Rayleigh/interferometry results. Here, S and P-polarized probe beams were used and the ratio in scattering yield was measured (S and P refer to polarization along  $z$  and  $y$ , respectively). For  $ka \ll 1$  in the Rayleigh or dipole scattering regime, no scattering is expected into the collection optics with P polarization. In the regime of  $ka \geq 0.3$ , however, there is a measurable Mie scattering. By measuring  $R(ka) = S_P(ka)/S_S(ka)$  where  $S_P$  and  $S_S$  are the 90° scattered energies into the collection optics with P and S incident polarizations, one can determine the average cluster size by comparison to the theoretical plot for  $R(ka)$ .<sup>39</sup> Using a Mie scattering code,<sup>40</sup> we determined average Ar cluster radii of 1170, 1250, 1360 Å at T = 143 K, 138 K, and 133 K, respectively. As shown in Fig. 5.13, the Mie result agrees well with that of shadowgraphy/interferometry technique.

## 5.5 Conclusions

In conclusion, we have developed an all-optical technique to characterize spatial distributions of cluster size and density produced by jet nozzle expansion. The method should give reasonable values for average cluster radius and density for a wide range of cluster size distributions even in the presence of some uncertainty in relative monomer concentration. For laser-cluster interaction experiments, the method has the advantage of using components of the main setup, avoiding complicated additional instrumentation.

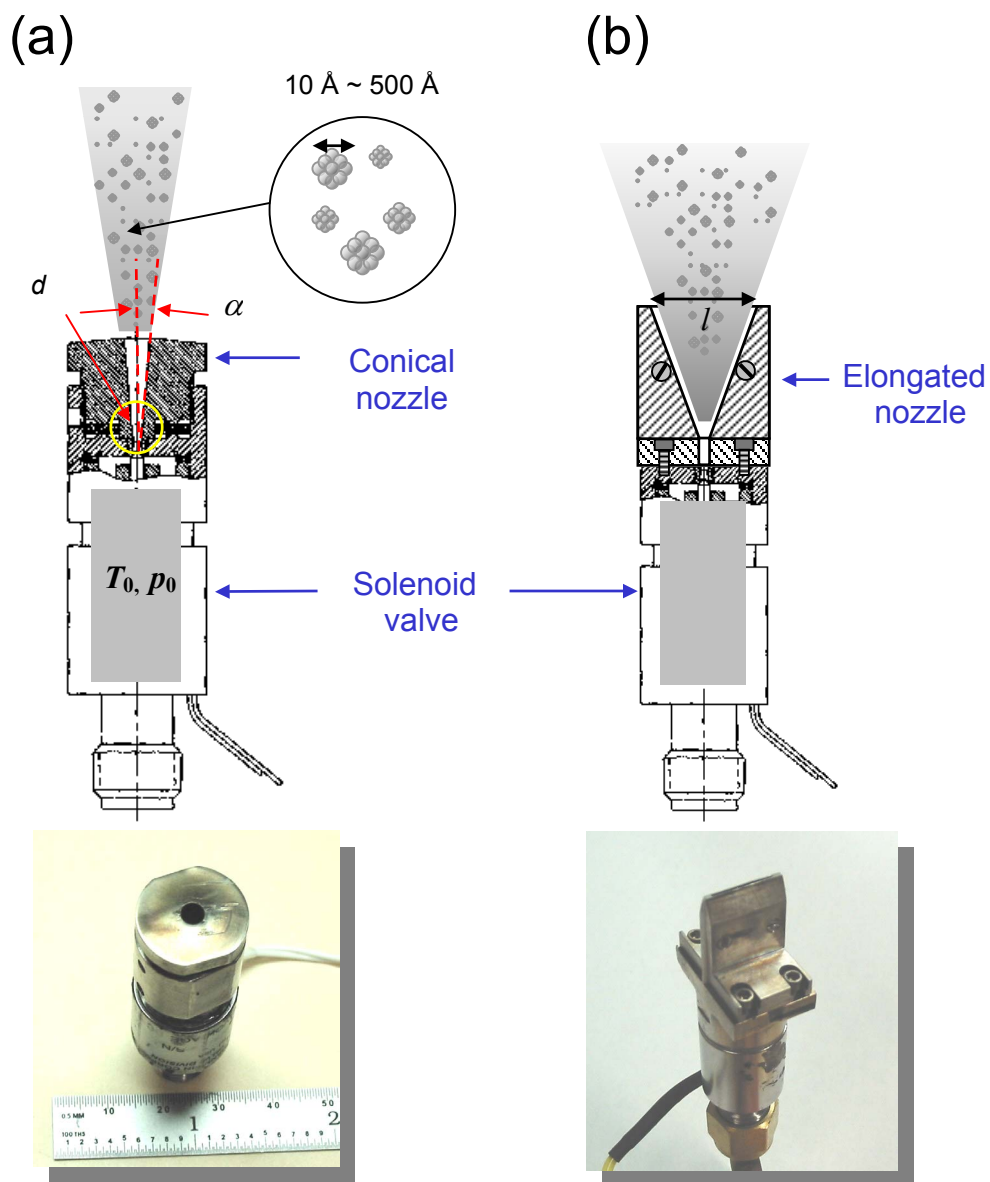


Figure 5.1: (a) Free jet condensation source for clusters consists of a solenoid valve and a supersonic conical nozzle ( $d = 0.5$  mm entrance orifice diameter,  $\alpha = 5^\circ$  expansion half angle, 12.7 mm nozzle length, and 3 mm diameter exit orifice) at a valve backing pressure of  $p_0$  and temperature  $T_0$ . (b) Gas jet with an elongated nozzle ( $l = 11.5$  mm length and 0.4 mm width).

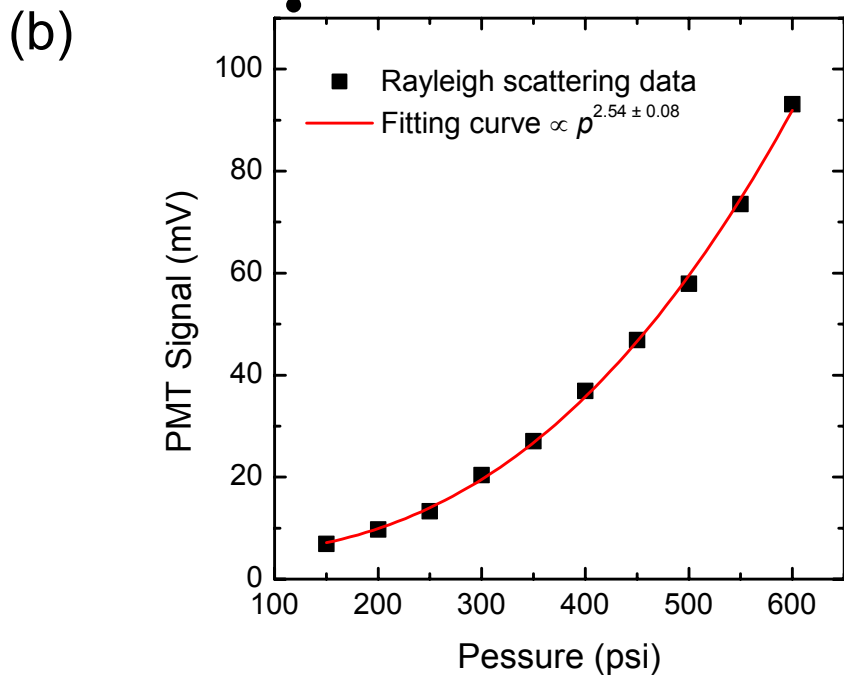
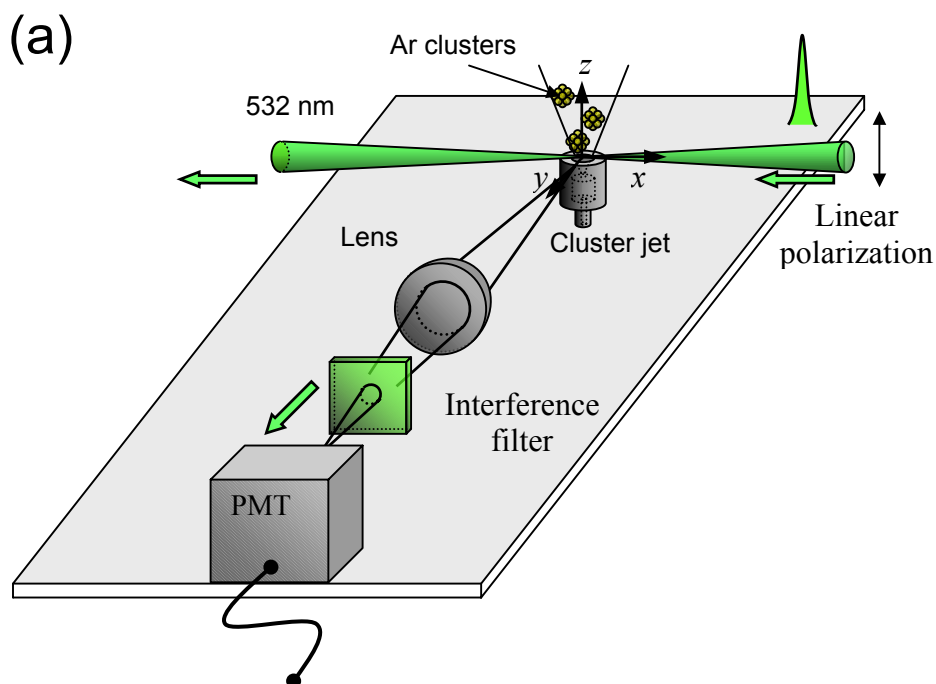


Figure 5.2: (a) Experimental layout for 90° Rayleigh scattering. A probe pulse is weekly focused in the cluster jet and scattered into the collecting lens followed by an interference filter and a photomultiplier tube (PMT). The scattered photon energy is registered by the PMT and plotted in (b) as a function of backing pressure with a polynomial least squares fit (red line).

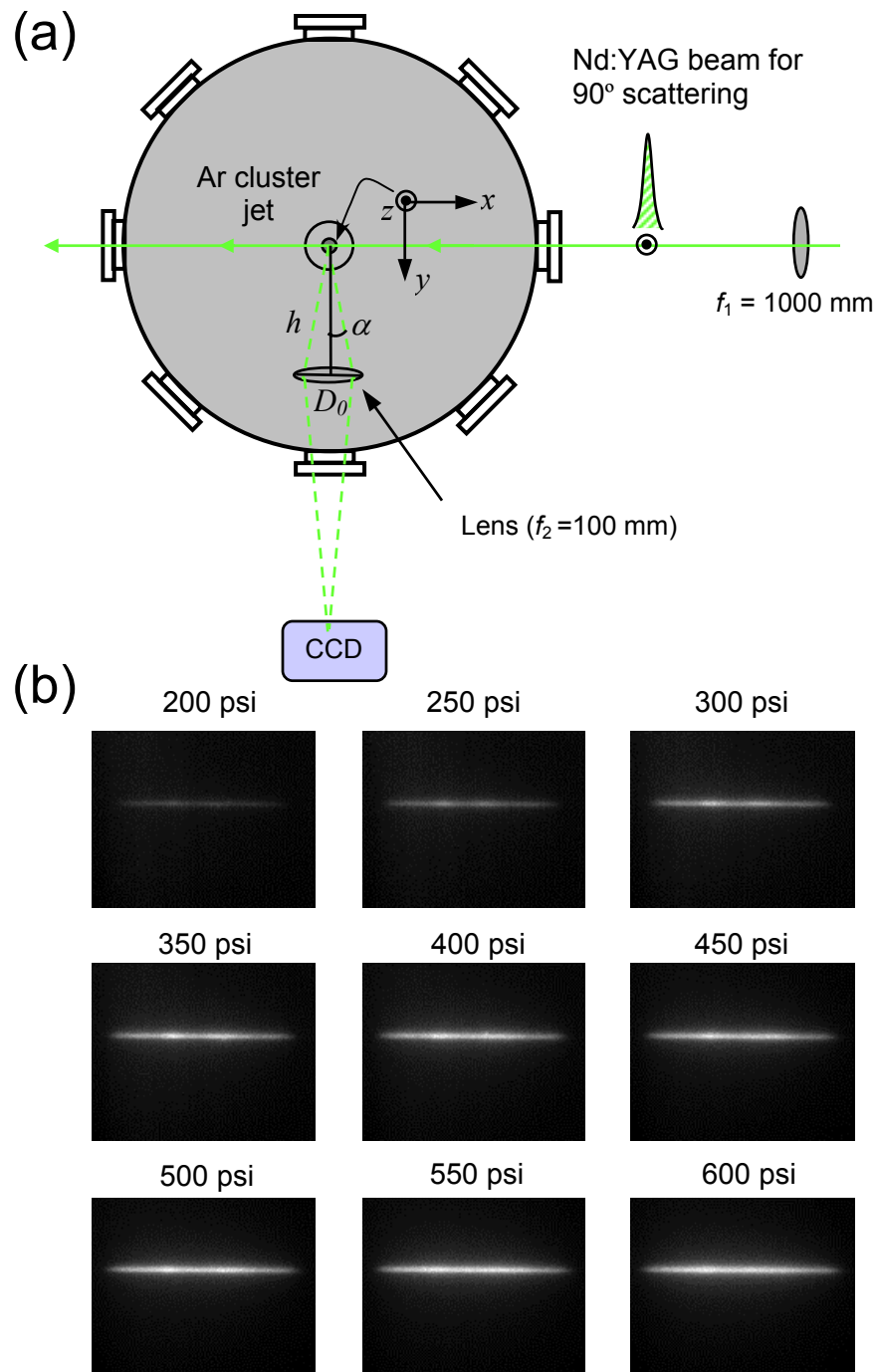


Figure 5.3: (a) 90° Rayleigh scattering experiment. (b) Rayleigh scattering images on the CCD camera at various backing pressures (images are 50-shot averaged).

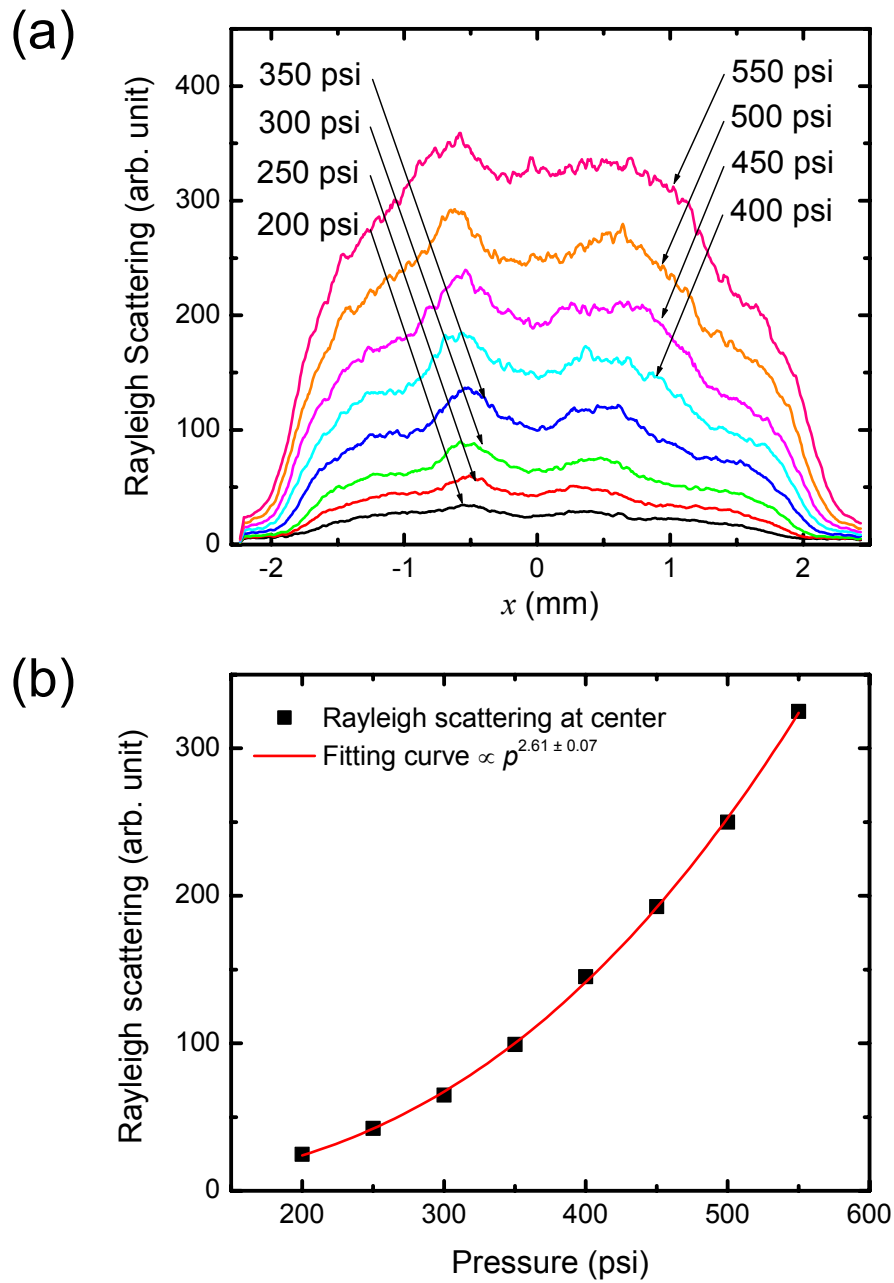


Figure 5.4: (a) 1D Rayleigh scattering profiles at various valve backing pressures for the conical gas jet. (b) On-axis Rayleigh scattering signal versus backing pressure with a polynomial least squares fit.

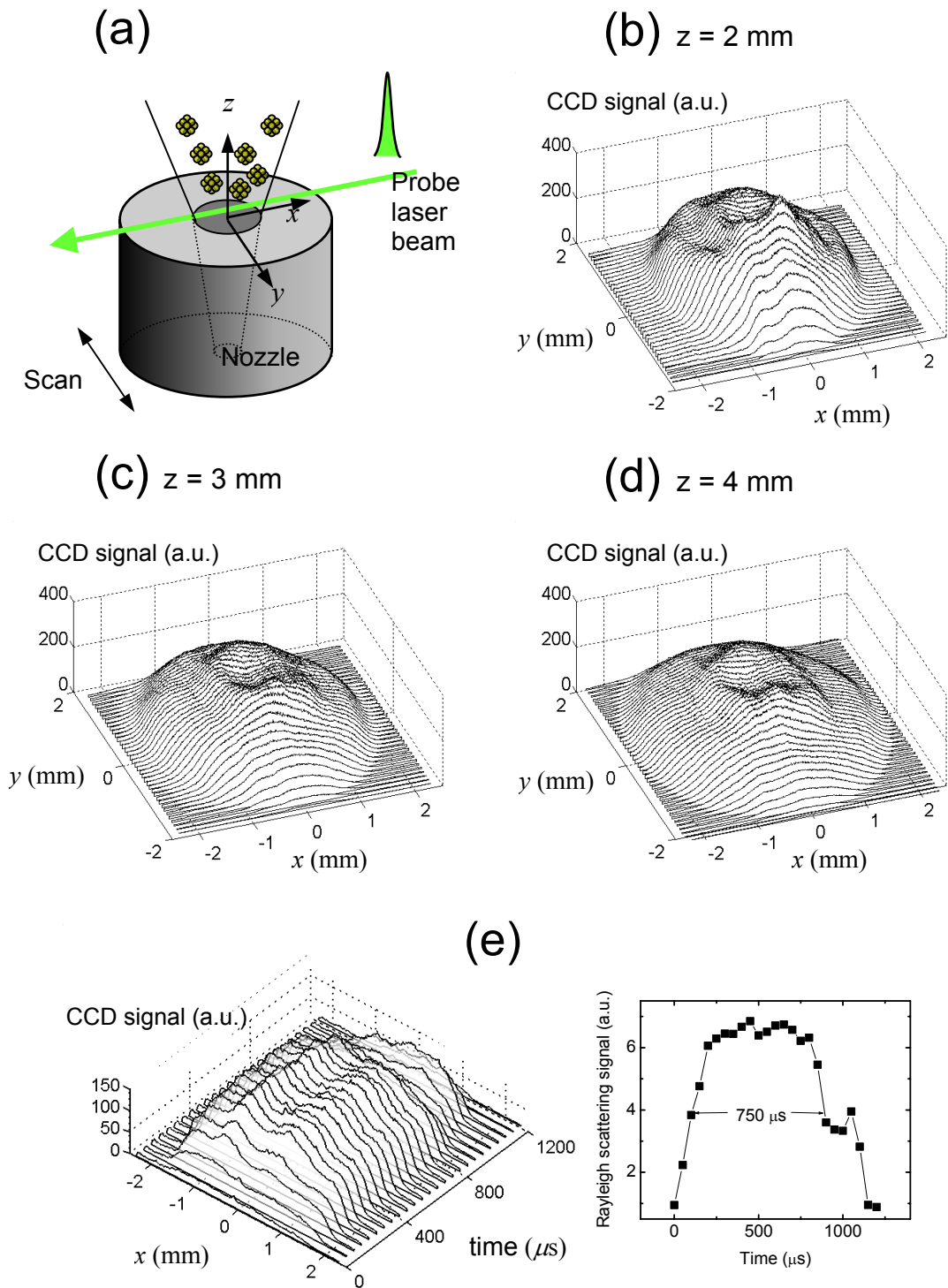


Figure 5.5: 2D Rayleigh scattering imaging profiles at the heights of (b)  $z = 2$  mm, (c) 3 mm, and (d) 4 mm from the nozzle exit orifice obtained by scanning the cluster jet with respect to the probe beam as shown in (a). One line represents one scan position. (e) 1D spatial and temporal Rayleigh scattering profiles at  $z = 2$  mm height from the nozzle.

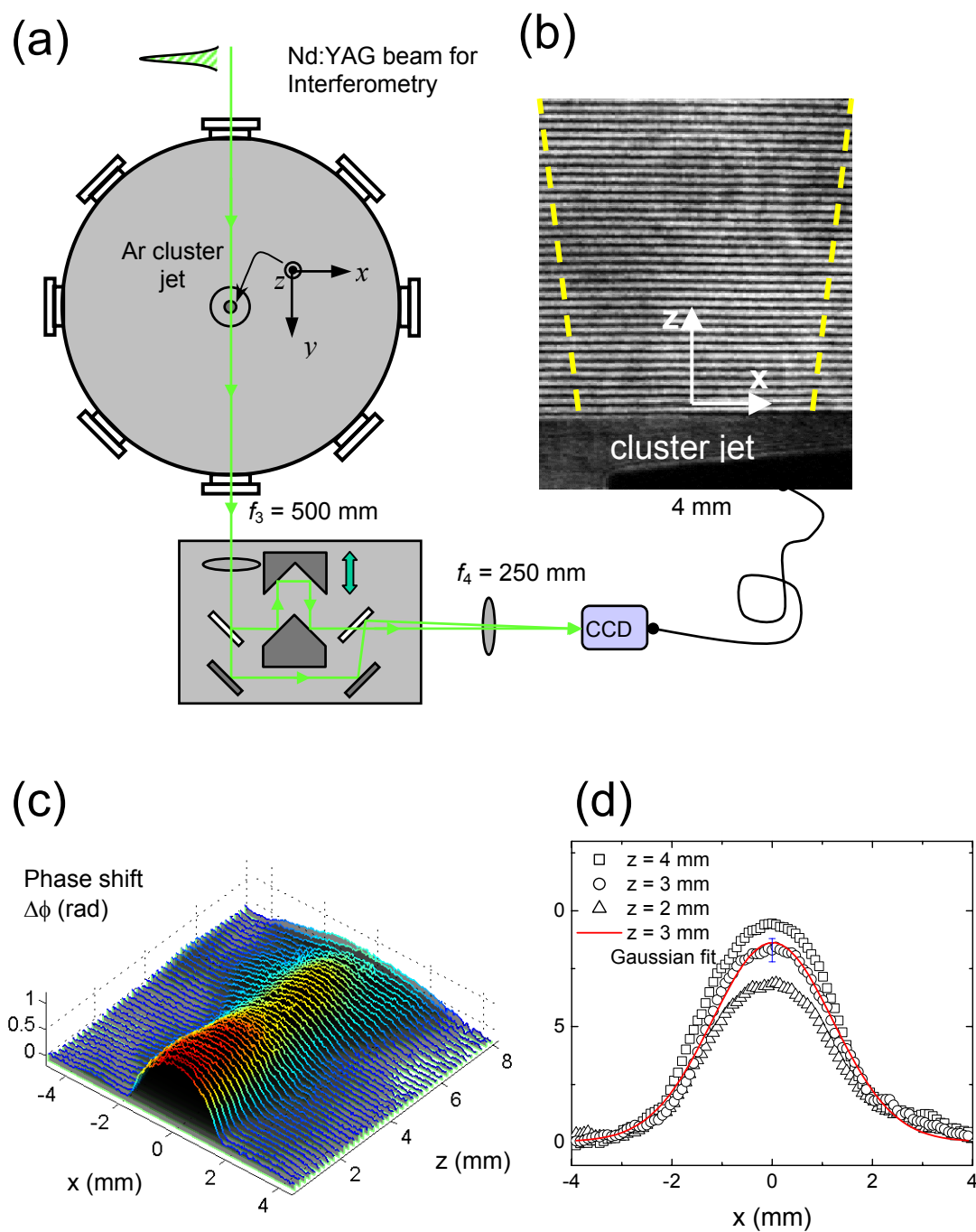
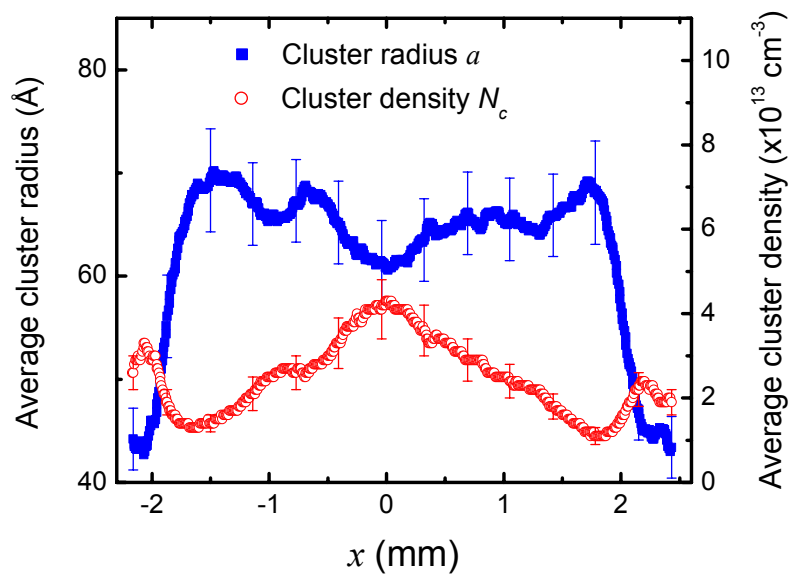


Figure 5.6: (a) Experimental layout for neutral cluster gas interferometry. The frequency-doubled 532 nm Nd:YAG pulse picks up a phase shift in the cluster gas jet as shown in (b) sample interferogram. (c) Extracted phase shift  $\Delta\phi(x, z)$  using FFT method from the raw interferogram. (d) Line-outs  $\Delta\phi(x)$  at  $z = 2$  mm (triangles), 3 mm (circles), and 4 mm (squares). The  $z = 3$  mm points are shown plotted with a Gaussian least squares fit (red line).

(a)



(b)

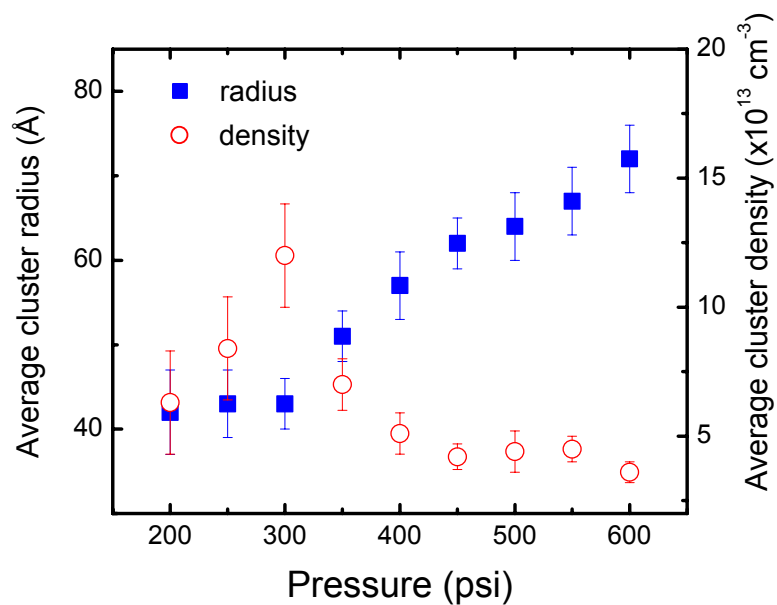


Figure 5.7: The average cluster radius and density across the conical gas jet. (b) On-axis average cluster radius and density as a function of pressure.

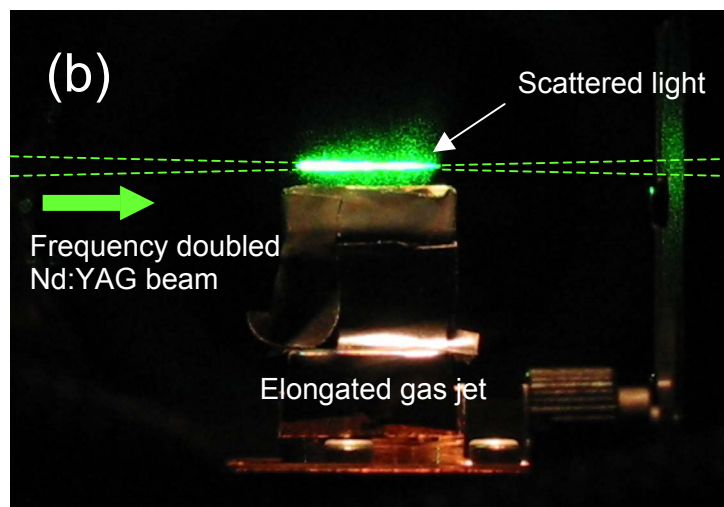
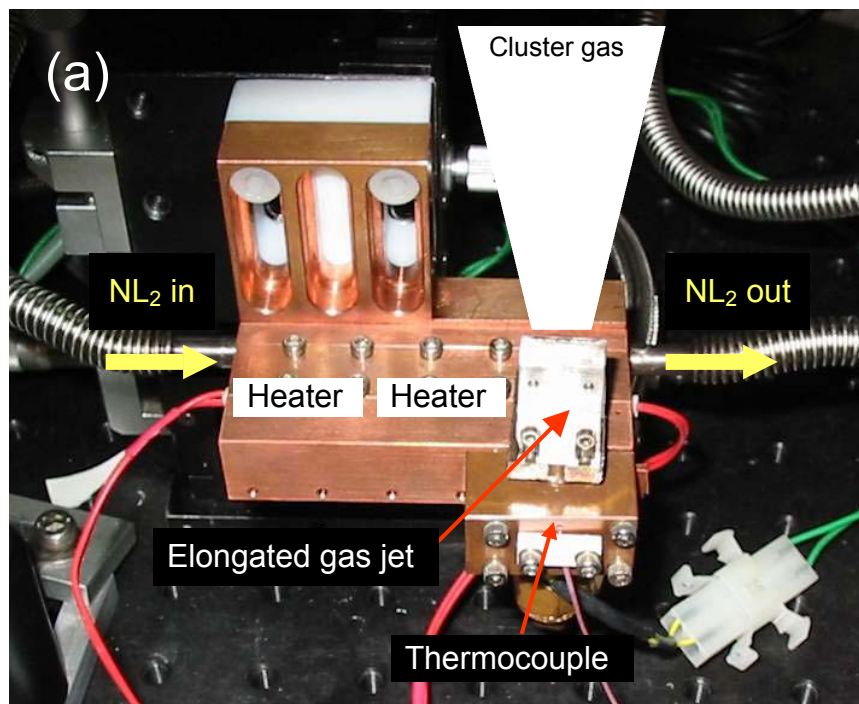


Figure 5.8: (a) Picture of the cryogenic elongated cluster source. The elongated gas jet, coolant tube, and heaters are clamped in the copper cryostat. The whole unit is mounted on a xyz stage inside a vacuum chamber. The cryostat temperature is monitored by a T-type thermocouple and controlled by both LN<sub>2</sub> cooling and solid-state cartridge heating. (b) Photograph of Rayleigh scattering of 532 nm probe pulse in the elongated Ar cluster gas jet at T = 153 K.

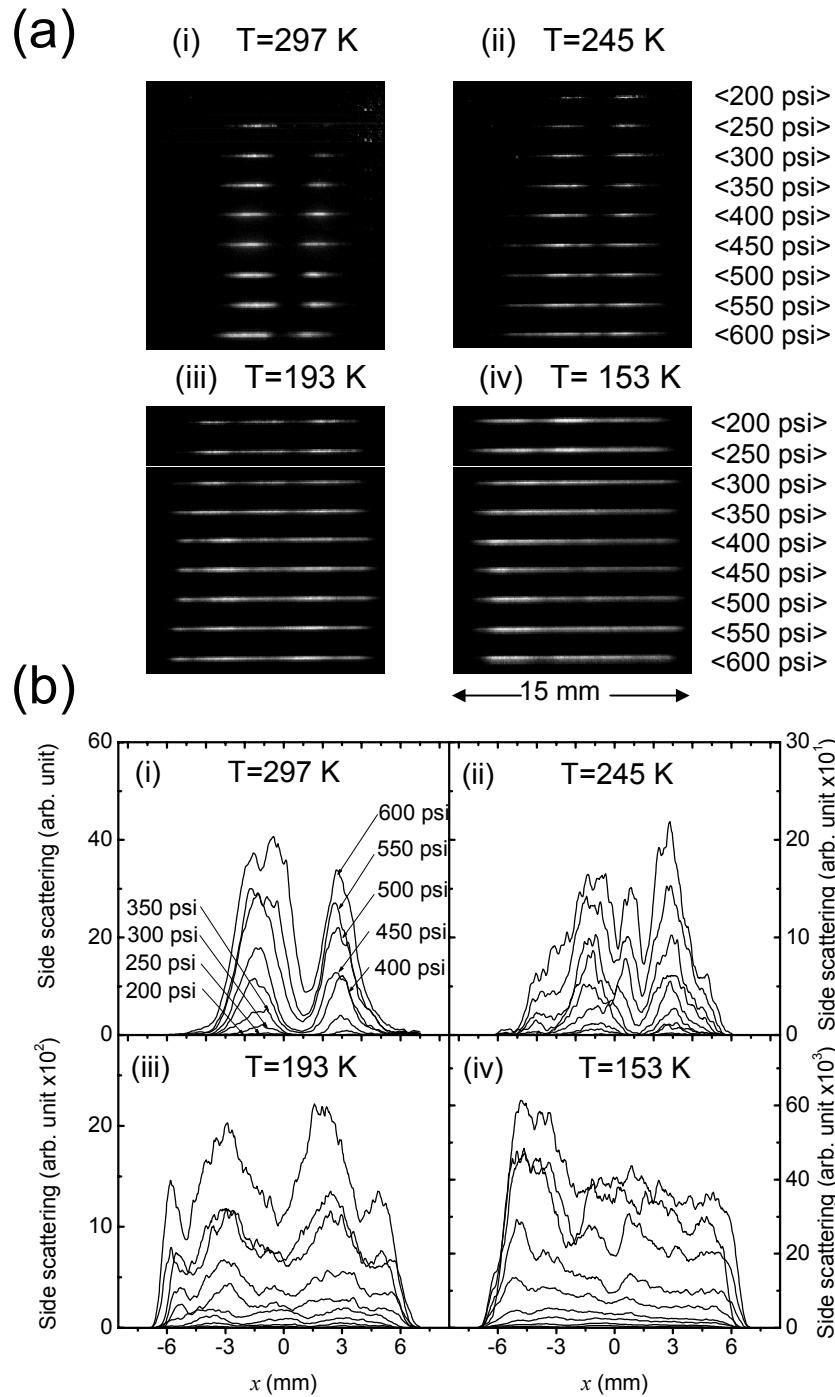
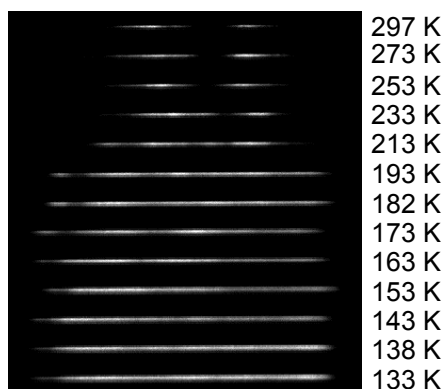
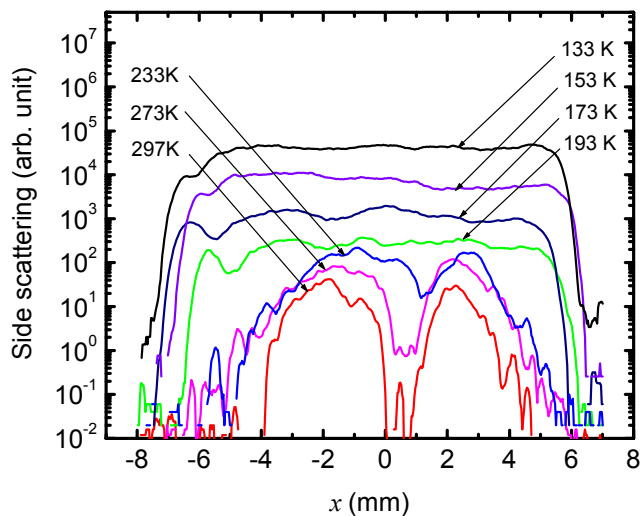


Figure 5.9: (a) Ar cluster Rayleigh scattering images and (b) 1D line-outs at various backing pressures and temperatures [(i) 24 °C, (ii) –28 °C, (iii) –80 °C, and (iv) –120 °C]. In these images, ND filters with calibrated optical densities (OD) were used to avoid CCD pixel saturation.

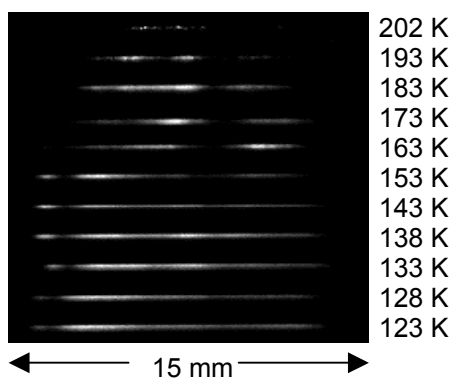
(a) Ar



(b) Ar



(c) N<sub>2</sub>



(d) N<sub>2</sub>

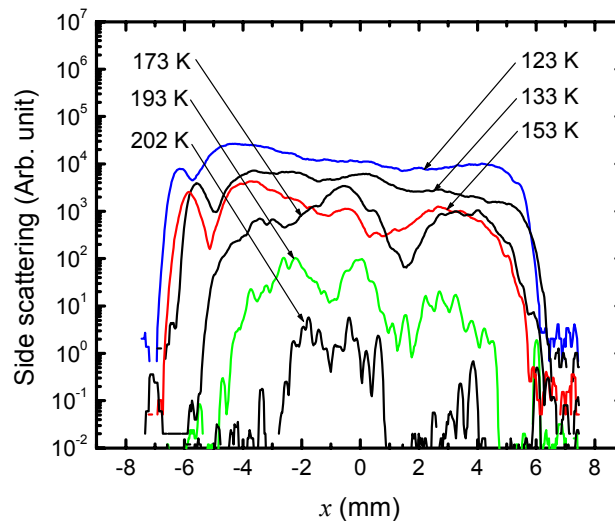


Figure 5.10: (a) Ar cluster Rayleigh scattering images and (b) central line-outs for the spatial distribution of Ar clusters in the elongated gas jet at 400 psi and various temperatures. (c) N<sub>2</sub> cluster Rayleigh scattering images and (d) central line-outs at 400 psi and various temperatures. ND filter transmissions are varied to avoid CCD sensitivity saturation in (a) and (c). For the jet conditions explored, scattering was more uniform from Ar than from N<sub>2</sub> sources.

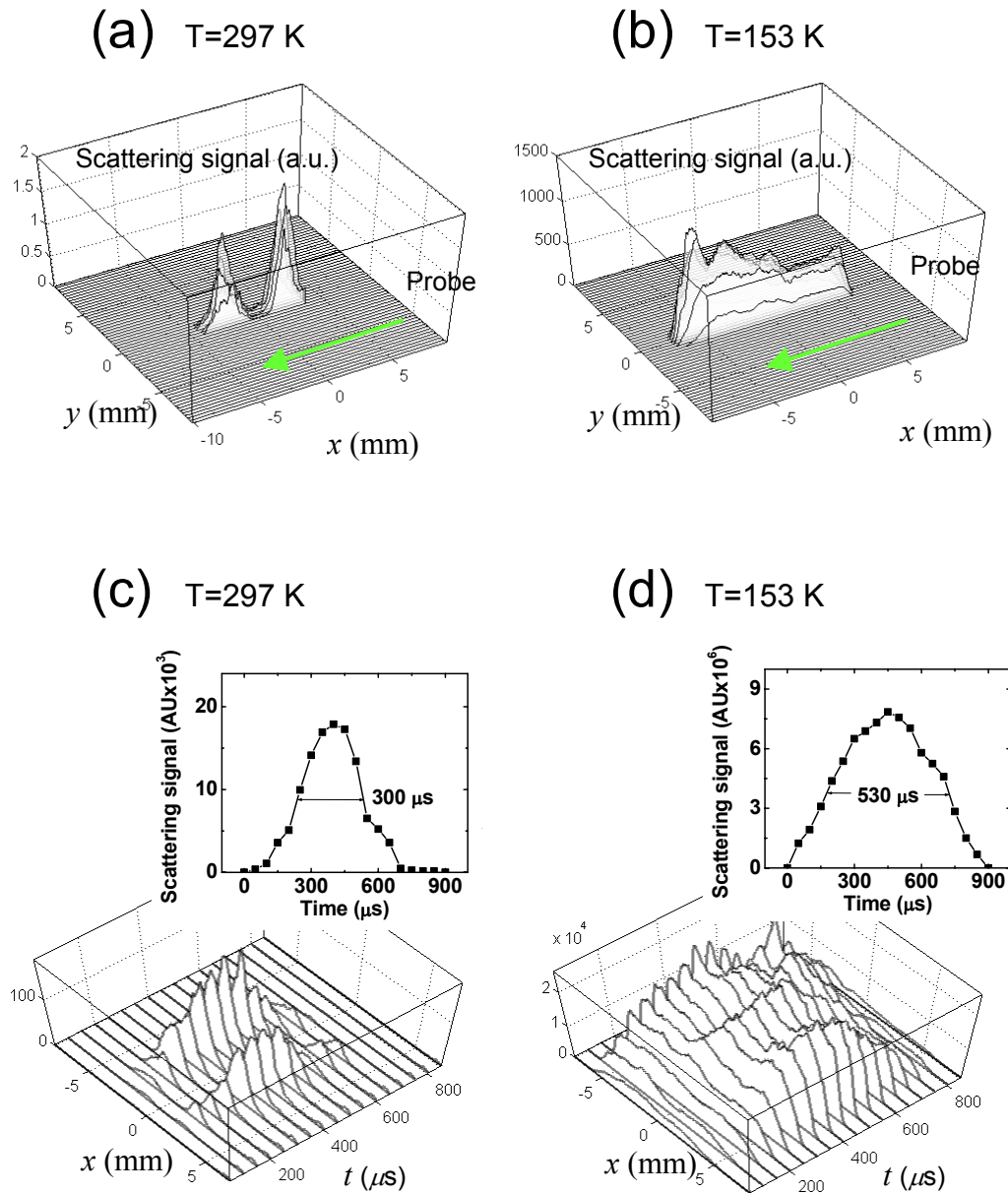


Figure 5.11: 2D Rayleigh scattering spatial profiles of the elongated Ar cluster gas jet at room temperature (T = 297 K) and (b) T = 153 K. 1D Rayleigh scattering profiles of the elongated Ar cluster jet as a function of time at (c) T = 297 K and (d) T = 153 K. The Rayleigh scattering becomes relatively uniform and enhanced by three orders of magnitude at T = 153 K compared to T = 297 K.

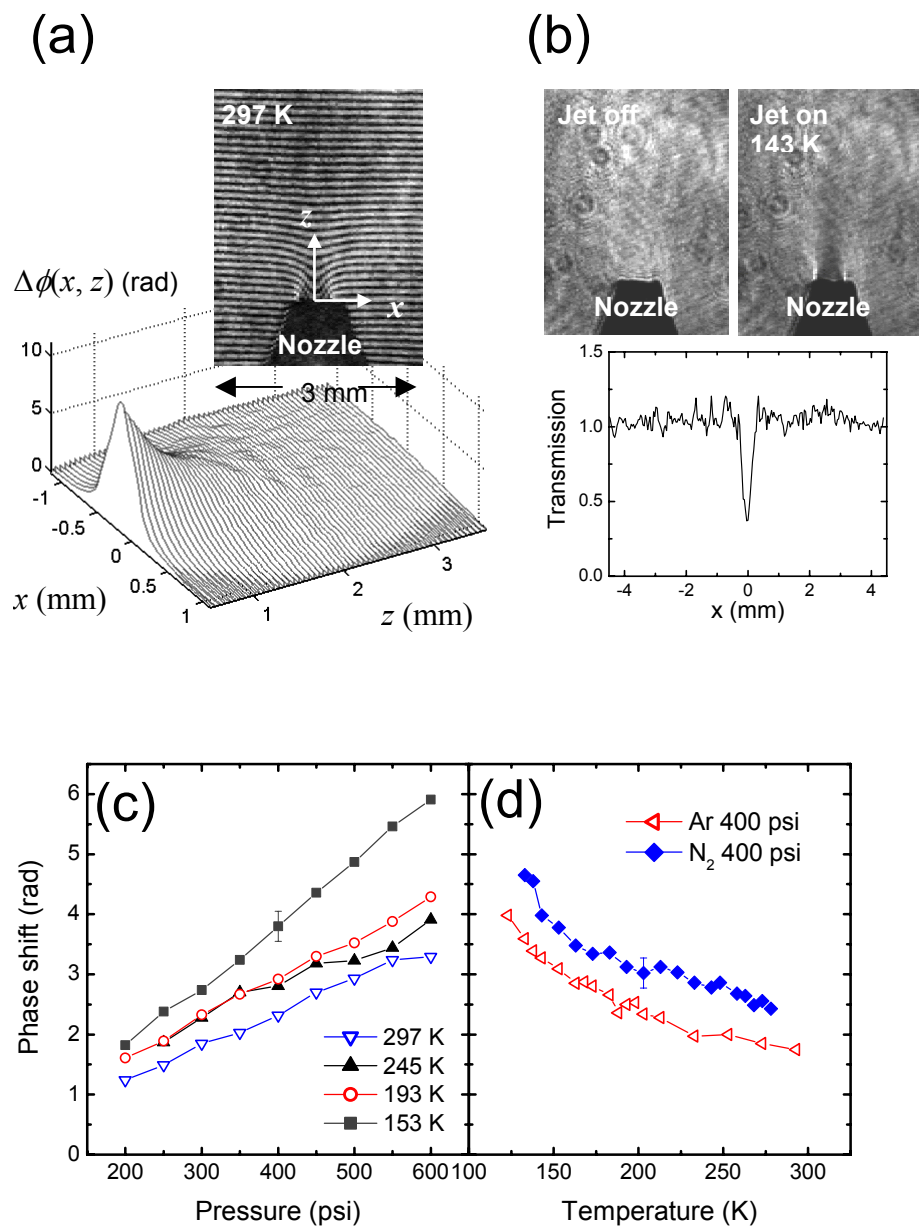


Figure 5.12: (a) Extracted phase profile  $\Delta\phi(x, z)$  from sample interferogram obtained at room temperature. The nozzle is  $90^\circ$  rotated with respect to the probe pulse, and the jet is viewed end-on. (b) Ar cluster nozzle shadowgrams with jet on and off for the measurement of probe intensity attenuation. The probe transmission line-out is shown at  $z = 1.53$  mm. (c)-(d) On-axis ( $x = 0$ ) phase shifts  $\Delta\phi_0$  at  $z = 1.53$  mm at various pressures and temperatures for argon and nitrogen clusters.

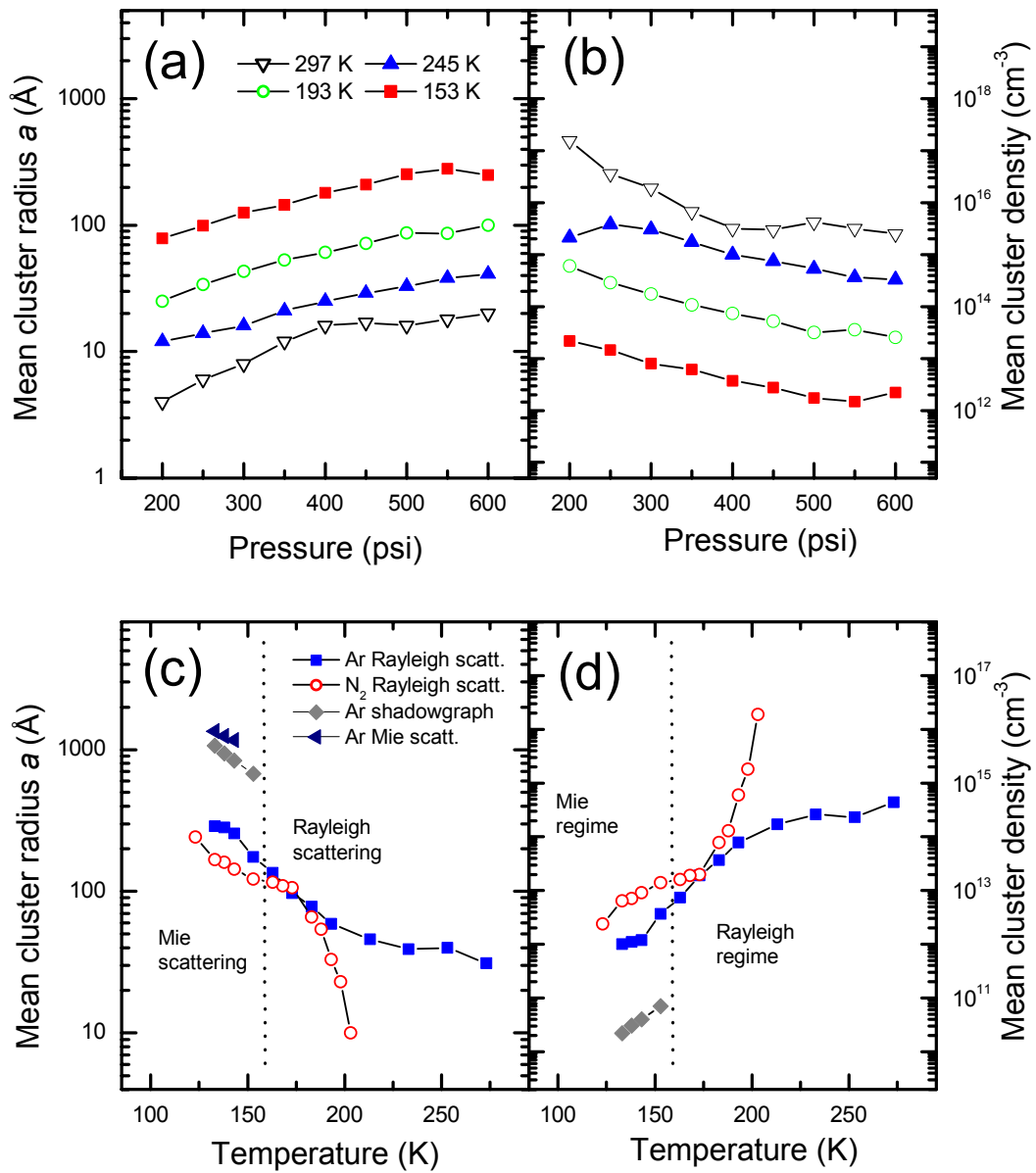


Figure 5.13: Average Ar cluster (a) sizes and (b) densities versus backing pressure at various temperatures  $T=297$  K,  $245$  K,  $193$  K, and  $153$  K at  $z = 1.53$  mm height from the elongated nozzle exit orifice. The temperature dependence of average Ar or  $N_2$  cluster (c) size and (d) density at  $400$  psi backing pressure. The average cluster size is also estimated from shadowgraphy and Mie scattering at low temperatures  $133$  K  $< T < 153$  K.

## Chapter 6: The interaction of intense laser pulses with atomic clusters

### 6.1 Introduction

Intense laser interaction with clusters, van der Waals- bonded agglomerations of up to  $\sim 10^7$  atoms, is of much current interest owing to applications which include the generation of x-rays,<sup>1-6</sup> fast electrons and ions,<sup>7-13</sup> and nuclear particles,<sup>14-17</sup> as well as control of beam propagation<sup>18</sup> and phase matching.<sup>19-21</sup> Although the manner in which a strongly heated cluster explodes in the intense laser field should strongly determine the details of the laser coupling, there is still uncertainty over how this happens.

In prior work, the ultrafast explosion dynamics of intense laser-heated clusters was inferred from the spectroscopic measurements of resulting energetic electrons, ions and extreme ultraviolet (EUV) and x-ray emission. Such measurements, however, cannot reveal the time-resolved evolution dynamics of laser-heated clusters because they are time-integrated. Hence, to reveal a more full picture of the laser-cluster coupling and resulting cluster explosion dynamics, we have developed ultrafast optical diagnostics, capable of measuring, on a femtosecond time scale, the transient evolution of laser-irradiated cluster plasma.

Presented in this chapter is a series of all-optically-diagnosed laser-cluster interaction experiments. We also present a one-dimensional (1D) laser-cluster interaction hydrodynamic model, whose predictions we compare to results of these measurements. The optical diagnostics include (i) time-resolved laser absorption/scattering and (ii) single-shot supercontinuum spectral interferometry (SSSI). The experimental work strongly

supports our laser-cluster interaction scenario in which the laser energy is resonantly absorbed in the critical plasma density layer at  $N_e \sim N_{\text{cr}}$ ,<sup>22</sup> rather than at  $N_e \sim 3N_{\text{cr}}$  predicted by uniform density model.<sup>23, 24</sup> For the cluster sizes of this experiment, the measured picosecond evolution timescale of laser-heated clusters can be understood in terms of plasma hydrodynamics.

## 6.2 1D plasma hydrodynamic laser-cluster interaction model

The assumption of uniform density expansion, described in Chapter 1, results in the near field cluster response

$$\mathbf{p} = \gamma \mathbf{E} = a^3 \left( \frac{\varepsilon - 1}{\varepsilon + 2} \right) \mathbf{E}, \quad (6.1)$$

where  $\mathbf{p}$  is the induced dipole moment of the cluster,  $\mathbf{E}$  is the laser field,  $\gamma$  is the cluster polarizability,  $a$  is the cluster radius (where  $ka \ll 1$ ), and  $\varepsilon = 1 - \xi + i(\nu/\omega)\xi$  is the dielectric function of the plasma internal to the cluster, taken to be of the Drude form. Here  $\xi = (1 + \nu^2/\omega^2)^{-1} N_e/N_{\text{cr}}$ ,  $N_e$  is the electron density,  $N_{\text{cr}} = m\omega^2/4\pi e^2$  is the critical density ( $m$  and  $e$  are the electron mass and charge),  $\nu$  is the collision frequency, and  $\omega = ck$  is the laser frequency. Resonant laser-cluster coupling occurs when  $\varepsilon + 2 = 0$ , or  $N_e/N_{\text{cr}} \sim 3$ . As the cluster expands at the sound speed  $c_s$ , the duration of the resonance is  $\delta t_{\text{res}} \approx$

$$\frac{2}{3} \frac{\nu}{\omega} \left( \frac{N_{e0}}{3N_{\text{cr}}} \right)^{1/3} \frac{a_0}{c_s} \text{ for initial radius } a_0 \text{ and electron density } N_{e0}.$$
<sup>22</sup> For typical clusters having

$a_0$  up to a few hundred Å,  $\delta t_{\text{res}} < 10$  fs, an interval much shorter than the apparent picosecond time scale for resonance indicated by recent absorption/scattering<sup>25, 26</sup> and x-ray<sup>27, 28</sup> measurements. This discrepancy cannot be explained by allowing for typical

cluster size distributions, which indicates that the uniform density model oversimplifies the laser-cluster interaction.

In this section, a 1D hydrodynamic model of intense laser-cluster interaction, developed by Milchberg,<sup>22</sup> is presented in which the laser field is treated self-consistently. The model solves the electric near field problem,  $\nabla \cdot (\epsilon \mathbf{E}) = 0$ , for a single cluster coupled with 1D radial Lagrangian hydrocode. Here  $\mathbf{E}$  is the self-consistent electric field due to the laser and cluster, and  $\epsilon$  is the space-dependent dielectric function of the cluster material. The near field treatment is valid for  $ka_{\max} \ll 1$ , where  $k$  is the laser wavenumber and  $a_{\max}$  is the expanding plasma-vacuum boundary. This is a good approximation for an initial cluster radius much smaller than the laser wavelength and for times not too late in the cluster expansion (typically  $\sim$  ps).

The dielectric function  $\epsilon$  of the cluster plasma is taken to be of the Drude form  $\epsilon(r) = 1 - \xi(r) + i(\nu(r)/\omega)\xi(r)$ , where  $\xi(r) = (1 + \nu(r)^2/\omega^2)^{-1}N_e(r)/N_{\text{cr}}$ ,  $N_e(r)$  is the electron density. Starting with a neutral cluster at solid density ( $\sim 10^{22}$  atoms  $\text{cm}^{-3}$ ), at each time step, the self-consistent electric field is solved from  $\nabla \cdot (\epsilon \mathbf{E}) = 0$  using the neutral, electron, and ion density profiles and the electron and ion temperatures from the previous time step. The resulting electric field ionizes and heats the cluster plasma, generating new electron/ion temperature and density profiles in the next time step and advancing the hydrodynamic evolution. These profiles, in turn, are used to solve  $\nabla \cdot (\epsilon \mathbf{E}) = 0$  for the  $\mathbf{E}$ -field at the next time step. The process, illustrated in Fig. 6.1(a), is repeated with a variable time step  $\Delta t$  (determined internally by numerical stability requirements) until the desired temporal window of “observation” ends. The calculation includes field<sup>29</sup> and collisional ionizations, collisional heating and thermal conduction, either gradient-based or with the flux limit.<sup>30</sup>

The dynamics also includes ponderomotive forces. An ideal gas equation is used for the equation of state, which is a reasonable assumption for these laser-produced cluster plasmas, especially at high temperature.

In the near-field limit, the electric field in the vicinity of a cluster is inherently two-dimensional (2D)  $\mathbf{E}(r, \theta)$ .<sup>22</sup> It is simplified to 1D (in radius) in this hydrocode. For an incident (external) laser electric field  $\mathbf{E}_L(t) = E_L(t)\hat{\mathbf{z}}$ , where  $\hat{\mathbf{z}}$  is the polarization unit vector, the code solves for the self-consistent scalar potential in spherical coordinates  $\Phi(\mathbf{r}, t) = u(r, t) \cos\theta$  inside and outside the cluster, giving the electric field  $\mathbf{E}(\mathbf{r}, t) = -\nabla\Phi(\mathbf{r}, t)$  [see Fig. 6.1(b)]. As the hydrodynamic variables are constrained to depend only on radius, we calculate the field's effect on the cluster via ionization, heating and ponderomotive forces by using an effective field  $E_{\text{eff}}(r) = \langle \mathbf{E} \cdot \mathbf{E}^* \rangle^{1/2}$ , where the angle brackets represent an average over solid angle.

The cluster polarizability  $\gamma$  can be also calculated by our laser-cluster interaction code. Determination of  $\gamma$  is made by superimposing a very long and weak probe pulse on the much faster cluster dynamics and calculating the resulting self-consistent scalar potential  $\Phi_{\text{probe}}(\mathbf{r}, t)$ , which is then matched at  $r > a_{\text{max}}$  to the known analytic solution outside the cluster  $\Phi_{\text{probe, out}}(\mathbf{r}, t) = \mathbf{r} \cdot \mathbf{E}_{\text{probe}}(t) + \mathbf{r} \cdot \mathbf{p}/r^3$ , where  $\mathbf{p} = \gamma \mathbf{E}_{\text{probe}}$  is the induced dipole moment of the cluster.

As an example of a 1D hydrocode simulation, we simulate the interaction of a 800 nm, 80 fs (FWHM), linearly-polarized laser pulse of  $10^{15}$  W/cm<sup>2</sup> peak intensity with an argon cluster of 300 Å radius and  $2.15 \times 10^{22}$  cm<sup>-3</sup> internal atomic density (from Table 5.1). The temporal pulse shape is Gaussian, with the pulse turning on at 1% peak power level at  $t = 0$ . In Figs. 6.2(a) and (b), we plot the electron density and the corresponding

electric field profiles for several times during the heating pulse. The average degree of ionization as a function of radius is also plotted in the inset of Fig. 6.2(a). The electron density rapidly reaches 10 times the critical density  $N_{\text{cr}} = 1.75 \times 10^{21} \text{ cm}^{-3}$  at 800 nm as fast as  $t \ll 60$  fs, forming a super-critical plasma ball with a dominant charge state of  $\text{Ar}^{1+}$ . This is due to ultrafast optical field ionization  $\text{Ar} \rightarrow \text{Ar}^{1+}$ . Once a sufficient density of electrons is generated by optical-field ionization, these electrons can effectively seed collisional avalanche ionization (from inelastic electron-atom and electron-ion collisions). As shown in the plot, the electron density substantially increases with time, ultimately producing  $\sim 3 \times 10^{23} \text{ cm}^{-3}$  electron density and  $\text{Ar}^{10+}$  ion state near the peak of the driving pulse at  $t = 400$  fs. In parallel, the cluster plasma radially expands due to the hydrodynamic pressure of the laser-heated electrons. As shown in Fig. 6.2(a), in general, the electron density profiles exhibit a nonuniform expansion, in contrast to the “uniform plasma model”. The ion density, also computed with the code, displayed the evolution profiles similar to the electron ones. This nonuniform plasma expansion is a natural consequence of the rapid evolution of a hot fluid. An interesting phenomenon, a mass compression of the electron and ion densities, occurs due to the “rocket effect” driven by the ablative pressure of the expanding plasma.

Figure 6.2(b) shows the corresponding electric field  $E(r, t)$  which is normalized to its magnitude in vacuum  $E_0(t)$  at each time. The electric field is significantly enhanced near the critical density layer  $N_e \sim N_{\text{cr}}$  during the entire pulse duration. The persistent resonance in the critical density surface at  $N_{\text{cr}}$  plays a dominant role in the laser energy coupling in the clusters. At very early times ( $t = 2$  fs) before plasma is formed, the field scaled relative to the vacuum value is less than unity, which is expected from dielectric

shielding where  $E/E_0 = 3/(\varepsilon + 2)$  and  $\varepsilon > 1$ .<sup>31</sup> Once plasma develops ( $t > 2$  fs), the electric field in the cluster core is significantly reduced with respect to the vacuum value, due to the supercritical plasma shielding where  $N_e > N_{\text{cr}}$ .

The transient real and imaginary polarizabilities of the exploding cluster are simulated for an initial 300 Å radius Ar cluster under the irradiation of a 80 fs laser pulse with  $10^{15}$  W/cm<sup>2</sup> peak intensity. Figure 6.3(a) and (b) show the results of the simulation. The real polarizability  $\text{Re}(\gamma) \equiv \gamma_r$  is positive for several hundred femtoseconds, and then goes negative and saturates at a constant negative value. The noise in the curve at long times is from the numerical instability. In general, the cluster dipole moment can be viewed as the integral of a dipole density over the cluster volume. That is,

$$\text{Re}(\mathbf{p}) = \gamma_r \mathbf{E}_L = -\frac{1}{4\pi} \int_V d^3r \xi \mathbf{E}_{\text{int}}, \quad (6.2)$$

where  $\mathbf{E}_{\text{int}}$  is the self-consistent field internal to the cluster, and  $-\xi \mathbf{E}_{\text{int}} / 4\pi$  is the dipole moment density. The real polarizability  $\gamma_r > 0$  when the integral is dominated by regions where  $N_e > N_{\text{cr}}$ , or equivalently  $-\xi \mathbf{E}_{\text{int}} \cdot \mathbf{E}_L / 4\pi > 0$ , so the material is locally polarized so as to oppose the external field. However, as the plasma expands, and more underdense plasma layers develop, the polarizability  $\gamma_r$  becomes negative if the response of subcritical ( $N_e < N_{\text{cr}}$ ) density layers dominates the integral. As the expansion continues, the response eventually relaxes to that of a sum of individual electrons, or a subcritical bulk plasma, as shown in Fig. 6.3(a). The imaginary polarizability in Fig. 6.3(b) explicitly shows the existence of the long-lived resonance absorption in a laser-heated cluster, lasting longer than a picosecond for these particular conditions. The code result also shows that a very brief  $3N_{\text{cr}}$  resonance absorption occurs early in the laser pulse when the electron density

remains relatively uniform prior to cluster expansion, and the entire electrons respond to the driving laser field at  $N_e \sim 3N_{\text{cr}}$ .

One of the limitations of the hydrocode is that it cannot take into account hot electrons that are generated in the laser-plasma interaction, such as the plasma wave breaking driven by the enhanced electric field at the critical density layer where the resonance absorption process occurs. In addition, the code is a 1D simulation, which cannot treat any possible asymmetric laser-cluster interactions for a given laser beam direction.<sup>12</sup> Nevertheless, our 1D hydrocode provides physical insight for the laser-cluster coupling dynamics, where most of characteristic features were confirmed with a recently developed 3D particle-in-cell (PIC) simulation.<sup>32</sup>

### 6.3 Scattering by laser-heated clusters

As a laser pulse interacts with clusters, light is absorbed and scattered in response to the time-varying cluster polarizability. Hence, a natural approach is to use absorption and scattering as a diagnostic to study the ultrafast laser-cluster coupling and the subsequent cluster explosion dynamics. In the near field limit, the laser power scattered by a cluster is proportional to  $|\mathbf{p}(t)|^2$ , where  $\mathbf{p}(t) = \chi(t)\mathbf{E}(t)$  is the pump-induced cluster dipole moment,  $\mathbf{E}(t)$  is the laser field, and  $\chi(t)$  is the transient cluster polarizability. For an ensemble of clusters with a random spatial distribution, the dependence of the side-scattering versus pump-probe delay follows the evolution of  $\overline{|\gamma(t)|^2} \propto \sum_j |\gamma_j(t)|^2$ , a sum over clusters in the observation volume, where cross terms in the sum have been neglected. We note that an interesting complication is that Rayleigh side scattering can be partially

coherent because  $N_c \lambda^3 < 1$  where  $N_c$  is the number of clusters per unit volume. Therefore, the measurement of side scattering yields provides information on the cluster polarizability evolution in intense laser fields.

### 6.3.1 Rayleigh scattering by laser-heated clusters

The experimental layout for Rayleigh scattering imaging of an intense laser pulse is schematically shown in Fig. 6.4(a). At a repetition rate of 10 Hz, 1.5-mJ 798-nm linearly polarized Ti:sapphire laser pulses with pulse duration in the range of 80 fs  $\sim$  1.45 ps were focused onto the conical cluster gas jet, described in Chapter 5, by a 150 mm (nominal) focal length BK 7 lens at  $f/20$ . The conical jet produces argon clusters of 180 Å  $\sim$  350 Å, expected from Hagena's scaling law,<sup>33,34</sup> at the backing pressures of 200 – 500 psi. The laser pulses, with peak intensity in the range of  $10^{14} - 10^{15}$  W/cm<sup>2</sup>, were substantially absorbed by the clusters, rapidly creating nano-cluster plasmas. Simultaneously, laser energy was scattered (Rayleigh scattering) during the interaction. Part of the scattered light was first collected by a  $f_1 = 250$  mm focal length lens (L1), located  $f_1$  distance away from the gas jet. Then the collected light was imaged to a CCD camera through an additional  $f_2 = 420$  mm lens (L2), placed  $f_1 + f_2$  distance from the first collecting lens. A sample 2D Rayleigh scattering image is shown in the inset of Fig. 6.4(a). The radiation detected was mostly from Rayleigh scattering, not from plasma recombination. This was confirmed with the measurement of the scattering spectrum and angular distribution.

The scattering angular distribution was measured by rotating the laser polarization using a  $\lambda/2$  wave plate [see Fig. 6.4(a)]. Plotted in Fig. 6.4(b), the scattering pattern and its  $\sin^2 \theta$  least squares fit confirm dipole scattering in the Rayleigh regime where  $ka < 1$ .

Typical 2D scattering images are also included in Fig. 6.4, exhibiting the strong angle-dependent Rayleigh scattering yield. There is, however, minor disagreement between the experimental data and the fit curve at  $\theta < 20^\circ$ ,  $80^\circ < \theta < 100^\circ$ , and  $\theta < 160^\circ$  because of the relatively poor angle resolved measurement with a half collection angle of  $\alpha = 6^\circ$  and the possible contribution of multiple scattering.

It is quite notable that all scattering images exhibit an interesting filamentary structure, reminiscent of feathers or fish bones. This kind of scattering pattern has been observed by many other research groups in their laser-gas jet experiments,<sup>35-37</sup> without comment. It is believed, at least in the case of clusters, that local cluster density fluctuations give rise to an interference pattern for the scattered light, and this ultimately produces strong angle-dependent intensity modulations, which manifest themselves as filaments in the scattering images. We are currently performing scattering calculation to test this idea.

### **6.3.2 The effect of laser prepulse**

Rayleigh scattering imaging is also quite useful for the diagnosis of laser prepulse effects in laser-cluster interactions. Typically, a laser prepulse plays a crucial role in intense laser matter interactions because, even with a moderate contrast ratio of  $10^4$ . For a  $10^{18}$  W/cm<sup>2</sup> pulse, the prepulse intensity easily reaches  $10^{14}$  W/cm<sup>2</sup>, enough to generate a hot preplasma from solid targets. In case of high intensity laser-cluster interaction, a prepulse can pre-ionize and pre-heat clusters, forming an expanding cluster plasma before the main pulse arrives. Consequently, the main pulse interacts only with a low density plasma or a weakly ionized atomic gas instead of neutral clusters. For example, with the

presence of  $10^{13} - 10^{15}$  W/cm<sup>2</sup> prepulses, dramatically suppressed x-ray signals were reported.<sup>23, 38</sup>

As a prepulse diagnostic in our laser-cluster experiment, 90° Rayleigh scattering was performed, as shown in Fig. 6.4(a). A photograph of the laser-irradiated cluster gas jet is shown in Figure 6.5(a), which also shows the main and pre-pulse. In this experiment, the prepulse contrast ratio was adjusted by detuning the triggering time to the internal [regenerative amplifier (RGA)] and external Pockels cells, allowing the variation of the prepulse leakage rate out of the RGA in our Ti:sapphire laser system (see Chapter 3 for details). Such prepulses arrive 16 ns in advance of the main pulse, with a contrast ratio of main to pre-pulse amplitude of  $10^2 \sim 10^4$ . This contrast ratio was monitored with a fast silicon PIN photodiode and an oscilloscope. The main pulse energy was measured to be 26 mJ with a peak intensity of  $2 \times 10^{17}$  W/cm<sup>2</sup>. With a poor pump-probe contrast ratio of  $< 10^3$ , we observed a segmented laser-produced plasma as shown in the inset of Fig. 6.5(a). This is also manifested in the 2D Rayleigh scattering in Fig. 6.5(b), indicating no Rayleigh scattering was present at the center of the laser focal volume. This is attributed to the fact that Ar clusters near the beam waist, where the laser peak intensity is highest, were destroyed by the prepulse, and therefore the Rayleigh scattering from clusters vanished. This is also evident in the interferogram, in Fig. 6.5(b), taken with a transverse probe pulse 1.2 ns after the pump (see Chapter 7 for our transverse interferometry diagnostic). The phase shift in the interferogram caused by the plasma electrons is noticeably reduced near the vacuum focus position compared to the periphery because the prepulse-produced Ar monomers couple much less laser energy and resultantly experience less plasma heating and ionization than when they are in cluster form. However, with a contrast ratio of  $> 10^4$ ,

the Rayleigh scattering and interferogram in Fig. 6.5(c) verify the presence of undestroyed clusters upon the main pulse arrival. This prepulse-free laser operation makes it possible to study the full interaction dynamics of high intensity laser pulses with clusters.

#### **6.4 Time-resolved two-color scattering and absorption experiment**

To investigate the time-varying coupling dynamics, we employed a collinear pump-probe technique for the measurement of scattering and absorption. Here the probe wavelength differs from the pump in order to discriminate it easily with a color filter.

The experimental setup was similar to that in Fig. 6.4(a) except that a short, variably delayed, weak 400 nm probe pulse was employed to perform two-color pump-probe absorption and scattering. The probe was obtained from frequency doubling a 80 fs, 800 nm Ti:sapphire laser pulse in a thin KDP crystal. The pump and probe with a variable delay were collinearly focused in the cluster gas jet at  $\sim f/20$ . The pump was removed from the beam and the probe was imaged onto a CCD camera. To reduce the measurement uncertainty associated with the shot-to-shot laser energy fluctuations, a reference pulse, obtained by splitting  $\sim 50\%$  of the probe pulse in a Michelson-type beam splitter, was also focused in the cluster target volume, laterally shifted with respect to the probe. Then it was recorded in the same CCD image, as shown in the insets of Fig. 6.6(a). The reference pulse always precedes the pump and does not overlap with the pump in the focal volume. Figure 6.6(a) shows the normalized transmission of probe versus the pump-probe delay  $\tau$ , under the irradiation of a 2.5 mJ ( $I_{\text{peak}} \sim 3 \times 10^{15}$  W/cm<sup>2</sup>) pump pulse in a gas of 180 Å (estimated at 200 psi using Hagena's scaling law) Ar clusters. The plot explicitly shows the

picosecond time scale for the resonant laser coupling for this cluster size, in agreement with the simulation result shown in Fig. 6.3(b).

The time-resolved scattering yield is plotted in Fig. 6.6(b) for the backing pressures of 200 and 400 psi (average radii 200 Å and 350 Å estimated from Hagena). The scattered 400 nm probe light was detected with a spectrally filtered (390 nm  $\pm$  10 nm) photomultiplier tube (PMT) at 90° to the pump beam direction. We note that the pump pulse alone also generated a second harmonic at 400 nm in the cluster gas target, and this radiation was also scattered by the clusters and registered by the PMT, generating a constant background signal independent of the pump-probe delay  $\tau$ . This background signal was subtracted from the plot in Fig. 6.6(b) to display only the probe scattering signal variations. The plot shows a  $\sim$ 2 ps time scale for resonant scattering, which is consistent with the experimental result for absorption at 200 psi. Although  $\gamma$  is smaller at 400 nm than at 800 nm for a given cluster,<sup>22</sup> both of results of Fig. 6.6(a) and (b) are in qualitative agreement with the variations of  $\gamma$  in Fig. 3(a) and (b).

### **6.5 Measurement of transient complex polarizability of laser-heated clusters**

In this section, we investigate the femtosecond explosion dynamics of intense laser-heated argon clusters by directly measuring the cluster transient complex polarizability with the use of our SSSI technique. We shall show that this SSSI measurement, along with the previous time-resolved absorption and scattering measurements, verifies the main features of our laser-cluster interaction model, in which the laser couples resonantly at the critical density region of the expanding clusters. This implies that clusters explode “layer-by-layer” rather than at uniform density.

### 6.5.1 Experimental setup and results

A schematic of the experimental arrangement is shown in Figure 6.7(a). Moderate energy (1 mJ) 800 nm, 80 fs pump pulses from a 10 Hz Ti:sapphire laser system were focused at  $f/20$  onto the supersonic conical gas jet, described in Chapter 5, backed with high pressure argon gas. The gas jet was operated in the backing pressure range 150 – 400 psi, with a pulse width of 450  $\mu$ s. Cluster size estimates using the Hagena parameter for our nozzle conditions give average argon cluster radii in the range 150 – 300 Å. The peak vacuum laser intensity was  $I_{\text{peak}} \sim 1 \times 10^{15}$  W/cm<sup>2</sup> in a 25  $\mu$ m FWHM focal spot, with a confocal parameter of  $2z_R \sim 3.5$  mm.

Our experiment determines the ensemble average transient polarizability  $\bar{\gamma}$  of the gas of laser-heated argon clusters, which is related to the refractive index  $n$  by  $n = (1 + 4\pi N_c \bar{\gamma})^{1/2} \approx 1 + 2\pi N_c \bar{\gamma}$ , where  $N_c$  is the number of clusters per unit volume. The transient index  $n$  was measured using our single-shot supercontinuum spectral interferometry (SSSI) diagnostic, as described in Chapter 2. Approximately 1 mJ was split from the main Ti:sapphire pulse and was focused in 1 atm air to produce a broad, 150 nm FWHM supercontinuum (SC) extending mainly to the short wavelength side of the pump pulse. After spatial filtering, the  $\sim 0.1$  mJ SC pulse was recollimated and split into equal energy probe and reference pulses. Temporal chirp of the SC to  $\sim 1.5$  ps was imposed on the pulses by a 25.4 mm thick SF4 glass window. The twin chirped SC pulses were recombined with the pump and collinearly focused with it into the interaction region, with the reference pulse leading the pump, and the probe superimposed on it. The SC beam was focused to a  $\sim 170$   $\mu$ m FWHM spot size, overfilling the pump spot. The pump and SC

beams were focused laterally away from the jet center so that the path length through the cluster gas was  $\sim 1$  mm (The central path through the jet was  $\sim 3$  mm). This eliminated the effects of probe beam refraction from the pump-induced index profile. The SC pulses were imaged from the exit of the jet onto the entrance slit of a spectrometer, providing 1D transverse space resolution. A CCD camera in the spectrometer's focal plane recorded the spectral interferogram of the reference and probe pulses, shown in Fig. 6.7(b), from which the time dependent phase shift  $\Delta\phi(x, t)$  and absorption  $A(x, t) = 1 - \exp(-\eta(x, t))$  of the probe pulse were extracted with  $\sim 10$  fs resolution in a temporal window up to 1.5 ps long. Here  $x$  is the transverse dimension ( $x = 0$  is the pump beam axis), and  $\eta$  is the small signal absorption coefficient. Figure 6.7(c) shows a perspective plot of the extracted phase  $\Delta\phi(x, t)$  profiles for the 350 psi case. The refractive indices  $n_r = \text{Re}(n)$  and  $n_i = \text{Im}(n)$  are related by  $\Delta\phi(x, t) = k_{\text{pr}}(n_r(x, t) - 1)L$  and  $\eta(x, t) = k_{\text{pr}}n_i(x, t)L$ , where  $L = 1$  mm is the interaction length through the cluster jet and  $k_{\text{pr}} = 2\pi/\lambda_{\text{pr}}$ , where  $\lambda_{\text{pr}} = 700$  nm is the SC central wavelength.

Figure 6.8(a) and (b) show  $\Delta\phi(x = 0, t)$  and  $\eta(x = 0, t)$  (and  $n_r - 1$  and  $n_i$ ) for a range of backing pressures. The phase shifts  $\Delta\phi$  are all positive for several hundred femtoseconds, and then become negative and saturate at constant negative values. With increasing backing pressure, the zero crossing moves to longer times and the relaxation to saturation occurs on increasing time scales. By contrast, laser ionization of a non-clustering helium gas jet shows purely negative-going phase shifts whose rise times are independent of jet backing pressure, as described in Chapter 4. The peak for each  $\eta$  curve occurs near the zero crossing point for its corresponding  $\Delta\phi$ . The curves for  $\eta$  broaden and the peaks move to longer times with increasing backing pressure. We note that the positive-going

spatial profile for  $\Delta\phi$  at early times shows that ultrafast laser-heated cluster gas can act as an optical self-guiding medium.<sup>18</sup>

### 6.5.2 Interpretation of results

For a pump laser with Gaussian FWHM pulsewidth 80 fs, center wavelength 800 nm, and peak intensity  $10^{15}$  W/cm<sup>2</sup>, Figs. 6.8(c) and (d) show calculation results for  $\text{Re}(\bar{\gamma}) = \bar{\gamma}_r$  and  $\text{Im}(\bar{\gamma}) = \bar{\gamma}_i$ , calculated by performing a weighted average over a 100% FWHM size distribution, for a range of average cluster sizes with atomic density  $\rho = 1.8 \times 10^{22}$  cm<sup>-3</sup>. We first discuss the long time behavior of  $\bar{\gamma}_r$ . At times  $t \gg \bar{a}_0 / c_s$ , the average cluster density profile will become progressively more uniform. Therefore,  $\bar{\gamma}$  predicted by our model and that predicted by the uniform density model<sup>23,24</sup> should converge to  $\bar{\gamma}_i \rightarrow \bar{\gamma}_{i,\text{long}} = 0$  and  $\bar{\gamma}_r \rightarrow \bar{\gamma}_{r,\text{long}} = -\rho \bar{a}_0^3 Z / 3N_{\text{cr}} = \text{const}$ , where  $Z$  is the average ionization state in the expanded plasma, which remains “frozen in” until long after cluster disassembly. The values for  $\bar{\gamma}_{r,\text{long}}$  are overlaid on the simulation results with dashed lines; agreement with the code results is excellent. At times greater than  $\sim 1$  ps, therefore, each cluster contributes an unchanging  $\bar{\gamma}_{r,\text{long}}$  to the overall refractive index. This implies that the refractive index of a gas of exploding clusters can assume the uniform plasma value long before they merge with one another. That is,  $n_r = 1 + 2\pi N_c \bar{\gamma}_{r,\text{long}} = 1 - N_{e,\infty} / 2N_{\text{cr}}$ , where  $N_{e,\infty}$  is the final uniform electron density of the bulk plasma. Transverse interferometry of the plasma from our 350 psi jet using a modified Mach-Zehnder interferometer, described in Chapter 7, gives  $N_{e,\infty} \sim 5 \times 10^{17}$  cm<sup>-3</sup>, giving  $-N_{e,\infty} / 2N_{\text{cr}} = -1.1 \times 10^{-4}$  for  $\lambda_{\text{pr}} = 700$

nm, in good agreement with the long time value of  $(n_r - 1)$  for the 350 psi case in Fig. 6.8(a). Using the code result of  $\bar{\gamma}_{r,\text{long}} \sim -7 \times 10^{-16} \text{ cm}^3$  (for 300 Å clusters) then gives  $N_c \sim 3 \times 10^{10} \text{ clusters/cm}^3$ . For 300 Å clusters, this corresponds to an average  $\sim 6 \times 10^{16} \text{ atoms/cm}^3$ , which is consistent with our measured  $N_{e,\infty}$  for  $Z \sim 10$ , which is itself consistent with previous EUV spectroscopy of argon clusters.<sup>27,28</sup> We note that peak values of  $\bar{\gamma}$  predicted by our model, and verified here, are  $\sim 100$  times smaller than in the uniform density model for similar clusters.<sup>22-24</sup> This has a major effect on propagation<sup>18</sup> and on cluster heating, where the power coupled to a cluster is proportional to  $\text{Im}(\gamma)|\mathbf{E}_L|^2$ .<sup>22</sup>

The crossover of  $\gamma_r$  from positive to negative values was expected from our hydrodynamic laser-cluster simulation result for single cluster polarizability, shown in Fig. 6.3(a). The real polarizability  $\gamma_r > 0$  when the integral in Eq. (6.2) is dominated by overdense or supercritical plasma layers ( $N_e > N_{\text{cr}}$ ). In the opposite limit of  $\gamma_r < 0$ , the subcritical  $N_e < N_{\text{cr}}$  response dominates the integral. The response eventually relaxes to that of a sum of individual electrons, or a subcritical bulk plasma ( $\gamma_r \rightarrow \gamma_{r,\text{long}}$ ). For larger clusters, the crossover occurs at longer times because there are more cluster “layers” to blow off toward subcritical density. The increase of  $\gamma_i$  over a few hundred femtoseconds corresponds to the evolution of the critical density layer on the cluster, and its decrease to zero at longer times occurs as the cluster average density drops below critical and continues lower.

The calculation reproduces the main features of the experimental results shown in Fig. 6.8(a). For larger clusters, the zero crossing of  $\bar{\gamma}_r$  ( $n_r - 1$ ) takes place at longer times and relaxation to the bulk response is slower. The peaks of  $\bar{\gamma}_i$  ( $n_i$ ) take place at longer

times and the widths increase. The main difference between the experiment and calculation is that the calculation underestimates (by  $\sim 2\times$ ) the ratio of peak positive to negative excursion of  $\bar{\gamma}_r$ . This may be related to an overestimation of the early time shielding of the laser field by the cluster plasma or to limitations of the 1D model. A full 3D model, however, would still show resonant coupling at the critical density region and the intra-cluster competition between the above critical and below critical density responses. It is that competition which is revealed by the experiment and which tells us how the cluster explodes.

## 6.6 Conclusions

The interaction of intense laser pulses with van der Waals-bonded clusters was measured using our ultrafast optical diagnostics: time-resolved laser absorption/scattering and single-shot supercontinuum spectral interferometry (SSSI). These diagnostics measured a subpicosecond time-scale for the onset of strong laser-cluster coupling and relaxation times of several picoseconds for cluster disassembly. This is for nano-scale clusters  $< 50$  nm under the irradiation of sub-picosecond (80 fs  $\sim$  1.5 ps) high intensity ( $>10^{15}$  W/cm<sup>2</sup>) laser pulses. In particular, the SSSI diagnostic has provided a picture of the evolution dynamics of intense laser-heated cluster plasma. It showed that the time evolution of the polarizability is characteristic of competition in the optical response between super-critical and sub-critical density regions of the expanding cluster. All of these diagnostics bear out the picture of the interaction derived from our laser-cluster interaction model and directly led to the discovery of laser self-focusing phenomenon in clustered gases.<sup>18</sup>

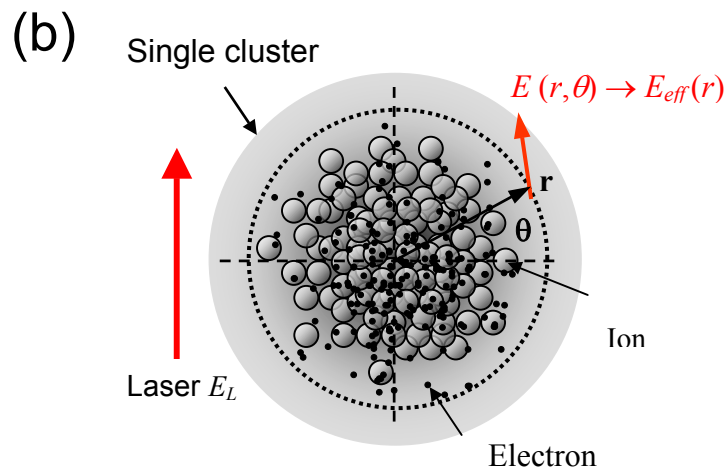
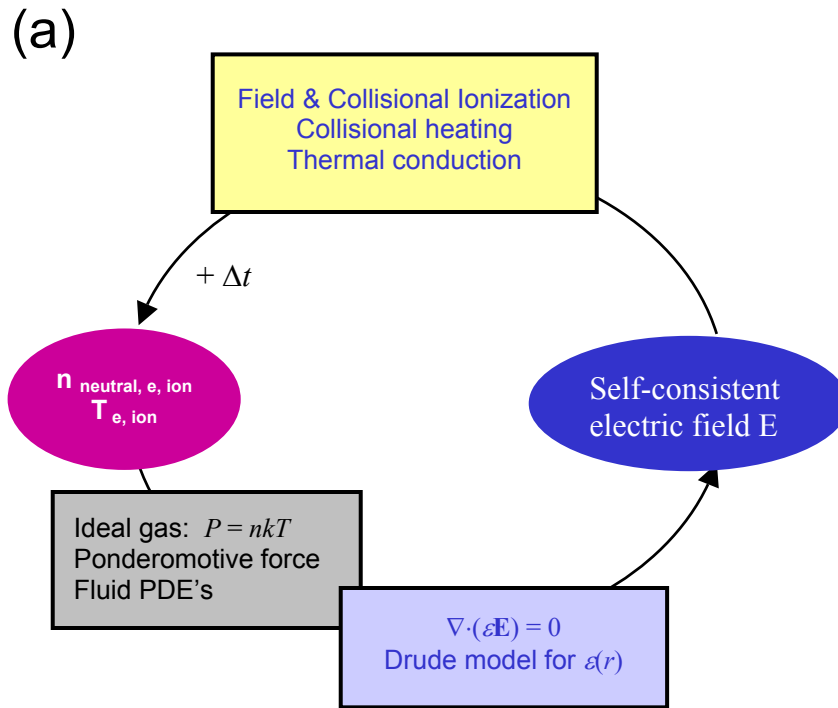


Figure 6.1: (a) Diagram of the hydrodynamic simulation code for intense laser-cluster interaction. It computes the self-consistent electric near field in a single cluster, coupled with 1D radial Lagrangian hydrodynamics. (b) For 1D calculation, the electric field  $E(r, \theta)$  is approximated to  $E_{\text{eff}}(r) = \langle E \cdot E^* \rangle^{1/2}$  averaged over solid angle.

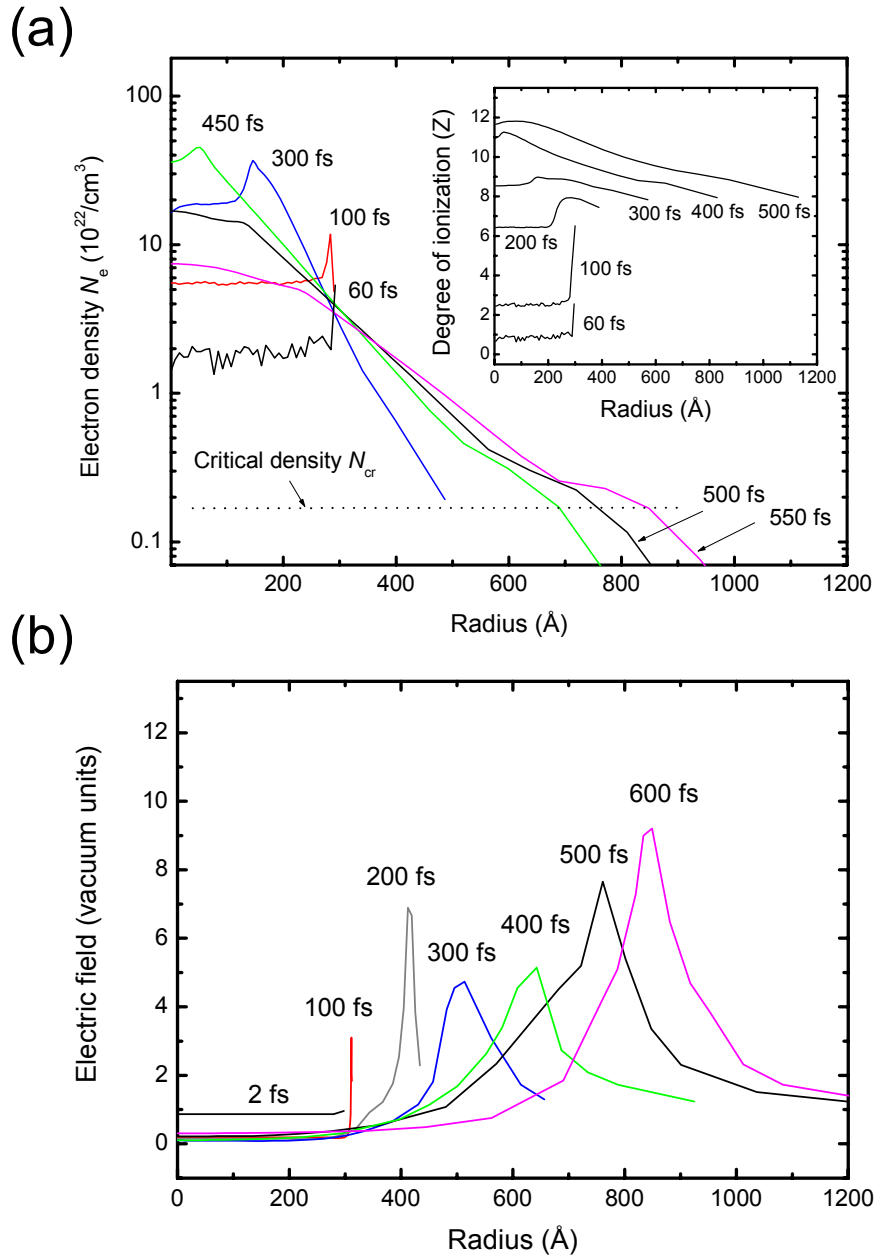


Figure 6.2: 1D hydrocode simulation results for the temporal evolution of (a) electron density and (b) electric field (normalized to vacuum value) profiles for an argon cluster of initial radius of 300  $\text{\AA}$ , irradiated by 800 nm, 300 fs FWHM Gaussian pulse with a peak intensity of  $10^{15}$  W/cm<sup>2</sup>. The average degree of ionization is also superimposed in (a).

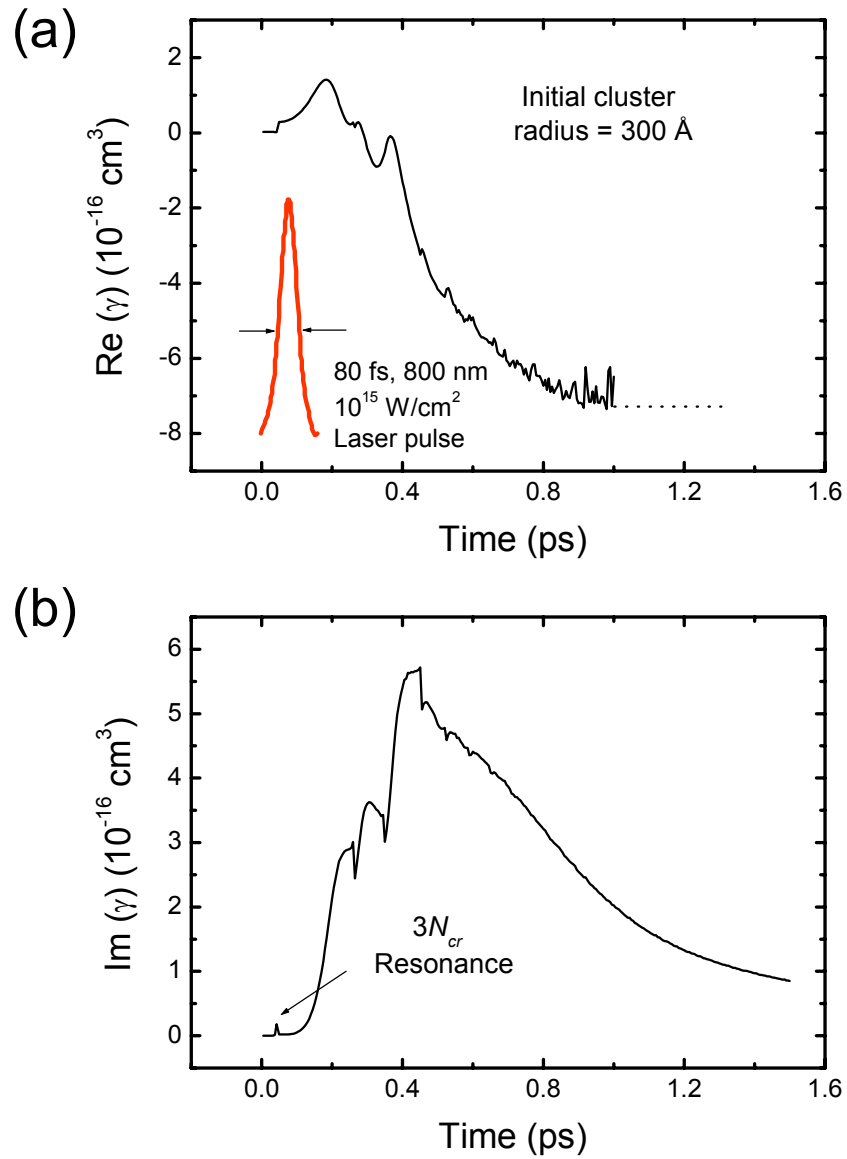


Figure 6.3: 1D hydrocode simulation results for the transient (a) real and (b) imaginary polarizability  $\gamma(t)$  of an exploding Ar cluster with 300 Å initial radius, irradiated by 800 nm, 80 fs (FWHM) Gaussian pulse with a peak intensity of  $10^{15} \text{ W/cm}^2$ .

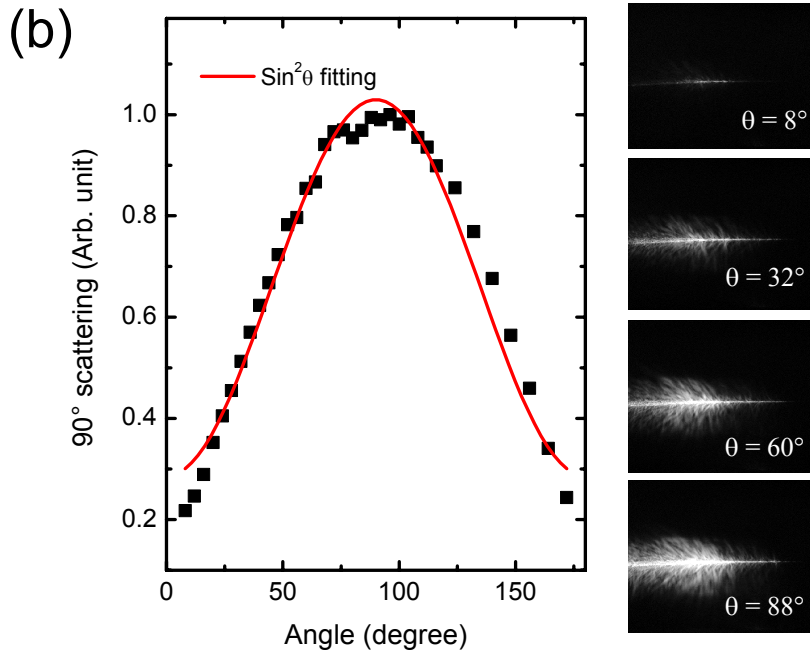
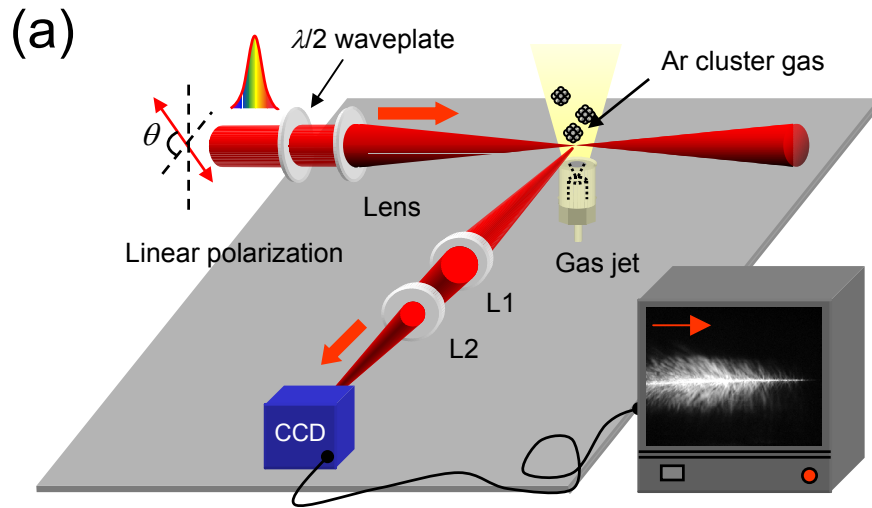


Figure 6.4: (a) Experimental setup for 90° Rayleigh scattering of an intense Ti:sapphire laser pulse in a gas of laser-heated clusters. (b) Scattering angular distribution of intense laser pulses interacting with clusters, measured with  $\theta$ -rotation of the linear laser polarization with respect to the CCD axis. A least squares fit of  $\sin^2 \theta$  and representative raw 2D scattering images at  $\theta = 8, 32, 60, \text{ and } 88^\circ$  are overlaid on the plot.

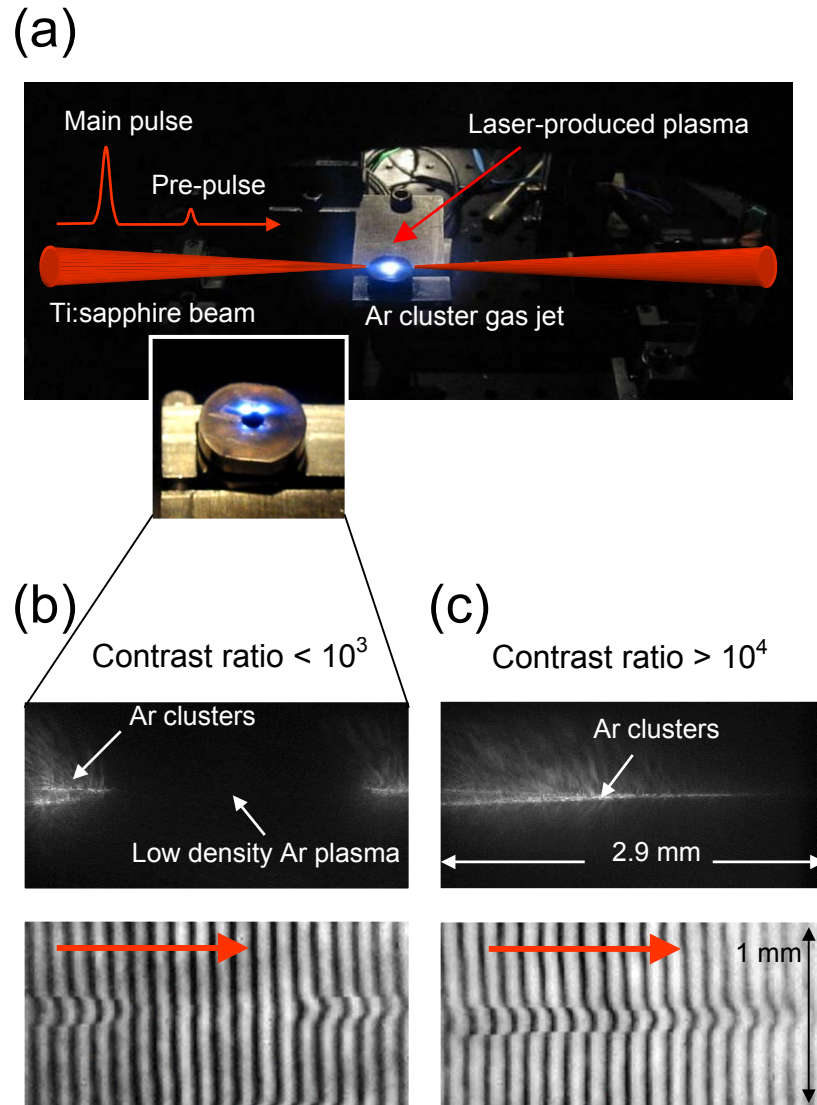


Figure 6.5: (a) Schematic of laser-cluster interaction with the presence of a laser prepulse. The inset shows a photograph of laser-irradiated clustered gas, imaging a segmented plasma recombination emission induced by laser prepulses. The side scattering of intense laser pulse and the corresponding interferograms are shown with a main to prepulse contrast ratio of (b)  $< 10^3$  and (c)  $> 10^4$ .

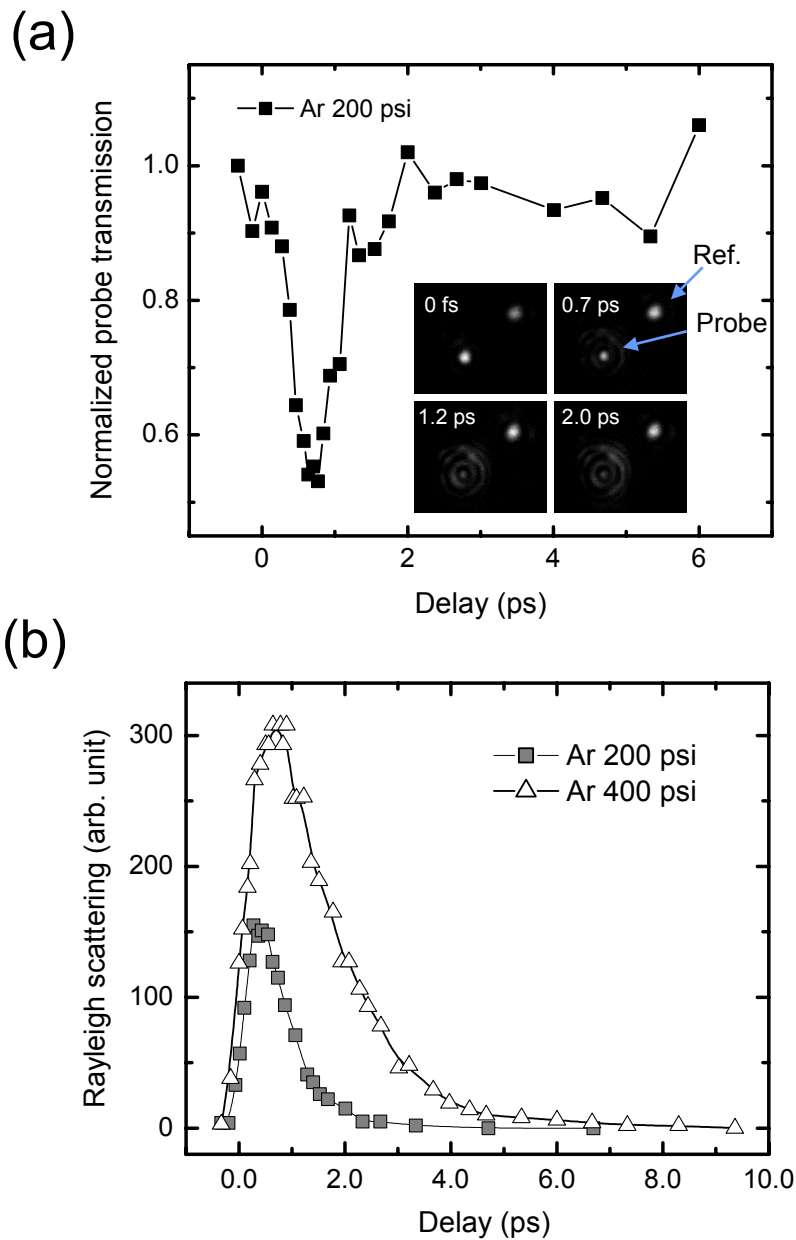


Figure 6.6: Time-resolved 400 nm probe (a) transmission and (b) 90° Rayleigh scattering as a function of pump-probe delay for an argon cluster gas at 200 and 400 psi backing pressures (average cluster radii 200 Å and 350 Å expected from Hagena), irradiated by a 2.5 mJ laser pump pulse. The inset shows the probe and reference intensity profiles imaged on the CCD detector.

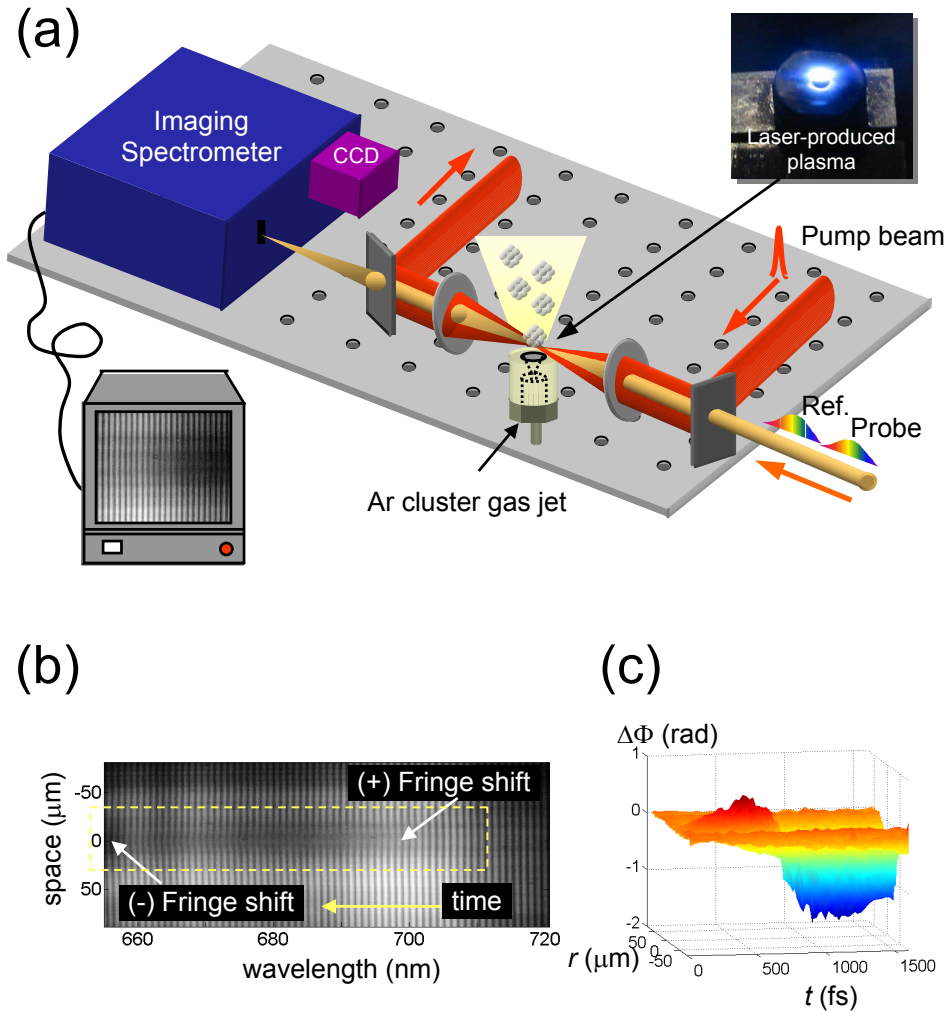


Figure 6.7: (a) Experimental setup, showing pump beam and chirped supercontinuum (SC) reference and probe pulses combined at a beam splitter and focused by a lens through the edge of a cluster jet. The pump is dumped and the reference and probe SC pulses are relayed by a lens to the imaging spectrometer where they interfere, producing a spectral interferogram. (b) Sample spectral interferogram indicating (+) fringe shifts at early times and (-) later. (c) Perspective plot of the phase shift  $\Delta\Phi$  (proportional to  $n_r - 1$ ) versus transverse coordinate and time at 350 psi.

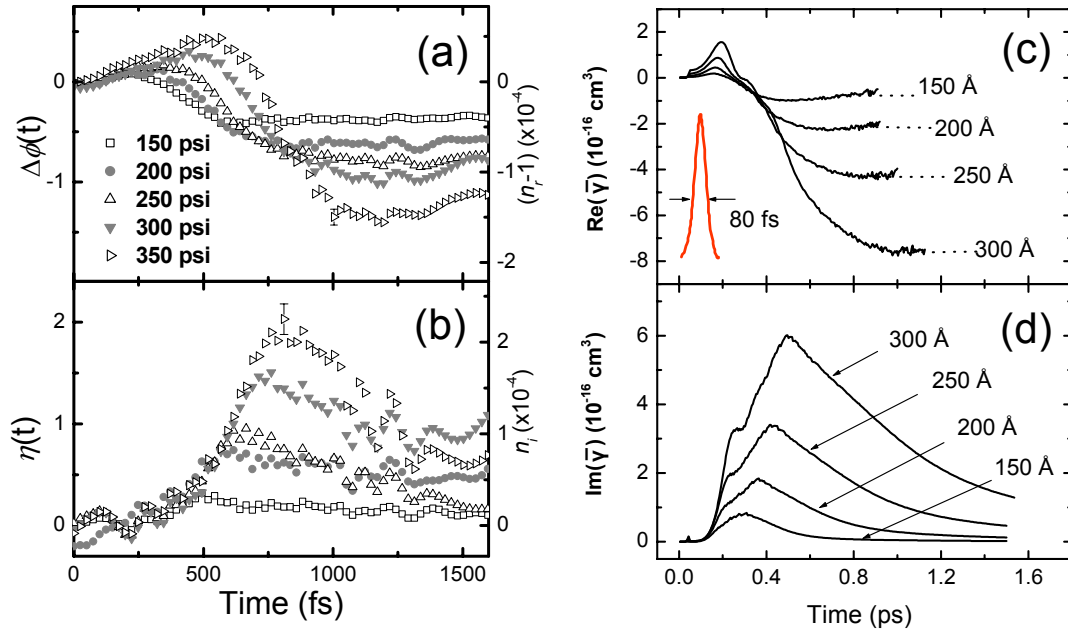


Figure 6.8: (a) Phase shift  $\Delta\phi$  (left scale) and corresponding real index shift  $n_r - 1$  (right scale) extracted from spectral interferograms, for backing pressures (cluster radii) 150 psi (150 Å), 200 psi (200 Å), 250 psi (235 Å), 300 psi (270 Å), and 350 psi (300 Å). (b) Small signal absorption coefficient (left scale) and corresponding imaginary index  $n_i$  (right scale). Plots are 10 shot averages. The error bars shown on the 350-psi plots represent the variance. (c) Calculation of  $\text{Re}(\bar{\gamma}(t))$  for average cluster sizes 150 – 300 Å. The noise at longer times is from the numerical computation. Values for  $\bar{\gamma}_{r, long}$  are shown as dotted lines. The temporal position of the pump laser pulse is shown. (d)  $\text{Im}(\bar{\gamma}(t))$  for the clusters of (c). The very small peaks in  $\text{Im}(\bar{\gamma})$  and steps in  $\text{Re}(\bar{\gamma})$  at  $t \sim 30$  fs are from the  $3N_{cr}$  resonance.

# Chapter 7: Ultrafast measurements of guiding of intense femtosecond laser pulses in a plasma channel

## 7.1 Introduction

Optical guiding of intense laser beams over distances greatly in excess of the Rayleigh length is essential for many applications which include extremely high harmonic generation,<sup>1</sup> x-ray lasers,<sup>2,3</sup> and laser-plasma-based charged particle accelerators.<sup>4</sup> These applications would benefit greatly from a large intensity-interaction length. Without any guiding scheme involved, the effective propagation length of such intense pulses is limited to the extent of the focal region, typically less than 1 mm, given by the twice the Rayleigh length  $2z_0 = 2\pi w_0^2 / \lambda$ , where  $w_0$  is the spot size ( $1/e^2$  radius in intensity) and  $\lambda$  is the wavelength.

Plasma is the unavoidable medium for intense pulse propagation: intensities of interest are generally in excess of minimum ionization thresholds of  $\sim 10^{13}$  W/cm<sup>2</sup> in neutral gas. In a manner analogous to guiding in an optical fiber, light can be guided in plasmas if the refractive index at beam center can be increased sufficiently with respect to the beam edge to balance the effect of diffraction. Due to the advent of CPA technology, capable of producing focused intensities in excess of  $10^{18}$  W/cm<sup>2</sup>, there has been a renewed interest in relativistic and charge displacement guiding, where the on-axis plasma refractive index increases by a relativistic enhancement of electron inertia near beam center or by ponderomotive expulsion of plasma electrons from the beam.<sup>5-10</sup> Unfortunately, this self-guiding process is susceptible to several instabilities<sup>11-13</sup> and separate control of the

guiding process and the desired application is not possible. Moreover, there are applications which use either lower intensities than those required for self-induced guiding, or require tailoring of the density profile and the transverse mode structure of the guided pulse.<sup>14</sup> Therefore, a preformed guiding structure, produced independently of the pulse to be guided, is preferred.

The first demonstration of high intensity optical guiding in a preformed plasma employed thermally-driven radial shock expansion of an elongated laser-induced plasma generated in an ambient gas in the line focus of an axicon lens.<sup>15, 16</sup> An axicon lens<sup>16-18</sup> was used to produce an elongated focus at intensities sufficient for gas breakdown and channel creation ( $\geq 10^{13}$  W/cm<sup>2</sup>). This is five orders of magnitude less intensity than required for self-induced effects such as relativistic self-focusing or charge-displacement channeling.<sup>5-10</sup> Using this preformed plasma channel, guiding of optical pulses for up to 100 Rayleigh lengths<sup>19</sup> and at intensities as high as  $\sim 10^{17}$  W/cm<sup>2</sup> was demonstrated.<sup>18</sup> In this scheme, the degree of control possible in the plasma waveguide exceeds that of almost any other known guiding structure, with the parameters of channel composition, density, depth, and curvature adjusted by choosing the gas type, density, guided pulse injection delay, and channel breakdown laser energy. This scheme is reviewed in the next section.

We note that high intensity guiding has also been demonstrated in hollow capillary tubes<sup>20-23</sup> and in high voltage capillary discharges.<sup>24, 25</sup> These methods are inherently of low repetition rate and there is little opportunity for control of the guiding structure or the composition of the guiding medium. The enclosed geometries in which these guides are produced have also prevented complete measurement of the electron density profile responsible for guiding.

## 7.2 Pre-formed plasma waveguide and taper issue

A plasma waveguide is formed through the hydrodynamic evolution of a laser-produced spark generated in the line focus of a conical lens (axicon)<sup>16</sup> in a background gas. In terms of wave optics, the plasma is generated and heated by a Bessel beam.<sup>26</sup> The initial plasma electrons are generated by multiphoton and optical field ionization (see Chapter 1) early in the laser pulse, and then they are heated by the laser pulse through inverse bremsstrahlung (IB) absorption, driving further ionization via electron-ion and electron-atom collisions. The heated electrons pull the cooler ions radially outward into the neutral background gas, driving the plasma expansion at the local ion sound speed,  $c_s = (\langle Z \rangle k_B T_e / m_i)^{1/2}$ , where  $Z$  is the average ionization,  $k_B$  is the Boltzmann constant,  $T_e$  is the electron temperature, and  $m_i$  is the ion mass. This results in an ion density minimum on axis and a density enhancement at the periphery (shock wave) from ion-atom and ion-ion collisions. Since the plasma remains essentially charge neutral, the electron density follows the ion density, providing a plasma density minimum on axis – the desired refractive index profile for guiding. The evolution of electron density profile in the plasma waveguide has been fully characterized<sup>27</sup> as have the optical properties of the guide.<sup>28</sup> The guiding of high intensity laser pulses ( $I \sim 10^{17}$  W/cm<sup>2</sup>) over a  $\sim 1.5$  cm length has also been successfully demonstrated.<sup>18</sup>

Figure 7.1(a) shows an axicon lens used to produce a long line-focus. A plane wave normally entering the flat side of the axicon (from left) will refract at the conical surface, forming a conical wave front which approaches the  $z$  axis at an angle

$$\gamma = \sin^{-1}(n \sin \alpha) - \alpha, \quad (7.1)$$

where  $\alpha$  is the axicon base angle and  $n$  is the refractive index of the axicon material. For a beam of radius  $R_b$  incident on the flat side of the axicon, the effective length of line focus is

$$z_d = (R_b - R_h) \left( \frac{1}{\tan \gamma} - \tan \alpha \right), \quad (7.2)$$

where  $R_h$  is the radius of the central hole in axicon. The hole in the axicon prevents axicon material damage due to internal focusing of the beam upon internal reflection at the conical surface. More importantly, it also allows the transmission of an injected pulse through the hole either in co- and counter-propagation directions.

Figure 7.1(b) shows a photograph of a plasma waveguide generated by focusing a Nd:YAG laser pulse through an axicon lens ( $\alpha = 30^\circ$ , 23.7 mm base diameter, and 2.2 mm hole diameter) in a backfill gas. The plasma waveguide length shown here is  $\sim 1.5$  cm for a typical beam diameter of  $\sim 1$  cm. An intense, counter-propagating Ti:sapphire laser pulse (artificial color) can be injected into the waveguide and guided over many Rayleigh lengths. This long interaction length ( $\geq 1$  cm) is a key-enabling element for the practical applications of laser-driven particle accelerators and high harmonic generation.

One of the major problems associated with the use of laser-generated preformed plasma waveguides is reduced pump pulse coupling that occurs owing to excessive waveguide taper at the ends.<sup>18,29</sup> In backfill gas targets, this taper results from the sharp falloff in Bessel beam line focus intensity near the ends of the focus.<sup>29</sup> For jets, the taper occurs even if the end is overfilled by the line focus. In that case, the taper is due to the 0.5  $\sim 1$  mm falloff scale length in the gas density at the jet edge.<sup>18</sup> The lower-density plasma near the end is less ionized and heated by the laser and consequently the radial shock development and radial expansion lags that of axial sections closer to the line focus center.

A promising solution to this problem is to use an auxiliary laser pulse to generate a short length of strongly heated plasma near the end of the axicon line focus. The goal is to produce a local plasma lens or “funnel”, grafted onto the end of the plasma waveguide, which can focus and match an injected intense pump pulse into the main waveguide. Favorable conditions for this occur either when the funnel plasma expands radially at a rate faster than the waveguide end due to greater heating there, or when it starts its expansion at a time earlier than the point of main waveguide generation.

### **7.3 Funnel-mouthed plasma waveguide generation and characterization**

#### **7.3.1 Experimental setup**

Figure 7.2 shows the experimental setup for generating a plasma waveguide with a funnel entrance structure and subsequent guiding of intense Ti:sapphire laser pulses in the preformed plasma channel. A 1064 nm, 100 ps, ~500 mJ laser pulse from a Nd:YAG laser system<sup>30,31</sup> generated the plasma waveguide at the ~1cm long line focus of a 30° base angle axicon in a static-filled gas of 640 torr of helium plus 10 torr of N<sub>2</sub>O, with an peak on-axis intensity of  $5 \times 10^{13}$  W/cm<sup>2</sup>. The gas N<sub>2</sub>O assists waveguide generation by field ionizing early in the Nd:YAG pulse and providing seed electrons for the uniform avalanche breakdown of helium (N<sub>2</sub>O has a relatively low breakdown threshold with a spark appearing at intensities slightly below  $10^{13}$  W/cm<sup>2</sup> for our 100 ps, 1060 nm Nd:YAG pulses). The funnel plasma was produced by focusing a 100 mJ portion of the Nd:YAG pulse through a lens (L1,  $f = 150$  mm) at the preformed waveguide entrance. The funnel generation pulse and Ti:sapphire injection pulse counter-propagate with respect to the axicon-focused waveguide generation pulse. The axial and transverse positioning of the

funnel plasma with respect to the axicon-generated waveguide was controlled by an external negative-positive lens pair in the funnel generation beam. By means of a long optical delay line (not shown), the funnel plasma can be generated with a negative through positive delay of  $-10$  ns to  $+3$  ns with respect to the plasma waveguide.

A  $\sim 40$  mJ, 70 fs pulse from our Ti:sapphire laser system, synchronized to the Nd:YAG waveguide generating laser as described in Appendix H, was injected into the plasma waveguide. The pump pulse was focused at the waveguide entrance by L1 at  $f/4$  with the peak intensity of  $\sim 10^{17}$  W/cm<sup>2</sup>. The injection angle and positioning of the Ti:sapphire pump pulse was controlled by mounting lens L1 on a three-dimensional (3D) stage equipped with motorized actuators. After guiding in the plasma channel, the pump pulse then propagated through the axicon and mirror holes, followed by a collection lens (L2), with most pump energy ( $\sim 99\%$ ) then dumped off a beam splitter (BS1) into a beam dump. The small leakage of the pump pulse through BS1 was used for the waveguide exit mode imaging with a CCD camera (CCD1). The Ti:sapphire and Nd:YAG laser systems were synchronized with a relative jitter less than 20 ps, as described in Appendix H.

To study the time-resolved coupling dynamics of intense laser pulses in the plasma waveguide, we employed three optical diagnostics – waveguide exit mode imaging, femtosecond transverse interferometry/shadowgraphy, and single-shot supercontinuum spectral interferometry (SSSI). The transverse waveguide exit modes of the pump and probe pulses were imaged by a lens L2 onto CCD1 with  $\sim 7$   $\mu\text{m}$  spatial resolution.

To diagnose the evolution of funnel-mouthed plasma waveguide and examine the pump pulse injection into the waveguide, femtosecond transverse interferometry/shadowgraphy<sup>32</sup> was used. A small portion of the diagnostic beam, split

from the main Ti:sapphire pump pulse, was sent transverse to the pump beam direction to sample plasma with time resolution limited by the probe pulse duration ( $\sim 70$  fs) and the time for propagation across the plasma. The adjustable optical delay allowed observation of the plasma waveguide evolution up to 5 ns after initial plasma creation. After sampling the plasma, the probe pulse was relay-imaged onto a CCD camera (CCD2) with two-lens imaging system [L3 ( $f_3 = 100$  mm) and L4 ( $f_4 = 300$  mm)] as shown in Fig. 7.2. It provided  $\sim 10$   $\mu\text{m}$  spatial resolution with  $3\times$  imaging magnification. To obtain an interferometric picture, a modified Mach-Zehnder interferometer was placed between L4 and CCD2. Since the probe beam diameter is  $\sim 10$  mm, whereas the plasma region is only a few hundred microns wide and a few millimeters long, it was possible to overlap the perturbed and unperturbed portions of the probe beam (and thus producing an interferogram) by vertically shearing the twin probe beams produced inside the interferometer arms. By blocking one of the interferometer arms, we could obtain plasma phase contrast images (shadowgrams).

Finally, we employed our single-shot supercontinuum spectral interferometry (SSSI) diagnostic to measure the refractive index transient induced by intense pump pulses injected into plasma waveguides. This diagnostic uses a chirped supercontinuum (SC) probe pulse, capable of measuring a transient phase shift with  $\sim 10$  fs (time) and  $\sim 7$   $\mu\text{m}$  (one-dimensional space) resolutions. It provides  $\sim 2$  ps observation window in a single-shot operation. Full details of the SSSI diagnostic are described in Chapter 2 and Appendix C.

### 7.3.2 Funnel generation and intense laser pulse injection

Figure 7.3 shows shadowgram and interferogram images of the end region of a plasma waveguide produced in a backfill gas target (640 torr He plus 10 torr  $\text{N}_2\text{O}$ ) with and

without funnels generated at its end, taken by the transverse probe pulse 4.3 ns after the waveguide generation (axicon) pulse. Transverse interferometry showed that beyond the entrance, the waveguides were fully ionized with an electron density of  $N_e \sim 4 \times 10^{19} \text{ cm}^{-3}$ , corresponding to the neutral helium density of  $N_{\text{He}} \sim 2 \times 10^{19} \text{ cm}^{-3}$  at 640 torr. The funnel-free waveguide is seen to have a significant taper, as seen in our previous work.<sup>18, 27, 29</sup> Here, a minimum end electron density falloff distance of  $\sim 0.5$  mm at the ends was observed from both shadowgraphy and interferometry. However, the addition of the funnel pulse removes the taper and widens the end region. The times in the figure refer to funnel pulse delay with respect to the axicon pulse. For the cases where the funnel pulse arrives in advance of the axicon pulse (negative delays), the waveguide end is significantly fatter than for the reverse situation. Under our conditions, the optimal delay for the funnel generation is  $-1.5$  ns, when it exhibits the most ideal entrance structure for pulse injection. In all cases, however, the waveguide end taper is mitigated to various degrees.

The injection of intense laser (pump) pulses into the waveguide was also examined with transverse shadowgraphy/interferometry. Figure 7.4 shows transverse shadowgrams and interferograms of the coupling of an injected Ti:sapphire laser pulse into a preformed waveguide entrance with a funnel generation beam off (a) and on (b). For both cases [(a) and (b)], the injection beam followed the axicon pulse by 2.8 ns. In case (b), the funnel generation pulse preceded the axicon pulse by 1.5 ns. For the funnel-free waveguide case [Fig. 7.4(a)], the pump pulse was not properly injected into the waveguide, and moreover, it produced unwanted ionization in the background gas near the waveguide entrance. This reduces the waveguide coupling efficiency. In contrast, with a funnel-mouthed waveguide

[Fig. 7.4(b)], the pump-induced ionization was substantially reduced, and the coupling is improved owing to the relatively wide opening of the waveguide entrance.

Coupling of an intense Ti:sapphire pump pulse to the waveguide (a) with and (a') without the funnel is shown in waveguide exit mode images of Fig. 7.5. As usual, the waveguide-free case shows a very large beam at the guide exit, which here overfills the imaging optics aperture. The waveguide case shows a bright lowest order exit mode with a focal spot of  $20 \mu\text{m}$  (FWHM) and the peak guided intensity of  $\sim 10^{17} \text{ W/cm}^2$ .

Figure 7.5(b) and (b') shows the exit mode of the SC probe beam with the waveguide off and on, respectively. Since the probe beam overfills the plasma waveguide in (b'), it exhibits a bright lowest order exit mode surrounded by rings, which are due to far field interference of portions of the probe beam which do not couple into the entrance.

We used our SSSI diagnostic to measure phase shifts induced by intense pump pulses injected into plasma waveguides. Preliminary results are for waveguides without funnels. Figure 7.5(c) and (c') shows SSSI interferograms for the cases of (c) no waveguide and no pump and (c') for the waveguide present but no pump. The swept frequency of the chirped supercontinuum (SC) pulses corresponds to the time interval shown in the images. There is no time-dependent fringe shift for case of (c). In case (c'), the waveguide is seen to trap the SC pulses. The injected SC pulses transversely overfill the waveguide. The bright region in the center is the trapped light. Above and below that is spatial interference (manifested by wide horizontal fringes) between light refracted away from the outside of the guide, and light that does not encounter the guide. The horizontal fringes correspond to the rings seen in Fig. 7.5(b').

Panel (c') is magnified and re-plotted in Fig. 7.6(a) to better see the fringes. Figure 7.6(b) shows a SSSI interferogram for the waveguide on with pump pulse injection. Here, it is clear that guided pump-induced transient fringe bending is imposed on the guided, co-propagating SC pulse, here corresponding to a transient negative phase shift. This is clearly seen in Fig. 7.6(c) where the extracted transient phase shift  $\Delta\Phi(x, t)$  imposed on the SC probe pulse is plotted, where  $x$  is a coordinate transverse to the guide. At this point, without having used the funnel, we attribute this phase shift to pump-induced ionization at the waveguide entrance (as noted, interferometry shows that beyond the entrance the waveguide is fully ionized). This is suggested by the negative sign of the phase shift, which corresponds to ionization, and by the temporal location of the shift beginning near the center of the chirped SC pulse time window, where the pump pulse is located. It is also seen that the bright strip of guided SC light widens at the same time that the fringe shift (phase shift) begins. The reason for this is not clear, and further experiments will elucidate the origin of this effect.

## **7.4 Generation of plasma waveguides in a cluster gas jet**

### **7.4.1 Self-focusing of intense laser pulses in a clustered gas**

In Chapter 6, we examined the time-resolved explosion dynamics of laser-heated clusters and found that the time variation of the complex cluster polarizability  $\gamma$  embodies the details of the cluster explosion dynamics. These experimental results directly predicted a new macroscopic phenomenon: *the self-focusing of intense laser pulses in a clustered gas*.<sup>33</sup> This self-focusing effect originates from the manner in which individual clusters heat up and explode in the presence of intense laser fields. This can occur at moderate

pulse intensities below  $\sim 10^{15}$  W/cm<sup>2</sup>, which implies that this effect is unrelated to either relativistic self-focusing or ponderomotive filamentation.<sup>5–10</sup>

Figure 7.7(a) shows this self-focusing picture. As an intense laser pulse propagates in a clustered gas, while ionizing and heating clusters,  $\text{Re}(\gamma) = \gamma_r$  starts positive and initially grows with time (see Chapter 6). This occurs faster on the laser beam axis, where the intensity is higher, than at the beam edge. Hence, for sufficiently short pulses, an ensemble of laser-heated clusters provides a refractive index structure suitable for beam self-lensing or waveguiding.

Figure 7.7(b) shows calculated radial profiles of ensemble-averaged (with a 100% FWHM size distribution) complex polarizability ( $\bar{\gamma}_r$  and  $\bar{\gamma}_i$ ) for 300 Å average radius argon clusters irradiated by a 100 fs Gaussian FWHM pump pulse with a peak intensity  $5 \times 10^{15}$  W/cm<sup>2</sup> and FWHM spot-size of 15 μm. Time  $t = 0$  corresponds to 1% of the laser peak intensity at the leading edge. The radially convex  $\delta n_r > 0$  region at early times in the  $\bar{\gamma}_r$  plot leads us to expect self-focusing.

Recently, we have demonstrated this self-focusing effect.<sup>33</sup> In this experiment, we varied the laser pulse width from 80 fs to 1.5 ps at fixed energy of 7.5 mJ. Figure 7.8(a) shows the beam root-mean-square (RMS) radius  $R_{\text{rms}}$  at the argon cluster jet exit plane and the energy transmission as a function of pulse width.  $R_{\text{rms}}$  has a minimum near 350 fs. However, for non-clustering helium gas jets produced by the same nozzle, the jet exit beam radius continuously increases as pulsewidth shortens, consistent with the mechanism of ionization-induced refraction. Pump pulse propagation in the cluster jet was visualized by side-probing the plasma left behind by the pump. Figure 7.8(b) shows selected transverse shadowgrams taken  $\sim 10$  ps after the pump enters on the left. The 1.4 ps image closely

follows the vacuum beam profile. As the pulse shortens, the region near the vacuum focus (VF) becomes tighter until it appears to pinch at 80 fs, where the negligible fringe shift in the corresponding interferogram [Fig. 7.8(c)] implies a very narrow self-focused channel at the pinch location.

The transient intensity profile, measured with the SSSI diagnostic, is shown in Fig. 7.8(d). Earlier than  $t \sim -400$  fs, the clusters are not yet ionized, and there is no phase or intensity perturbation to the probe. Past  $t \sim -400$  fs, a radially widening intensity reduction of the probe begins (onset of pump-heated cluster absorption of the probe), which forms an effective beam diameter. We take the onset of Ar ionization (at  $\sim 10^{14}$  W/cm<sup>2</sup>)<sup>34</sup> to occur at  $\sim -400$  fs. This sets the location of the pump pulse peak as indicated by the vertical dashed line. The white boundary is caused by interference between the periphery of the phase shifted part of the probe beam (which propagates through the exploding cluster gas) and the unshifted part, which does not encounter the heated clusters. This beam diameter then abruptly increases over a  $\sim 300$  fs interval around  $t = 0$ . There is a strong reduction in beam intensity during this interval. These results are consistent with our model for the cluster transient polarizability [see Fig. 7.7(b)]: At early times, a positive profile in  $\bar{\gamma}_r$  restrains beam divergence. During the  $\sim 300$  fs interval around  $t = 0$ ,  $\bar{\gamma}_r$  changes sign and the disturbed portion of the probe exit beam increases in size. Finally, and convincingly, the strong enhancement in absorption over the beam size-change interval is consistent with the maximum in  $\bar{\gamma}_i$  reached during the sign change of  $\bar{\gamma}_r$ . This is consistent with the minimum beam transmission for  $\tau \sim 350$  fs pulses shown in Fig. 7.8(a).

#### 7.4.2 Generation of plasma waveguides in cluster jets

The density in an individual cluster is solid-like, while the volume average density can be variable up to that of typical gas at several atmospheres. Even for low volume average densities, an intense laser pulse can strongly couple to individual clusters owing to their high local density. This suggests the possibility of producing preformed plasma waveguides in a lower range of average density than in the usual case of laser-heated unclustered gas. The need for lower densities is motivated by the fact that the best-matched laser pulsewidth for resonant wakefield generation scales as  $\tau \sim \omega_p^{-1} \propto N_e^{-1/2}$ , which requires densities of a few times  $10^{17} \text{ cm}^{-3}$  and below for  $\sim 100$  fs pump pulses (see Chapter 1). Such low densities are not easily accessible with standard avalanche breakdown of unclustered gas, which favor densities of a few times  $10^{18} \text{ cm}^{-3}$  and higher.<sup>16</sup>

We note here that avalanche pre-ionization schemes such as short pulse field ionization<sup>35</sup> or electrical discharge<sup>36</sup> in unclustered gas targets do not help in cases when desired electron density is below  $\sim 10^{18} \text{ cm}^{-3}$ . At early times in the avalanche breakdown, the electron density grow as

$$N_e(t) \sim N_{e0} \exp(SN_0 t), \quad (7.3)$$

where  $N_{e0}$  is the seed electron density,  $S$  is the collisional ionization rate, and  $N_0$  is the initial gas density. The most important factor by far is  $N_0$ , since it appears in the exponent. The initial electron density is a prefactor, and sensitivity to its value is lost after several e-folding times of the avalanche process as saturation is approached. The solid density values for  $N_0$  in clusters favors strong local avalanche ionization, independent of the number of clusters per unit volume.

Here, we propose plasma waveguide generation method which combines the self-guiding of short laser pulses in cluster jets with their strong absorption in the clusters.<sup>37</sup> The idea is to circumvent the high initial density requirement imposed by efficient inverse bremsstrahlung breakdown in unclustered gas targets, and to achieve a tight, elongated line focus in an end-injected geometry. Some typical numbers can be worked out.

From the complex polarizability measurement of Chapter 6, examination of Fig. 6.8 shows that the times where  $\Delta\phi \propto n_r - 1$  is at peak positive values (where guiding can occur) corresponds to values of  $n_i$  that are at more than half their maximum value (the maximum in  $n_i$  occurs near the zero crossing point for  $n_r - 1$ ). So guiding is accompanied by strong absorption. How strong is the absorption? The absorption strongly depends on the laser pulse duration, as shown in Chapter 6. For higher density cluster jets with  $N_c \sim 10^{11}$  clusters/cm<sup>3</sup> (such as in the center of our jet) and a 800 fs pulse duration with a peak intensity of  $I_{\text{peak}} \sim 10^{15}$  W/cm<sup>2</sup>, the measured value of  $n_i$  from Fig. 6.8 would be scaled linearly with the cluster number density increase, giving  $n_i = 2\pi N_c \gamma_i \sim 4 \times 10^{-4}$  (for the 350 psi case, corresponding to 300 Å average radius clusters) with  $\gamma_i \sim 6 \times 10^{-16}$  cm<sup>3</sup>. The corresponding damping length is  $(kn_i)^{-1} \sim 300 \mu\text{m}$  for a  $\lambda = 0.8 \mu\text{m}$  pump pulse, where  $k$  is the laser wavenumber. So essentially complete absorption can take place in less than 1 mm. However, for the shorter pulse duration of 80 fs, the estimated absorption length is  $(kn_i)^{-1} \sim 20$  mm with  $\gamma_i \sim 10^{-17}$  cm<sup>3</sup>.

Here, we present preliminary results on plasma waveguide generation via the combined effects of self-focusing and strong absorption of intense laser pulses in clusters. To produce a long laser-cluster interaction length and consequent waveguide generation, an elongated cluster jet was used.

Figure 7.9(a) shows a photograph of a cryogenically cooled argon cluster gas jet (see Chapter 5) irradiated by a 70 fs, 50 mJ, 800 nm Ti:sapphire laser pulse (where the vacuum focus is located in the middle of jet). The  $\sim 1$  cm long plasma recombination emission is shown imaged. The elongated cluster source and its characterization are described in Chapter 5. Figure 7.9(b)-(c) shows shadowgrams and interferograms of the long range propagation of the pump pulse for a valve temperature of  $T = 153$  K ( $-120$  °C) and gas jet backing pressure of 400 psi for a transverse probe delay of (b) 20 ps and (c) 2 ns after the pump. This preliminary result shows that a long ( $\sim 1$  cm) plasma channel can be generated by the combined effect of self-focusing and strong absorption of laser pulses in clusters. Upon approaching the center of the jet, the pump has lost its energy substantially due to absorption, and little further plasma is produced to the right.

To check for qualitative agreement with our model for laser-heated clusters, described in Chapter 6, the absorption length can be estimated and compared with the measured one ( $\sim 1$  cm). Here, the estimated absorption length is  $(kn_i)^{-1} \sim 1.3$  cm, where  $n_i = 2\pi N_c \gamma_i \sim 1 \times 10^{-5}$  and  $\gamma_i \sim 10^{-17}$  cm<sup>3</sup>, obtained from the average cluster radius  $a \sim 300$  Å and density  $N_c \sim 1.7 \times 10^{11}$  cm<sup>-3</sup> in the cryogenically cooled elongated jet (see Chapter 5), with an assumption of 80% monomer concentration. The interferograms in Fig. 7.9(b)-(c) show that the laser-heated zone within the cluster jet expands radially on a few nanosecond timescale and a plasma waveguide is formed in the usual manner.

## 7.5 Conclusions

We have presented the concept of funnel-mouthed plasma waveguides in backfill gas targets and its implementation for enhanced coupling of intense short laser pulses. We

have characterized the funnel structure at the waveguide entrance with various optical diagnostics. In particular, we have measured transient phase shifts generated by intense pump pulses injected into plasma waveguides using single-shot supercontinuum spectral interferometry (SSSI).

We have also demonstrated that short pulse heated clustered gases can act as an optical guiding medium and are highly absorbing. Consequently, this leads to a method for plasma waveguide generation at average densities substantially lower than current typical values in non-clustered gases. We have recently demonstrated that injected pulses can be well guided by such waveguides and that these guides show greatly reduced taper and low on-axis electron densities.

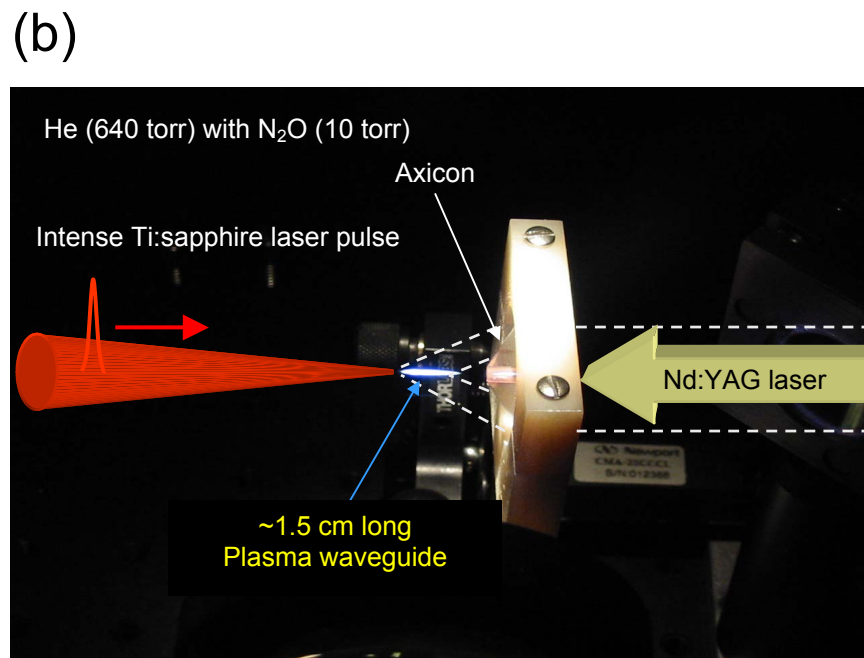
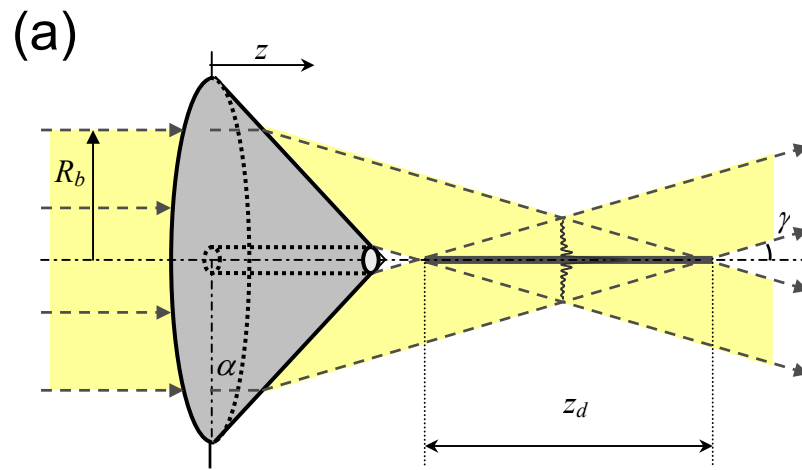


Figure 7.1: (a) Conical lens (axicon) and its use to generate a line focus. (b) Generation of a plasma waveguide by focusing Nd:YAG laser through an axicon lens in a backfill gas of 640 torr of helium plus 10 torr of  $N_2O$ . Intense Ti:sapphire laser pulses can be coupled into the waveguide and guided over many Rayleigh lengths.

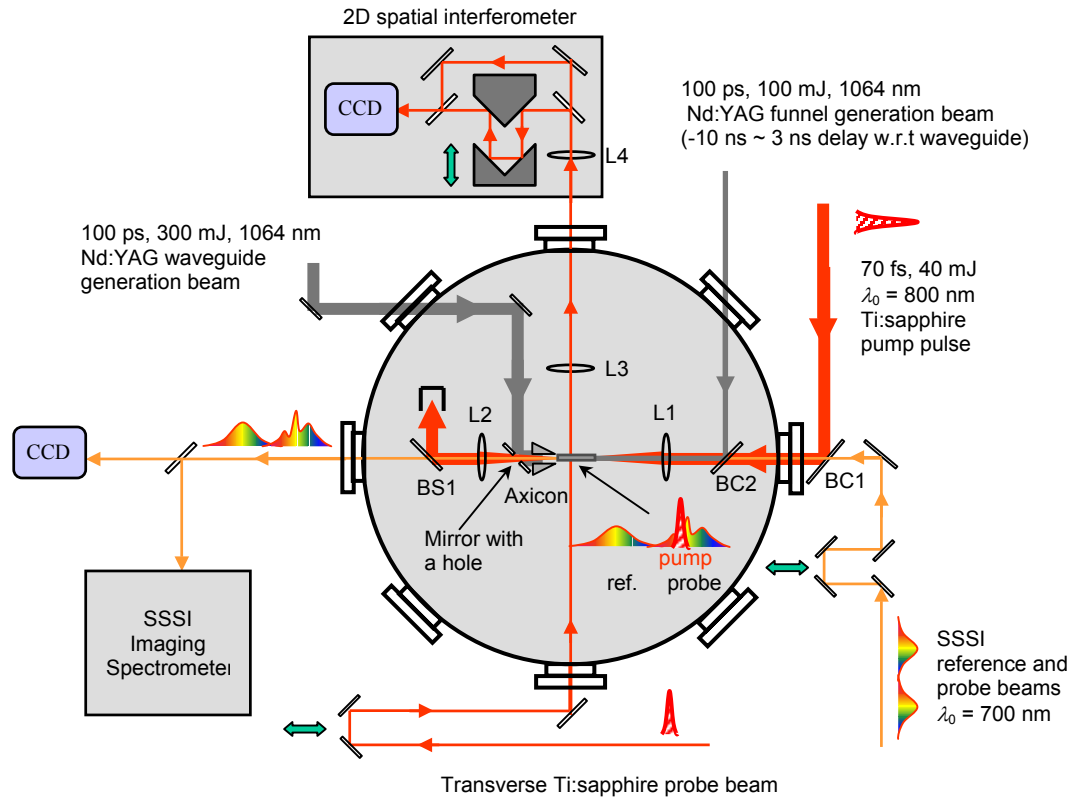


Figure 7.2: Experimental layout for guiding of intense Ti:sapphire laser pulses in a pre-formed plasma channel generated by focusing Nd:YAG laser pulses with an axicon. A plasma funnel is generated at the entrance of the plasma waveguide by focusing part of Nd:YAG laser pulses with the Ti:sapphire pump pulse lens. The funnel generation pulse is independently adjustable in time and space with respect to both the waveguide generation pulse (axicon pulse) and the injected pump pulse. Included are transverse interferometry/shadowgraphy and longitudinal imaging/SSSI diagnostics.

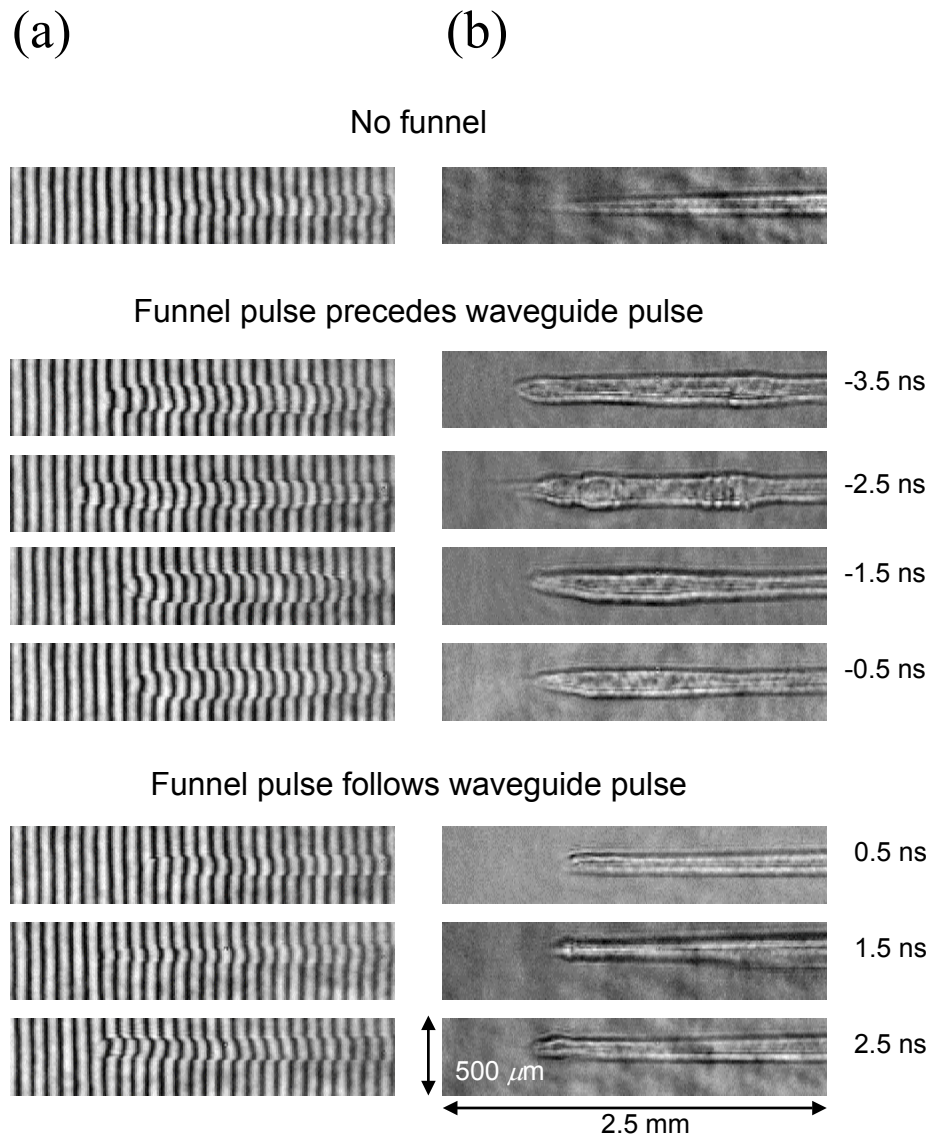


Figure 7.3: Shadowgrams and interferograms of waveguide end region showing typical taper for case of no funnel pulse, and taper removed for cases of funnel pulse at various delays before and after the waveguide generation pulse.

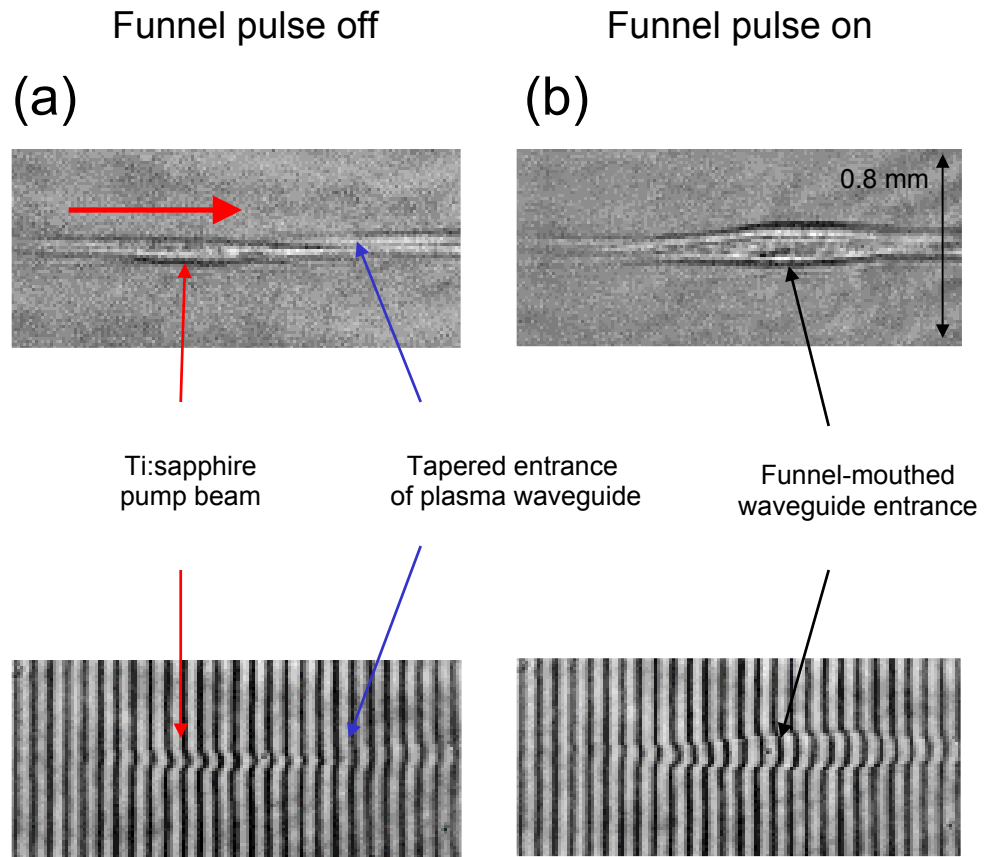


Figure 7.4: Transverse shadowgrams and interferograms of an injected Ti:sapphire laser pulse (40 mJ, 70 fs, 800 nm) into the entrance of plasma waveguide with the funnel generation beam (a) off and (b) on.

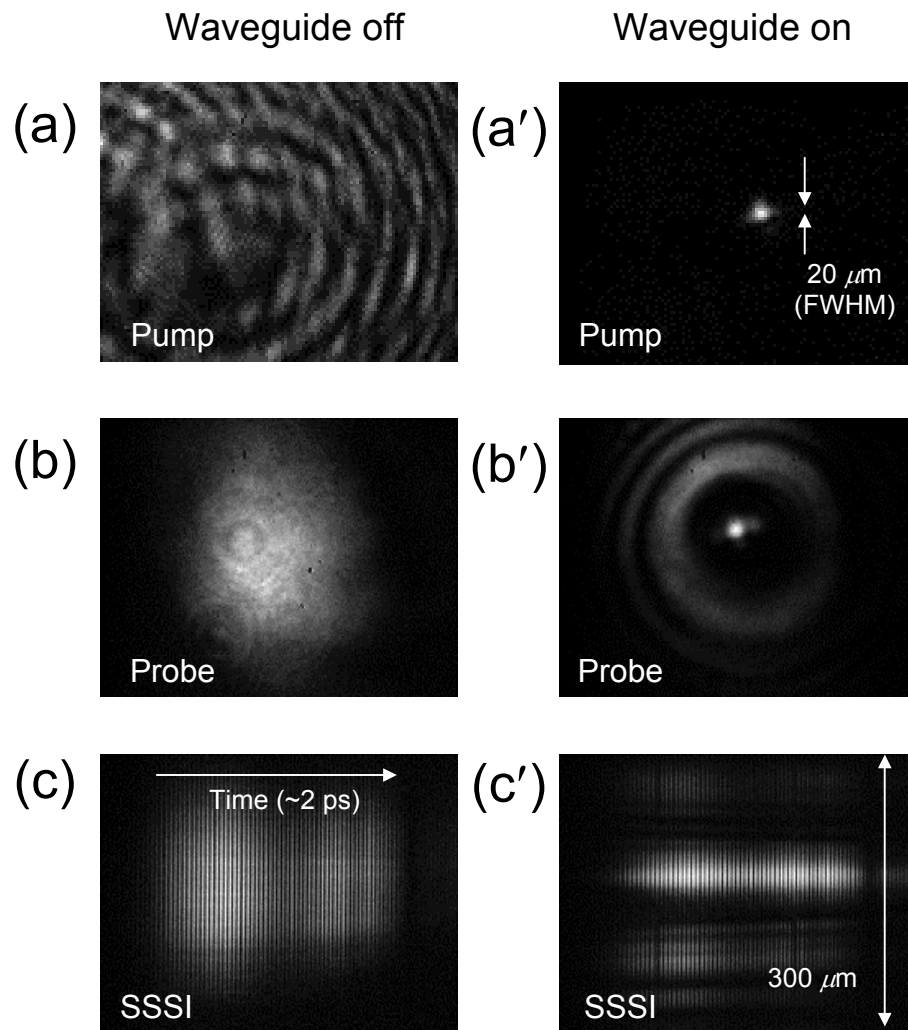


Figure 7.5: Images of (a) pump and (b) probe on the waveguide exit plane when no waveguide present. [(a')-(b')] with presence of waveguide. Single-shot supercontinuum spectral interferograms for case of waveguide (c) off and (c') on.

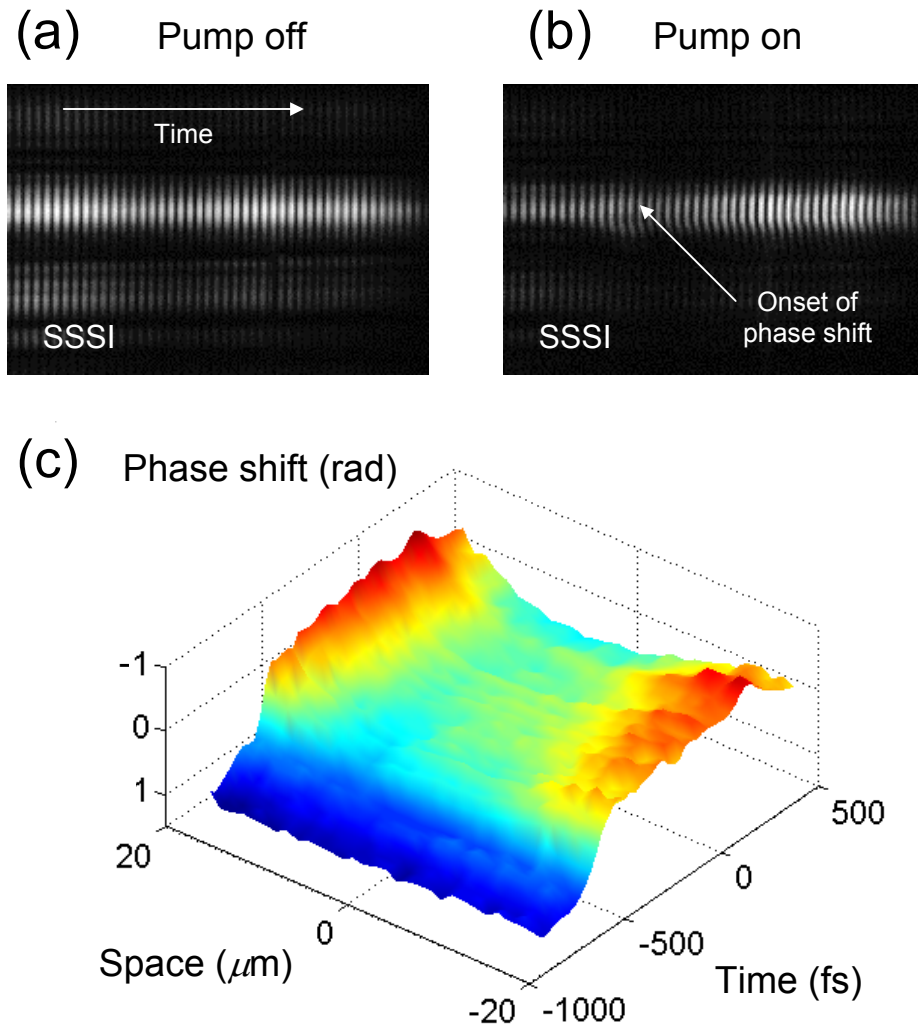


Figure 7.6: Single-shot supercontinuum spectral interferogram (SSSI) for cases of pump pulse (a) off and (b) on into the plasma waveguide. (c) Extracted transient phase shift of probe pulse by an intense pump pulse injected into the plasma waveguide.

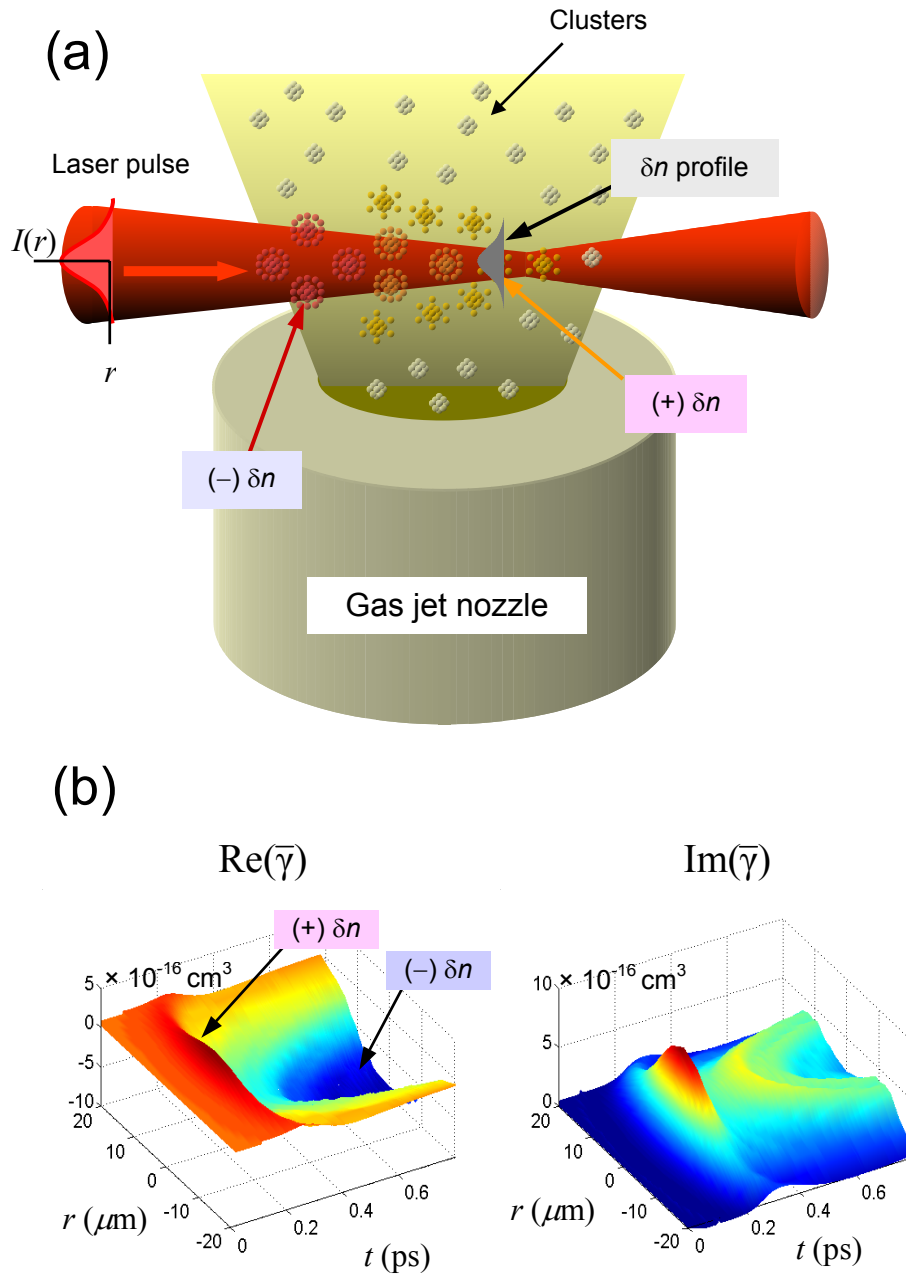


Figure 7.7: (a) Schematic of self-focusing of intense laser pulses in a gas of clusters. (b) Perspective plots of  $\text{Re}(\bar{\gamma})$  and  $\text{Im}(\bar{\gamma})$  versus radius and time calculated for a gas of  $300 \text{ \AA}$  average radius clusters (with a 100% FWHM size distribution) heated by a 100 fs pulse of peak intensity of  $5 \times 10^{15} \text{ W/cm}^2$  in a  $15 \mu\text{m}$  FWHM spot.

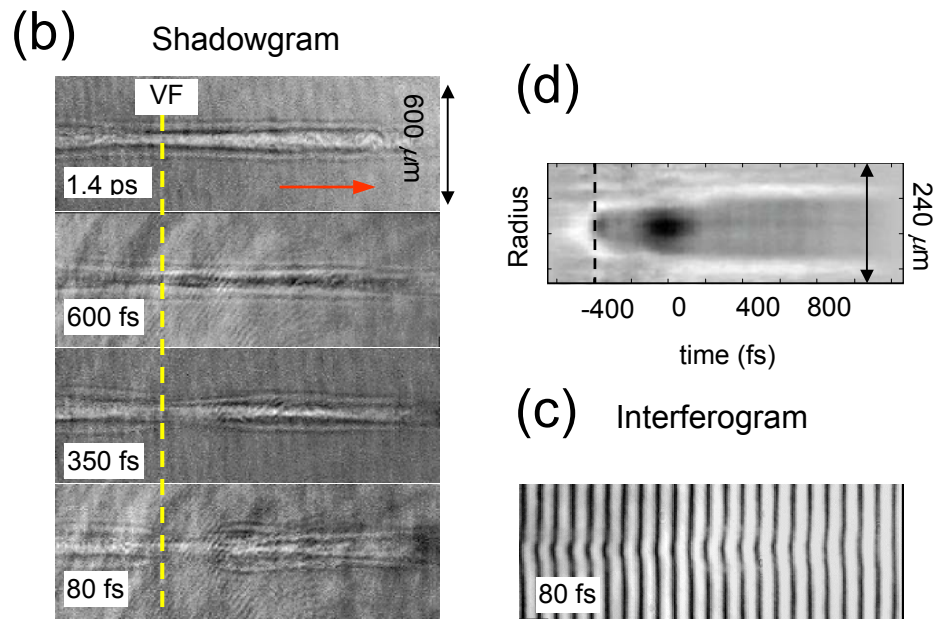
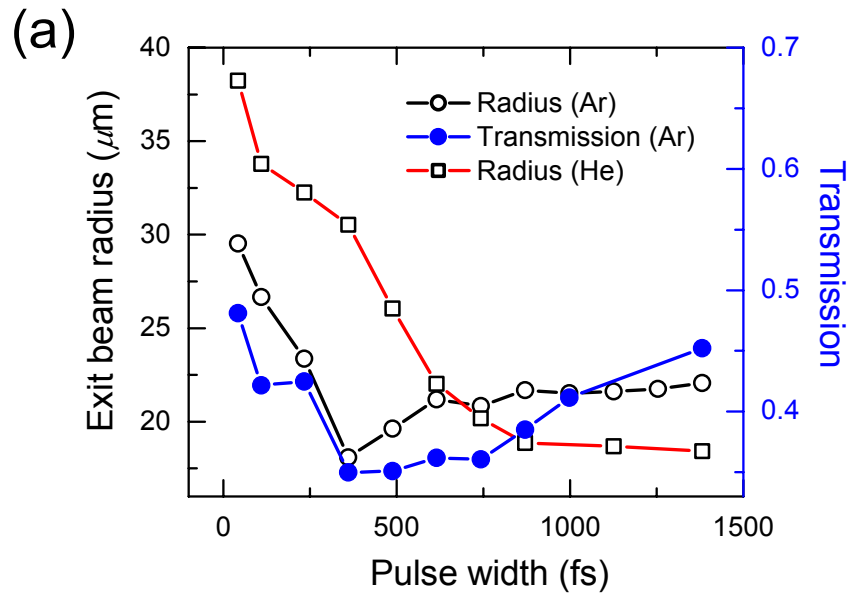
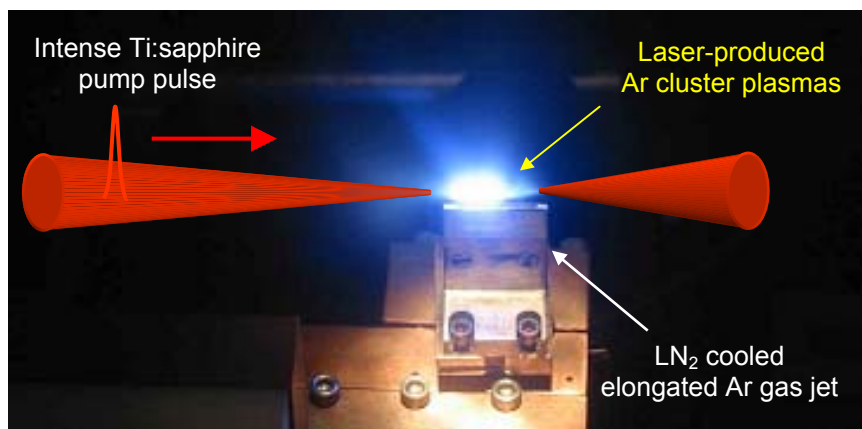


Figure 7.8: (a) Pump beam root-mean-square (RMS) radius at jet exit and transmission versus pulse width. (b) Transverse shadowgrams of pump beam tracks in cluster jet 10 ps after pump enters from left for selected pump pulse widths. VF: location of vacuum focus. (c) Interferogram corresponding shadowgraph for the 80 fs pump pulse. (d) Transient intensity profile of SC probe.

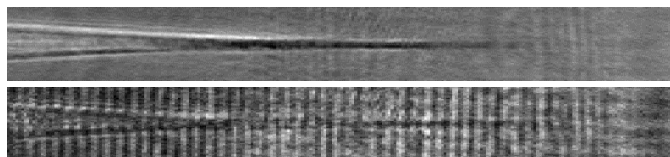
(a)



(b)

$t = 20$  ps after pump

Pump pulse →



(c)

$t = 2$  ns after pump

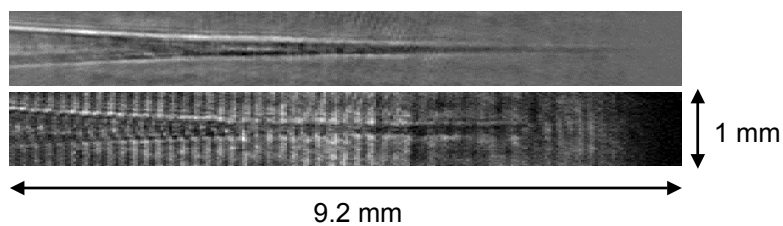


Figure 7.9: (a) Photograph of cryogenically cooled elongated Ar cluster gas jet irradiated by a 50 mJ, 70 fs Ti:sapphire pump pulse. Shadowgrams and interferograms at  $T = 153$  K ( $-120$  °C) and 400 psi valve backing pressure for the probe delays of (b) 20 ps and (c) 2 ns after the pump beam.

## Appendix A: Historical evolution of high peak power lasers

Starting from the first demonstration of the laser in the early 1960's,<sup>1</sup> there has been a remarkable increase in laser peak power over the past several decades, as shown in Fig. A.1. Early lasers were free running to produce kilowatt ( $1 \text{ kW} = 10^3 \text{ W}$ ) pulses as short as micro- to milliseconds, producing peak intensities up to  $\sim 10^9 \text{ W/cm}^2$ . Since then, peak powers dramatically increased from kilowatt to gigawatt ( $1 \text{ GW} = 10^9 \text{ W}$ ) due to the advent of Q-switching (for nanosecond pulse generation)<sup>2-4</sup> and mode locking (picosecond and femtosecond).<sup>5-7</sup> At this point, further power increase was restricted by the nonlinear (Kerr) response of optical materials internal to the laser. At laser peak power in excess of megawatt, optical materials exhibit an intensity-dependent nonlinear refractive index,  $n = n_0 + n_2 I$ , where  $n_0$  is the normal (low intensity) refractive index,  $n_2$  is the nonlinear index of refraction, and  $I$  is the laser intensity.<sup>8</sup> This nonlinear refractive index produces an unwanted nonlinear phase contribution given by<sup>9</sup>

$$B(r, t) = \frac{2\pi n_2}{\lambda} \int_0^L I(r, z, t) dz, \quad (\text{A.1})$$

where  $\lambda$  is the vacuum wavelength and  $L$  is the propagation length in the optical material. For high intensity laser propagation ( $B > 1$ ), this nonlinear phase retardation induces sufficient wave-front distortion to lead to self-focusing of laser pulses, leading to catastrophic beam filamentation and irreversible laser material damage.<sup>10</sup>

To circumvent this power increase limitation, the chirped pulse amplification (CPA) technique was introduced.<sup>11-13</sup> In the CPA scheme, ultrashort pulses are not directly amplified, but they are first stretched and then amplified. In this process, one can achieve

the same energy gain in the laser amplifiers, while reducing the peak power (= energy / time) by the factor of the pulse-stretching ratio. Here the pulse stretching is accomplished by introducing different group velocities for different frequency components (dispersion), which effectively spreads out the pulse. Due to the dispersion, the instantaneous frequency of the stretched pulse changes with time, or is *chirped*, and thus the name “Chirped Pulse Amplification (CPA)”. After leaving the amplification chain, the stretched pulses are recompressed to achieve the highest peak power.

This CPA concept is shown in Fig. A.2. First, a laser oscillator produces an ultrashort optical pulse. Prior to any amplification, the pulse is stretched by a factor of  $\sim 10^4$  in the stretcher from the femtosecond to the nanosecond regime. This pulse stretching reduces the peak intensity accordingly and the energy of the stretched pulse can be safely increased in the amplifier without inducing any nonlinear effects. After a gain of energy by  $10^8 \sim 10^{10}$ , the pulse is finally compressed back to the femtosecond regime, routinely giving peak power in excess of a terawatt ( $1 \text{ TW} = 10^{12} \text{ W}$ ) and peak focused intensity of greater than  $10^{18} \text{ W/cm}^2$ .

The CPA technique has substantially increased laser peak powers from the gigawatt to terawatt regimes in many small tabletop university facilities, as shown in Fig. A.1, and it has also pushed the limit up to the petawatt ( $1 \text{ PW} = 10^{15} \text{ W}$ ) level using larger amplifier facilities, which can be no longer classified as tabletop. Today, high power lasers being developed at large facilities such as national laboratories are capable of delivering subpicosecond pulses of petawatt peak powers and focused intensities approaching  $10^{21} \text{ W/cm}^2$ .<sup>14, 15</sup> This is a remarkable increase in the laser peak power of over 10 orders of magnitude within the last 40 years. Figure A.3 summarizes the history of the development

of subpicosecond terawatt and petawatt lasers <sup>13, 16-43</sup> using CPA technology. The labels are names of current laser facilities around the world.

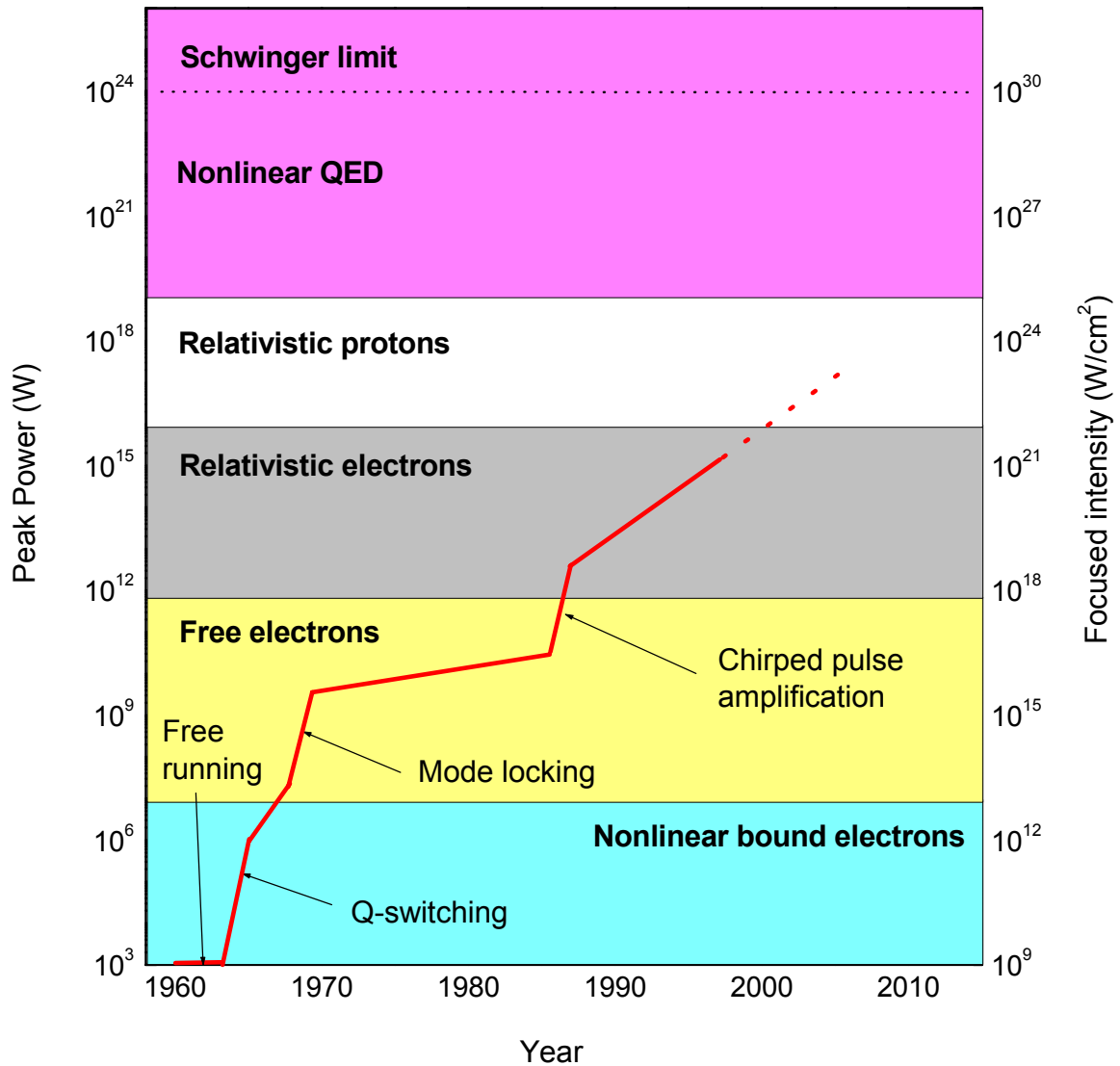


Figure A.1: Increases in peak power and focused intensity of tabletop lasers with year, showing thresholds for various physical phenomena [Adapted and modified from M. D. Perry and G. Mourou, *Science* **264**, 917 (1994); G. A. Mourou, C. P. J. Barty, and M. D. Perry, *Phys. Today* **51**, 22 (January 1998)].

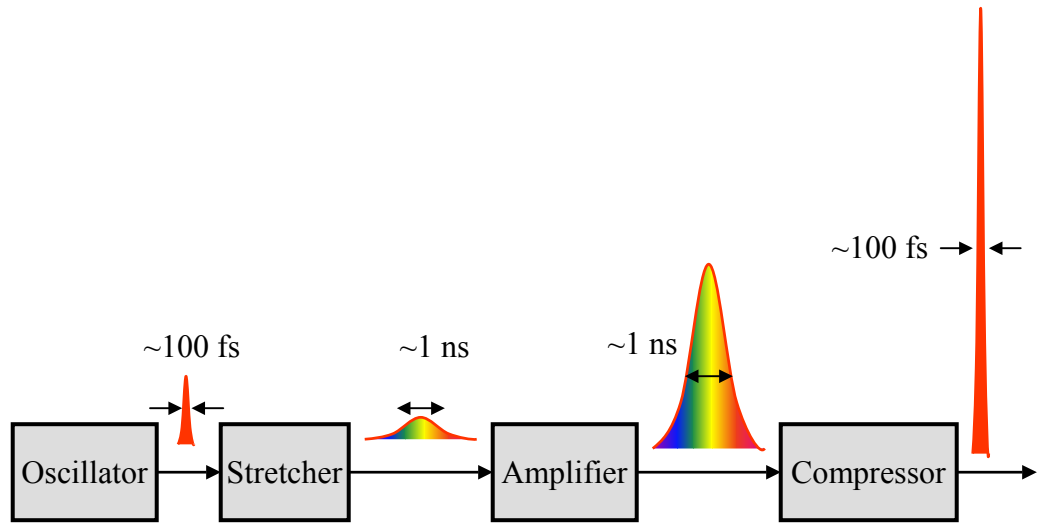


Figure A.2: Schematic of concept of chirped pulse amplification (CPA) technique.

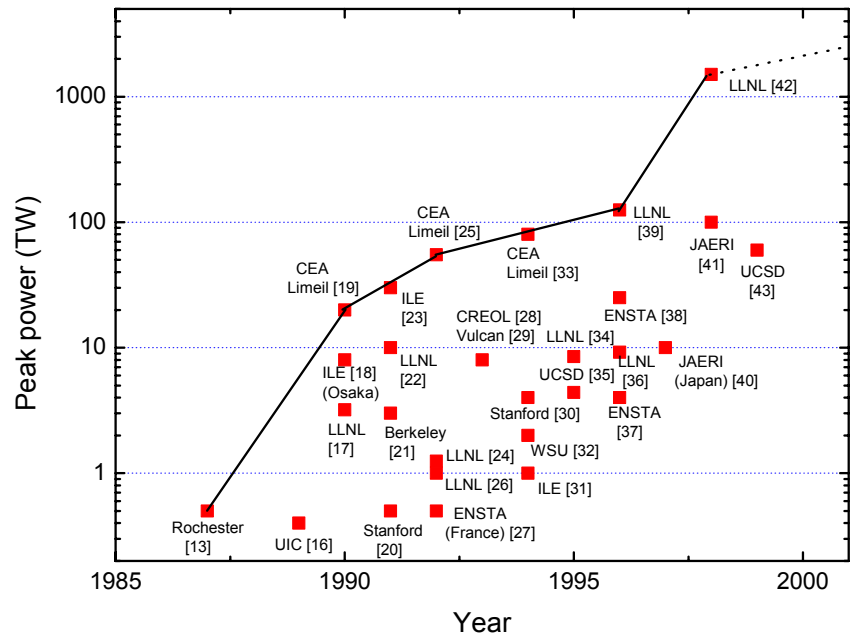


Figure A.3: Development of terawatt and petawatt subpicosecond lasers with chirped pulse amplification (CPA) technology.

## Appendix B: Brief overview of high intensity laser physics

The evolution of laser technology, described in Appendix A, has enabled the study of high intensity physics not possible before in the laboratory experiments. Figure A.1 also shows the regimes of interest with increasing laser peak intensities – nonlinear bound electrons, free electrons, relativistic electrons, relativistic protons, and nonlinear quantum electrodynamics (QED) regimes.<sup>1</sup>

In the bound electron regime, where the peak laser intensity lies up to  $\sim 10^{13}$  W/cm<sup>2</sup>, valence electrons in atoms exhibit a strong nonlinear response to an incident laser field. This characterizes the main feature of nonlinear optics, which has many interesting phenomena and applications.<sup>2,3</sup> For example, the nonlinearity (even at  $10^6$  W/cm<sup>2</sup>) produces an intensity-dependent refractive index in an optical medium as described in Appendix A. Due to the higher nonlinearity on the beam axis (because of higher intensity), this (Kerr) nonlinearity makes the medium act as a lens. With a strong Kerr nonlinearity, an intense laser can self-focus in the medium, competing with its natural diffraction if the laser power exceeds the critical self-focusing power given by<sup>3</sup>

$$P_c = \frac{\lambda^2}{2\pi n_0 n_2}, \quad (\text{B.1})$$

where  $P_c \sim$  megawatt (MW) for solids and  $P_c \sim$  gigawatt (GW) for gases.

In the free electron regime ( $10^{13} \sim 10^{18}$  W/cm<sup>2</sup>), bound electrons can be liberated from atoms owing to the suppressed Coulomb atomic potential by the intense laser electric field. They then form a laser-produced plasma, exhibiting numerous characteristics of laser–plasma interaction. One of applications in this regime is high harmonic generation

(HHG).<sup>4-9</sup> Ultrashort and coherent soft x-ray pulses can be generated with interaction of high intensity femtosecond laser pulses with atoms. In a semi-classical model,<sup>10, 11</sup> bound electrons are liberated by an intense laser field, and they gain kinetic energy (ponderomotive potential energy,  $U_p$ ) in the oscillating laser electric field. After half of the laser period (when the laser exhibits the opposite phase of electric field), the quasi-free electrons return back to their parent ions and with some probabilities they recombine to the ground state of atoms, emitting photons with the energy of the ionization potential plus the kinetic energy of electrons gained in the laser field. In this picture, the highest photon energy of harmonic is given by<sup>10, 11</sup>

$$(\hbar\omega)_{\max} \approx U_i + 3.17U_p, \quad (\text{B.2})$$

where  $U_i$  is the ionization potential and the second term represents the highest kinetic energy obtained in the oscillating laser field. Due to the extremely short temporal duration of high harmonics (as short as a few femtoseconds) and low divergence in the forward direction, they can be potentially used for time-resolved x-ray diffraction or absorption to study the chemical and biochemical reactions and atomic structure with an extremely short time resolution. Recently, this HHG has been directly applied to attosecond (as =  $10^{-18}$  s) spectroscopy,<sup>12-16</sup> in which attosecond extreme-ultraviolet (XUV) pulses are generated<sup>13, 14</sup> and used to probe laser-induced dynamics with an unprecedented time resolution.<sup>15, 16</sup> Indeed, it has allowed the study of the atomic inner shell process such as the relaxation dynamics of core-excited atoms occurring on the attosecond time scale.<sup>15</sup>

In the nonlinear relativistic regime ( $\geq 10^{18}$  W/cm<sup>2</sup>), the quiver motion of electrons in the oscillating laser electric field is relativistic. For example, at an intensity of  $10^{19}$  W/cm<sup>2</sup>, the electric field of laser is close to  $10^{11}$  V/cm from Eq. (1.2), almost twenty times larger

than the Coulomb atomic field  $E_{\text{at}} \sim 5 \times 10^9$  V/cm. At this strong field strength, free electron can gain a cycle-averaged quiver energy (ponderomotive potential energy) of 0.6 MeV from Eq. (1.5) (for laser wavelength  $\lambda = 0.8 \mu\text{m}$ ), which is larger than the electron rest mass  $m_e c^2 = 0.5$  MeV. At this intensity ( $10^{19}$  W/cm<sup>2</sup>), the electron quiver velocity approaches  $0.91 c$ . In addition, at such high intensities ( $>10^{18}$  W/cm<sup>2</sup>),  $\mathbf{v} \times \mathbf{B}$  force in the Lorentz force becomes important, inducing many nonlinear relativistic effects.

Another promising application in the intensity regime ( $\geq 10^{18}$  W/cm<sup>2</sup>) is tabletop laser-driven charged particle accelerators. For a laser intensity of  $10^{18}$  W/cm<sup>2</sup>, the laser electric field reaches  $E \sim 30$  GV/cm from Eq. (1.2). Such a field would potentially accelerate electrons up to 3 TeV energies for only 1 m length, well exceeding the current limit of large scale ( $\sim$  kilometer) synchrotron and linacs. Unfortunately, this strong electric field cannot be directly used for charged particle acceleration because the electric field oscillates transversely to its propagation. However, when an intense laser pulse is focused in plasma, it pushes plasma electrons out of way by the ponderomotive force (the gradient of the radiation pressure), and this charge displacement initiates a longitudinal plasma (Langmuir) wave oscillating at a plasma frequency  $\omega_p = \sqrt{4\pi N_e e^2 / m_e}$ , where  $N_e$  is the plasma density. If the laser pulse duration is of the order of  $\omega_p^{-1}$ , then it can resonantly excite a large amplitude plasma wave (wakefield) as shown in Fig. 1.6. This plasma wave travels at close to the speed of light along the laser propagation direction. It was proposed by Tajima and Dawson in 1979 that this longitudinal electric field of the plasma wake could be used to trap and accelerate charged particles to high energies.<sup>17</sup> The maximum static electric field  $E_{\text{max}}$  of the longitudinal plasma waves resulting from the charge displacement is given by

$$E_{\max} = \sqrt{4\pi N_e m_e c^2} = m_e c (\omega_p / e), \quad (\text{B.3})$$

or  $E_{\max} [\text{V/cm}] = 0.94\sqrt{N_e [\text{cm}^{-3}]}$ . For instance, a plasma with a density of  $N_e = 10^{18} \text{ cm}^{-3}$  can support an electric field  $E_{\max} = 100 \text{ GV/m}$ , which is approximately three orders of magnitude greater than that in conventional synchrotrons and RF linacs, where the electric field is limited to  $\sim 100 \text{ MV/m}$  by the material breakdown in the wave structures. This large electric field gradient is capable of accelerating electrons up to GeV levels on an optical table. Many research groups have reported the acceleration of electrons up to a few hundreds of MeV with electric fields of several tens of GV/m.<sup>18</sup>

Other intense laser–matter interaction applications in the intensity range of  $10^{15} \sim 10^{20} \text{ W/cm}^2$  include bright and x-ray generation in laser-produced plasmas,<sup>19,20</sup> remote sensing metrology, medical physics, laboratory astrophysics with intense lasers,<sup>21,22</sup> and optically induced unclear physics.<sup>23,24</sup> Long pulse (nanosecond) but still high intensity research area is inertial confinement fusion (ICF)<sup>25,26</sup> using a fast-ignition concept.<sup>27</sup>

In the regime of intensity in excess of  $10^{22} \text{ W/cm}^2$ , ions and protons start to show relativistic motions in the laser field, affecting the relativistic plasma dynamics. In the ultrastrong intensity regime where  $I > 10^{25} \text{ W/cm}^2$ , the vacuum begins to act nonlinearly with vacuum polarizability, and quantum electrodynamics (QED) can be examined. Furthermore, near the intensity of  $10^{30} \text{ W/cm}^2$ , the laser field can reach the QED critical field strength (or known as Schwinger field  $E_S = (m^2 c^3)/(e\hbar) = 1.3 \times 10^{16} \text{ V/cm}$ ), at which the electric field could spontaneously break down vacuum, generating electron-positron pairs.<sup>28,29</sup> This occurs when an electron is accelerated to its rest-mass energy in a Compton wavelength,  $\lambda_C = (2\pi\hbar)/(mc)$ . Since current laser technology does not allow accessing this

critical intensity, several approaches have been made to reach the Schwinger limit with present laser intensities. One example is to focus an intense laser pulse into relativistic counter-propagating electron bunches. In the rest frame of electrons, the electric field is increased by a factor of  $2\gamma$ , where  $\gamma$  is the relativistic factor. With this scheme, 30% of the Schwinger limit was obtained with an observation of nonlinear Compton scattering<sup>30</sup> and electron-positron pair production in multiphoton light-by-light scattering.<sup>31</sup>

So far, we have described a variety of physical phenomena unique in intense laser–matter interaction and their potential applications. More details can be found in review papers.<sup>32–35</sup>

## Appendix C: Spectral interferometry (SI)

### C.1 Theoretical background

The laser electric field can be expressed in the time domain as

$$E(t) = \text{Re}\left(E_0(t)e^{-i\omega_0 t + i\Phi(t)}\right), \quad (\text{C.1})$$

where  $E_0(t)$  is the square root of laser intensity,  $\omega_0$  is the carrier frequency,  $\Phi(t)$  is the temporal phase, and  $\text{Re}$  denotes the real part of the complex laser field and will be henceforth omitted. Similarly, its spectral counterpart  $\tilde{E}(\omega)$  is given by

$$\tilde{E}(\omega) = \tilde{E}_0(\omega)e^{i\phi(\omega)}, \quad (\text{C.2})$$

where  $\tilde{E}_0(\omega)$  is the spectral amplitude and  $\phi(\omega)$  is a spectral phase function of  $(\omega - \omega_0)$ .

Here,  $E(t)$  and  $\tilde{E}(\omega)$  are uniquely linked by the following Fourier transform relations:

$$\tilde{E}(\omega) = \int_{-\infty}^{+\infty} E(t)e^{i\omega t} dt \quad (\text{C.3.1})$$

$$E(t) = \frac{1}{2\pi} \int_{-\infty}^{+\infty} \tilde{E}(\omega)e^{-i\omega t} d\omega. \quad (\text{C.3.2})$$

Equations (C.3.1) and (C.3.2) imply that either time or frequency representation of the field completely characterizes the laser pulse. To describe  $\tilde{E}(\omega)$ , one needs to know  $\tilde{E}_0(\omega)$  and  $\phi(\omega)$ . Whereas  $\tilde{E}_0(\omega)$  can be simply determined from the measurement of spectral power  $\tilde{E}_0(\omega) = \sqrt{I(\omega)}$ ,  $\phi(\omega)$  can be hardly obtained with linear interferometry techniques,<sup>1</sup> and the measurement of  $\phi(\omega)$  alone is already a vast research area.

In general, the spectral phase  $\phi(\omega)$  can be expanded in terms of a Taylor series around the carrier frequency  $\omega_0$  as

$$\phi(\omega) = \phi(\omega_0) + \phi'(\omega - \omega_0) + \frac{1}{2}\phi''(\omega - \omega_0)^2 + \frac{1}{6}\phi'''(\omega - \omega_0)^3 \dots, \quad (\text{C.4})$$

where the first-order dispersion  $\phi' = (d\phi/d\omega)_{\omega=\omega_0}$  gives the time shift, and the second-order dispersion  $\phi'' = (d^2\phi/d\omega^2)_{\omega=\omega_0}$  (also called group delay dispersion or GDD) describes a linear chirp, and higher order dispersions such as third-order dispersion (TOD)  $\phi^{(3)} = (d^3\phi/d\omega^3)_{\omega=\omega_0}$ , fourth-order dispersion (4OD)  $\phi^{(4)} = (d^4\phi/d\omega^4)_{\omega=\omega_0}$ , and higher orders lead to a nonlinear chirp. The notation  $\beta_n = 1/n! (d^n\phi/d\omega^n)_{\omega_0}$  is used for the dispersion terms.

## C.2 Principle of spectral interferometry (SI)

A reference pulse  $E_r(t)$  and a  $\tau_0$ -delayed probe pulse  $E_{pr}(t) = E_r(t - \tau_0)e^{i\Delta\Phi(t-\tau_0)}$ , upon which a time-dependent phase shift  $\Delta\Phi(t)$  has been imposed, interfere in the frequency domain according to

$$\begin{aligned} \left| \tilde{E}_r(\omega) + \tilde{E}_{pr}(\omega) \right|^2 &= \left| \tilde{E}_{r0}(\omega)e^{i\phi_r(\omega)} + \tilde{E}_{pr0}(\omega)e^{i\phi_{pr}(\omega)} \right|^2 \\ &= \left| \tilde{E}_{r0}(\omega) \right|^2 + \left| \tilde{E}_{pr0}(\omega) \right|^2 + 2\left| \tilde{E}_{r0}(\omega) \right| \left| \tilde{E}_{pr0}(\omega) \right| \cos[\Delta\phi(\omega)] \end{aligned} \quad (\text{C.6})$$

where  $\tilde{E}_r(\omega) = \tilde{E}_{r0}(\omega)e^{i\phi_r(\omega)}$  and  $\tilde{E}_{pr}(\omega) = \tilde{E}_{pr0}(\omega)e^{i\phi_{pr}(\omega)}$  are the Fourier transforms of  $E_r(t)$  and  $E_{pr}(t)$  via Eq. (C.3.1), the spectral amplitudes  $\tilde{E}_{r0,pr0}$  and phases  $\phi_{r,pr}$  are real, and  $\Delta\phi(\omega) = \phi_{pr}(\omega) - \phi_r(\omega) + \omega\tau_0$  is the spectral phase difference between the probe and reference pulses.

To understand Eq. (C.6), we consider a few examples of spectral interference. Figure C.1 shows various electric fields and their corresponding spectra for Gaussian reference  $E_r(t) = \exp(-4 \ln 2 t^2 / \tau_e^2 - i\omega_0 t)$  and  $\tau_0$ -delayed probe  $E_{pr}(t) = T_0 E_r(t - \tau_0) e^{i\Delta\Phi}$  pulses under an external phase modulation  $\Delta\Phi$ . The central wavelength is taken to be  $\lambda_0 = 400$  nm and the pulse durations are  $\tau_e = 50$  fs. Plotted in Fig. C.1(a), under the absence of external phase modulation (i.e.,  $\Delta\Phi = 0$ ),  $\tau_0 = 250$  fs and  $T_0 = 1$ , the spectrum  $|\tilde{E}_r(\omega) + \tilde{E}_{pr}(\omega)|^2$  exhibits strong modulations with a period of  $\delta\omega = 2\pi/\tau_0$  or  $\delta\lambda = -\lambda^2(c\tau_0)^{-1} = 2.13$  nm (for  $\tau_0 = 250$  fs). However, in (b) with a  $\Delta\Phi = \pi$  applied to the probe and  $T_0 = 1$ , the spectral modulation shifts by  $\Delta\phi = \pi$  compared to (a). With a twice-longer reference-probe separation ( $\tau_0 = 500$  fs) in (c), the spectral modulation frequency also increases by a factor of two, while maintaining the  $\pi$ -phase shift. If the reference and probe intensities are different (i.e.,  $T_0^2 \neq 1$ ), the fringe visibility of spectral modulations is reduced to  $V = (I_{\max} - I_{\min}) / (I_{\max} + I_{\min}) = 2T_0 / (1 + T_0^2)$  where  $I_{\max}$  and  $I_{\min}$  are the maximum and minimum spectral intensities in the immediate neighborhood of the modulations. For example, if the probe intensity transmission is  $T_0^2 = 0.1$  as shown in (d), then the modulation becomes weaker but is still distinct enough to identify the externally applied  $\pi$ -phase shift.

A question may arise as to how two temporally separated pulses can interfere with each other to make interference fringes. A physical explanation, previously given by Tokunaga *et al.*,<sup>2</sup> is that the reference and probe pulses are temporally stretched by the linear dispersion of the grating in a spectrometer (which is used in the actual SI diagnostic) and then they overlap in time and space in the image plane of the spectrometer, where they interfere. Figure C.2 illustrates the pulse stretching and interference mechanism inside a

spectrometer. Reference  $E_r(t)$  and probe  $E_{pr}(t)$  pulses with a  $\tau_0$  separation enter the spectrometer through the slit. The  $\lambda$ -wavelength components of both  $E_r(t)$  and  $E_{pr}(t)$  diffract at an angle of  $\theta_m$  according to the grating equation  $d\sin\theta_m = m\lambda$  where  $d$  is the grating groove period and  $m$  (integer) is the order of the diffraction principal maxima. As shown in Fig. C.2(a), grating diffraction stretches the pulse duration of the  $\lambda$ -component by  $D_0\sin\theta/c$  where  $D_0$  is the beam size on the grating. The stretched  $\lambda$ -components of  $E_r(t)$  and  $E_{pr}(t)$  interfere on the CCD camera plane to record the total intensity  $I_{tot}(\lambda)$ , the amplitude of which strongly depends on the reference-probe relative phase  $\Delta\phi(\lambda)$  and separation  $\tau_0$ . If  $n\lambda_n = c\tau_0$ , where  $n$  is an integer, and  $\Delta\phi(\lambda_n) = 0$ , then the  $\lambda_n$ -components of both reference and probe pulses interfere constructively to yield a maximum in  $I_{tot}(\lambda)$ . However, for  $(n + 1/2)\lambda_n = c\tau_0$ , they exhibit destructive interference, minimizing  $I_{tot}(\lambda)$ . Here, the spectral modulation period  $\delta\omega$  can be determined from the separation of two adjacent constructive interference peaks as  $\delta\omega = \omega_{n+1} - \omega_n = 2\pi c(\lambda_{n+1}^{-1} - \lambda_n^{-1}) = 2\pi/\tau_0$ . In addition, the use of an imaging spectrometer shown in Fig. C.2(b) provides spectral intensity modulations  $I_{tot}(x, \lambda)$  with 1D space ( $x$ ) information.

The shift in the spectral intensity modulation is directly related to the reference-probe phase shift  $\Delta\phi$ . If such phase shifts are time dependent, then spectral interferometry (SI) can be used to extract them. In particular, for a pump pulse  $E_p(t)$ , one can examine the pump-induced phase variations  $\Delta\Phi(t)$  in a target medium by locating  $E_p(t)$  after  $E_r(t)$  but before, during, or after  $E_{pr}(t)$  and monitoring the spectral intensity modulation shift  $\Delta\phi$  imposed on  $E_{pr}(t)$  with a spectrometer. In a multiple-shot experiment, by varying the pump-probe separation  $\tau$ , one can map out the entire pump-induced phase shift  $\Delta\Phi(t)$ . Such an

experiment gives a useful result if (a) there is shot-to-shot reproducibility and (b) the pulse width of  $E_r(t)$  and  $E_{pr}(t)$  are narrow compared to the variation timescale of  $\Delta\Phi(t)$ . This technique will be discussed in the next section.

### C.3 Demonstration of multi-shot spectral interferometry

As an experimental demonstration of a time-resolved SI diagnostic, we performed a pump-probe experiment in a helium gas target. The goal was the observation of the femtosecond time-resolved dynamics of helium ionization in intense pump laser fields. Figure C.3(a) shows the experimental setup. An intense 800-nm 100-fs pump pulse with a peak intensity  $I_{\text{peak}} \sim 10^{17}$  W/cm<sup>2</sup> was focused in a helium gas jet collinearly with weak 400-nm sub-100-fs twin pulses (reference and probe). The pump induces femtosecond optical-field-ionization in the helium gas, transiently modifying the macroscopic refractive index of the gas (see Chapters 1 & 4 for a detailed description of laser-induced ionization). A reference pulse, preceding the pump in time, does not experience any perturbation. However, the  $\tau$ -delayed probe pulse picks up a phase shift due to the refractive index change that precedes it. The reference and probe pulses were imaged onto the slit of an imaging spectrometer.

The insets in Fig. C.3(b) show the spectral interferograms of the reference and probe, recorded on the CCD on the image plane of the spectrometer, with the pump pulse (i) off and (ii) on at a delay of  $\tau = 180$  fs. After the gas jet, the pump pulse is removed from the beam by a high reflectivity 800 nm mirror which allows passage of the 400 nm reference and probe pulses to the spectrometer. The vertical ( $x$ ) and horizontal ( $\lambda$ ) axes are space and wavelength, respectively. There is a noticeable phase shift in the center of (ii)

where the pump ionized the helium. The central line-outs are plotted in (iii) with the pump-off (dashed line) and pump-on (solid line), exhibiting a clear spectral modulation shift.

Here the fringe shift  $\Delta\lambda/\delta\lambda$  is proportional to  $\Delta\phi(\tau)$  where  $\Delta\lambda$  is the wavelength shift of the fringe peak and  $\delta\lambda$  is the wavelength separation of two adjacent fringe peaks. By varying the pump-probe delay  $\tau$  with a fixed reference-probe separation  $\tau_0$ , the ionization-induced phase shift  $\Delta\phi(\tau)$  is mapped out as shown in Fig. C.3(b). The plot shows the rapid onset of free electron density from the neutral gas under the illumination of an intense femtosecond laser pulse.

This experiment confirms that SI can be utilized as a time-resolved optical diagnostic in the multi-shot pump-probe regime. This multi-shot spectral interferometry, however, is extremely vulnerable to the shot-to-shot instability of the laser in energy, pulsewidth, mode quality, and pointing as well as shot-to-shot variations in target conditions. These fluctuations enhance measurement errors and thereby deteriorate the retrieved phase information. For sufficiently large fluctuations, the recovered transient could potentially be completely masked. To overcome this problem, single-shot spectral interferometry (SSI) is strongly demanded. SSI and our method (SSSI) are discussed in Chapter 2 of this dissertation.

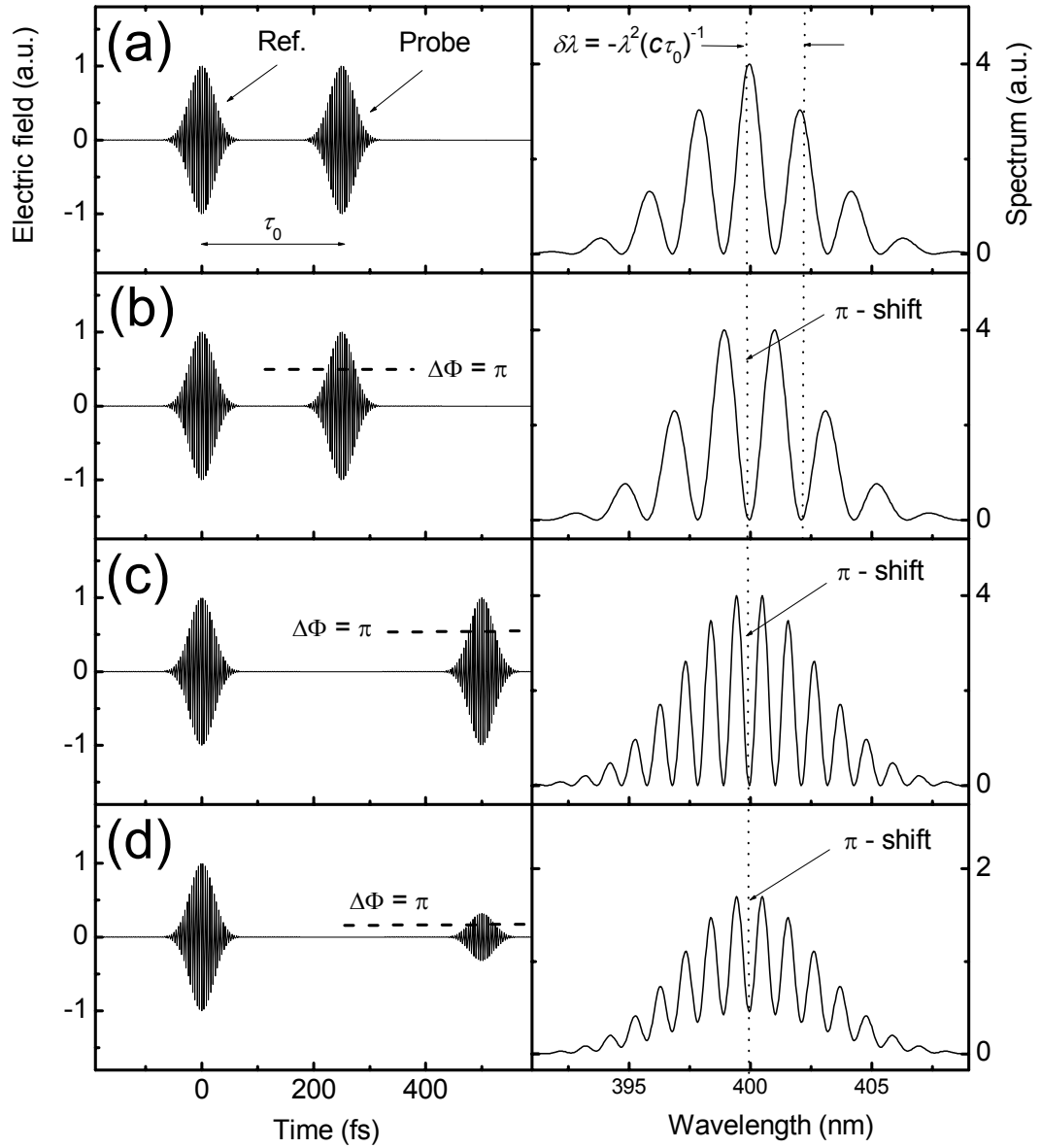


Figure C.1: Electric fields and the corresponding spectra of a Gaussian reference pulse  $E_r(t) = \exp(-4 \ln 2 t^2 / \tau_e^2 - i\omega_0 t)$  and  $\tau_0$ -delayed probe pulse  $E_{pr}(t) = T_0 E_r(t - \tau_0) e^{i\Delta\Phi}$ , upon which a phase shift  $\Delta\Phi$  and amplitude transmission  $T_0$  has been imposed. For (a)-(c),  $T_0^2 = 1$ . For (d),  $T_0^2 < 1$ .

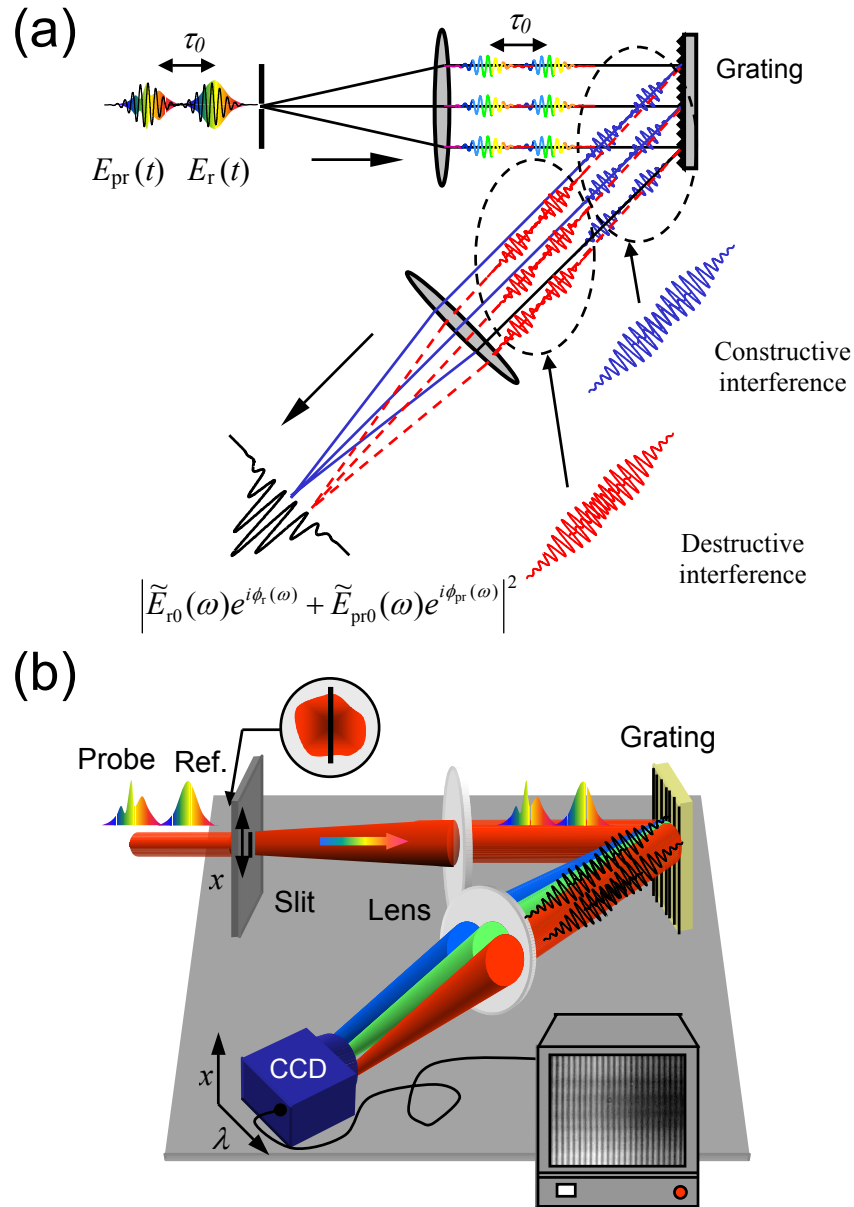


Figure C.2: (a) Diagram showing how two temporally separated pulses, reference  $E_r(t)$  and probe  $E_{pr}(t)$ , can interfere each other in the frequency domain.  $E_r(t)$  and  $E_{pr}(t)$  are stretched in time after the grating diffraction inside a spectrometer, then temporally overlapping and interfering on the imaging plane of spectrometer. (b) Perspective view of an imaging spectrometer, capable of providing spectral intensity modulations  $I(x, \lambda)$  with 1D space information.

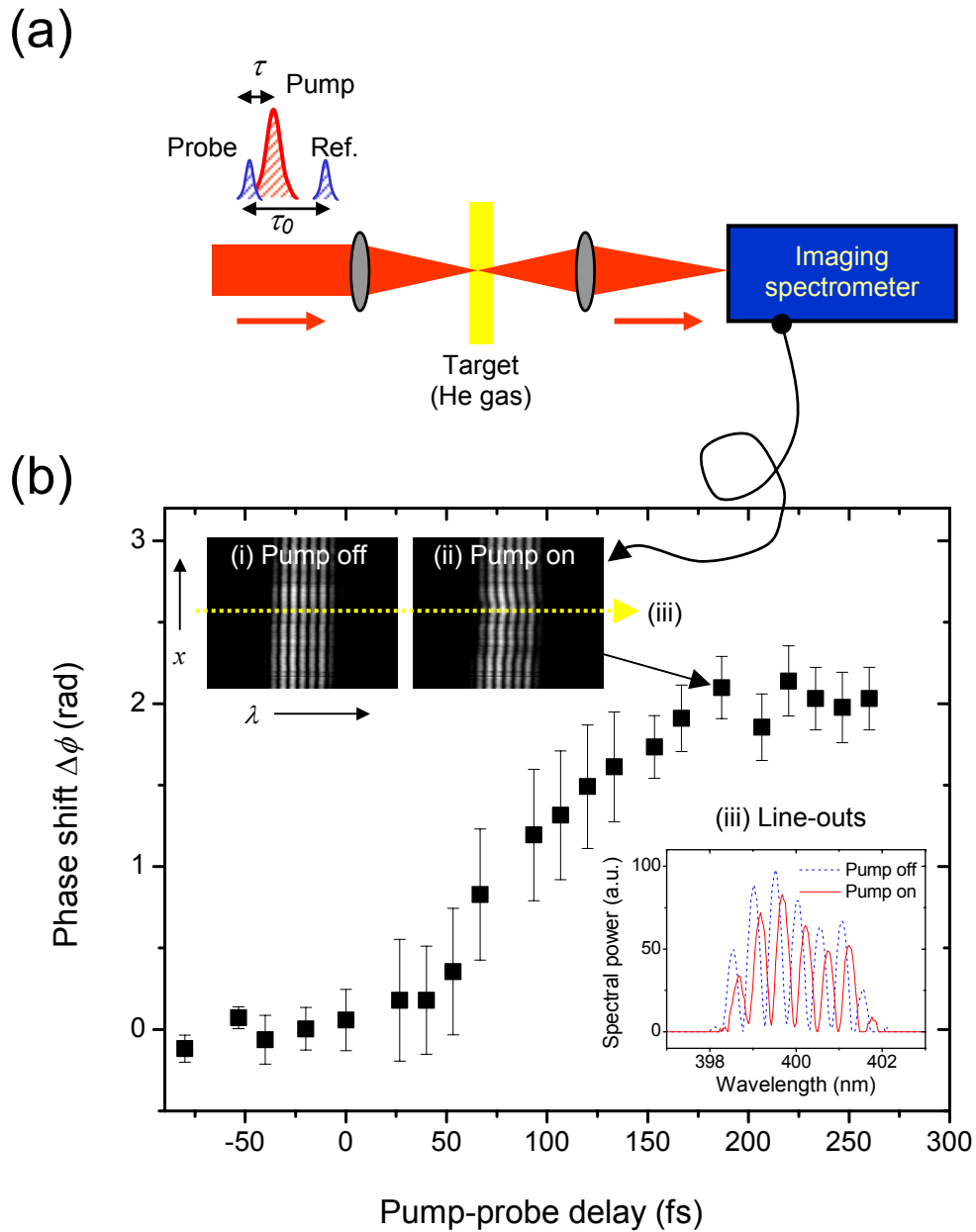


Figure C.3: (a) Schematic of general multi-shot spectral interferometry scheme. Here it was applied to the femtosecond ionization of helium. See text for details. (b) Plots of the probe phase shift  $\Delta\phi$  versus pump-probe delay  $\tau$ . The central lineouts of the spectral interferograms are plotted in (iii) with the pump-off (dashed line) and pump-on (solid line) modes.

## Appendix D: Generation of a supercontinuum light pulse

The laser-based generation of supercontinuum (SC) or coherent white light is essential to provide the large optical bandwidths necessary for the excellent temporal resolution associated with the chirped spectral interferometry diagnostic. SC generation in condensed media was first reported by Alfano and Shapiro.<sup>1,2</sup> Later, SC generation was extended to other bulk media,<sup>3,4</sup> liquids,<sup>3,5</sup> and gases.<sup>6-9</sup> SC generation in transparent condensed media is attractive owing to the source compactness and the typically broad spectral bandwidth. For example, SC with  $\Delta\lambda > \sim 200$  nm in a sapphire window was demonstrated.<sup>3,4</sup>

Typically, the onset of SC occurs at a laser power of  $P \approx P_{\text{cr}}$  where  $P_{\text{cr}} = \lambda^2 (2\pi n_0 n_2)^{-1}$ , where  $n_0$  is the normal refractive index and  $n_2$  is the nonlinear refractive index coefficient, is the critical power for self-focusing in the medium producing SC (see Chapter 3). Generally, the yield of SC increases with laser intensity. However, at  $P > P_{\text{cr}}$ , small-scale multi-filament SC is formed. As shown in Fig. D.1(a), the SC generated in a sapphire window at  $P > P_{\text{cr}}$  ( $P_{\text{cr}} \approx 3\text{MW}$  for sapphire glass) is multiply filamented with associated severe spatial and temporal phase distortion. The inset shows a sample interferogram, obtained from the interference between an SC pulse and a  $\sim$  ps delayed SC twin replica, clearly exhibiting significant spatio-temporal phase distortions. To produce a coherent single filament SC, which is indispensable for interferometry, the pump power needs to be limited to  $P_{\text{cr}}$ . This limits maximum useable femtosecond pump energies in bulk media to the microjoule range. The result of this limitation on pump energy is sub-

nanojoule SC pulses. This too low for an adequate signal-to-noise ratio in our single-shot experiments, where background contributions from pump-induced nonlinearities or from plasma emission are significant.

To increase the SC energy in a single filament, we used atmospheric pressure air as the nonlinear medium for SC generation ( $P_{cr} = 1.8$  GW for 1 atm air at 787 nm). Figure D.1(b) shows the SC spectrum generated from  $f/8$  focusing of a  $\sim 1$  mJ, 80 fs pulse in 1 atm of air. The broad bandwidth is generated from self-phase modulation owing to the neutral gas nonlinear response ( $n_2$ ) to the laser field as well as from ultrafast field ionization. The overall spectral bandwidth of our generated SC is  $\sim 200$  nm, but the SC spectrum above 740 nm was cut off by a 800 nm mirror (used to filter the pump pulse from the collinear pump, probe, and reference beams), leaving the SC pulse with a useable  $\sim 100$  nm bandwidth. Produced by this method, SC pulses contained up to  $\sim 1$  mJ of energy.

Figure D.1(b), a 1D spectrally resolved image of the end of the filament, shows that our air SC source originated from a single filament in the focal region. The central spatial “hole” in the image is created by the 800 nm filter mirror, which removes the pump and its nearby spectral components. A strong spatial chirp is seen where the SC average wavelength is increasingly blue-shifted with radius. This “conical emission” (CE) is a universal phenomenon in SC generation, observed in all nonlinear media used thus far.<sup>1, 2, 10-13</sup> Even though CE was first reported three decades ago, its detailed origin is currently under debate with various proposed mechanisms: four-photon parametric generation (FPPG),<sup>1, 10</sup> Čerenkov-type processes,<sup>11</sup> moving focus model,<sup>12</sup> and others. In general, the CE-induced spatial chirp can be unfavorable for the implementation of SSSI and must be reduced or eliminated. In our experiment, the spatial chirp was reduced by filtering the SC

with a pinhole, resulting in a SC pulse energy reduction. A better scheme might be to generate and guide SC pulses in a hollow fiber made of fused silica and filled with various gases.<sup>14, 15</sup> The waveguiding process can spatially mix the transverse distribution of SC wavelengths and phases to produce a beam with transversely spatially uniform spectral phase properties.

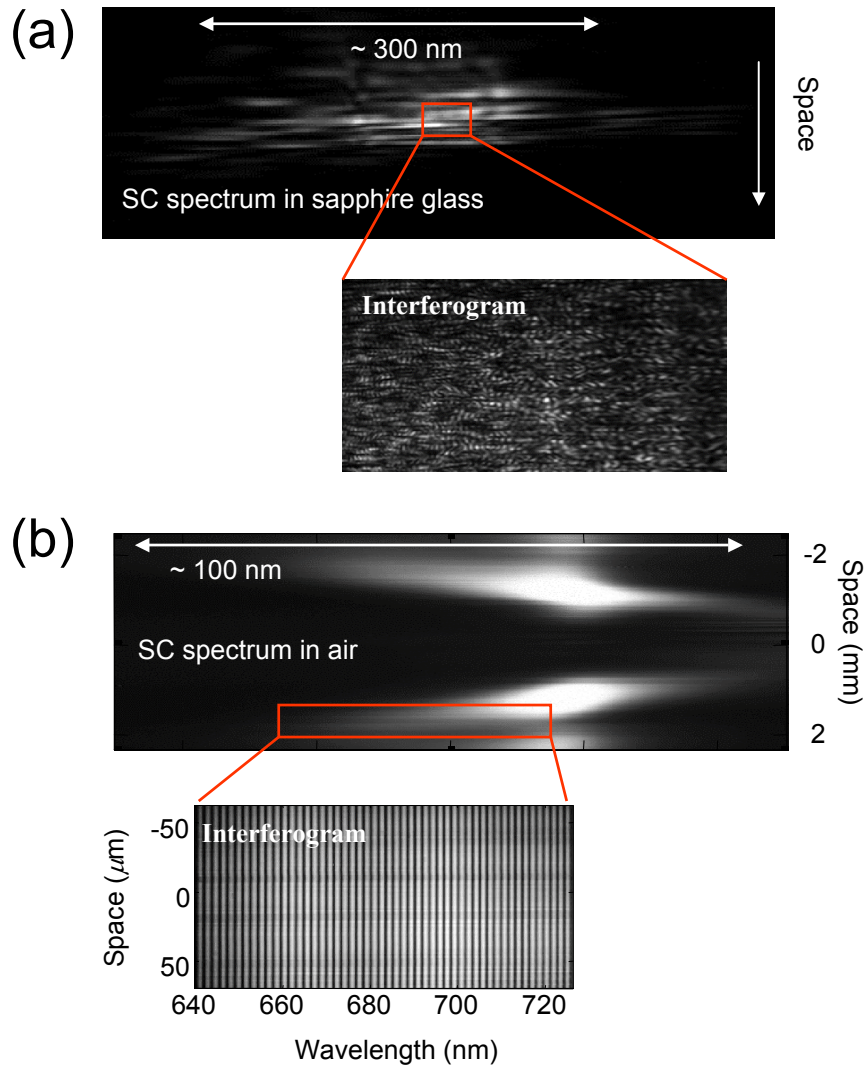


Figure D.1: Spectra of supercontinuum (SC) light generated by a femtosecond Ti:sapphire laser pulse focused in (a) sapphire window at  $P > P_{\text{cr}}$  and (b) atmospheric pressure air. Each inset shows the spectral interferogram, obtained from interference between the SC pulse and a  $\sim$ ps delayed SC twin replica. The spectral fringes in (a) are completely washed out due to the multi-filament SC generation with phase disruptions, whereas a single SC filament with a coherent  $\sim 100$  nm spectral bandwidth was obtained in (b).

## Appendix E: Transient phase measurement with a chirped pulse

### E.1 Description of chirped pulses in time and frequency domains

A linearly chirped pulse with a Gaussian spectrum is expressed as

$$\tilde{E}(\omega) = E_0 \exp\left(-\alpha(\omega - \omega_0)^2 + i\beta(\omega - \omega_0)^2\right), \quad (\text{E.1})$$

where the spectral width (FWHM)  $\Delta\omega$  is

$$\Delta\omega = \sqrt{2 \ln 2 / \alpha} \quad (\text{E.2})$$

and  $\beta = \frac{1}{2}(\partial^2 \phi / \partial \omega^2)_{\omega_0}$  is the group delay dispersion. The corresponding temporal field

$E(t)$  can be obtained from Eq. (E.1) with an inverse Fourier transform as follows.

$$\begin{aligned} E(t) &= \frac{1}{2\pi} \int_{-\infty}^{+\infty} \tilde{E}(\omega) \exp(-i\omega t) d\omega \\ &= iE_0 \sqrt{(\hat{\alpha} + i\hat{\beta}) / \pi} \exp\left(-\hat{\alpha}t^2 - i\omega_0 t - i\hat{\beta}t^2\right), \end{aligned} \quad (\text{E.3})$$

where  $\hat{\alpha} \equiv \alpha/4(\alpha^2 + \beta^2)$ ,  $\hat{\beta} \equiv \beta/4(\alpha^2 + \beta^2)$ , and  $\omega(t) = -d\Phi(t)/dt = \omega_0 + 2\hat{\beta}t$  is the

instantaneous frequency. The chirp coefficient  $a$  is defined as

$$a \equiv \frac{1}{2\hat{\beta}} = \frac{2(\alpha^2 + \beta^2)}{\beta} = 2\beta \left(1 + (2 \ln 2)^2 \beta^{-2} \Delta\omega^{-4}\right). \quad (\text{E.4})$$

Form Eq. (E.3), the FWHM pulse duration of the chirped beam  $\Delta t$  is given by

$$\Delta t = \sqrt{\frac{2 \ln 2}{\hat{\alpha}}} = \sqrt{\frac{8 \ln 2 (\alpha^2 + \beta^2)}{\alpha}} = \frac{4 \ln 2}{\Delta\omega} \left(1 + \frac{\beta^2 \Delta\omega^4}{(2 \ln 2)^2}\right)^{1/2}. \quad (\text{E.5})$$

## E.2 Derivation of temporal resolution associated with direct mapping

Suppose that a chirped probe pulse  $E(t)$  experiences an external small Gaussian phase modulation  $\Delta\Phi(t, \tau) = \delta \exp\left(-4 \ln 2 (t - \tau)^2 / \tau_e^2\right)$ , where  $|\delta| \ll 1$  and  $\tau$  is the relative delay between the probe and perturbation and  $\tau_e$  is the modulation FWHM. Then, the perturbed probe phase  $E_{\text{pert}}(t)$  which is modulated by  $\Delta\Phi(t, \tau)$ , is expressed as

$$\begin{aligned} E_{\text{pert}}(t) &= E(t) \exp(i\Delta\Phi(t, \tau)) \\ &\approx E(t)(1 + i\Delta\Phi(t, \tau)) \\ &= E(t) + \Delta E(t, \tau), \end{aligned} \quad (\text{E.6})$$

where  $\Delta E(t, \tau) = -\delta E_0 \sqrt{(\hat{\alpha} + i\hat{\beta})/\pi} \exp\left(-\hat{\alpha}t^2 - s^2(t - \tau)^2 - i\omega_0 t - i\hat{\beta}t\right)$  and  $s = 4 \ln 2 / \tau_e^2$ .

With a Fourier transform, the corresponding spectral field  $\tilde{E}_{\text{pert}}(\omega, \tau)$  is obtained as

$$\begin{aligned} \tilde{E}_{\text{pert}}(\omega, \tau) &= \text{FT}[E(t) + \Delta E(t, \tau)] \\ &= \tilde{E}(\omega) + \Delta\tilde{E}(\omega, \tau), \end{aligned} \quad (\text{E.7})$$

where

$$\begin{aligned} \Delta\tilde{E}(\omega, \tau) &= \int_{-\infty}^{+\infty} \Delta E(t, \tau) \exp(i\omega t) dt \\ &= -\delta E_0 \sqrt{\frac{\hat{\alpha} + i\hat{\beta}}{\hat{\alpha} + s^2 + i\hat{\beta}}} \exp(-s^2 \tau^2) \exp\left(\frac{(2s^2 \tau + i(\omega - \omega_0))^2}{4(\hat{\alpha} + s^2 + i\hat{\beta})}\right) \end{aligned} \quad (\text{E.8})$$

$$\frac{\Delta\tilde{E}(\omega, \tau)}{\tilde{E}(\omega)} = -\delta \sqrt{\frac{\hat{\alpha} + i\hat{\beta}}{\hat{\alpha} + s^2 + i\hat{\beta}}} \exp(-s^2 \tau^2) \exp\left(\frac{(2s^2 \tau + i(\omega - \omega_0))^2}{4(\hat{\alpha} + s^2 + i\hat{\beta})} + (\alpha - i\beta)(\omega - \omega_0)^2\right). \quad (\text{E.9})$$

For  $\omega = \omega_0$ , Eq. (E.9) becomes

$$\frac{\Delta\tilde{E}(\omega = \omega_0, \tau)}{\tilde{E}(\omega = \omega_0)} = -\delta \sqrt{\frac{\hat{\alpha} + i\hat{\beta}}{\hat{\alpha} + s^2 + i\hat{\beta}}} \exp\left(\frac{4s^4 \tau^2}{4(\hat{\alpha} + s^2 + i\hat{\beta})} - s^2 \tau^2\right) \propto \exp\left(-\frac{\tau^2}{T^2}\right), \quad (\text{E.10})$$

where

$$T^2 = \frac{1}{s^2} + 4(\alpha - i\beta) = \frac{\tau_e}{4\ln 2} + 4(\alpha - i\beta). \quad (\text{E.11})$$

As the external modulation duration approaches a  $\delta$ -function in the limit of impulse perturbation [i.e.  $\tau_e \rightarrow 0$  and  $T^2 \rightarrow 4(\alpha - i\beta)$ ], then from Eq. (E.10) we obtain

$$\left| \frac{\Delta\tilde{E}(\tau)}{\tilde{E}(\omega)} \right|^2 \propto \exp\left(-\frac{\tau^2}{2(\alpha^2 + \beta^2)/\alpha}\right) = \exp\left(-\frac{\tau^2}{\tau_{\text{res}}^2}\right), \quad (\text{E.12})$$

where  $\tau_{\text{resol}} = \sqrt{2(\alpha^2 + \beta^2)/\alpha}$  is the decay time of  $|\Delta\tilde{E}(\tau)/\tilde{E}(\omega)|$ , equivalent to the minimum time interval that contributes to the phase shift at the fixed probe frequency  $\omega = \omega_0$  in response to the impulse perturbation. Here  $\tau_{\text{resol}}$  represents the temporal resolution of the chirped pulse with the direct mapping method. From Eq. (E.2),  $\tau_{\text{resol}}$  is expressed as

$$\begin{aligned} \tau_{\text{resol}} &= \sqrt{\frac{2(\alpha^2 + \beta^2)}{\alpha}} \\ &\approx \frac{1}{\Delta\omega} [1 + \beta^2 \Delta\omega^4]^{1/2}. \end{aligned} \quad (\text{E.13})$$

Tokunaga *et al.* derived a similar expression for the temporal resolution  $\tau_{\text{resol}}$ , expressed as  $\tau_{\text{resol}} = 2[\alpha^2 + \beta^2]^{1/4} \approx 2\Delta\omega^{-1}[1 + \beta^2\Delta\omega^4]^{1/4}$ .<sup>1</sup> We note that the difference between that result and ours arises from the interpretation of Eq. (E.9) to define the relaxation time.

### E.3 Direct mapping: simulation

To illustrate the dependence of temporal resolution on the chirp and spectral bandwidth, we simulate spectral probe phase variations perturbed by an external phase modulation  $\Delta\Phi_{\text{ext}}(t)$ , as shown in Fig. E.1. Gaussian reference and probe pulses have (a)  $\Delta\lambda$

= 4 nm, (b) 8 nm, and (c) 32 nm bandwidths (FWHM) and (i)  $\tau_e = 100$  fs, (ii)  $\tau_e = 200$  fs, and (iii)  $\tau_e = 400$  fs pulse durations (FWHM) at  $\lambda_0 = 400$  nm with mutual separation  $\tau_0 = 1$  ps. This gives different chirp rates from Eq. (E.4). Suppose that an external phase modulation (dashed lines)  $\Delta\Phi_{\text{ext}}(t)$  is applied to the probe pulse where  $\Delta\Phi_{\text{ext}}(t) = 0$  for  $t \leq -50$  fs,  $(\pi/100)(t+50)$  for  $-50 \text{ fs} \leq t < 50 \text{ fs}$ , and  $\pi$  for  $t > 50$  fs, respectively. The retrieved temporal phases  $\Delta\Phi_{\text{ret}}(t)$  using the direct mapping technique are plotted with solid lines. We observe that, for a given spectral bandwidth, the increase of chirp [from (i) to (iii)] gradually degrades the retrieved temporal phase, and therefore the effective temporal resolution is degraded. For a fixed probe/reference pulse duration, the error associated with  $\Delta\Phi_{\text{ret}}(t)$  decreases with increasing spectral bandwidth [from (a) to (c)]. This simulation implies that better temporal resolution can be obtained with broader spectral bandwidth and smaller chirps. A large chirp, which is necessary for a wide temporal observation window, can induce unwanted phase distortions and degrade the temporal resolution, as predicted by Eq. (E.13).

#### E.4 Derivation of transient phase shifts using Fourier transform

A  $\tau_0$ -delayed probe pulse  $E_{\text{pr}}(t)$ , experiencing a pump-induced time-varying transmission  $T(t)$  and phase shift  $\Delta\Phi(t)$ , with respect to a reference pulse  $E_{\text{r}}(t)$ , is expressed as

$$E_{\text{pr}}(t) = T(t - \tau_0)E_{\text{r}}(t - \tau_0)e^{i\Delta\Phi(t - \tau_0)}. \quad (\text{E.14})$$

From Eq. (E.14), we get the probe phase shift  $\Delta\Phi(t - \tau_0)$  as follows:

$$\begin{aligned}
\Delta\Phi(t - \tau_0) &= \text{Im} \left[ \ln \left( \frac{E_{\text{pr}}(t)}{T(t - \tau_0)E_r(t - \tau_0)} \right) \right] \\
&= \text{Im} \left[ \ln \left( \frac{E_{\text{pr}}(t)}{E_r(t - \tau_0)} \right) \right] - \text{Im}[T(t - \tau_0)] \\
&= \text{Im} \left[ \ln \left( \frac{E_{\text{pr}}(t)}{E_r(t - \tau_0)} \right) \right].
\end{aligned} \tag{E.15}$$

Using the Fourier transform from Eq. (C.3.2), the reference and probe pulses in the time domain can be rewritten in the frequency domain as follows:

$$\begin{aligned}
\Delta\Phi(t - \tau_0) &= \text{Im} \left[ \ln \left( \frac{\int \tilde{E}_{\text{pr}}(\omega) e^{-i\omega t} d\omega}{\int \tilde{E}_r(\omega) e^{-i\omega(t - \tau_0)} d\omega} \right) \right] \\
&= \text{Im} \left[ \ln \left( \frac{\int \tilde{E}_{\text{pr}0}(\omega) e^{i\phi_r(\omega) + i\Delta\phi(\omega)} e^{-i\omega(t - \tau_0)} d\omega}{\int \tilde{E}_{r0}(\omega) e^{i\phi_r(\omega)} e^{-i\omega(t - \tau_0)} d\omega} \right) \right],
\end{aligned} \tag{E.16}$$

where  $\phi_{r, \text{pr}}(\omega)$  is the reference and probe spectral phase, respectively, and

$\Delta\phi(\omega) = \phi_{\text{pr}}(\omega) - \phi_r(\omega) + \omega\tau_0$  is the spectral phase difference between the probe and

reference pulses. With introduction of a dummy variable,  $t' = t - \tau_0$ , we finally obtain

$$\Delta\Phi(t') = \text{Im} \left[ \ln \left( \frac{\int \tilde{E}_{\text{pr}0}(\omega) e^{i\phi_r(\omega) + i\Delta\phi(\omega)} e^{-i\omega t'} d\omega}{\int \tilde{E}_{r0}(\omega) e^{i\phi_r(\omega)} e^{-i\omega t'} d\omega} \right) \right]. \tag{E.17}$$

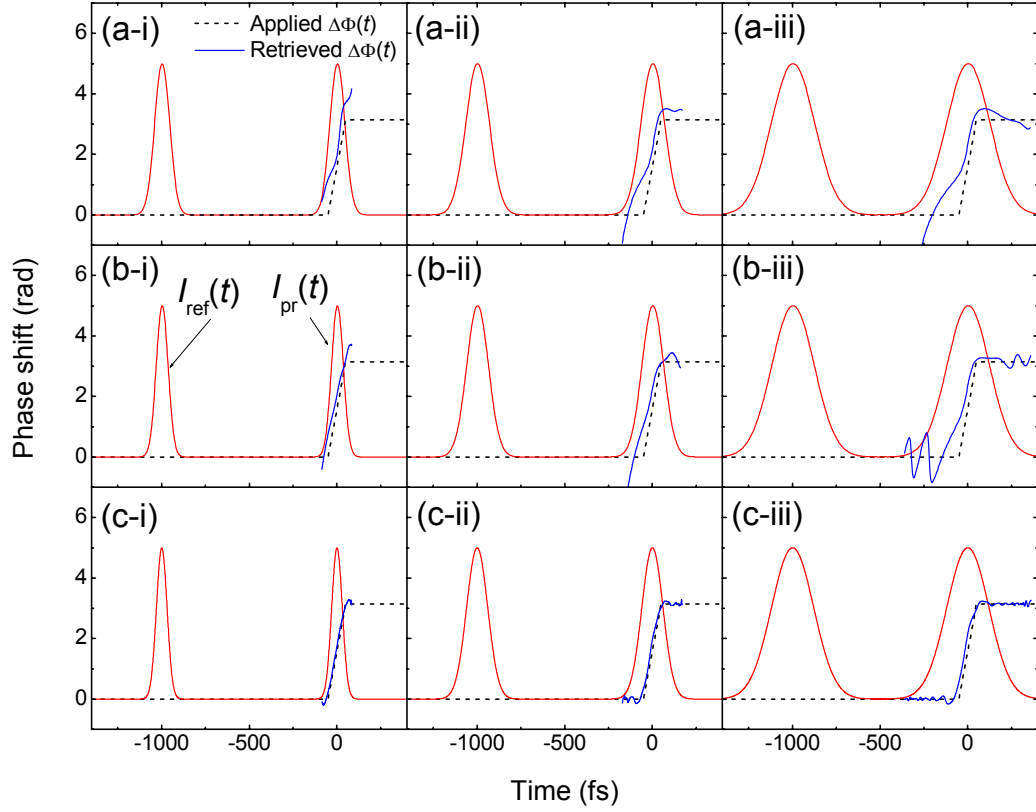


Figure E.1: Simulation results for the retrieved phase  $\Delta\Phi_{\text{ret}}(t)$  (solid lines) with the direct mapping method. An external phase modulation (dashed lines)  $\Delta\Phi_{\text{ext}}(t) = 0$ ,  $(\pi/100)(t+50)$ , and  $\pi$  for  $t < -50$  fs,  $-50$  fs  $< t < 50$  fs, and  $t > 50$  fs, respectively, is applied to the probe pulse. The reference and probe spectral bandwidths (FWHM) are (a)  $\Delta\lambda = 4$  nm, (b) 8 nm, and (c) 32 nm at  $\lambda_0 = 400$  nm, and the pulse durations  $\tau_e$  (FWHM) are (i)  $\tau_e = 100$  fs, (ii)  $\tau_e = 200$  fs, and (iii)  $\tau_e = 400$  fs.

## Appendix F: Fourier-transform fringe analysis

### F.1 Interferometric fringe analysis with Fourier-transform technique

A general expression for a 2-dimensional (2D) interferometric laser intensity profile, shortly an interferogram, is given by

$$I(x, y) = I_1(x, y) + I_2(x, y) + 2\sqrt{I_1 I_2} |\gamma| \cos[2\pi f_0 x + \phi(x, y)] \quad (\text{F.1})$$

where  $I_{1,2}(x, y)$  are the individual laser intensities,  $|\gamma|$  is the degree of mutual coherence of the interfering waves,  $f_0$  is the spatial-carrier frequency of interferogram, and  $\phi(x, y)$  is the relative phase of laser fields that we wish to uncover. We introduce the Fourier-transform method, developed by Taketa *et al.*,<sup>1</sup> to extract the phase  $\phi(x, y)$  from Eq. (F.1).

Following the notations of Taketa *et al.*, we write Eq. (F.1) as

$$I(x, y) = a(x, y) + b(x, y) \cos[2\pi f_0 x + \phi(x, y)] \quad (\text{F.2})$$

where  $a(x, y)$  presents the combination of  $I_{1,2}(x, y)$  and any nonuniform background illuminations. For the convenience of mathematical treatments, we rewrite Eq. (F.2) as

$$I(x, y) = a(x, y) + c(x, y) \exp(2\pi i f_0 x) + c^*(x, y) \exp(-2\pi i f_0 x) \quad (\text{F.3})$$

where

$$c(x, y) = \frac{1}{2} b(x, y) \exp[i\phi(x, y)] \quad (\text{F.4})$$

and  $c^*(x, y)$  is the complex conjugate of  $c(x, y)$ .

The fringe pattern in Eq (F.3) is then Fourier transformed with respect to  $x$ , giving

$$\tilde{I}(f_x, y) = \tilde{A}(f_x, y) + \tilde{C}(f_x - f_0, y) + \tilde{C}^*(f_x + f_0, y) \quad (\text{F.5})$$

where  $\tilde{I}(f_x, y)$ ,  $\tilde{A}(f_x, y)$ ,  $\tilde{C}(f_x - f_0, y)$ , and  $\tilde{C}^*(f_x + f_0, y)$  are the Fourier spectra of  $I(x, y)$ ,  $a(x, y)$ , and  $c(x, y)$ , respectively, and  $f_x$  is the spatial frequency in the  $x$ -direction. Here the spatial variations of  $a(x, y)$ ,  $b(x, y)$ , and  $\phi(x, y)$  must be slow compared to the spatial frequency  $f_0$ . With a use of filter function, only  $\tilde{C}(f_x - f_0, y)$  spectrum is extracted from Eq. (F.5) and translated by  $f_0$  toward the origin to obtain  $\tilde{C}(f_x, y)$ . In this process, the unwanted background intensity profile  $a(x, y)$  is filtered out. Again using the inverse Fourier transform of  $\tilde{C}(f_x, y)$ , we obtain  $c(x, y)$ . To get  $\phi(x, y)$  from the retrieved  $c(x, y)$ , we apply a complex logarithm to Eq. (F.4) as shown as

$$\ln[c(x, y)] = \ln[\frac{1}{2}b(x, y)] + i\phi(x, y) \quad (\text{F.6})$$

From Eq. (F.6), finally the phase  $\phi(x, y)$  and envelope intensity  $b(x, y)$  can be obtained as

$$\phi(x, y) = \text{Im}[\ln(c(x, y))] = \tan^{-1} \frac{\text{Im}[c(x, y)]}{\text{Re}[c(x, y)]} \quad (\text{F.7})$$

$$b(x, y) = 2|c(x, y)| \quad (\text{F.8})$$

where Re and Im represent the real and imaginary parts of  $c(x, y)$ .

Figure F.1 shows an experimental illustration of this Fourier-transform fringe analysis process. Starting with a (a) raw interferometric fringes  $I(x, y = y_0)$ , lined-out from an experimental interferogram at  $y = y_0$ , the Fourier transform of  $I(x, y)$ , i.e.  $\tilde{I}(f_x, y)$ , is computed using a FFT algorithm, and the modulus of  $\tilde{I}(f_x, y)$  is plotted in Fig. F.1(b).  $\tilde{I}(f_x, y)$  has a central DC-component  $\tilde{A}(f_x, y)$  and two AC spectra:  $\tilde{C}(f_x - f_0, y)$  and  $\tilde{C}^*(f_x + f_0, y)$ . Only  $\tilde{C}(f_x - f_0, y)$  is selected with a square-filter function and shifted by  $f_0$  toward the origin to produce  $\tilde{C}(f_x, y)$ . Applying an inverse Fourier transform to

$\tilde{C}(f_x, y)$  with a use of fast-Fourier-transform (FFT) algorithm, we obtain  $c(x, y)$ . Figure F.1(c) shows the modulus of  $b(x, y)$  and the phase  $\phi(x, y)$ , computed from  $c(x, y)$  using Eqs. (F.7) and (F.8).

The usual case of computer-based phase extraction function restrict the phase angle in range of  $-\pi$  and  $+\pi$ . To handle  $|\phi(x, y)| > \pi$ , a phase unwrapping subroutine was performed to avoid phase discontinuities.

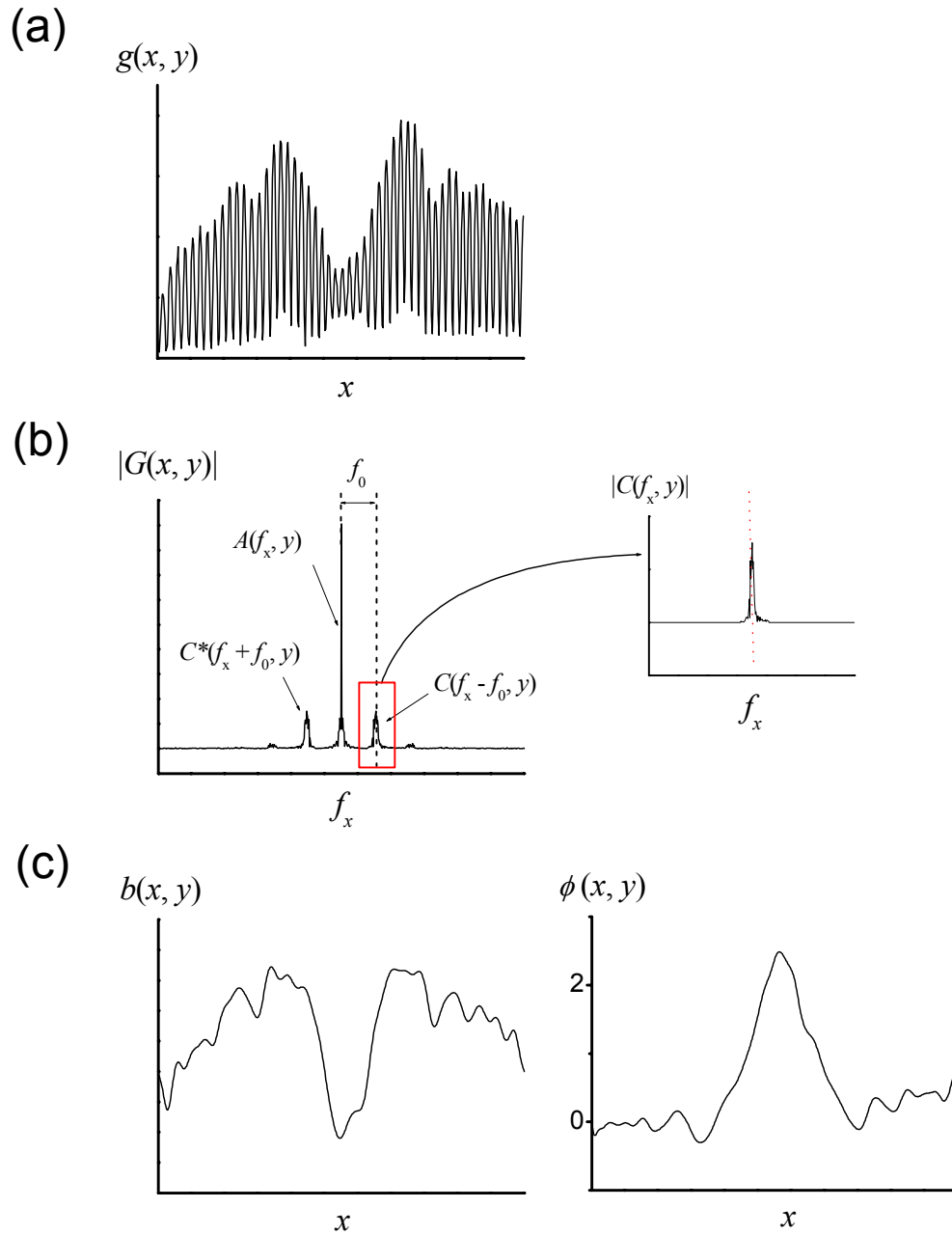


Figure F.1: Fourier-transform process showing various stages to extract the envelope intensity and phase profiles. (a) 1-D raw interferometric intensity profile  $g(x, y)$ . (b) Modulus of Fourier transform  $|G(x, y)|$  containing a DC-component  $A(f_x, y)$  and AC-spectra  $C(f_x - f_0, y)$  and  $C^*(f_x + f_0, y)$ .  $C(f_x - f_0, y)$  spectrum is selected with a filter function and shifted toward center by  $f_0$  to make  $C(f_x, y)$ . (c) Modulus  $b(x, y)$  and phase  $\phi(x, y)$  obtained from the inverse Fourier transform of  $C(f_x, y)$ .

## Appendix G: Optical material dispersion

To describe the dispersion of common optical material, we use the following Sellmeier formula for the expression of their index of refraction.

$$n^2(\lambda) = 1 + \frac{B_1\lambda^2}{\lambda^2 - C_1} + \frac{B_2\lambda^2}{\lambda^2 - C_2} + \frac{B_3\lambda^2}{\lambda^2 - C_3} \quad (\text{G.1})$$

where  $\lambda$  is the wavelength and expressed in units of  $\mu\text{m}$ . The values  $B_1, B_2, B_3, C_1, C_2,$  and  $C_3$  for various sample optical glass can be found in reference.<sup>1</sup> When a laser light passes through a material with a thickness of  $L$ , the light acquires a phase shift given by

$$\phi(\omega) = \frac{L}{c} \omega n(\omega) \quad (\text{G.2})$$

where  $c$  is the speed of light and  $\omega = 2\pi c/\lambda$  is the laser angular frequency.

From Eq. (G.2), the first order  $\phi'$  (time shift), second order  $\phi''$  (GDD), third order  $\phi'''$  (TOD), and fourth order  $\phi''''$  (4OD) dispersions can be obtained as follows

$$\frac{d\phi(\omega)}{d\omega} = \frac{L}{c} \left( n(\omega) + \omega \frac{dn(\omega)}{d\omega} \right) = \frac{L}{c} \left( n(\lambda) - \lambda \frac{dn(\lambda)}{d\lambda} \right) \quad (\text{G.3})$$

$$\frac{d^2\phi(\omega)}{d\omega^2} = \frac{L}{c} \left( 2 \frac{dn(\omega)}{d\omega} + \omega \frac{d^2n(\omega)}{d\omega^2} \right) = \frac{L\lambda^3}{2\pi c^2} \frac{d^2n(\lambda)}{d\lambda^2} \quad (\text{G.4})$$

$$\frac{d^3\phi(\omega)}{d\omega^3} = \frac{L}{c} \left( 3 \frac{d^2n(\omega)}{d\omega^2} + \omega \frac{d^3n(\omega)}{d\omega^3} \right) = -\frac{L\lambda^4}{4\pi^2 c^3} \left( 3 \frac{d^2n(\lambda)}{d\lambda^2} + \lambda \frac{d^3n(\lambda)}{d\lambda^3} \right) \quad (\text{G.5})$$

$$\begin{aligned} \frac{d^3\phi(\omega)}{d\omega^3} &= \frac{L}{c} \left( 4 \frac{d^3n(\omega)}{d\omega^3} + \omega \frac{d^4n(\omega)}{d\omega^4} \right) = \\ &= \frac{L\lambda^5}{8\pi^3 c^4} \left( 12 \frac{d^2n(\lambda)}{d\lambda^2} + 8\lambda \frac{d^3n(\lambda)}{d\lambda^3} + \lambda^2 \frac{d^4n(\lambda)}{d\lambda^4} \right) \end{aligned} \quad (\text{G.6})$$

Table G.1 also shows GDD, TOD, and 4OD values for various optical material at a central wavelength of 800 nm.

Table G.1: GDD, TOD, 4OD for a variety of optical glasses at 800 nm.<sup>1</sup>

Optical material	GDD $d^2\phi/d\omega^2$ (fs <sup>2</sup> )	TOD $d^3\phi/d\omega^3$ (fs <sup>3</sup> )	4OD $d^4\phi/d\omega^4$ (fs <sup>4</sup> )
Schott BK7	447	3318	-97
Schott F2	1051	659	91
Schott SF4 [ref. 2]	1717	1073	310
Schott SF10	1594	1010	280
Fused silica	362	272	-106
CaF <sub>2</sub>	279	162	-28
MgF <sub>2</sub> (ne)	206	143	-51
Sapphire (ne)	567	409	-144

Figure G.1 shows various glass material dispersion plots with (a) index of refraction (b) group delay dispersion (GDD) (c) third order dispersion (TOD), and (d) fourth order dispersion (4OD) in the optical wavelength range.

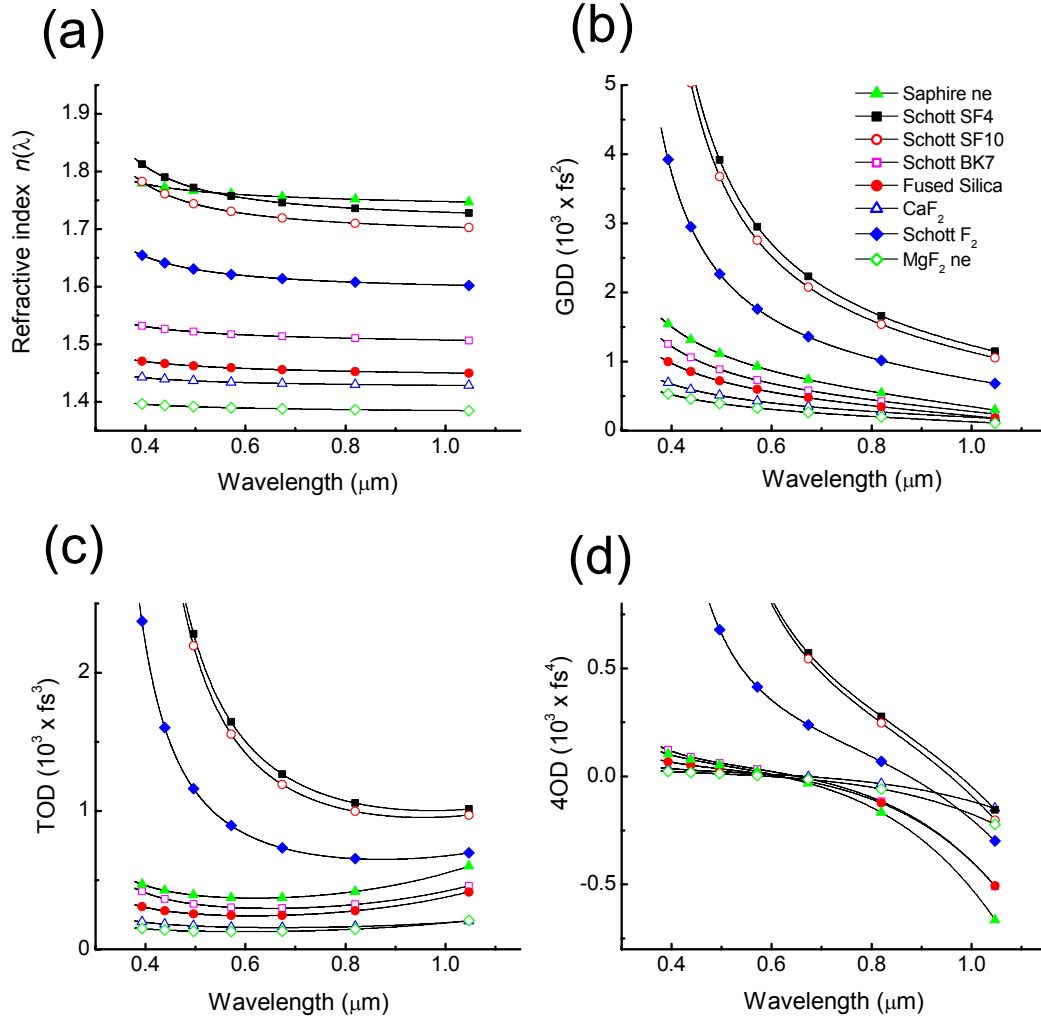


Figure G.1: Material dispersion with (a) index of refraction (b) group delay dispersion (GDD) (c) third order dispersion (TOD), and (d) fourth order dispersion (4OD) for various glass in the optical wavelength range.

## Appendix H: Synchronization of Ti:sapphire and Nd:YAG laser systems

The Ti:sapphire and Nd:YAG laser systems were synchronized by externally locking the optical pulse phases of two laser systems, including oscillators and amplifiers (see Fig. H.1). The Nd:YAG oscillator (Coherent Antares) was actively mode-locked by using a 38.15 MHz rf mode-locker driver, and one output signal from the driver was frequency-doubled at a repetition rate of  $f = 76.3$  MHz and used as the reference to the Ti:sapphire oscillator. The required synchronization was achieved with a use of electronic feedback loop stabilization module (Spectra-Physics, Lok-to-Clock model 3930) to lock the Ti:sapphire oscillator cavity length at  $L = 1.97$  m ( $f = 76.3$  MHz) constantly via a piezo-driven mirror, matching the pulse train phase with that from the Nd:YAG laser oscillator.<sup>1</sup> Another 38.15 MHz reference was frequency-divided down to 10 Hz and used to externally trigger both of the Nd:YAG and Ti:sapphire laser amplifier systems synchronously at a repetition rate of 10 Hz.<sup>2</sup> This synchronization of two laser systems enabled us to vary the injection timing of Ti:sapphire pump pulse into the plasma channel with an electronic delay. The relative firing jitter was less than 20 ps, measured from the cross-correlation experiment where the output beams of the Nd:YAG and Ti:sapphire oscillator were sum-frequency mixed of in a 1-mm KDP crystal.<sup>3</sup>

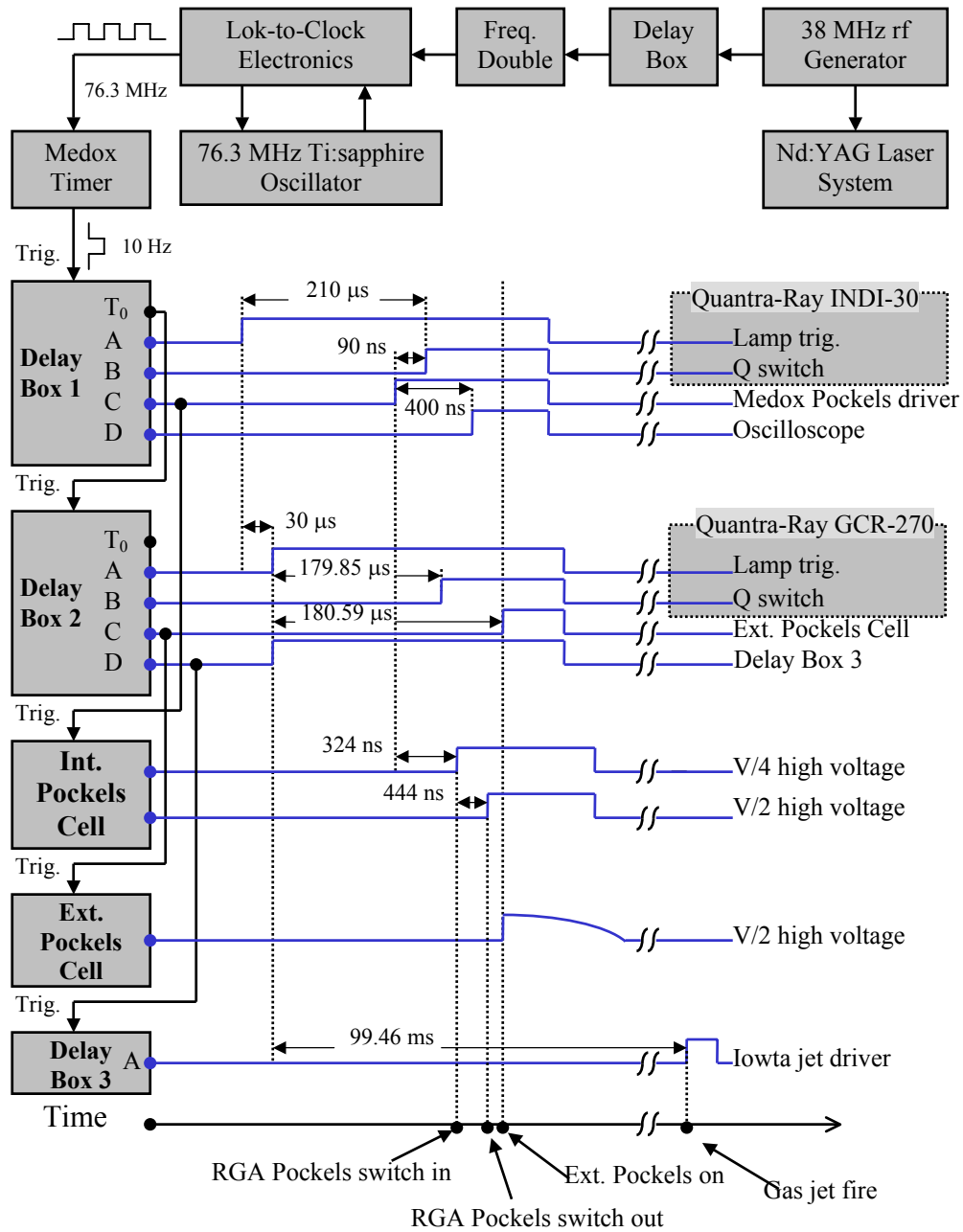


Figure H.1: Schematic diagram for the electronic signal synchronizations of Ti:sapphire and Nd:YAG laser systems using the rf generator (Coherent 7600 Mode-locker), Delay box (EG&G Model DB463), Lok-to-Clock electronics (Spectra-Physics Model 3930), Medox timer (Medox Electro-Optics), Delay box 1 & 2 (Stanford Research Systems DG535), and Delay box 3 (Berkeley Nucleonics Corporation Model 555).

## Chapter 1 References

1. T. H. Maiman, *Nature* **187**, 493 (1960).
2. L. D. Landau and E. M. Lifshits, *The Classical Theory of Fields*, 4th edition (Pergamon, Oxford, 1975).
3. S. Y. Chen, A. Maksimchuk, and D. Umstadter, *Nature (London)* **396**, 653 (1998).
4. L. V. Keldysh, *Sov. Phys. JETP* **20**, 1307 (1965).
5. C. Mainfray and C. Manus, *Rep. Prog. Phys.* **54**, 1333 (1991).
6. S. Augst, D. Strickland, D. D. Meyerhofer, S. L. Chin, and J. H. Eberly, *Phys. Rev. Lett.* **63**, 2212 (1989).
7. R. R. Freeman and P. H. Bucksbaum, *J. Phys. B* **24**, 325 (1991).
8. L. Spitzer, Jr., *Physics of Fully Ionized Plasmas*, 2nd edition (Interscience, New York, 1967).
9. S. Eliezer, *The Interaction of High-Power Lasers with Plasmas* (Institute of Physics Publishing, Bristol, 2002).
10. L. Schlessinger and J. Wright, *Phys. Rev. A* **20**, 1934 (1979).
11. T. Ditmire, *Phys. Rev. E* **54**, 6735 (1996).
12. C. H. Lee, *Picosecond Optoelectronic Devices* (Academic, New York, 1984).
13. <http://usa.hamamatsu.com/hpspdf/guidetostreak.pdf>
14. C. Rullière, *Femtosecond Laser Pulses: Principles and Experiments*, (Springer, Berlin, 1998).
15. D. J. Kane and R. Trebino, *Opt. Lett.* **18**, 823 (1993).
16. R. Trebino, K. W. DeLong, D. N. Fittinghoff, J. N. Sweetser, M. A. Krumbügel, B. A. Richman, D. J. Kane, *Rev. Sci. Instrum.* **68**, 3277 (1997).

17. R. Trebino, *Frequency-Resolved Optical Gating: The Measurement of Ultrashort Laser Pulses* (Kluwer Academic Publishers, Boston, 2000).
18. C. Iaconis, and I. A. Walmsley, *Opt. Lett.* **23** 792 (1998).
19. C. Iaconis, and I. A. Walmsley, *IEEE J. Quantum Electron.* **35**, 501 (1999).
20. C. W. Siders, G. Rodriguez, J. L. W. Siders, F. G. Omenetto, and A. J. Taylor, *Phys. Rev. Lett.* **87**, 263002 (2001).
21. F. Krausz, *Opt. & Photon. News* **13**, 62 (May 2002).
22. R. Kienberger, M. Hentschel, M. Uiberacker, Ch. Spielmann, M. Kitzler, A. Scrinzi, M. Wieland, Th. Westerwalbesloh, U. Kleineberg, U. Heinzmann, M. Drescher, and F. Krausz, *Science* **297**, 1144 (2002).
23. M. Drescher, M. Hentschel, R. Kienberger, M. Uiberacker, V. Yakovlev, A. Scrinzi, Th. Westerwalbesloh, U. Kleineberg, U. Heinzmann, and F. Krausz, *Nature (London)* **419**, 803 (2002).
24. S. Augst, D. D. Meyerhofer, D. Strickland and S. L. Chin, *J. Opt. Soc. Am. B* **8**, 858 (1991).
25. D. N. Fittinghoff, P. R. Bolton, B. Chang, and K. C. Kulander, *Phys. Rev. Lett.* **69**, 2642 (1992).
26. W. M. Wood, C. W. Siders, and M. C. Downer, *Phys. Rev. Lett.* **67**, 3523 (1991).
27. W. M. Wood, C. W. Siders, and M. C. Downer, *IEEE Trans. Plasma Sci.* **21**, 20 (1993).
28. A. McPherson, T. S. Luk, B. D. Thompson, K. Boyer, and C. K. Rhodes, *Appl. Phys. B* **57**, 337 (1993).

29. A. McPherson, T. S. Luk, B. D. Thompson, A. B. Borisov, O. B. Shiryaev, X. Chen, K. Boyer, and C. K. Rhodes, *Phys. Rev. Lett.* **72**, 1810 (1994).
30. A. McPherson, B. D. Thompson, A. B. Borisov, K. Boyer, and C. K. Rhodes, *Nature (London)* **370**, 631 (1994).
31. T. Ditmire, R. A. Smith, R. S. Marjoribanks, G. Kulcsár, and M. H. R. Hutchinson, *Appl. Phys. Lett.* **71**, 166 (1997).
32. T. Mocek, C. M. Kim, H. J. Shin, D. G. Lee, Y. H. Cha, K. H. Hong, and C. H. Nam, *Appl. Phys. Lett.* **76**, 1819 (2000).
33. T. Mocek, C. M. Kim, H. J. Shin, D. G. Lee, Y. H. Cha, K. H. Hong, and C. H. Nam, *Phys. Rev. E* **62**, 4461 (2000).
34. T. Ditmire, J. W. G. Tisch, E. Springate, M. B. Mason, N. Hay, R. A. Smith, J. Marangos, and M. H. R. Hutchinson, *Nature (London)* **386**, **54** (1997).
35. Y. Fukuda, K. Yamakawa, Y. Akahane, M. Aoyama, N. Inoue, H. Ueda, and Y. Kishimoto, *Phys. Rev. A* **67**, R061201 (2003).
36. Y. L. Shao, T. Ditmire, J. W. G. Tisch, E. Springate, J. P. Marangos, and M. H. R. Hutchinson, *Phys. Rev. Lett.* **77**, 3343 (1996).
37. L. M. Chen, J. J. Park, K.-H. Hong, J. L. Kim, J. Zhang, and C. H. Nam, *Phys. Rev. E* **66**, R025402 (2002).
38. L. M. Chen, J. J. Park, K. H. Hong, I. W. Choi, J. L. Kim, J. Zhang, and C. H. Nam, *Phys. Plasmas* **9**, 3595 (2002).
39. T. Ditmire, J. Zweiback, V. P. Yanovsky, T.E. Cowan, G. Hays, and K. B. Wharton, *Nature (London)* **398**, 489 (1999).

40. J. Zweiback, R. A. Smith, T. E. Cowan, G. Hays, K. B. Wharton, V. P. Yanovsky, and T. Ditmire, *Phys. Rev. Lett.* **84**, 2634 (2000).
41. J. Zweiback, T. E. Cowan, R. A. Smith, J. H. Hartley, R. Howell, C. A. Steinke, G. Hays, K. B. Wharton, J. K. Crane, and T. Ditmire, *Phys. Rev. Lett.* **85**, 3640 (2000).
42. G. Grillon, Ph. Balcou, J.-P. Chambaret, D. Hulin, J. Martino, S. Moustazis, L. Notebaert, M. Pittman, Th. Pussieux, A. Rouse, J-Ph. Rousseau, S. Sebban, O. Sublemontier, and M. Schmidt, *Phys. Rev. Lett.* **89**, 065005 (2002).
43. T. Ditmire, T. Donnelly, A. M. Rubenchik, R. W. Falcone, and M. D. Perry, *Phys. Rev. A* **53**, 3379 (1996).
44. T. Ditmire, E. Springate, J. W. G. Tisch, Y. L. Sha, M. B. Mason, N. Hay, J. P. Marangos, and M. H. R. Hutchinson, *Phys. Rev. A* **57**, 369 (1998).
45. C. Rose-Petruck, K. J. Schafer, K. R. Wilson, and C. P. J. Barty, *Phys. Rev. A* **55**, 1182 (1997).
46. M. Lezius, S. Dobosz, D. Normand, and M. Schmidt, *Phys. Rev. Lett.* **80**, 261 (1998).
47. W. A. Schroeder, F. G. Omenetto, A. B. Borisov, J. W. Longworth, A. McPherson, C. Jordan, K. Boyer, K. Kondo, C. K. Rhodes, *J. Phys. B* **31**, 5031 (1998).
48. H. M. Milchberg, S. J. McNaught, and E. Parra, *Phys. Rev. E* **64**, 056402 (2001).
49. V. Kumarappan, M. Krishnamurthy, and D. Mathur, *Phys. Rev. Lett.* **87**, 085005 (2001).
50. J. Zweiback, T. Ditmire, and M. D. Perry, *Phys. Rev. A* **59**, R3166 (1999).
51. J. Zweiback, T. Ditmire, and M. D. Perry, *Opt. Express* **6**, 236 (2000).

52. E. Parra, I. Alexeev, J. Fan, K. Y. Kim, S. J. McNaught, H. M. Milchberg, *Phys. Rev. E* **62**, R5931 (2000).
53. I. Yu. Skobelev et al., *Zh. Eksp. Teor. Fiz.* **121**, 1124 (2002) [*JETP* **94**, 966 (2002)].
54. K. Y. Kim, I. Alexeev, and H. M. Milchberg, *Phys. Rev. Lett.* **90**, 023401 (2003).
55. I. Alexeev, T. Antonsen, K.Y. Kim, and H.M. Milchberg, *Phys. Rev. Lett.* **90**, 103402 (2003).
56. T. D. Donnelly, T. Ditmire, K. Neuman, M. D. Perry, and R. W. Falcone, *Phys. Rev. Lett.* **76**, 2472 (1996).
57. J. W. G. Tisch, T. Ditmire, D. J. Fraser, N. Hay, M. B. Mason, E. Springate, J. P. Marangos, and M. H. R. Hutchinson, *J. Phys. B* **30**, L709 (1997).
58. J. W. G. Tisch, *Phys. Rev. A* **62**, R41802 (2000).
59. G. D. Kubiak, L. J. Bernardez, K.D. Krenz, D. J. O'Connell, R. Gutowski, and A. M. M. Todd, *OSA Trends Opt. Photonics Ser.* **4**, 66 (1996).
60. J. Kirz, C. Jacobsen, and M. Howells, *Q. Rev. Biophys.* **28**, 33 (1995).
61. T. Taguchi, T. M. Antonsen, Jr., H. M. Milchberg, submitted to *Phys. Rev. Lett.*
62. F. Brunel, *Phys. Rev. Lett.* **59**, 53 (1987).

## Chapter 2 References

1. Cl. Froehly, A. Lacourt, and J. Ch. Viénot, *J. Opt. (Paris)* **4**, 183 (1973).
2. E. Tokunaga, A. Terasaki, and T. Kobayashi, *Opt. Lett.* **17**, 1131 (1992).
3. J. P. Geindre, P. Audebert, A. Rousse, F. Fallies, J. C. Gauthier, A. Mysyrowicz, A. Dos Santos, G. Hamoniaux, and G. A. Antonetti, *Opt. Lett.* **19**, 1997 (1994).
4. E. Tokunaga, A. Terasaki, and T. Kobayashi, *J. Opt. Soc. Am. B* **12**, 753 (1995).

5. K.Y. Kim, I. Alexeev, and H.M. Milchberg, *Appl. Phys. Lett.* **81**, 4124 (2002).
6. P. Salières, L. Le Déroff, T. Auguste, P. Monot, P. d'Oliverira, D. Campo, J.-F. Hergott, H. Merdji, and B. Carré, *Phys. Rev. Lett.* **83**, 5483 (1999).
7. J.-F. Hergott, T. Auguste, P. Salières, L. Le Déroff, P. Monot, P. d'Oliverira, D. Campo, H. Merdji, and B. Carré, *J. Opt. Soc. Am. B* **20**, 171 (2003).
8. R. Evans, A. D. Badger, F. Falliès, M. Mahdieh, T. A. Hall, P. Audebert, J.-P. Geindre, J.-C. Gauthier, A. Mysyrowicz, G. Grillon, and A. Antonetti, *Phys. Rev. Lett.* **77**, 3359 (1996).
9. J. R. Marquès, J. P. Geindre, F. Amiranoff, P. Audebert, J. C. Gauthier, A. Antonetti, and G. Grillon, *Phys. Rev. Lett.* **76**, 3566 (1996).
10. C. W. Siders, S. P. Le Blanc, D. Fisher, T. Tajima, and M. C. Downer, *Phys. Rev. Lett.* **76**, 3570 (1996).
11. J. R. Marquès, F. Dorchies, F. Amiranoff, P. Audebert, J. C. Gauthier, Geindre, A. Antonetti, T. M. Antonsen, Jr., P. Chessa, and P. Mora, *Phys. Plasmas* **5**, 1162 (1998).
12. E. Takahashi, H. Honda, E. Miura, N. Yugami, Y. Nishida, K. Katsura, and K. Kondo, *Phys. Rev. E* **62**, 7247 (2000).
13. H. Kotaki, M. Kando, T. Oketa, S. Masuda, J. K. Koga, S. Kondo, and K. Nakajima, *Phys. Plasmas* **9**, 1392 (2002).
14. A. Benuzzi-Monaix, M. Koenig, and J. M. Boudenne, *Phys. Rev. E* **60**, R2488 (1999).
15. C. Y. Chien, B. La Fontaine, A. Desparois, Z. Jiang, T. W. Johnston, J. C. Kieffer, H. Pépin, and F. Vidal, *Opt. Lett.* **25**, 578 (2000).

16. E. Tokunaga, A. Terasaki, and T. Kobayashi, *J. Opt. Soc. Am. B* **13**, 496 (1996).
17. J.-P. Geindre, P. Audebert, S. Rebibo, and J.-C. Gauthier, *Opt. Lett.* **26**, 1612 (2001).
18. S. P. Le Blanc, E. W. Gaul, N. H. Matlis, A. Rundquist, and M.C. Downer, *Opt. Lett.* **25**, 764 (2000).
19. K. Y. Kim, I. Alexeev, and H.M. Milchberg, *Opt. Express* **10**, 1563 (2002).
20. K. Y. Kim, I. Alexeev, and H. M. Milchberg, *Phys. Rev. Lett.* **90**, 023401 (2003).
21. M. Takeda, H. Ina, and S. Kobayashi, *J. Opt. Soc. Am.* **72**, 156 (1982).
22. G. Rodriguez and A. J. Taylor, *Opt. Lett.* **23**, 858 (1998).
23. C. J. K. Richardson, J. B. Spicer, R. D. Huber, and H. W. H. Lee, *Opt. Lett.* **26**, 1105 (2001).
24. A. Brodeur and S. L. Chin, *J. Opt. Soc. Am. B* **16**, 637 (1999).
25. R. R. Alfano, *The Supercontinuum Laser Source* (Springer-Verlag, New York, 1989).
26. P. B. Corkum and C. Rolland, *IEEE J. Quantum Elect.* **25**, 2634 (1989).
27. D. J. Kane and R. Trebino, *Opt. Lett.* **18**, 823 (1993).

### Chapter 3 References

1. D. Strickland and G. Mourou, *Opt. Commun.* **56**, 219 (1985).
2. P. Maine, D. Strickland, P. Bado, M. Pessot, and G. Mourou, *IEEE J. Quantum Electron.* **24**, 398 (1988).
3. P. F. Moulton, MIT Lincoln Laboratory Report No. 1982:3 (1982).
4. P. F. Moulton, *J. Opt. Soc. Am. B* **3**, 125 (1986).

5. W. Koechner, *Solid-State Laser Engineering* (Springer, Heidelberg, 1996).
6. S. Backus, C. G. Durfee, III, M. M. Murnane, and H. C. Kapteyn, *Rev. Sci. Instrum.* **69**, 1207 (1998).
7. A. Rundquist, C. Durfee, Z. Chang, G. Taft, E. Zeek, S. Backus, M. M. Murnane, H. C. Kapteyn, I. Christov, and V. Stoev, *Appl. Phys. B* **65**, 161 (1997).
8. C. G. Durfee, III, S. Backus, M. M. Murnane, and H. C. Kapteyn, *IEEE J. Select. Topics Quantum Electron.* **4**, 395 (1998).
9. K. Yamakawa, M. Aoyama, S. Matsuoka, H. Takuma, D. N. Fittinghoff, and C. P. J. Barty, *IEEE J. Select. Topics Quantum Electron.* **4**, 385 (1998).
10. S. P. Nikitin, Ph. D. dissertation, (University of Maryland, 1998).
11. I. S. Alexeev, Ph. D. dissertation, (University of Maryland, 2003).
12. D. E. Spence, P. N. Kean, and W. Sibbett, *Opt. Lett.* **16**, 42 (1991).
13. D. E. Spence and W. Sibbett, *J. Opt. Soc. Am. B* **8**, 2053 (1991).
14. L. Spinelli, B. Couillard, N. Goldblatt, and D. K. Negus, in *Conference on Lasers and Electro-Optics*, Vol. 10 of 1991 OSA Technical Digest Series (Optical Society of America, Washington D.C., 1991), paper CPDP7.
15. J. Squier, F. Salin, G. Mourou, and D. Harter, *Opt. Lett.* **16**, 324 (1991).
16. C.-P. Huang, H. C. Kapteyn, J. W. McIntosh, and M. M. Murnane, *Opt. Lett.* **17**, 129 (1992).
17. F. Krausz, Ch. Spielmann, T. Brabec, E. Wintner, and A. J. Schmidt, *Opt. Lett.* **17**, 204 (1992).
18. C.-P. Huang, M. T. Asaki, S. Backus, M. M. Murnane, and H. C. Kapteyn, *Opt. Lett.* **17**, 1289 (1992).

19. F. Salin, J. Squier, and M. Piché, *Opt. Lett.* **16**, 1674 (1991).
20. S. Chen and J. Wang, *Opt. Lett.* **16**, 1689 (1991).
21. T. Brabec, Ch. Spielmann, and F. Krauz, *Opt. Lett.* **16**, 1961 (1991).
22. D. Huang, M. Ulman, L. H. Acioli, H. A. Haus, and J. G. Fujimoto, *Opt. Lett.* **17**, 511 (1992).
23. T. Brabec, Ch. Spielmann, P. F. Curley, and F. Krauz, *Opt. Lett.* **17**, 1292 (1992).
24. R. W. Boyd, *Nonlinear Optics* (Academic Press, San Diego, 1992).
25. D. H. Sutter, G. Steinmeyer, L. Gallmann, N. Matuschek, F. Morier-Genoud, U. Keller, V. Scheuer, G. Angelow, T. Tschudi, *Opt. Lett.* **24**, 631 (1999).
26. P. M. W. French, *Rep. Prog. Phys.* **58**, 169 (1995).
27. R. L. Fork, O. E. Martinez, and J. P. Gordon, *Opt. Lett.* **9**, 150 (1984).
28. O. E. Martinez, J. P. Gordon, and R. L. Fork, *J. Opt. Soc. Am. A* **1**, 1003 (1984).
29. R. L. Fork, C. H. Brito, P. C. Becker, and C. V. Shank, *Opt. Lett.* **12**, 483 (1987).
30. D. T. Reid, M. Padgett, C. McGowan, W. E. Sleat, and W. Sibbett, *Opt. Lett.* **22**, 233 (1997).
31. J. K. Ranka, A. L. Gaeta, A. Baltuska, M. S. Pshenichnikov, and D. A. Wiersma, *Opt. Lett.* **22**, 1344 (1997).
32. M. Pessot, P. Maine, and G. Mourou, *Opt. Commun.* **62**, 419 (1987).
33. O. E. Martinez, *IEEE J. Quantum Electron.* **QE-23**, 59 (1987).
34. A. Öffner, US Patent 3,748.015.
35. G. Cheriaux, P. Rousseau, F. Salin, and J. P. Chambaret, B. Walker, and L. F. DiMauro, *Opt. Lett.* **21**, 414 (1996).
36. J. Zhou, C.-P. Huang, M. M. Murnane, and H. C. Kapteyn, *Opt. Lett.* **20**, 64 (1995).

37. C. Le Blanc, P. Curley, and F. Salin, *Opt. Commun.* **131**, 391 (1996).
38. F. G. Patterson and M D. Perry, *J. Opt. Soc. Am. B* **8**, 2384 (1991).
39. L. M. Frantz and J. S. Nodvik, *J. Appl. Phys.* **34**, 2346 (1963).
40. A. Siegman, *Lasers* (University Science Books, Mill Valley, 1986).
41. M. D. Perry, T. Ditmire, and B. C. Stuart, *Opt. Lett.* **19**, 2149 (1994).
42. E. B. Treacy, *IEEE J. Quantum Electron.* **QE-5**, 454 (1969).
43. B.E. Lemoff and C. P. J. Barty, *Opt. Lett.* **18**, 1651 (1993).
44. W.E. White, F. G. Patterson, R. L. Combs, D. F. Price, and R. L. Shepherd, *Opt. Lett.* **18**, 1343 (1993).
45. A. Braun, G. Korn, X. Liu, D. Du, J. Squier, and G. Mourou, *Opt. Lett.* **20**, 73 (1995).
46. A. Yariv, *Quantum Electronics*, 3rd Ed. (John Wiley & Sons, New York, 1989) p.487.
47. Y. H. Cha, Y. I. Kang, C. H. Nam, *J. Opt. Soc. Am. B* **16**, 1220 (1999).
48. A. M. Weiner, *Prog. Quant. Electron* **19**, 161 (1995).
49. C. P. J. Barty, G. Korn, F. Raksi, C. Rose-Petruck, and J. Squier, A.-C. Tien, K. R. Wilson, V. V. Yakovlev, and K. Yamakawa, *Opt. Lett.* **21**, 219 (1996).
50. F. Verluise, L. Laude, Z. Cheng, Ch. Spielmann, and P. Tournois, *Opt. Lett.* **25**, 575 (2000).
51. P. Tournois, *Opt. Commun.* **140**, 245 (1997).

#### **Chapter 4 References**

1. L .V. Keldysh, *Sov. Phys. JETP* **20**, 1307 (1965).

2. S. Augst, D. Strickland, D. D. Meyerhofer, S. L. Chin, and J. H. Eberly, *Phys. Rev. Lett.* **63**, 2212 (1989).
3. P. B. Corkum, *Phys. Rev. Lett.* **71**, 1994 (1993).
4. A. McPherson, G. Gibson, H. Jara, U. Johann, T. S. Luk, I. McIntyre, K. Boyer, and C. K. Rhodes, *J. Opt. Soc. Am. B* **4**, 595 (1987).
5. M. Ferray, A L'Huillier, X. F. Li, L. A. Lompré, G. Mainfray and C. Manus, *J. Phys. B: At. Mol. Opt. Phys.* **21**, L31 (1988).
6. C. E. Max, J. Arons, and A. B. Langdon, *Phys. Rev. Lett.* **33**, 209 (1974).
7. J. Fuchs, G. Malka, J. C. Adam, F. Amiranoff, S. D. Baton, N. Blanchot, A. Héron, G. Laval, J. L. Miquel, P. Mora, H. Pépin, and C. Rousseaux, *Phys. Rev. Lett.* **80**, 1658 (1998).
8. T. Tajima and J. M. Dawson, *Phys. Rev. Lett.* **43**, 267 (1979).
9. A. M. Perelomov, V. S. Popov, and M. V. Terent'ev, *Zh. Eksp. Teor. Fiz.* **50**, 1393 (1966) [*Sov. Phys. JETP* **23**, 924 (1966)].
10. M. V. Ammosov, N. B. Delone, and V. P. Krainov, *Zh. Eksp. Teor. Fiz.* **91**, 2008 (1986) [*Sov. Phys. JETP* **64**, 1191 (1987)].
11. J. Fan, E. Parra, and H. M. Milchberg, *Phys. Rev. Lett.* **84**, 3085 (2000).
12. R. L. Kelly, *J. Phys. Chem. Ref. Data Suppl.* **16**, 1 (1987).
13. J. R. Marquès, J. P. Geindre, F. Amiranoff, P. Audebert, J. C. Gauthier, A. Antonetti, and G. Grillon, *Phys. Rev. Lett.* **76**, 3566 (1996).
14. C. W. Siders, S. P. Le Blanc, D. Fisher, T. Tajima, and M. C. Downer, *Phys. Rev. Lett.* **76**, 3570 (1996).

15. J. R. Marquès, F. Dorchies, F. Amiranoff, P. Audebert, J. C. Gauthier, Geindre, A. Antonetti, T. M. Antonsen, Jr., P. Chessa, and P. Mora, *Phys. Plasmas* **5**, 1162 (1998).
16. P. Monot, T. Auguste, L. A. Lompré, G. Mainfray, and C. Manus, *J. Opt. Soc. Am. B* **9**, 1579 (1992).
17. S. P. Nikitin, Y. Li, T. M. Antonsen, and H. M. Milchberg, *Opt. Comm.* **157**, 139 (1998).
18. Pollock, *Fundamentals of Optoelectronics* (Irwin, Chicago, 1995), Chap. 9.
19. C. W. Siders, G. Rodriguez, J. L. W. Siders, F. G. Omenetto, and A. J. Taylor, *Phys. Rev. Lett.* **87**, 263002 (2001).

### Chapter 5 References

1. E. W. Becker, K. Bier, and W. Henkes, *Z. Physik* **146**, 333 (1956).
2. O. F. Hagen and W. Obert, *J. Chem. Phys.* **56**, 1793 (1972).
3. O. F. Hagen, *Z. Phys. D* **4**, 291 (1987).
4. J. Wörmer, V. Guzielski, J. Stapelfeldt, and T. M. Möller, *Chem. Phys. Lett.* **159**, 321 (1989).
5. O. F. Hagen, *Rev. Sci. Instrum.* **63**, 2374 (1992).
6. O. F. Hagen, in *Molecular Beams and Low Density Gasdynamics*, edited by P. P. Wegener, (Dekker, New York, 1974), pp. 93-181.
7. B. M. Smirnov, *Clusters and Small Particles in Gases and Plasmas* (Springer-Verlag, New York, 2000), p 2.
8. O. Abraham, S. -S. Kim, and G. D. Stein, *J. Chem. Phys.* **75**, 402 (1981).

9. A. J. Bell, J. M. Mestdagh, J. Berlande, X. Biquard, J. Cuvellier, A. Lallement, P. Meynadier, O. Sublemontier, and J. -P. Visticot, *J. Phys. D* **26**, 994 (1993).
10. T. Ditmire, T. Donnelly, A. M. Rubenchik, R. W. Falcone, and M. D. Perry, *Phys. Rev. A* **53**, 3379 (1996).
11. A. M. Bush, A. J. Bell, J. G. Frey, and J. -M. Mestdagh, *J. Phys. Chem. A* **102**, 6457 (1998).
12. J. D. Jackson, *Classical Electrodynamics*, 2nd ed. (Wiley, New York, 1975).
13. R. A. Smith, T. Ditmire, and J. W. G. Tisch, *Rev. Sci. Instrum.* **69**, 3798 (1998).
14. R. Karnbach, M. Joppien, J. Stapelfeldt, and J. Wörmer, and T. Möller, *Rev. Sci. Instrum.* **64**, 2838 (1993).
15. J. Farges, M. F. de Feraudy, B. Raoult, and G. Torchet, *J. Chem. Phys.* **78**, 5067 (1983).
16. J. Farges, M. F. de Feraudy, B. Raoult, and G. Torchet, *J. Chem. Phys.* **84**, 3491 (1986).
17. H. Burghoff and J. Gspann, *Z. Naturforsch. A* **22**, 684 (1967).
18. J. Cuvellier, P. Meynadier, P. de Pujo, O. Sublemontier, J.-P. Vistico, J. Berlande, A. Lallement, and J.-M. Mestdagh, *Z. Phys. D* **21**, 265 (1991).
19. A. De Martino, M. Benslimane, M. Châtelet, C. Crozes, F. Pradère, and H. Vach, *Z. Phys. D* **27**, 185 (1993).
20. M. Lewerenz, B. Schilling, and J. P. Toennies, *Chem. Phys. Lett.* **206**, 381 (1993).
21. U. Buck and R. Krohne, *J. Chem. Phys.* **105**, 5408 (1996).
22. M. Macler and Y. K. Bae, *J. Phys. Chem. A* **101**, 145 (1997).
23. R. Klingelhöfer and H. O. Moser, *J. Appl. Phys.* **43**, 4575 (1972).

24. J. Wörmer, M. Joppien, and T. Möller, *Chem. Phys. Lett.* **182**, 632 (1991).
25. G. D. Stein, *J. Chem. Phys.* **51**, 938 (1969).
26. J. A. Clumpner, *J. Chem. Phys.* **55**, 5042 (1971).
27. J. B. Tatum and W. A. Jaworski, *J. Quant. Spectrosc. Radiat. Transfer* **38**, 319 (1987)
28. D. Gibson, Parker Hannifin Corporation (private communication).
29. M. Takeda, H. Ina, and S. Kobayashi, *J. Opt. Soc. Am.* **72**, 156 (1982).
30. T. R. Clark, Jr., Ph. D. dissertation, (University of Maryland, 1998).
31. T. Auguste, M. Bougeard, E. Caprin, P. D'Oliveira, and P. Monot, *Rev. Sci. Instrum.* **70**, 2349 (1999).
32. V. Malka, C. Coulaud, J. P. Geindre, V. Lopez, Z. Najmudin, D. Neely, and F. Amiranoff, *Rev. Sci. Instrum.* **71**, 2329 (2000).
33. C. Tarrío and S. E. Schnatterly, *Phys. Rev. B* **45**, 4020 (1992).
34. A. C. Sinnock and B. L. Smith, *Phys. Rev.* **181**, 1297 (1969).
35. K. J. Mendham, N. Hay, M. B. Mason, J. W. G. Tisch, and J. P. Marangos, *Phys. Rev. A* **64**, 055201 (2001).
36. J. Fan, T. R. Clark, H. M. Milchberg, *Appl. Phys. Lett.* **73**, 3064 (1998).
37. E. Parra, Ph. D. dissertation, (University of Maryland, 2002).
38. J. W.G. Tisch, in *Atoms, Solids, and Plasmas in Super-Intense Laser Fields*, edited by D. Batani, C. J. Joachain, S. Martellucci, and A. N. Chester, (Kluwer Academic/Plenum Publisher, New York, 2001), pp. 99 – 118.
39. M. Kerker, *The Scattering of Light* (Academic Press, New York, 1969).
40. [http://omlc.orgi.edu/calc/mie\\_calc.html](http://omlc.orgi.edu/calc/mie_calc.html)

## Chapter 6 References

1. A. McPherson, T. S. Luk, B. D. Thompson, A. B. Borisov, O. B. Shiryaev, X. Chen, K. Boyer, and C. K. Rhodes, *Phys. Rev. Lett.* **72**, 1810 (1994).
2. A. McPherson, T. S. Luk, B. D. Thompson, K. Boyer, and C. K. Rhodes, *Appl. Phys. B* **57**, 337 (1993).
3. A. McPherson, B. D. Thompson, A. B. Borisov, K. Boyer, and C. K. Rhodes, *Nature (London)* **370**, 631 (1994).
4. T. Ditmire, R. A. Smith, R. S. Marjoribanks, G. Kulcsár, and M. H. R. Hutchinson, *Appl. Phys. Lett.* **71**, 166 (1997).
5. T. Mocek, C. M. Kim, H. J. Shin, D. G. Lee, Y. H. Cha, K. H. Hong, and C. H. Nam, *Appl. Phys. Lett.* **76**, 1819 (2000).
6. T. Mocek, C. M. Kim, H. J. Shin, D. G. Lee, Y. H. Cha, K. H. Hong, and C. H. Nam, *Phys. Rev. E* **62**, 4461 (2000).
7. Y. L. Shao, T. Ditmire, J. W. G. Tisch, E. Springate, J. P. Marangos, and M. H. R. Hutchinson, *Phys. Rev. Lett.* **77**, 3343 (1996).
8. L. M. Chen, J. J. Park, K.-H. Hong, J. L. Kim, J. Zhang, and C. H. Nam, *Phys. Rev. E* **66**, R025402 (2002).
9. L. M. Chen, J. J. Park, K. H. Hong, I. W. Choi, J. L. Kim, J. Zhang, and C. H. Nam, *Phys. Plasmas* **9**, 3595 (2002).
10. T. Ditmire, J. W. G. Tisch, E. Springate, M. B. Mason, N. Hay, R. A. Smith, J. Marangos, and M. H. R. Hutchinson, *Nature (London)* **386**, 54 (1997).
11. M. Lezius, S. Dobosz, D. Normand, and M. Schmidt, *Phys. Rev. Lett.* **80**, 261 (1998).

12. V. Kumarappan, M. Krishnamurthy, and D. Mathur, Phys. Rev. Lett. **87**, 085005 (2001).
13. V. Kumarappan, M. Krishnamurthy, and D. Mathur, Phys. Rev. A **66**, 033203 (2002).
14. T. Ditmire, J. Zweiback, V. P. Yanovsky, T.E. Cowan, G. Hays, and K. B. Wharton, Nature (London) **398**, 489 (1999).
15. J. Zweiback, R. A. Smith, T. E. Cowan, G. Hays, K. B. Wharton, V. P. Yanovsky, and T. Ditmire, Phys. Rev. Lett. **84**, 2634 (2000).
16. J. Zweiback, T. E. Cowan, R. A. Smith, J. H. Hartley, R. Howell, C. A. Steinke, G. Hays, K. B. Wharton, J. K. Crane, and T. Ditmire, Phys. Rev. Lett. **85**, 3640 (2000).
17. G. Grillon, Ph. Balcou, J.-P. Chambaret, D. Hulin, J. Martino, S. Moustazis, L. Notebaert, M. Pittman, Th. Pussieux, A. Rouse, J-Ph. Rousseau, S. Sebban, O. Sublemontier, and M. Schmidt, Phys. Rev. Lett. **89**, 065005 (2002).
18. I. Alexeev, T. Antonsen, K.Y. Kim, and H.M. Milchberg, Phys. Rev. Lett. **90**, 103402 (2003).
19. T. D. Donnelly, T. Ditmire, K. Neuman, M. D. Perry, and R. W. Falcone, Phys. Rev. Lett. **76**, 2472 (1996).
20. J. W. G. Tisch, T. Ditmire, D. J. Fraser, N. Hay, M. B. Mason, E. Springate, J. P. Marangos, and M. H. R. Hutchinson, J. Phys. B **30**, L709 (1997).
21. J. W. G. Tisch, Phys. Rev. A **62**, R41802 (2000).
22. H. M. Milchberg, S.J. McNaught, and E. Parra, Phys. Rev. E **64**, 056402 (2001).

23. T. Ditmire, T. Donnelly, A. M. Rubenchik, R. W. Falcone, and M. D. Perry, *Phys. Rev. A* **53**, 3379 (1996).
24. T. Ditmire, E. Springate, J. W. G. Tisch, Y. L. Sha, M. B. Mason, N. Hay, J. P. Marangos, and M. H. R. Hutchinson, *Phys. Rev. A* **57**, 369 (1998).
25. J. Zweiback, T. Ditmire, and M. D. Perry, *Phys. Rev. A* **59**, R3166 (1999).
26. J. Zweiback, T. Ditmire, and M. D. Perry, *Opt. Express* **6**, 236 (2000).
27. E. Parra, I. Alexeev, J. Fan, K. Y. Kim, S. J. McNaught, H. M. Milchberg, *Phys. Rev. E* **62**, R5931 (2000).
28. I. Yu. Skobelev et al., *Zh. Eksp. Teor. Fiz.* **121**, 1124 (2002) [*JETP* **94**, 966 (2002)].
29. M. V. Ammosov, N. B. Delone, and V. P. Krainov, *Zh. Eksp. Teor. Fiz.* **91**, 2008 (1986) [*Sov. Phys. JETP* **64**, 1191 (1987)].
30. W. L. Kruer, *The Physics of Laser Plasma Interaction* (Addison-Wesley, Redwood City, CA, 1988).
31. J. D. Jackson, *Classical Electrodynamics*, 2nd ed. (Wiley, New York, 1975).
32. T. Taguchi, T. M. Antonsen, Jr., H. M. Milchberg, submitted to *Phys. Rev. Lett.*
33. O. F. Hagena and W. Obert, *J. Chem. Phys.* **56**, 1793 (1972).
34. O. F. Hagena, *Rev. Sci. Instrum.* **63**, 2374 (1992).
35. C. Gahn, G. D. Tsakiris, A. Pukhov, J. Meyer-ter-Vehn, G. Pretzler, P. Thirolf, D. Habs, and K. J. Witte, *Phys. Rev. Lett.* **83**, 4772 (1999).
36. C. Gahn, G. D. Tsakiris, G. Pretzler, K. J. Witte, P. Thirolf, D. Habs, C. Delfin, and C.-G. Wahlström, *Phys. Plasmas* **9**, 987 (2002).

37. G. S. Sarkisov, V. Yu. Bychenkov, V. N. Novikov, V. T. Tikhonchuk, A. Maksimchuk, S.-Y. Chen, R. Wagner, G. Mourou, and D. Umstadter, *Phys. Rev. E* **59**, 7042 (1999).
38. T. Auguste, P. D'Oliveira, S. Hulin, P. Monot, J. Abdallah, Jr., A. Ya. Faenov, I. Yu. Skobelev, A. I. Magunov, and T. A. Pikuz, *Pis'ma Zh. Éksp. Teor. Fiz.* **72**, 54 (2000) [*JETP Lett.* **72**, 38 (2000)].

### Chapter 7 References

1. H. M. Milchberg, C. G. Durfee III, and T. J. McIlrath, *Phys. Rev. Lett.* **75**, 2494 (1995).
2. Y. Nagata, K. Midorikowa, M. Obara, H. Tashiro, K. Toyoda, *Phys. Rev. Lett.* **71**, 3774 (1993).
3. B. E. Lemoff, G. Y. Yin, C. L. Gordon III, C. P. J. Barty, S. E. Harris, *Phys. Rev. Lett.* **74**, 1574 (1995).
4. E. Esarey, P. Sprangle, J. Krall, A. Ting, *IEEE Trans. Plasma Sci.* **24**, 252 (1996).
5. A. B. Borisov, A. V. Borovskiy, V. V. Korobkin, A. M. Prokhorov, O. B. Shiryayev, X. M. Shi, T. S. Luk, A. McPherson, J. C. Solem, K. Boyer, and C. K. Rhodes, *Phys. Rev. Lett.* **68**, 2309 (1992).
6. P. Monot, T. Auguste, P. Gibbon, F. Jakober, G. Mainfray, A. Dulieu, M. Louis-Jacquet, G. Malka, and J. L. Miquel, *Phys. Rev. Lett.* **74**, 2953 (1995).
7. K. Krushelnick, A. Ting, C. I. Moore, H. R. Burris, E. Esarey, P. Sprangle, and M. Baine, *Phys. Rev. Lett.* **78**, 4047 (1997).

8. R. Wagner, S.-Y. Chen, A. Maksimchuk, and D. Umstadter, *Phys. Rev. Lett.* **78**, 3125 (1997).
9. J. Fuchs, G. Malka, J. C. Adam, F. Amiranoff, S. S. Baton, N. Blanchot, A. Héron, G. Laval, J. L. Miquel, P. Mora, H. Pépin, and C. Rousseaux, *Phys. Rev. Lett.* **80**, 1658 (1998).
10. C. E. Clayton, K. C. Tzeng, D. Gordon, P. Muggli, W. B. Mori, C. Joshi, V. Malka, Z. Najmudin, A. Modena, D. Neely, and A. E. Dangor, *Phys. Rev. Lett.* **81**, 100 (1998).
11. P. Sprangle, E. Esarey, and A. Ting, *Phys. Rev. Lett.* **64**, 2011 (1990).
12. T. M. Antonsen and P. Mora, *Phys. Rev. Lett.* **69**, 2204 (1992).
13. P. Sprangle, E. Esarey, J. Krall, and G. Joyce, *Phys. Rev. Lett.* **69**, 2200 (1992).
14. G. Shvets, J. S. Wurtele, T. C. Chiou, and T. C. Katsouleas, *IEEE Trans. Plasma Sci.* **24**, 351 (1996).
15. C. G. Durfee III and H. M. Milchberg, *Phys. Rev. Lett.* **71**, 2409 (1993).
16. C. G. Durfee III and H. M. Milchberg, *Phys. Rev. E* **51**, 2368 (1995).
17. J. Fan, T. R. Clark, and H. M. Milchberg, *Appl. Phys. Lett.* **73**, 3064 (1998).
18. S. P. Nikitin, I. Alexeev, J. Fan, and H. M. Milchberg, *Phys. Rev. E* **59**, R3839 (1999).
19. H. M. Milchberg, T. R. Clark, C. G. Durfee III, and T. M. Antonsen, *Phys. Plasmas* **3**, 2149 (1996).
20. S. Jackel, R. Burris, J. Grun, A. Ting, C. Manka, K. Evans, and J. Kosakowski, *Opt. Lett.* **20**, 1086 (1995).

21. M. Borghesi, A. J. Mackinnon, R. Gaillard, O. Willi, A. A. Offenberger, Phys. Rev. E **57**, R4899 (1998).
22. F. Dorchies, J. R. Marquès, B. Cros, G. Matthieussent, C. Courtois, T. Vélikorousov, P. Audebert, J. P. Geindre, S. Rebibo, G. Hamoniaux, and F. Amiranoff, Phys. Rev. Lett. **82**, 4655 (1999).
23. B. Cros, C. Courtois, G. Malka, G. Matthieussent, J. R. Marquès, F. Dorchies, F. Amiranoff, S. Rebibo, G. Hamoniaux, N. Blanchot, and J. L. Miquel, IEEE Trans. Plasma Sci. **28**, 1071 (2000).
24. Y. Ehrlich, C. Cohen, and A. Zigler, Phys. Rev. Lett. **77**, 4186 (1996).
25. Y. Ehrlich, C. Cohen, D. Kaganovich, A. Zigler, R. F. Hubbard, P. Sprangle, and E. Esarey, J. Opt. Soc. Am. B **15**, 2416 (1998).
26. J. Fan, E. Parra, and H. M. Milchberg, Phys. Rev. Lett. **84**, 3085 (2000).
27. T. R. Clark and H. M. Milchberg, Phys. Rev. Lett. **78**, 2373 (1997).
28. T. R. Clark and H. M. Milchberg, Phys. Rev. E **61**, 1954 (2000).
29. S. P. Nikitin, T. M. Antonsen, T. R. Clark, Y. Li, and H. M. Milchberg, Opt. Lett. **22**, 1787 (1997).
30. T. R. Clark, Ph. D. Dissertation, (University of Maryland, 1998).
31. J. Fan, Ph. D. Dissertation, (University of Maryland, 2002).
32. I. S. Alexeev, Ph. D. Dissertation, (University of Maryland, 2003).
33. I. Alexeev, T. M. Antonsen, K. Y. Kim, and H. M. Milchberg, Phys. Rev. Lett. **90**, 103402 (2003).
34. S. Augst, D. Strickland, D. D. Meyerhofer, S. L. Chin, and J. H. Eberly, Phys. Rev. Lett. **63**, 2212 (1989).

35. P. Volfbeyn, E. Esarey, and W. P. Leemans, *Phys. Plasmas* **6**, 2269 (1999).
36. E. W. Gaul, S. P. Le Blanc, A. R. Rundquist, R. Zgadzaj, H. Langhoff, and M. C. Downer, *Appl. Phys. Lett.* **77**, 4112 (2000).
37. K. Y. Kim *et al.*, in *Advanced Accelerator Concepts: Tenth Workshop*, edited by C. E. Clayton and P. Muggli, (AIP, New York, 2002), pp. 646 – 653.

### Appendix A References

1. T. H. Maiman, *Nature* **187**, 493 (1960).
2. R. W. Hellwarth, *Bull. Am. Phys. Soc.* **6**, 414 (1961).
3. F. J. McClung and R. W. Hellwarth, *Proc. IRE* **51**, 46 (1963).
4. W. G. Wagner and B. A. Lengyel, *J. Appl. Phys.* **34**, 2040 (1963).
5. L. E. Hargrove, R. L. Fork, and M. A. Pollack, *Appl. Phys. Lett.* **5**, 4 (1964).
6. H. W. Moker, R. J. Collins, *Appl. Phys. Lett.* **7**, 270 (1965).
7. A. J. DeMaria, D. A. Stetser, H. Heynau, *Appl. Phys. Lett.* **8**, 174 (1966).
8. R. W. Boyd, *Nonlinear Optics* (Academic Press, San Diego, 1992).
9. A. Siegman, *Lasers* (University Science Books, Mill Valley, 1986).
10. Y. R. Shen, *Principles of Nonlinear Optics* (Wiley, New York, 1984).
11. C. E. Cook, *Proc. IRE* **48**, 310 (1960).
12. D. Strickland and G. Mourou, *Opt. Commun.* **56**, 219 (1985).
13. P. Maine, D. Strickland, P. Bado, M. Pessot, and G. Mourou, *IEEE J. Quantum Electron.* **24**, 398 (1988).
14. M. D. Perry and G. Mourou, *Science* **264**, 917 (1994).

15. D. M. Pennington, C. G. Brown, T. E. Cowan, S. P. Hatchett, E. Henry, S. Herman, M. Kartz, M. Key, J. Koch, A. J. MacKinnon, M. D. Perry, T. W. Phillips, M. Roth, T. C. Sangster, M. Singh, R. A. Snavely, M. Stoyer, B. C. Stuart, and S. C. Wilks, *IEEE J. Select. Topics Quantum Electron.* **6**, 676 (2000).
16. T. S. Luk, A. McPherson, G. Gibson, K. Boyer, and C. K. Rhodes, *Opt. Lett.* **14**, 1113 (1989).
17. M. D. Perry, F. G. Patterson, and J. Weston, *Opt. Lett.* **15**, 381 (1990).
18. K. Yamakawa, C. P. J. Barty, H. Shiraga, and Y. Kato, *IEEE J. Quantum Electron.* **QE-27**, 288 (1991).
19. C. Sauteret, D. Husson, G. Thiell, S. Seznec, G. Gray, A. Migus, and G. Mourou, *Opt. Lett.* **16**, 238 (1991).
20. J. B. Kmetec, J. J. Macklin, and J. F. Young, *Opt. Lett.* **16**, 1001 (1991).
21. A. Sullivan, H. Hamster, H. C. Kapteyn, S. Gordon, W. White, H. Nathel, R. J. Blair, and R. W. Falcone, *Opt. Lett.* **16**, 1406 (1991).
22. F. G. Patterson, R. Gonzales, and M. D. Perry, *Opt. Lett.* **16**, 1107 (1991).
23. K. Yamakawa, H. Shiraga, Y. Kato, and C. P. J. Barty, *Opt. Lett.* **16**, 1593 (1991).
24. W.E. White, F. G. Patterson, R. L. Combs, D. F. Price, and R. L. Shepherd, *Opt. Lett.* **18**, 1343 (1993).
25. C. Rouyer, É. Mazataud, I. Allais, A. Pierre, S. Seznec, and C. Sauteret, *Opt. Lett.* **18**, 214 (1993).
26. T. Ditmire and M. D. Perry, *Opt. Lett.* **18**, 426 (1993).
27. C. Le Blanc, G. Grillon, J. P. Chambaret, A. Migus, and A. Antonetti, *Opt. Lett.* **18**, 140 (1993).

28. P. Beaud, M. Richardson, E. J. Miesak, and B. H. T. Chai, *Opt. Lett.* **18**, 1550 (1993).
29. C. N. Danson *et al.*, *Opt. Commun.* **103**, 392 (1993).
30. C. P. J. Barty, C. L. Gordon III, and B. E. Lemoff, *Opt. Lett.* **19**, 1442 (1994).
31. K. Yamakawa, H. Sugio, H. Daido, M. Nakatsuka, Y. Kato, and S. Nakai, *Opt. Commun.* **112**, 37 (1994).
32. J. Zhou, C.-P. Huang, M. M. Murnane, and Henry C. Kapteyn, *Opt. Lett.* **20**, 64 (1995).
33. N. Blanchot, C. Rouyer, C. Sauteret, and A. Migus, *Opt. Lett.* **20**, 395 (1995).
34. T. Ditmire, H. Nguyen, and M. D. Perry, *Opt. Lett.* **20**, 1142 (1995).
35. C. P. J. Barty, T. Guo, C. Le Blanc, F. Raksi, C. Rose-Petruck, J. Squier, K. R. Wilson, V. V. Yakovlev, and K. Yamakawa, *Opt. Lett.* **21**, 668 (1996).
36. A. Sullivan, J. Bonlie, D. F. Price, and W. E. White, *Opt. Lett.* **21**, 603 (1996).
37. P. F. Curley, C. Le Blanc, G. Cheriaux, G. Darpentigny, P. Rousseau, F. Salin, J. P. Chambaret, A. Antonetti, *Opt. Commun.* **131**, 72 (1996).
38. J. P. Chambaret, C. Le Blanc, G. Chériaux, P. Curley, G. Darpentigny, P. Rousseau, G. Hamoniaux, A. Antonetti, and F. Salin, *Opt. Lett.* **21**, 1921 (1996).
39. B. C. Stuart, M. D. Perry, J. Miller, G. Tietbohl, S. Herman, J. A. Britten, C. Brown, D. Pennington, V. Yanovsky, and K. Wharton, *Opt. Lett.* **22**, 242 (1997).
40. K. Yamakawa, M. Aoyama, S. Matsuoka, H. Takuma, C. P. J. Barty, and D. Fittinghoff, *Opt. Lett.* **23**, 525 (1998).
41. K. Yamakawa, M. Aoyama, S. Matsuoka, T. Kase, Y. Akahane, and H. Takuna, *Opt. Lett.* **23**, 1468 (1998).

42. M. D. Perry, D. Pennington, B. C. Stuart, G. Tietbohl, J. A. Britten, G. Brown, S. Herman, B. Golick, M. Kartz, J. Miller, H. T. Powell, M. Vergino, and V. Yanovsky, *Opt. Lett.* **24**, 160 (1999).
43. B. C. Walker, C. Tóth, D. N. Fittinghoff, T. Guo, D. Kim, C. Rose-Petruck, J. A. Squier, K. Yamakawa, K. R. Wilson, and C. P. J. Barty, *Opt. Express* **5**, 196 (1999).

### Appendix B References

1. G. A. Mourou, C. P. J. Barty, and M. D. Perry, *Phys. Today* **51**, 22 (January 1998).
2. R. W. Boyd, *Nonlinear Optics* (Academic Press, San Diego, 1992).
3. Y. R. Shen, *Principles of Nonlinear Optics* (Wiley, New York, 1984).
4. A. McPerson, G. Gibson, H. Jara, U. Johann, T. S. Luk, I. A. McIntyre, K. Boyer, and C. K. Rhodes, *J. Opt. Soc. Am. B* **4**, 595 (1987).
5. X. F. Li, A. L'Huillier, M. Ferray, L. A. Lompré, and G. Mainfray, *Phys. Rev. A* **39**, 5751 (1989).
6. A. L'Huillier, K. J. Schafer, and K. C. Kulander, *Phys. Rev. Lett.* **66**, 2200 (1991).
7. J. L. Krause, K. J. Schafer, and K. C. Kulander, *Phys. Rev. Lett.* **68**, 3535 (1992).
8. A. L'Huillier and Ph. Balcou, *Phys. Rev. Lett.* **70**, 774 (1993).
9. J. J. Macklin, J. D. Kmetec, and C. L. Gordon III, *Phys. Rev. Lett.* **70**, 766 (1993).
10. P. B. Corkum, *Phys. Rev. Lett.* **71**, 1994 (1993).
11. K. C. Kulander, K. J. Schafer, and J. L. Krause, in *Proceedings of the Workshop on Super-Intense Laser Atom Physics (SILAP) III*, edited by B. Piraux (Plenum Press, New York, 1993).

12. F. Krausz, *Opt. & Photon. News* **13**, 62 (May 2002).
13. P. M. Paul, E. S. Toma, P. Breger, G. Mullot, F. Augé, Ph. Balcou, H. G. Muller, and P. Agostini, *Science* **292**, 1689 (2001).
14. M. Hentschel, R. Kienberger, Ch. Spielmann, G. A. Reider, N. Milosevic, T. Brabec, P. Corkum, U. Heinzmann, M. Drescher, and F. Krausz, *Nature* **414**, 509 (2001).
15. R. Kienberger, M. Hentschel, M. Uiberacker, Ch. Spielmann, M. Kitzler, A. Scrinzi, M. Wieland, Th. Westerwalbesloh, U. Kleineberg, U. Heinzmann, M. Drescher, and F. Krausz, *Science* **297**, 1144 (2002).
16. M. Drescher, M. Hentschel, R. Kienberger, M. Uiberacker, V. Yakovlev, A. Scrinzi, Th. Westerwalbesloh, U. Kleineberg, U. Heinzmann, and F. Krausz, *Nature (London)* **419**, 803 (2002).
17. T. Tajima and J. M. Dawson, *Phys. Rev. Lett.* **43**, 267 (1979).
18. W. P. Leemans and E. Esarey, *Advanced Accelerator Concepts: Eight Workshop*, edited by Lawson, Bellamy, and Brosius, (AIP, New York, 1999).
19. C. Rischel, A. Rousse, I. Uschmann, P. A. Albouy, J. P. Geindre, P. Audebert, J. C. Gauthier, E. Förster, J. L. Martin, and A. Antonetti, *Nature (London)* **490**, 390 (1997).
20. C. W. Siders, A. Cavalleri, K. Sokolowski-Tinten, Cs. Tóth, T. Guo, M. Kammler, M. Horn von Hoegen, K. R. Wilson, D. von der Linde, C. P. J. Barty, *Science* **286**, 1340 (1999).
21. B. A. Remington, D. Arnett, R. P. Drake and H. Takabe, *Science* **284**, 1488 (1999).

22. M. J. Edward, A. J. MacKinnon, J. Zweiback, K. Shigemori, D. Ryutov, A. M. Rubenchik, K. A. Keilty, E. Liang, B. A. Remington, and T. Ditmire, *Phys. Rev. Lett.* **87**, 085004 (2001).
23. K. W. D. Ledingham *et al.*, *Phys. Rev. Lett.* **84**, 899 (2000).
24. T. E. Cowan *et al.*, *Phys. Rev. Lett.* **84**, 903 (2000).
25. J. Lindl, *Phys. Plasmas* **2**, 3933 (1995).
26. J. D. Lindl, *Inertial Confinement Fusion: The Quest for Ignition and Energy Gain Using Indirect Drive* (Springer-Verlag, New York, 1998).
27. M. Tabak, J. Hammer, M. E. Glinsky, W. L. Kruer, S. C. Wilks, J. Woodworth, E. M. Campbell, M. D. Perry, and R. J. Mason, *Phys. Plasmas* **1**, 1626 (1994).
28. W. Heisenberg and H. Z. Euler, *Z. Phys.* **98**, 714 (1936).
29. J. Schwinger, *Phys. Rev.* **82**, 664 (1951).
30. C. Bula *et al.*, *Phys. Rev. Lett.* **76**, 3116 (1996).
31. D. L. Burke *et al.*, *Phys. Rev. Lett.* **79**, 1626 (1997).
32. C. J. Joshi and P. B. Corkum, *Phys. Today* **48**, 36 (January 1995).
33. P. Gibbon and E. Förster, *Plasma Phys. Controll. Fusion* **38**, 769 (1996).
34. M. Protopapas, C. H. Keitel, and P. L. Knight, *Rep. Prog. Phys.* **60**, 389 (1997).
35. T. Brabec and F. Krausz, *Rev. Mod. Phys.* **72**, 545 (2000).

### Appendix C References

1. V. Wong and I. A. Walmsley, *Opt. Lett.* **19**, 287 (1994).
2. E. Tokunaga, A. Terasaki, and T. Kobayashi, *J. Opt. Soc. Am. B* **12**, 753 (1995).

## Appendix D References

1. R. R. Alfano, and S. L. Shapiro, Phys. Rev. Lett. **24**, 584 (1970).
2. R. R. Alfano, *The Supercontinuum Laser Source* (Springer-Verlag, New York, 1989).
3. A. Brodeur and S. L. Chin, J. Opt. Soc. Am. B **16**, 637 (1999).
4. C. J. K. Richardson, J. B. Spicer, R. D. Huber, and H. W. H. Lee, Opt. Lett. **26**, 1105 (2001).
5. W. L. Smith, P. Liu, and N. Bloembergen, Phys. Rev. A **15**, 2396 (1977).
6. J. H. Glowina, J. Misewich, and P. P. Sorokin, J. Opt. Soc. Am. B **3**, 1573 (1986).
7. P. B. Corkum, C. Rolland, and T. Srinivasan-Rao, Phys. Rev. Lett. **57**, 2268 (1986).
8. P. B. Corkum and C. Rolland, IEEE J. Quantum Elect. **25**, 2634 (1989).
9. H. Nishioka, W. Odajima, K. Ueda, and H. Takuma, Opt. Lett. **20**, 2505 (1995).
10. Q. Xing, K. M. Yoo, and R. R. Alfano, Appl. Opt. **32**, 2087 (1993)
11. I. Golub, Opt. Lett. **15**, 305 (1990).
12. O. G. Kosareva, V. P. Kandidov, A. Brodeur, C. Y. Chien, and S. L. Chin, Opt. Lett. **22**, 1332 (1997).
13. B. D. Paul, M. L. Dowell, A. Gallagher, and J. Cooper, Phys. Rev. A **59**, 4784 (1999).
14. M. Nisoli, S. De Silvestri, and O. Svelto, Appl. Phys. Lett. **68**, 2793 (1996).
15. M. Nisoli, S. De Silvestri, O. Svelto, R. Szipöcs, K. Ferencz, Ch. Spielmann, S. Sartania, and F. Krausz, Opt. Lett. **22**, 522 (1997).

### **Appendix E References**

1. E. Tokunaga, A. Terasaki, and T. Kobayashi, *J. Opt. Soc. Am. B* **13**, 496 (1996).

### **Appendix F References**

1. M. Takeda, H. Ina, and S. Kobayashi, *J. Opt. Soc. Am.* **72**, 156 (1982).

### **Appendix G References**

1. CVI Laser Corp., *Laser Optics and Coatings Catalog*, (CVI, Albuquerque, 2002).
2. Schott Glass Technologies Inc., *Schott Optical Glass Catalog*, (1992).

### **Appendix H References**

1. S. P. Nikitin, Ph. D. dissertation, (University of Maryland, 1998).
2. J. Fan, Ph. D. dissertation, (University of Maryland, 2002).
3. S. P. Nikitin, T. M. Antonsen, T. R. Clark, Y. Li, and H. M. Milchberg, *Opt. Lett.* **22**, 1787 (1997).